Electroanalysis in nanoparticle assemblies

Electroanalysis in Nanoparticle Assemblies

by

Susan J. Stott
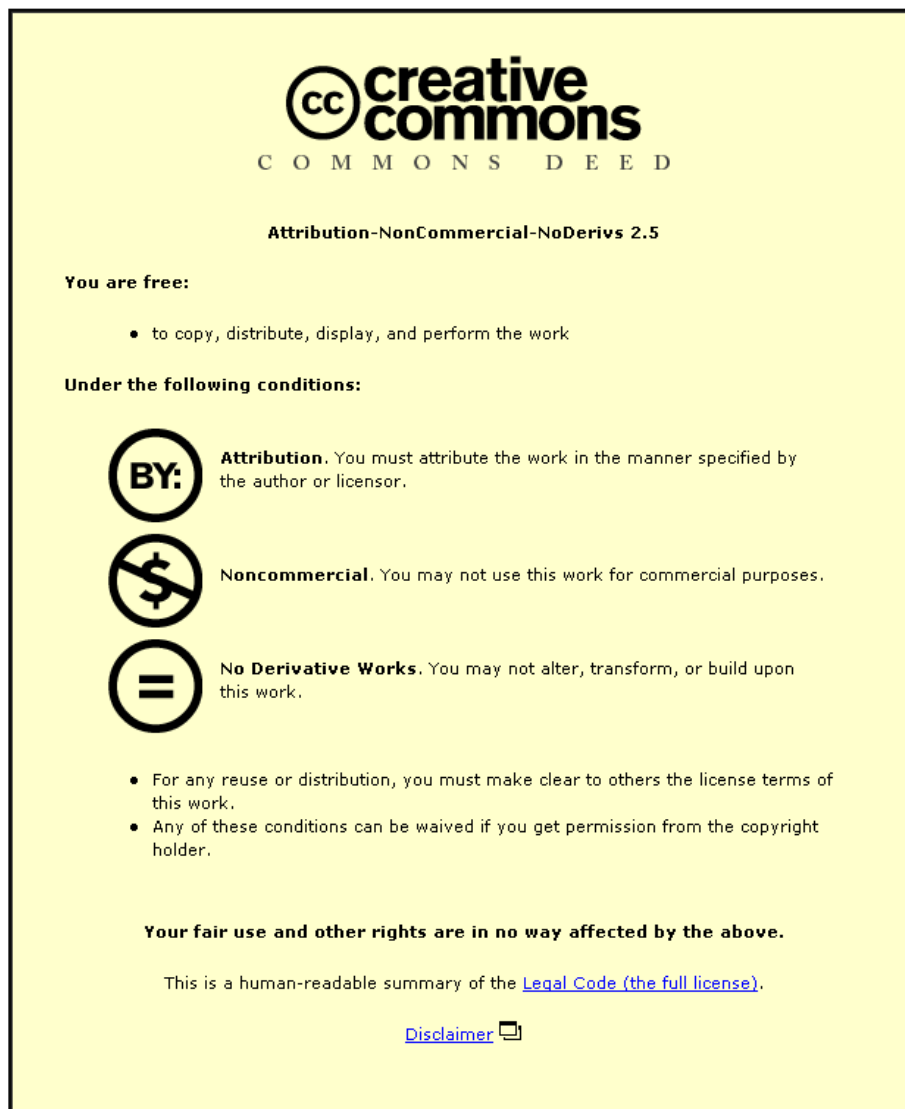
Doctoral Thesis

Submitted in partial fulfilment of the requirements

for the award of

Doctor of Philosophy

of

Loughborough University

May 2007

Loughborough University

Contents

Acknowledgements

A big thank you goes to:

- The RSC and the EPSRC for the Analytical Science Studentship
- My supervisors Roger Mortimer and Frank Marken
- The physical chemistry research groups at Loughborough and Bath Universities
- Loughborough University final year project student Avinder S. Bhambra for assistance with the TiO_2 mono-layer work in chapter 2
- Visiting PhD student Galyna Shul for assistance with the droplet work in chapter 4
- Pauline King at Loughborough University for XRD characterisation of TiO_2 and CeO_2 nanoparticles
- Sandie Dann at Loughborough University for XRD characterisation of TiC nanoparticles
- John Bates at Loughborough University for assistance obtaining FEGSEM and TEM images
- John Spray at Loughborough University for cutting the ITO coated glass to size
- Karen Edler in Bath for SAXS-WAXS characterisation on TiO_2 Nafion® nanoparticles

Abstract

This thesis is concerned with the deposition of nanoparticle films onto boron-doped diamond and tin-doped indium oxide (ITO) surfaces and the characterisation of the films using electron microscopy, powder diffraction methods and quartz crystal microbalance (QCM) data. The redox behaviour of the porous films was examined using cyclic voltammetry in various media to investigate potential electroanalytical applications.

TiO_2 (anatase) mono-layer films were immobilised onto an inert boron-doped diamond substrate. Cyclic voltammetry experiments allowed two distinct steps in the reduction - protonation processes to be identified that are consistent with the formation of Ti(III) surface sites accompanied by the adsorption of protons. Preliminary data for electron transfer processes at the reduced TiO_2 surface such as the dihydrogen evolution process and the 2 electron - 2 proton reduction of maleic acid to succinic acid are discussed.

Novel multi-layer TiO_2 films were deposited with a variety of organic binder molecules onto ITO substrates. The redox reactivity of Cu^{2+} with 1,4,7,10-tetraazacyclododecane- 1,4,7,10-tetrayl- tetrakis (methyl-phosphonic acid) in solution and immobilised on an electrode surface are investigated. The influences of film thickness, scan rate, and pH on the electrochemistry of immobilised pyrroloquinoline quinone was investigated with two possible electron transport processes observed. The thickness of TiO_2 phytate films was found to change the shape of the resulting cyclic voltammograms dramatically. Computer simulation and impedance spectroscopy allowed insights into the diffusion of electrons to be obtained. 1,1'-Ferrocenedimethanol was employed as an adsorbing redox system to study the voltammetric characteristics of carboxymethyl-γ-cyclodextrin films and evidence for two distinct binding sites is considered. The apparent transport coefficients for dopamine and $Ru(NH_3)_6^{3+}$ are estimated for TiO_2 Nafion® films.

The electrochemical processes in biphasic electrode systems for the oxidation of

water-insoluble *N,N*-didodecyl-*N′,N′*-diethyl-benzene-diamine (DDPD) pure and dissolved in di-(2-ethyl-hexyl)phosphate (HDOP) immersed in aqueous electrolyte media are described. Transfer of the anion from the aqueous electrolyte phase into the organic phase accompanies the oxidation of pure DDPD. In the presence of HDOP, oxidation is accompanied by proton exchange. The electrochemically driven proton exchange process occurs over a wide pH range. Organic microdroplet deposits of DDPD in HDOP at basal plane pyrolytic graphite electrodes are studied using voltammetric techniques and compared to the behaviour of organic microphase deposits in mesoporous TiO_2 thin films. Two types of TiO_2 thin film electrodes were investigated, (i) a 300-400 nm film on ITO and (ii) a 300-400 nm film on ITO sputter-coated with a 20 nm porous gold layer. The latter biphasic design is superior.

Titanium carbide (TiC) nanoparticles were deposited onto ITO electrodes. Partial anodic oxidation and formation of novel core-shell TiC-TiO_2 nanoparticles was observed at applied potentials positive of 0.3 V *vs.* SCE. Significant thermal oxidation of TiC nanoparticles by heating in air occurs at 250 °C leading to core-shell TiC-TiO_2 nanoparticles, then TiO_2 (anatase) at *ca.* 350 °C, and TiO_2 (rutile) at temperatures higher than 750 °C. The electrocatalytic properties of the core-shell TiC-TiO_2 nanoparticulate films were surveyed for the oxidation of hydroquinone, ascorbic acid, dopamine and nitric oxide (NO) in aqueous buffer media.

Mono- and multi-layer CeO_2 deposits on ITO are shown to be electrochemically active. A reduction assigned to a Ce(IV/III) process has been observed and follow-up chemistry in the presence of phosphate discovered. The interfacial formation of $CePO_4$ has been proven and effects of the deposit type, pH and phosphate concentration on the process analysed. The electrochemistry of multi-layer CeO_2 nanoparticulate films in organic solvent is shown to be more stable.

Keywords

Titania, titanium carbide, ceria, nanoparticle, assembly, ITO, cyclic voltammetry, biphasic voltammetry, electroanalysis.

List of Abbreviations

a	activity of redox species (M)
a	constant
A	electrode area (m^2)
A	frequency factor
A.C.	alternating current
ADC	analogue to digital converter
B_m	width in radians of the diffraction peaks (at half maximum height) of the test sample
B_s	width in radians of the diffraction peaks (at half maximum height) of a highly crystalline standard sample ($0.1°$)
bppg	basal plane pyrolytic graphite
BSE	backscattered electrons
c	concentration (M)
C	capacitor
C	capacitance (F)
CCD	charged couple device
CeO_2	cerium (IV) oxide or ceria
CHHCA	1,2,3,4,5,6-cyclohexanehexacarboxylic acid
d	distance between discrete crystallographic planes
D	diffusion coefficient ($m^2\ s^{-1}$)
D_{app}	apparent diffusion coefficient
D.C.	direct current
DDPD	N,N-Didodecyl-$N',N'-$ diethyl-benzene-1,4-diamine
e^-	electron
E	potential (V)
EDX	energy-dispersive X-ray analysis
E_e	equilibrium potential (V)
EELS	electron energy-loss spectroscopy
E_m	maximum potential amplitude (V)
E_{mid}	midpoint potential (V)
$E^{o'}$	formal reduction potential (V)

E_p	peak potential (V)
E_{pk}	peak potential (V)
f	frequency (Hz)
f_0	resonant frequency of the fundamental mode of quartz crystal resonator (Hz)
F	Faraday constant (96485 C mol^{-1})
FEGSEM	field emission gun scanning electron microscopy
GPES	general purpose electrochemical system
HDOP	di-(2-ethyl-hexyl)phosphate or dioctylphosphate
HOMO	highest occupied molecular orbital
i	magnitude of current
i_m	maximum current amplitude (A)
i_o	standard exchange current
i_p	peak current (A)
I	current (A)
I_p	peak current (A)
$I_{p,a}/I_{p,c}$	ratio of the anodic and cathodic peak current
ITIES	interface between two immiscible electrolyte solutions
ITO	tin-doped indium oxide
j	flux of reactant reaching the electrode surface (mol m^{-2} s^{-1})
k	Boltzmann constant (1.381 x 10^{-23} JK^{-1})
k_o	heterogeneous rate constant
$K_{partitioning}$	equilibrium partitioning coefficient
K_{red}	binding constant
LUMO	lowest unoccupied molecular orbital
m	mass (g)
MRI	magnetic resonance imaging
n	integer
n	number of electrons
NADH	dihydronicotinamide adenine dinucleotide
NO	nitric oxide
O	oxidised form of redox species
PAA	poly(acrylic acid)

PAH	poly(allylamine hydrochloride)
PDDA	polydiallyldimethylammonium
PEI	poly(etherimide)
PQQ	pyrroloquinoline quinone
PSS	poly(sodium 4-styrenesulfonate)
q	charge density ($C\ m^{-2}$)
Q	tangent of the scattering angle in SAXS/WAXS
QCM	quartz crystal microbalance
r	particle radius
R	reduced form of redox species
R	resistor
R	resistance (Ω)
R	universal gas constant (8.314 $JK^{-1}mol^{-1}$)
Ref.	references
$[R]_0$	concentration of reactant at the electrode surface (M)
RT	room temperature
SAD	selective area electron diffraction
SAXS	small angle X-ray scattering
SCE	saturated calomel electrode
SED	secondary electrons detection
SEM	scanning electron microscopy
STEM	scanning transmission electron microscopy
t	crystallite thickness (Å)
t	time (seconds)
T	absolute temperature (K)
TAPA	1,4,7,10- tetraazacyclododecane- 1,4,7,10-tetrayl- tetrakis (methyl-phosphonic acid)
TEM	transmission electron microscopy
TiC	titanium carbide
TiO₂	titanium (IV) oxide or titania
U	potential (V)
v	potential scan rate (Vs^{-1})
v$_{trans}$	potential scan rate transition point (Vs^{-1})

V	electrode volume (m^3)
WAXS	wide angle X-ray scattering
x	potential (V)
x_o	constant shift in potential (V)
XRD	X-ray diffraction
z_i	the charge of the ion
Z	impedance (Ω)
Z$'$	real part of impedance (Ω)
Z$''$	imaginary part of impedance (Ω)
α	transfer coefficient
δ	film thickness (m)
$\Delta G^{\ddagger}_{red}$	free energy of activation
η	viscosity (centipoises)
η	overpotential (V)
θ	angle between the atomic planes and the incident X-ray beam in XRD
θ	fraction of the electrode surface covered by the adsorbate
θ	phase difference in impedance spectroscopy
λ	wavelength (Å)
μ_i	chemical potential (V)
$\widetilde{\mu}_i$	electrochemical potential (V)
μ_i^0	standard chemical potential (V)
μ_q	shear modulus of quartz (2.947 x 10^{11} g cm^{-1} s^2)
ρ_q	density of quartz (2.648 g/cm^3)
Φ_i	the electrical potential of the ion (V)

Chapter 1

Introduction

1.1. Aims

The main aims of the work contained in this thesis were:

1. To form new functionalised mesoporous membranes from inorganic TiO_2 and CeO_2 nanoparticles and organic binder precursors, to investigate and characterise their properties, and to employ them as tools in electroanalysis.

2. To investigate novel designs based on biphasic membranes in addition to simple membrane systems filled with one phase.

3. To form, characterise and investigate potential electro-catalytic properties of nanoparticle films composed of TiC and core-shell TiC-TiO_2.

1.2. Introduction to Nanoparticles

A nanoparticle can be described as a microscopic particle whose size is between 1 nm and 100 nm in diameter.[1] Materials composed of nano-scale particles are of interest, as they have properties between those described by solid-state physics in bulk materials and the quantum effects of atoms and molecules.[2] A range of chemical and physical properties have been shown to be dependent on the size of the particles, including optical properties, magnetic properties, melting points, and surface reactivity.[3] An example of this is the ability to lower the sintering temperature of a material by bringing it into a nanoparticulate state. In the field of electrochemistry and fuel cell technology, another desirable property of materials constructed of nanoparticles, is a high chemical potential. This is due to an inherent large surface area to volume ratio and therefore the ability to convey a large number of active sites.[4]

Nanoparticles can be formed from a range of materials with various properties. For example metal,[5] dielectric[6] and semiconductor[7] nanoparticles have been formed, as well as hybrid structures such as core-shell nanoparticles.[8] It is possible to form structures on a nanoscale, with nanospheres,[9] nanorods,[10] and nanotubes[11] being just a few of the shapes that have been grown. More unusual nanostructures include semiconductor quantum dots[12] and nanocrystals.[13] The development of different shaped nanostructures with varying properties has led to their use in a wide range of areas, for instance power/energy,[14] medical,[15] engineering,[16] consumer goods,[17] environmental[18] and electronic[19,20] applications. The applications of nanoparticles are not confined to recent years, with clusters of gold nanoparticles reported to have been used over 2000 years ago to generate vivid colours in Roman glass.[2]

The manufacture of nanoparticles can be divided into four main synthetic routes, (i) wet chemical processes, (ii) mechanical processes, (iii) 'form-in-place' processes and (iv) gas phase synthesis. Wet chemical processes (e.g. colloidal chemistry and sol-gels), entail the mixture of well-defined quantities of ionic solutions under controlled heat, temperature and pressure conditions to promote the formation of insoluble compounds that precipitate out of solution. A large variety of mono-dispersed compounds can be produced cheaply using this technique (including inorganic, organic and some metals) with a high degree of control over the particle size.

Mechanical processes (e.g. grinding and milling) are a simple, low cost method of producing fine inorganic and metal powder materials from coarse feedstock powders. Disadvantages include extensive particle size distributions, agglomeration of the powders and contamination from the process equipment. 'Form-in-place' processes (e.g. lithography, vacuum deposition and spray coatings) allow the fabrication of nanostructured layers and coatings on a substrate. These nanoparticle deposits can then be scraped from the substrate if necessary, to give a dry powder, however this tends to be an inefficient route for the production of dry nanoparticle powders.

Gas phase synthesis consists of a number of techniques including laser ablation, flame pyrolysis, high temperature evaporation and plasma synthesis. Laser ablation involves the physical erosion and evaporation of a material onto a substrate and can be utilised to manufacture a large number of nanomaterials, however the production rates are slow.

It is necessary to consider possible negative aspects of nanoparticles along with the good. In a world where the threat of terrorist attack is in the media on a regular basis, the idea of tailored microscopic particles being readily produced and released could cause concern.

1.3. Film Deposition Techniques

The ability to make organised films composed of macromolecules and nanoparticles is very important. There are many different methods used for the assembly of very thin films with varying levels of molecular order and stability. These include spin coating,[21] solution casting,[22] thermal deposition,[23] layer-by-layer assembly,[24] self-assembly,[25] and Langmuir-Blodgett techniques.[26] The optimum combinations of molecular order and stability of films will determine their practical usefulness.[27] Freestanding liquid crystalline films are among the most ordered macromolecular films[28] but they are unstable.

It is possible to construct amphiphile multi-layers with a thickness from 5-500 nm using the Langmuir-Blodgett (LB) method. The term Langmuir-Blodgett comes from the names of a research scientist and his assistant, Irving Langmuir and Katherine Blodgett, who discovered unique properties of thin films in the early 1930s.[29]

A LB film contains one or more layer of an organic material, deposited from the surface of a liquid onto a solid by immersing (or emersing) the solid substrate into (or from) the liquid. A mono-layer is added with each immersion or emersion step, as a result films with very accurate thickness can be formed. The mono-layers are

usually comprised of polar molecules with a hydrophilic head and a hydrophobic tail (e.g. fatty acids). The deposition process is schematically shown in Figure 1.1A.

The amphiphilic nature of the molecules dictates the orientation of the molecules at the interface (air/water or oil/water) in such a way that the polar head group is immersed in the water and that the long hydrocarbon chain is pointing towards air or oil. The hydrocarbon chain of the substance used for mono-layer studies has to be long enough in order to be able to form an insoluble mono-layer. If the hydrocarbon chain is too short (though still insoluble in water), the amphiphile on the water surface tend to form micelles. These micelles are water soluble, which prevents the build-up of a mono-layer at the interface. Conversely if the length of the chain is too long the amphiphile tends to crystallize on the water surface and therefore does not form a mono-layer. The optimal length for the hydrocarbon chain is difficult to determine because the ability to form a film also depends on the polar component of the amphiphile. The amphiphile molecules are deposited onto the water surface in solution with a volatile organic solvent that evaporates to leave the floating mono-layer. Consequently it is necessary for the amphiphile to be soluble in an organic solvent that is highly volatile and water insoluble (chloroform or hexane are commonly used).

A further complication of the LB technique is the need to maintain a constant molecular density or surface pressure while simultaneously dipping the solid substrate up and down through the liquid phase. This is achieved using a computer controlled feedback system between an electrobalance measuring the surface pressure and a barrier moving mechanism controlling the available area for the mono-layer molecules.

The LB-technique is one of the most frequently used deposition procedures for the preparation of thin films as it enables (i) the precise control of the mono-layer thickness, (ii) homogeneous deposition of the mono-layer over large areas and (iii) the possibility to make multi-layer structures with varying layer composition. An additional advantage of the LB technique is that mono-layers can be deposited on almost any kind of solid substrate.
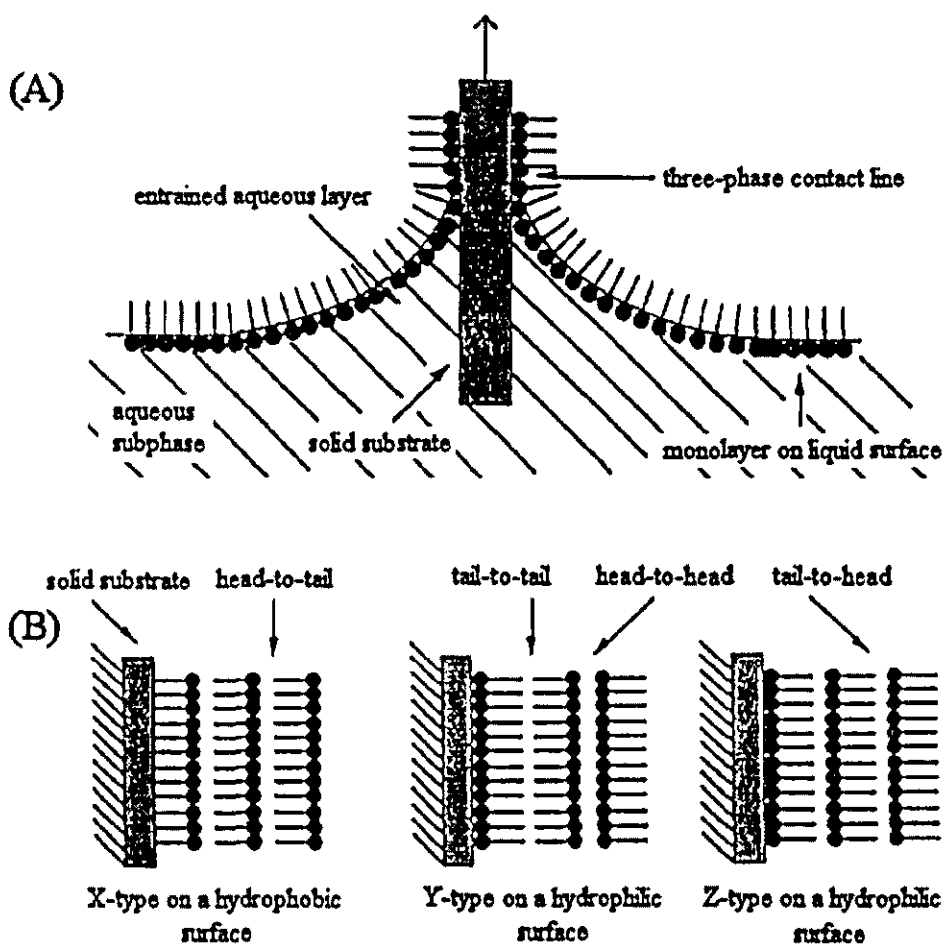
Figure 1.1. A) Deposition of a floating mono-layer on a solid substrate and (B) different types of deposited LB films.[30]

The successive deposition of mono-layers on the same substrate leads to the production of different types of LB multi-layer films (see Figure 1.1B). The most common example is the Y-type multi-layer, which is produced when the mono-layer deposits to the solid substrate in both up and down directions. When the mono-layer deposits only in the up or down direction the multi-layer structure is called either Z-type or X-type. Intermediate structures are occasionally observed for some LB multi-layers and are often referred to be XY-type multi-layers

However LB films possess inherent flaws at the lipid grain borders. The presence of inhomogenities in the floating mono-layer, high solution viscosity, incorrect surface conditions and contraction of the film while drying all contribute to possible flaws in the film deposited.[31]

In biomaterials in particular, another method called monolayer self-assembly can be applied to surface modification and is based on the strong preferential adsorption of a molecule to a substrate surface. Silane and thiol compounds have been shown to form dense mono-layers on silicon and gold surfaces respectively with the organic tail group pointing outwards from the substrate surface (see Figure 1.2).[32]

Self-assembled mono-layer films form rapidly on the substrate, however it is often necessary to use adsorption times of 15 hours or more to obtain well-ordered, defect-free films, furthermore adsorption times of two to three days are favoured for the formation of the highest-quality mono-layers. This technique typically allows the self-assembly of mono-layer films 2 - 5 nm thick.[33] The application of molecules with different tail groups means the resulting chemical surface functionality can be widely varied. Alternatively, it is also possible to chemically functionalise the tail groups by performing reactions after assembly of the mono-layer. The deposition of molecules with a functional group on each end also allows the manufacture of multi-layer films.
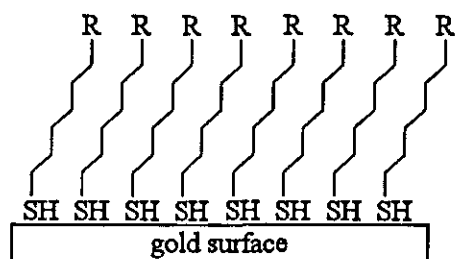
Figure 1.2. Example of a self assembled mono-layer for a thiol compound on a gold substrate surface.

An additional method that is widely used for the industrial manufacture of thin films is spin coating.[34] A typical spin coating deposition process involves placing a solution of the film components onto the middle of a substrate and then spinning the substrate at high speed (typically around 3000 rpm). Centripetal acceleration will cause the fluid to spread across the surface, with excess fluid spinning off the edges of the substrate, leaving a thin layer of deposit on the surface. The applied solvent is usually volatile, and simultaneously evaporates, thus the higher the angular speed of

rotation, the thinner the film. The thickness of the film also depends on the nature of the solution (e.g. concentration, viscosity, drying rate, surface tension). Subtle variations in the parameters that define the spin process can therefore result in large variations in the coated film. After spinning is stopped many applications require that heat treatment or "firing" of the coating be performed along with any necessary further chemical modification. One of the most important factors in spin coating is repeatability since edge effects are often seen as the fluid flowing uniformly outward must form droplets at the edge to be thrown off and removed.

Thermal deposition offers another method of depositing films, typically involving the accumulation of macromolecules onto a substrate in a controlled atmosphere at temperatures greater than 950 °C.[35] However, these methods do not allow the molecular order in the films to be controlled.

A further method for film self-assembly that utilises the alternate adsorption of oppositely charged macromolecules such as polymers,[36] nanoparticles[37] and proteins[38] was first reported by Decher[39] in 1991. The assembly of alternating layers of oppositely charged species is simple and provides the opportunity to form 5-500 nm thick films with mono-layers of various substances and compositions. Successful layer-by-layer procedures are reported where the components possess high mass and multiple binding sites making the deposition sufficiently irreversible allowing the next layer to be deposited. Investigations into the influence of the average molecular weight of polymers on film formation noted that those with higher molecular weights typically produced more stable films.[40] The average thickness of a single layer deposited will depend on a number of other factors including the size and concentration of the two alternately charged species. For multi-layer films, the intermolecular forces (hydrophobic,[41] ion-dipole, dipole-dipole and hydrogen bonding[42]) will influence the structure of the film deposited.

These multi-layer films deposited using layer-by-layer procedures have a lower molecular order than Langmuir-Blodgett or freestanding films (due to lack of mono-dispersity of the nanoparticle building block) but they have the advantage of high strength and easy preparation and modification.[27] This layer-by-layer or directed

assembly methodology was employed here to form thin oxide – organic composite films for application in electroanalysis. Investigating novel methods of manufacturing and applying nano-scale surface modified electrodes can have a number of benefits and may lead to new insights and mechanisms.

1.4. Electrochemical Theory & Techniques

1.4.1. Introduction to Electrochemistry & Electrode Processes

The field of electrochemistry includes a large number of topics[43] including:

1. Different phenomena (electrophoresis and corrosion)
2. Devices (electroanalytical sensors, electrochromic displays, batteries and fuel cells)
3. Technologies (e.g. the electroplating of metals and the large-scale production of aluminium and chlorine)

The main focus of section 1.4 is the application of electrochemical methods to the study of chemical systems, however the basic principles of electrochemistry described are relevant to all three areas of interest listed above.

Electrochemical experiments are concerned with the processes and factors that influence the transport of charge between two adjacent chemical phases, typically between an electronic conductor (electrode), immersed in an ionic conductor (electrolyte solution). Electrochemical experiments are achieved by completing an electrical circuit between two electrodes immersed in the solution phase. On application of a sufficient potential between the two electrodes in the presence of a suitable reactant, a current will start to flow. The flow of electrons in the electrode is transformed into a flow of cations and anions in solution. Chemical reactions are required to couple electron flow and ion flow and occur simultaneously at both electrodes. Usually only the process at one of the electrodes (the working electrode) is of interest.

A simple example of an electrode process involves the transfer of electrons between an inert metal electrode and an ion or molecule in solution. However electrode reactions are not restricted to simple electron transfer reactions and it is possible to observe a wide range of chemistry at an electrode surface.[44]

For example, the reactant may be:

1. Inorganic, organic or bioorganic
2. Solid (including the electrode itself), a gas or the solvent as well as a dissolved species
3. Neutral, cationic or anionic

It is also possible that the electrode may not be a metal; alternatives include materials with metal type conductivity (e.g. carbons, oxides and conducting polymers), a semi-conductor or an insulator. The composition of the electrode can also vary greatly from a bulk material, to a coating on a conducting substrate or a complex structure (e.g. a porous gas electrode).

1.4.2. Equilibrium Electrochemistry

The simple case of an electron transfer process between an inert metal electrode and an ion or molecule in solution can be represented by equation 1.1 in which n electrons are transferred.

$$O_{(aq)} + ne^-_{(m)} \rightleftharpoons R_{(aq)} \qquad (1.1)$$

At equilibrium, i.e. in the absence of any net current, the concentrations of O (oxidised form of redox species) and R (reduced form of redox species) are equal and cannot change, forcing the working electrode to take up the equilibrium potential for the solution.

This equilibrium potential, E_e, may be measured directly using a digital voltmeter or

calculated from the Nernst equation (equation 1.2).

$$E_e = E_e^{o'} + \frac{2.3RT}{nF} \log \frac{a_{ox}}{a_{red}}$$
(1.2)

Where E is the electrode potential, R is the universal gas constant (8.314 $JK^{-1}mol^{-1}$), T is the absolute temperature (K), F is the Faraday constant (96485 C mol^{-1}) and a_{ox} and a_{red} are the activities of oxidised and reduced species respectively. For low concentrations, the activity of the ions is assumed to be equal to their concentrations.

For the general electrode reaction in equation 1.3, the Nernst equation is given by equation 1.4, where $E_e^{o'}$ is the formal equilibrium electrode potential.

$$pP + qQ + ne^- \rightleftharpoons xX + yY$$
(1.3)

$$E_e = E_e^{o'} + \frac{2.3RT}{nF} \log \frac{(a_P)^p (a_Q)^q}{(a_X)^x (a_Y)^y}$$
(1.4)

$E_e^{o'}$ is frequently replaced by E_e^o, the standard equilibrium electrode potential, where the concentrations of O and R have unit activity and the potential is measured relative to the standard hydrogen electrode (SHE).[45]

Equilibrium electrochemical measurements enable thermodynamic parameters (reaction free energies, entropies, and enthalpies) and equilibrium constants (solubility products and activities) to be readily obtained.

1.4.3. Electrolysis

The application of a potential (different to E_e) to the electrochemical cell will induce the flow of current, which stimulates the exchange of electrons between the

electrode and active molecules in solution (e.g. Fe^{3+}). This exchange of electrons alters the oxidation state of the molecule, and electrolysis occurs. The transfer of electrons can occur in either direction, at an anode, electrons pass from the solution phase to the electrode as the electroactive species is oxidised (equation 1.5).

$$Fe^{2+}_{(aq)} \rightarrow Fe^{3+}_{(aq)} + e^-_{(m)} \qquad (1.5)$$

Conversely, at a cathode, the electron flow is in the opposite direction where a molecule in solution accepts an electron from the electrode so that the electroactive species in solution is reduced (equation 1.6).

$$Fe^{3+}_{(aq)} + e^-_{(m)} \rightarrow Fe^{2+}_{(aq)} \qquad (1.6)$$

Many species are electro-active and the potential at which oxidation or reduction occurs is characteristic of the particular species.[46,47,48]

The magnitude of the current (i) is given by equation 1.7.

$$i = nFAj \qquad (1.7)$$

Where n is the number of electrons, A is the electrode area (cm^2), and j is the 'flux' of reactant reaching the electrode surface (mole cm^{-2} s^{-1}). For a kinetically limited process, j is defined by equation 1.8.

$$j = k_0[R]_0 \qquad (1.8)$$

Where k_0 is the heterogeneous rate constant for the electron transfer reaction and $[R]_0$ the concentration of the reactant at the electrode surface. Equation 1.8 assumes that the reaction rate is first order, this is often but not always observed.

The act of inducing a current through the electrochemical cell and the resultant conversion of the redox active species at the electrode/electrolyte interface, will alter $[R]_0$ so that it is no longer equal to the concentration of R in the bulk of the

electrolyte solution. This can be explained by the tendency for the rate of depletion of R at the electrode surface through electrolysis to be faster than the rate at which R is replenished by diffusion from the bulk solution.

The observed current therefore may be dependent on the mass transport of reactants and products to and from the electrode surface. Alternatively the rate-determining factor could be the rate of electron transfer. From the size of the current, both the thermodynamics (the ability of the molecules to exchange electrons) and the kinetics (chemical rate constant) can be determined.

1.4.4. The Rate of Electron Transfer

For the simple reaction (equation 1.9) where a single electron is transferred, the first-order heterogeneous rate constants for the forward (reductive) and back (oxidative) electron transfer reactions are defined by k_{red} and k_{ox}.

$$O_{(aq)} + e^-_{(m)} \underset{k_{ox}}{\overset{k_{red}}{\rightleftharpoons}} R_{(aq)} \qquad (1.9)$$

Using equations 1.7 and 1.8, the current for the reductive (i_c) and oxidative (i_a) components of reaction 1.9 can be predicted.

$$i_c = FAk_{red}[O]_o \qquad (1.10)$$

$$i_a = FAk_{ox}[R]_o \qquad (1.11)$$

The net current, i, is equal to the sum of the anodic (i_a) and cathodic (i_c) currents, and can by estimated using equation 1.12.

$$i = FA\left(k_{ox}[R]_o - k_{red}[O]_o\right) \qquad (1.12)$$

At equilibrium, in the absence of any net flow of current, the fluxes of material ($k_{red}[O]_o$ and $k_{ox}[R]_o$) to the electrode surface are balanced.

A number of parameters can control the rate of an electron transfer reaction including:

1. The electrode potential

2. Mass transport of redox species between the bulk solution and electrode surface

3. Reactivity of the redox species, i.e. ease of oxidation or reduction

4. Possible chemical reaction steps that precede or follow the electron transfer step

5. The nature of the electrode surface

6. The structure of the interfacial region over which the transfer of electrons occurs

Assuming that electron transfer reactions behave in a comparable manner to chemical rate processes, it is possible to apply a transition state model (Figure 1.3) that views the transfer of electrons as proceeding by the reactants, $O_{(aq)} + e^-_{(m)}$, overcoming an energy barrier. The maximum in the free energy plot is called the transition state before the formation of $R_{(aq)}$, the product.
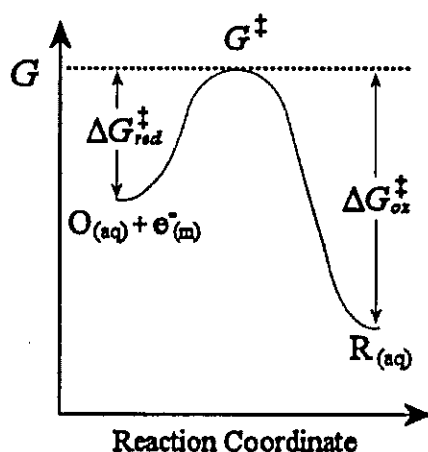
Figure 1.3. Free energy plot for a simple one electron reduction of species $O_{(aq)}$.[45]

Equation 1.13 shows how transition state theory can be used to predict the rate of the reduction reaction (k_{red}).

$$k_{red} = A\exp\left(\frac{-\Delta G_{red}^{\ddagger}}{RT}\right) \qquad (1.13)$$

Where $\Delta G_{red}^{\ddagger}$ is the free energy of activation and A is a 'frequency factor' accounting for the rate of collision of the electroactive molecule with the electrode surface.

1.4.5 The Butler-Volmer Equation

The application of transition state theory to electrode kinetics leads to equation 1.14, the Butler-Volmer equation and the ability to predict how the observed current flowing at the working electrode varies as a function of the overpotential, η, and transfer coefficient, α. The first exponential term describes the anodic component current and the second term gives the cathodic contribution. The overpotential is the deviation of potential from the equilibrium potential whereas the transfer coefficient reflects the sensitivity of the transition state to the drop in potential between the electrode and electrolyte solution. α can take values between zero and one, if α is close to zero, the transition state resembles the reactants in its potential dependence, however, if α approaches one, the transition state behaves like the products. Typically for many reactions α is close to 0.5, suggesting that the transition state has intermediate properties.

$$i = i_o\left(\frac{[R]_o}{[R]_{bulk}}\exp\left\{\frac{(1-\alpha)F\eta}{RT}\right\} - \frac{[O]_o}{[O]_{bulk}}\exp\left\{\frac{-\alpha F\eta}{RT}\right\}\right) \qquad (1.14)$$

If the solution under investigation is well stirred, the surface concentrations of the reactants will be equal to the concentration of reactant in the bulk solution. Under these conditions equation 1.14 can be simplified to give equation 1.15.

$$i = i_o\left(\exp\left\{\frac{(1-\alpha)F\eta}{RT}\right\} - \exp\left\{\frac{-\alpha F\eta}{RT}\right\}\right) \qquad (1.15)$$

Where the standard exchange current, i_o, is proportional to the standard rate constant (k^o), and defined by equation 1.16.

$$i_o = FAk^o [R]_{bulk}^{\alpha} [O]_{bulk}^{1-\alpha}$$

(1.16)

The variation of current with overpotential predicted by equation 1.14 is shown in Figure 1.4 where the total current is the sum of the i_c and i_a components. In going from either direction from E_e, the magnitude of the current rises rapidly due to the exponential factors dominating, but at extreme η, the current levels off. In these level regions, mass transfer rather than heterogeneous kinetics limits the current.
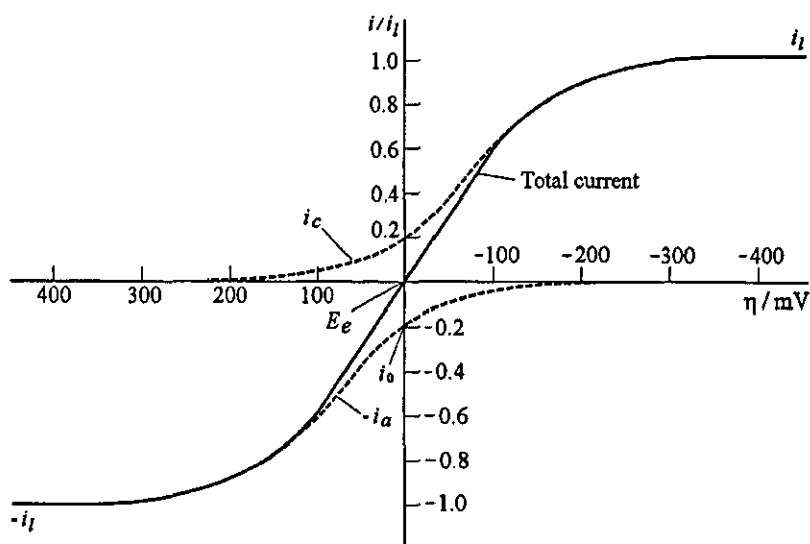
Figure 1.4. Plot to show the variation of current as a function of the overpotential. The dashed lines show the component currents i_c and i_a.[43]

Figure 1.5 shows the variation of i with η predicted by equation 1.15 where no mass transfer effects are observed. For a 'reversible' electrode process, i_o is large (e.g. 10^{-6} A/cm^2) and little or no applied overpotential is needed to drive the reaction resulting in the effortless flow of current in both cathodic and anodic directions (Figure 1.5a). Where i_o is small (i.e. 10^{-9} A/cm^2), for example in an 'irreversible' electron transfer reaction, a high overpotential is necessary to induce current flow (Figure 1.5b).
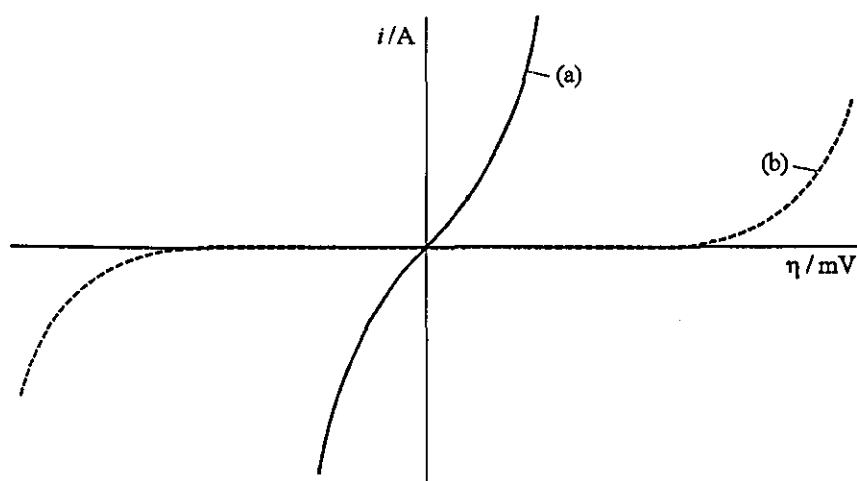
Figure 1.5. Plot to show the variation of current as a function of the overpotential for (a) a reversible and (b) an irreversible electrode reaction.[43]

Figure 1.4 shows that at low values of overpotential (close to the equilibrium potential), both the anodic and cathodic current components in equation 1.15 are significant. However, if the overpotential is increased to a value where the anodic reaction is driven, it is possible to omit the cathodic component simplifying the Butler-Volmer equation (equation 1.17).

$$\ln i = \ln i_o + \frac{(1-\alpha)F}{RT}\eta \qquad (1.17)$$

Similarly, at negative overpotentials where the cathodic process is driven, it is possible to omit the anodic component (equation 1.18).

$$\ln(-i) = \ln i_o - \frac{\alpha F}{RT}\eta \qquad (1.18)$$

Equations 1.17 and 1.18 are known as the Tafel equations which are typically applied in plots of $\ln |i|$ *vs.* overpotential or Tafel plots (Figure 1.6). Analysis of the slope results in an estimate for the transfer coefficient whereas the intercept of the extrapolated Tafel lines with the y –axis gives an estimate for the standard exchange current.

Anodic Process   Cathodic Process

$\log |i|$

$\text{Slope} = \dfrac{(1 - \alpha) F}{2.3 RT}$

$\text{Slope} = \dfrac{-\alpha F}{2.3 RT}$

-3.5

-4.5

-5.5 $\log i_0$

-6.5

200   150   100   50   -50   -100   -150   -200

η / mV
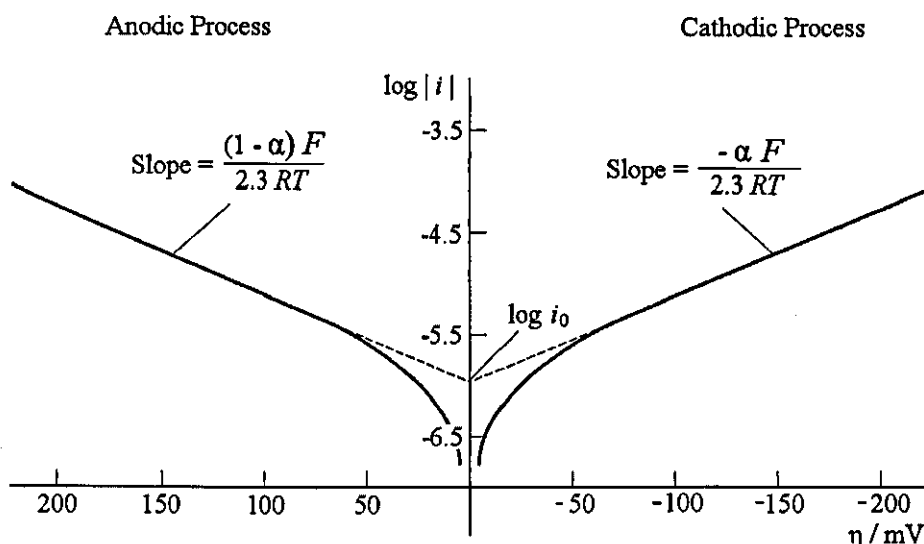
Figure 1.6. Tafel plots for the anodic and cathodic sections of a current – overpotential curve.[44]

For η values less than 10 mV, close to E_e, the cathodic and anodic exponential terms in equation 1.15 can be expanded. Neglecting squared and higher terms results in equation 1.19 which shows that the net current is linearly related to the overpotential in a narrow potential range near E_e.

$$i = i_o \frac{nF}{RT} \eta \qquad\qquad (1.19)$$

The ratio of η/i is called the charge transfer resistance and relates to the reciprocal of the slope in i-η curves where the curve passes through the origin, and acts as a 'convenient index of kinetic facility'.[43]

1.4.6. Mass Transport

In order for electron transfer to proceed, the reactant species must be transported from the bulk solution to the electrode interface. The reaction products will themselves diffuse away from the electrode surface. Depending on the experimental conditions, three transport processes are significant, (i) diffusion, (ii) convection and (iii) migration (Figure 1.7).
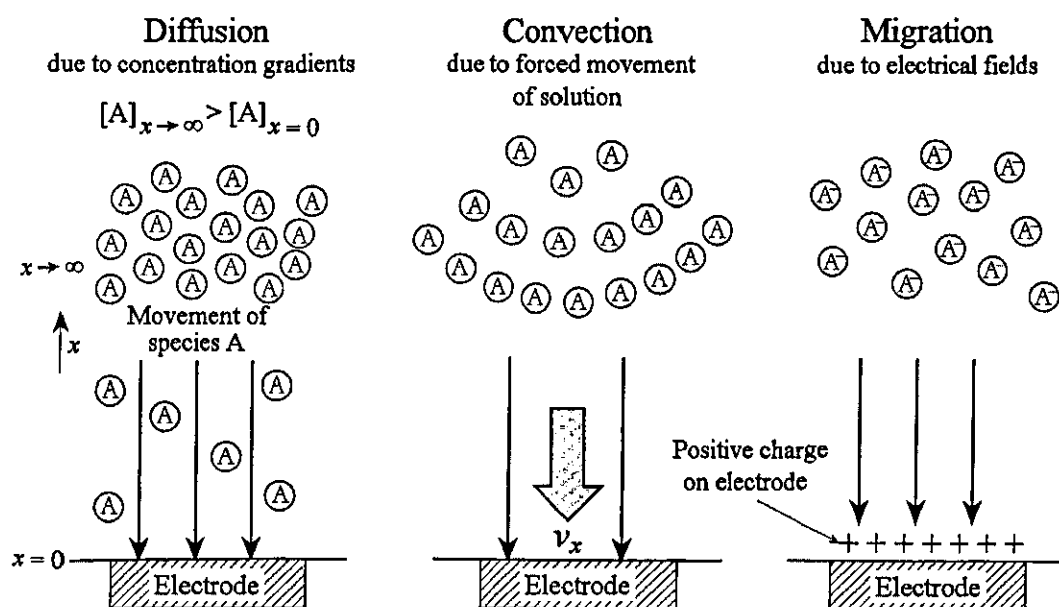
Figure 1.7. Figure to represent the three different modes of mass transport for electroactive material in solution to the electrode surface.[49]

1.4.6.1. Diffusion

Diffusion occurs when there are uneven concentration distributions and is therefore responsible for the transport of species from a region of concentrated solution to a region that is more dilute, until the composition of the system is equal. The rate of diffusion at a given point in solution is dependent on the concentration gradient. Fick's laws of diffusion allow the linear diffusion to a planar surface to be described quantitatively. Fick's first law (equation 1.20) describes the rate of diffusion (flux) of species A through a plane parallel to the electrode surface at distance x, where the concentration gradient is $\partial[A]/\partial x$ and D_A is the diffusion coefficient (m^2s^{-1}).

$$j = -D_A \frac{\partial[A]}{\partial x} \qquad (1.20)$$

Typically, the measure of change in concentration of the electroactive species at a certain point (e.g. adjacent to the electrode surface) as a function of time is of more use. This can be achieved by considering the difference in flux of species A entering through one plane and leaving through a parallel plane separated by distance ∂x

during the time interval ∂t. Fick's second law (equation 1.21) allows the prediction of variation in concentration of A with time close to the electrode surface.

$$\frac{\partial [A]}{\partial t} = D_A \frac{\partial^2 [A]}{\partial x^2}$$

(1.21)

Diffusion is an integral part of an electrode reaction. For the simple electron transfer process in equation 1.1, the conversion of O to R at the electrode surface will lower the concentration of O at the surface relative to that in the bulk solution. Equally, the concentration of R at the electrode surface will be higher than in bulk solution. The resulting concentration gradients provide the driving force for diffusion.

1.4.6.2. Convection

Convection is the movement of species due to mechanical force acting on the electrolyte solution. 'Natural' convection can occur in unstirred solutions, where thermal gradients adjacent to the electrode surface are generated by the exo- or endo- thermicity of the electron transfer process. Alternatively, it is possible that a slight difference in density of the reactant in bulk solution and the product created at the electrode surface will cause movement of the solution in the cell. Natural convection is hard to predict and therefore generally undesirable.

Forced convection can be achieved by introducing an external perturbation such as bubbling gas through the solution, pumping the solution, stirring the solution or by using hydrodynamic electrodes (rotating disc electrodes, channel electrodes and dropping mercury electrodes). The introduction of forced convection in certain electrochemical experiments swamps any influence from natural convection, ensuring greater experimental reproducibility. The use of hydrodynamic electrodes allows the flow of solution to be quantified and the pattern of mass transport to the electrode surface to be predicted. Equation 1.22 is the convection analogue of equation 1.21 where the concentration changes as a result of the movement of solution at a velocity v_x.

$$\frac{\partial[A]}{\partial t} = -v_x \frac{\partial[A]}{\partial x}$$ (1.22)

1.4.6.3. Migration

Migration can be defined as the movement of charged particles due to electrostatic forces or potential gradient. A potential field is created in all electrochemical cells on application of a voltage and consequently migration will be influential in the transport of charged species through the cell solution and is shown to be the mechanism by which charge balance is maintained. The migratory flux is proportional to the ion concentration, the electric field and ionic mobility, which is dependent on the ionic charge, ionic size and solution viscosity. The influence of migration on the electroactive species in the electrochemical cell can be eliminated by addition of a high concentration chemically and electrochemically inert supporting electrolyte. The availability of background ions to preserve electroneutrality ensures that electric fields do not build up in the cell solution as electrolysis proceeds. This ensures that the electroactive species must be transported to the electrode by diffusion and/or convection, with no migration.

1.4.6.4. Transport in electrolysis

Laboratory based electrochemical experiments are typically conducted under two classes of conditions, (a) diffusion only conditions and (b) convective-diffusion experiments. In experiments that are performed in totally unstirred solutions composed of a large excess of supporting electrolyte, diffusion is the predominant means of mass transport. Before the application of a potential, the solution composition is constant, however during the course of a simple electron transfer process, a concentration gradient is induced at the electrode surface, forcing a flux of species A from the bulk solution (equation 1.20). As the electrolysis reaction proceeds, a diffusion layer is established close to the electrode surface where $[A]_0$ does not equal $[A]_{bulk}$. Figure 1.8 illustrates how the diffusion layer thickness grows as electrolysis continues.
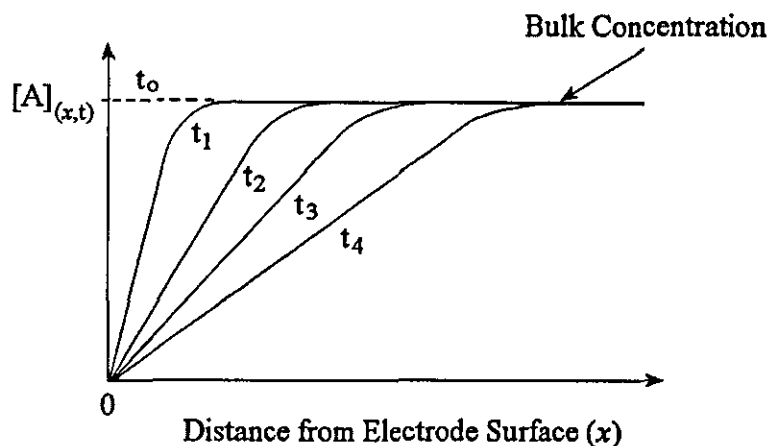
Figure 1.8. A diagram illustrating the growth of the diffusion layer thickness as a function of time.[45]

A degree of natural convection will occur in the bulk solution limiting the ability of the diffusion layer to expand. The more natural convection occurs, the thinner the final diffusion layer thickness will be and the quicker it is possible to establish a constant or steady state diffusion layer thickness. Under steady state conditions transport in the diffusion layer occurs via diffusion alone, whilst natural mixing maintains $[A]_{bulk}$ outside the diffusion layer.

Convective-diffusion experiments are carried out with a well-defined convective procedure in addition to diffusion providing extra reactant material at the electrode surface resulting in a larger current flow than under diffusion only conditions. Migration is still avoided by the addition of the supporting electrolyte.

In contrast, industrial electrochemical processes can be conducted under a wide range of mass transport methods (unstirred solutions, gas purging, pumped electrolytes and moving electrodes) in order to obtain the necessary rate of mass transport at the minimum expenditure.[44]

1.4.7. The Experimental Measurement of Electrolysis Mechanisms

The measurement of electrode currents as a function of the applied voltage in electrolysis is known as voltammetry and can provide information about the

mechanism of the electrode process of interest. The theoretical concepts introduced in sections 1.4.1 – 1.4.6 form the basis for the interpretation of voltammetric experiments.

The main instrumentation needed for voltammetry is a potentiostat, which applies a potential to the electrochemical cell and measures the resulting current. The voltammogram or plot of current versus the applied potential is displayed on a computer. Contemporary potentiostats typically use a three-electrode arrangement as shown in Figure 1.9.
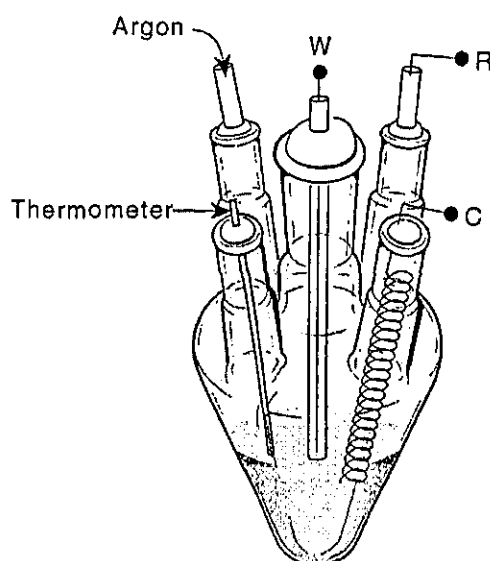
Figure 1.9. Schematic showing a typical electrochemical cell, including R, the reference electrode, W, the working electrode, C the counter electrode, a thermometer and argon gas inlet/outlet.

The desired potential is applied between a 'working electrode' and a 'reference electrode'. The electron transfer process of interest occurs at the working electrode. The 'counter electrode' provides the current necessary to sustain this electron transfer process. This configuration prevents the reference electrode from being subjected to large currents that could alter its potential. It is possible to use a two-electrode configuration when conducting low-current experiments. In this instance, the counter electrode is absent and the reference electrode is subjected to the entire cell current.

The working electrode can be fabricated from a range of materials, well-known examples include liquid mercury drops and discs composed of platinum, gold or carbon (glassy carbon or graphite). The composition of the working electrode in this investigation includes conducting substrates (boron doped diamond, tin-doped indium oxide and basal plane pyrolytic graphite) with and without mono/multi-layer nanoparticle deposits.

The counter or auxiliary electrode is typically composed of a piece of platinum (gauze or wire) or carbon (rod or disc) of large surface area placed directly into the cell solution. As current flows through the counter electrode, it must have a sufficiently high surface area relative to the working electrode to ensure it does not limit the current flowing in the total circuit. As the current measured in a voltammetric experiment flows between the counter and working electrode, if a reduction reaction is being studied at the working electrode, a balancing oxidation reaction (e.g. electrolysis of the solvent) occurs at the counter electrode. Conversely if an oxidation process is studied at the working electrode, a reduction reaction occurs at the counter electrode. The use of a salt bridge in conjunction with the counter electrode in large-scale bulk electrolysis reactions conducted over a lengthy time scale minimises contamination of the cell solution with products generated at the counter electrode.[49] The counter electrode in this investigation was a large piece of platinum gauze.

A reference electrode is included to provide a well-defined potential with respect to which all measurements are made. The potential of the working electrode is held relative to a stable reference electrode. Many reference electrodes have been devised for electrochemical studies in aqueous and non-aqueous solvents including:

1. Standard hydrogen electrode (SHE)

   $Pt, H_{2\,(a=1)}/H^{+}_{(a=1)}$
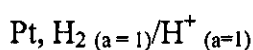
2. Saturated calomel electrode (SCE) (used in this investigation)

   $Hg/Hg_2Cl_{2\,(s)}, KCl_{(aq.)}$
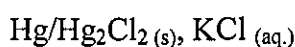
3. Silver-silver chloride electrode

   $Ag/AgCl_{(s)}, KCl_{(aq.)}$
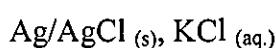
4. Mercury-mercury (I) sulphate electrode

   Hg/Hg_2SO_4 (s), K_2SO_4 (aq.)
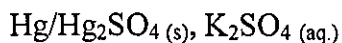
5. With a non-aqueous solvent, a silver salt system may be preferred

   Ag/Ag^+ (0.01M $AgNO_3$ in CH_3CN)

The primary reference is the SHE with a potential equal to 0V at all temperatures, however the SHE suffers from the disadvantages of being susceptible to poisoning and the inability to be used in solutions containing chemically reducible species. Reference electrodes composed of a metal in contact with one of its sparingly soluble salts, placed in a solution containing a strongly ionised salt with a common anion are of more use (e.g. SCE). The potential adopted by the reference electrode (relative to the SHE) is then controlled by the activity of the anion in solution due to the unit activity of reactants in standard states.[47] Due to the difficulty in finding a reference electrode for non-aqueous solvent experiments that does not contaminate the electrolyte solution, Ag or Pt wire quasi-reference electrodes are frequently used. The unknown potential of the metal wire will not change during a series of measurements providing there is essentially no change in the bulk electrolyte solution allowing an acceptably reproducible reference potential to be achieved after calibration, typically using ferrocene.[43]

The cell solution for typical electrochemical experiments contains a solvent, a high concentration of a background electrolyte and the electroactive species. A wide range of solvents is routinely used in electrochemical studies including water (the most common), acetonitrile, methanol, and tetrahydrofuran. The most important properties for the solvent are to be liquid at the experimental temperature and to be able to dissolve high concentrations of electrolyte to create a reasonably conducting solution. It is also essential that the solvent is compatible with the chemistry occurring at the electrode surface and that the reactant for the electrode process is soluble to the desired extent.[44]

The addition of a supporting electrolyte with a high degree of ionisation into cations and anions provides several important benefits including:

1. Increases the solution conductivity making it less resistive to the flow of current, resulting in current flow depending upon the interfacial reaction of interest and not bulk solution conductivity.

2. Controls the distance at the electrode/solution interface over which the electrical potential drops (electrical double-layer) to approximately 10-20 Å. This is essential for the prevention of migration as well as being compatible for electrons tunnelling between the electrode and reactant in solution.

3. Maintains an effectively constant ionic strength in solution during electrolysis due to the relatively high concentration of supporting electrolyte compared to the concentration of reactants and products. This ensures that the activity coefficients of the reactants and products are equal and able to cancel out in the Nernst equation.

The electrochemical cell contains an inlet/ outlet for an inert gas that displaces electroactive oxygen from the solution. Typical inert gases include high purity nitrogen and argon. Nitrogen is normally used due to its low cost and wide availability however, for very air-sensitive conditions, argon is preferred as it is heavier than air.[49]

In the absence of constant temperature conditions it is necessary to use an electrochemical cell with a thermostat-controlled jacket as voltammetric responses can display significant temperature dependence.

Electrochemical experiments may be classified based on their time dependence. Often the current measured at the working electrode is independent of time and a function only of the applied potential. These are known as the steady-state conditions. Experiments with time dependence can give more information but are more complex to analyse. These are known as transient techniques.

1.4.8. Linear Sweep Voltammetry

A well-known and widely applied transient technique is voltammetry; it is easy to use and enables information to be obtained readily. Voltammetric experiments are

carried out in a stationary solution relying on diffusion to transport reactants to the electrode surface. The mass transport of the electroactive species A to the electrode surface can be predicted using equation 1.21 (Fick's second law).

The potential of the working electrode is swept from an initial value E_1 where A cannot undergo electron transfer, to a final potential E_2, where the electron transfer is driven rapidly. The applied potential E is a function of the speed at which the potential is swept (v_s) and the time of the sweep (t) given by equation 1.23.

$$E(t) = E_1 - v_s t \qquad (1.23)$$

The terms 'reversible' and 'irreversible' have been used to characterise two extremes in the electrode kinetics observed for the simple electron transfer process shown in equation 1.9. The difference in electrode kinetics produces voltammetric responses with characteristic features indicative for each of these extremes.

Figure 1.10 illustrates (a) the potential ramp and (b) the resulting current response for the O/R couple where it has (i) reversible and (ii) irreversible electrode kinetics.
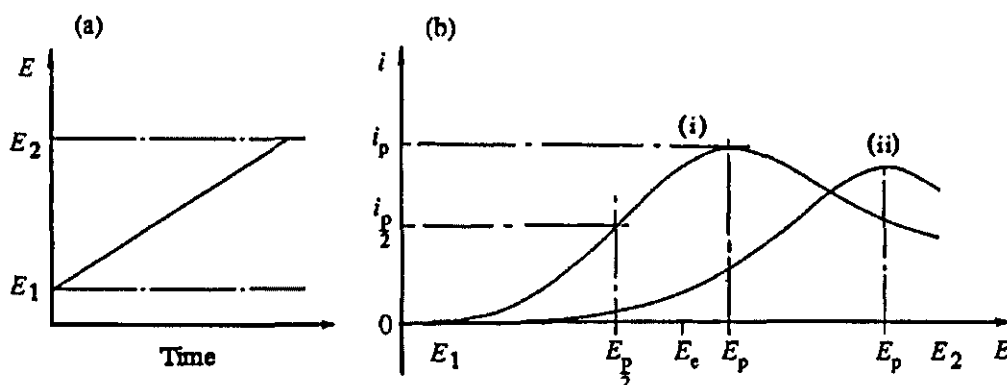
Figure 1.10. (a) The linear potential sweep and (b) corresponding current response for (i) a reversible and (ii) an irreversible electron transfer reaction.[45]

In the case of a reversible system, a substantial flow of current is observed when the electrode reaches a potential greater than E_e, the equilibrium potential. This

indicates that as soon as the redox process becomes thermodynamically viable it takes place as a result of rapid electron transfer. As the potential rises further, the electrochemical rate constant for the forward reaction increases causing a rise in current. Initially the current rises exponentially with potential but as larger potentials are applied (more negative for a reduction) the increase becomes less than exponential before reaching a maximum. The maximum in the current/voltage curve reflects the balance between the increasing rate constant and a decrease in surface concentration of reactant.

The maximum current is known as the peak current or i_p. Once the i_p is reached, the size of the current flowing is controlled by the rate of diffusion of reactant to the electrode surface. The fall in current after i_p is a result of the increase in diffusion layer thickness produced by further electrolysis of the solution.

In contrast very little current flow is seen for the irreversible system until the potential is much greater than E_e. This is an example of the overpotential that has to be applied to drive the reaction. Therefore E_p occurs at larger potentials in irreversible systems.

Two important points of comparison between reversible and irreversible voltammograms are the E_p and i_p observed.

For the reversible system,

1. E_p is constant and independent of scan rate

2. $$\left| E_p - E_{\frac{p}{2}} \right| = 2.20 \frac{RT}{nF} \tag{1.24}$$

3. i_p is larger for a reversible system than for an irreversible system for the same voltage scan rate.

The i_p (A) can be determined using the Randles Sevčik equation (equation 1.25a and 1.25b (assuming T is equal to 298 K)) where n is the number of electrons, A is the electrode area (m^2), D is the diffusion coefficient (m^{2}s^{-1}), v is the potential scan rate

(Vs^{-1}), $[A]_0$ is the concentration of A in the bulk solution (mol m^{-3}), and in equation 1.25b, the numerical constant has the units C mol^{-1} V$^{-1/2}$.

$$i_p = 0.446 \, nFA \, c \sqrt{\frac{nFvD}{RT}} \qquad (1.25a)$$

$$i_p = 2.69x10^5 n^{3/2} AD^{1/2} v^{1/2} [A]_0 \qquad (1.25b)$$

While for the irreversible electron transfer,

1. $\left| E_p \right|$ shifts by approximately $1.16\dfrac{RT}{\alpha nF}$ for each tenfold increase in v

2. $\left| Ep - E_{\frac{p}{2}} \right| = 1.86\dfrac{RT}{\alpha nF} \qquad (1.26)$

3. i_p is smaller for an irreversible system than for a reversible system for the same voltage scan rate

$$\left| i_p \right| = 2.99 \times 10^5 n^{3/2} \alpha^{1/2} AD_A^{1/2} v_s^{1/2} [A]_{bulk} \qquad (1.27)$$

The differences reflect the contrasting electrode kinetics for the reversible and irreversible electrode processes. In the case of a reversible system the electrode kinetics are such that for potentials near E_e both k_{red} and k_{ox} are large, whereas electrolysis in irreversible systems proceeds with negligible back reaction. The terms reversible and irreversible are extreme cases; electron transfer processes with intermediate electrode kinetics exist and are typically referred to as quasi-reversible.

For any system, i_p is directly proportional to the concentration of reactant and increases with voltage scan rate, v_s. The increase of i_p with v_s can be explained by Fick's first law (equation 1.20). This equation indicates that i_p reflects the concentration gradient of reactant near the electrode, which in turn is controlled by the diffusion layer thickness. If the electrode potential is swept more rapidly, relatively less time is available for electrolysis and the depletion of reactant near the electrode is reduced, resulting in a thinner diffusion layer and hence a steeper concentration gradient. The resulting larger flux gives rise to an enhanced i_p.[45]

1.4.9. Cyclic Voltammetry

Linear sweep voltammetry can be extended so that when the potential reaches the value E_2 the direction of sweep is reversed and the electrode potential is scanned back to the original value, E_1. This is known as cyclic voltammetry and is the main method employed here to characterise the mesoporous metal oxide film deposits produced.

The shape of the forward sweep of the voltammogram is identical to that observed in linear-sweep voltammetry and will be dependent on the reversibility of the redox couple. On reaching E_2, the potential is swept back; oxidising species R generated at the working electrode during the forward potential scan, resulting in a current response opposite in sign to the forward scan. The current initially increases due to the high concentration of R present in the diffusion layer and the more favourable rate constant as the potential becomes more positive. As R present in the diffusion layer is reconverted to O, a peak is reached as before and the current drops.

The reversibility of the system is again reflected in the E_p value and peak size seen in the reverse scan. Figure 1.11 shows the cyclic voltammogram for a reversible redox couple where the forward and reverse i_p are approximately the same size and separated by a potential of *ca.* 59 mV (at 25°C) independent of scan rate.
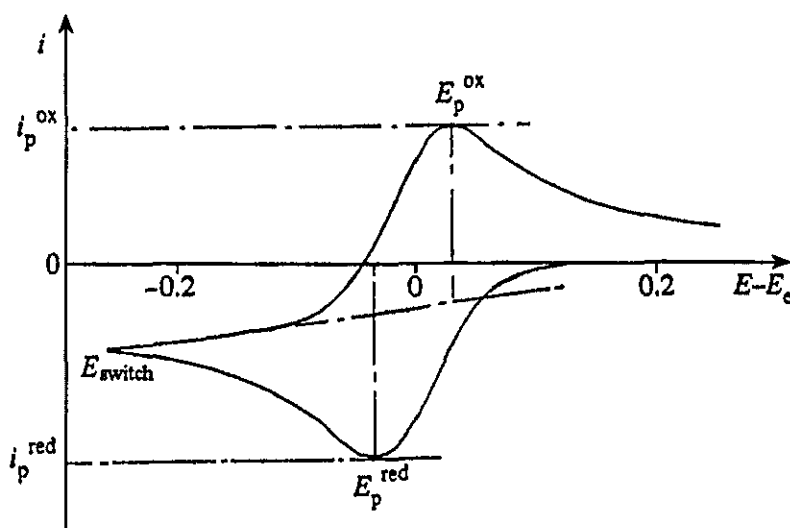
Figure 1.11. Figure to show the important features of a cyclic voltammogram for a reversible redox system. Modified from reference 45.

If n electrons are transferred the following points can be used as diagnostic tests for the form of cyclic voltammograms in a reversible electrode process at 298 K.

1. $\Delta E_p = \left| E_p^{ox} - E_p^{red} \right| = 2.20 \dfrac{RT}{nF} = \dfrac{59}{n}$ mV   (1.28)

2. $\left| E_p - E_{p/2} \right| = \dfrac{59}{n}$ mV   (Using equation 1.24)

3. $\left| \dfrac{i_p^{ox}}{i_p^{red}} \right| = 1$

4. $i_p \propto v^{1/2}$ (Using the Randles Sevčik equation (equation 1.25))

5. E_p is constant and independent of v and can be estimated from equation 1.29

$$E_p = E^{0'} - \left(\frac{RT}{nF} \right) \left[1.109 + 0.5 \ln \left(\frac{D_O}{D_R} \right) \right]$$ (1.29)

6.   At potentials beyond E_p, $i^{-2} \propto t$

Again not all electron transfer processes are reversible, the cyclic voltammetric behaviour for an irreversible system shows a very large overpotential is needed for the reverse reaction meaning the reverse peak is only seen at potentials significantly greater than E_e. The size of the reverse peak with respect to the forward peak is dependent on the scan rate and can be completely absent when the reverse electron-transfer process does not occur at a measurable rate (Figure 1.12).
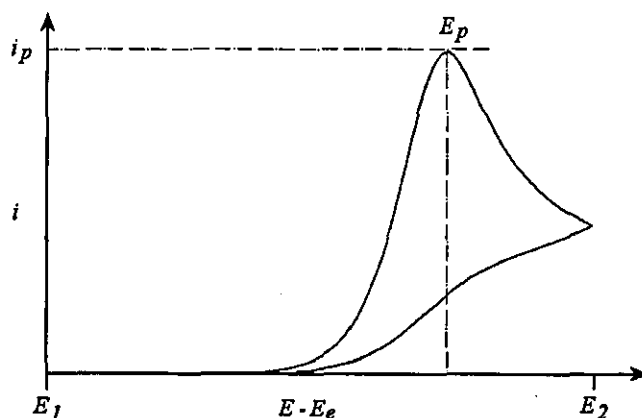
Figure 1.12. Figure to show the cyclic voltammogram for an irreversible redox system. Modified from reference 49.

This difference in voltammetric response allows the reversibility of the redox couple to be determined. If *n* electrons are transferred the following points can be used as diagnostic tests for the form of cyclic voltammograms in an irreversible electrode process.

1. $\Delta E_p > \dfrac{59}{n}$ mV , if a reverse peak is observed

2. $\left| E_p - E_{p/2} \right| = \dfrac{48}{\alpha n}$ mV   (Using equation 1.26)

3. $i_p \propto v^{1/2}$ (Using equation 1.27)

4. $\left| E_p \right|$ shifts by approximately $\dfrac{30}{\alpha n}$ mV for each tenfold increase in *v*

For an intermediate case or quasi-reversible redox couple, a reverse peak similar in size to the forward sweep is observed but the peak to peak separation is now dependent on the scan rate and i_p is no longer proportional to the square root of the scan rate (Figure 1.13).
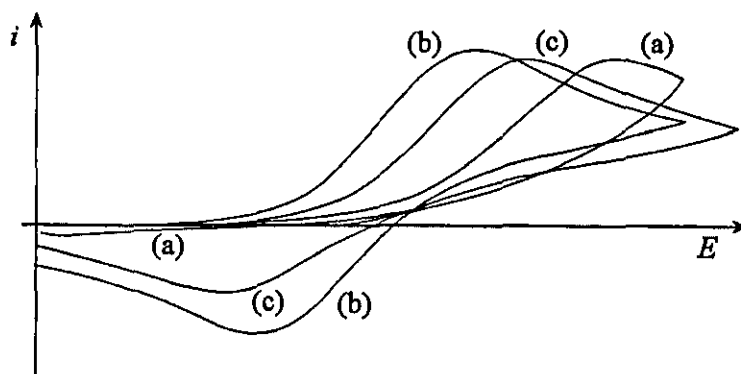
Figure 1.13. Figure to show the cyclic voltammogram for (a) an irreversible, (b) a reversible and (c) a quasi-reversible electron transfer reaction.[45]

If *n* electrons are transferred the following points can be used as diagnostic tests for the form of cyclic voltammograms in quasi-reversible electrode processes.

1. i_p increases with $v^{1/2}$, but is not proportional

2. $\left| \dfrac{i_p^{ox}}{i_p^{red}} \right| = 1$, provided $\alpha_R = \alpha_O = 0.5$

3. $\Delta E_p > \dfrac{59}{n}$ mV, and increases with faster v as E_p^{ox} shifts to more negative

potentials and E_p^{red} shifts to more positive potentials with increasing v

1.4.10. Voltammetry of Coupled Reactions

Electrolysis is widely used to synthesise both organic and inorganic chemicals since the redox product is not always chemically stable and is therefore capable of undergoing further reaction at the electrode surface or in electrolyte solution. Cyclic voltammetry is a useful technique for probing these complex electrolysis mechanisms by detecting and identifying reaction intermediates through the observed deviation from ideal reversible current responses.

The reaction sequence of coupled voltammetric measurements is typically classified using an 'E' and 'C' notation where 'E' denotes a heterogeneous electron transfer at the electrode surface and 'C' represents a homogeneous chemical reaction in solution.

1.4.10.1. The EC Mechanism

The 'E' and 'C' terms appear in the order the reaction steps proceed, for example the EC reaction mechanism in Figure 1.14 shows an electron transfer (E) followed by a first-order homogeneous decay (C) of the electrochemically generated species (R).[45]

$$\text{E:} \qquad O_{(aq)} + n e^-_{(m)} \; \rightleftharpoons \; R_{(aq)}$$

$$\text{C:} \qquad R_{(aq)} \; \xrightarrow{\;k_{EC}\;} \; P_{(aq)}$$
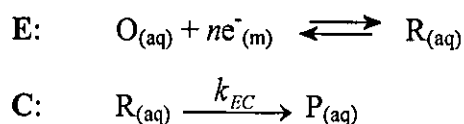
Figure 1.14. Figure to illustrate an EC mechanism in a coupled electrolysis reaction.[44]

For an EC reaction in an unstirred solution (i.e. under diffusion controlled mass transport) the initial electroactive species O is not lost by any homogeneous reaction and consequently [O] only changes as a result of diffusion described by equation 1.21. However, it is necessary to modify the diffusion equation for species R to quantify the loss of R via chemical reaction at a rate $k_{EC}[R]$ (equation 1.30).

$$\frac{\partial [R]}{\partial t} = D_R \frac{\partial^2 [R]}{\partial x^2} - k_{EC}[R]$$

(1.30)

Equation 1.30 indicates that the magnitude of the rate constant k_{EC} will have a strong influence on [R] at the electrode surface and therefore if k_{EC} is significantly fast then as soon as R is formed at the electrode surface, it is lost due to chemical reaction. Figure 1.15 shows the difference in cyclic voltammetry observed for an EC mechanism compared to that for a stable reversible electron transfer process. The forward voltammetric sweep is similar in both mechanisms, however in the return potential sweep, the reverse peak is lost since R has reacted. This is a chemically irreversible system rather than an electrochemically irreversible electron transfer that is dependent on a high overpotential to drive the reverse reaction.
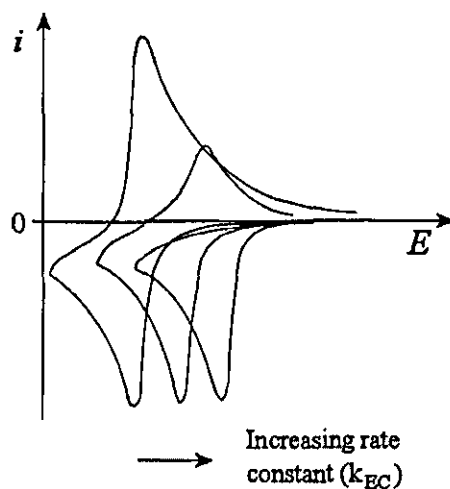
Figure 1.15. Cyclic voltammograms to illustrate the influence of k_{EC} in an EC mechanism on the observed current response.[45]

If k_{EC} is very slow, little or no difference is observed in the reverse sweep compared to the stable cyclic voltammetry, as R is not significantly depleted by reaction.

Intermediate reaction rates give rise to voltammograms where the size of the reverse peak varies reflecting the stability of the species R, therefore the relative heights of the back peaks can be used to estimate the rate of the chemical reaction in solution.

It is necessary to consider the potential scan rate in the analysis of EC mechanisms, as when the timescale of the experiment is short with respect to the half-life of R (i.e. at fast v) there is less time for R to react resulting in an enhanced back peak in the voltammogram. Similarly at slower scan rates, more time is available for R to be converted to P and no reverse peak is observed.

The magnitude of the rate constant is also seen to effect the position of the redox peak in the forward sweep. As the rate constant increases, the current response shifts anodically for a reduction (cathodically for an oxidation) as the electron transfer processes occurs more readily. This is a result of the chemical reaction step disturbing (by removing R) the equilibrium surface concentrations of O and R predicted by the Nernst equation at a particular potential. In order to re-establish the equilibrium at the electrode surface, the electron transfer reaction is driven towards the right-hand side, generating more species R creating an anodic shift in voltammetric wave.[45]

1.4.10.2. The ECE Mechanism

An extension of the EC reaction is the ECE electrolysis mechanism (Figure 1.16). The initial electrochemical and homogeneous chemical reaction steps are identical to the EC system however the product formed in the chemical step is also electroactive.

$$E: \quad O_{(aq)} + ne^-_{(m)} \rightleftharpoons R_{(aq)}$$

$$C: \quad R_{(aq)} \xrightarrow{k_{ECE}} M_{(aq)}$$

$$E: \quad M_{(aq)} + ne^-_{(m)} \rightleftharpoons P_{(aq)}$$
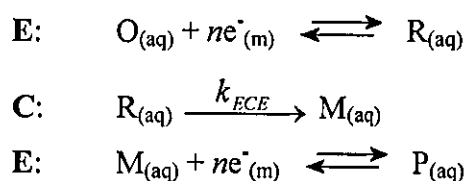
Figure 1.16. Figure to illustrate an ECE mechanism in a coupled electrolysis reaction.[44]

The electron transfer step for the redox couple M/P may occur at a higher or lower potential depending on the relative ease of electron transfer compared to the redox couple O/R. Figure 1.17 shows the cyclic voltammogram recorded for an ECE mechanism where O is more readily reduced than M. In the forward reductive sweep, the first peak corresponds to the reduction of O to R followed by a second reduction peak at more negative potentials, where M is reduced to P. The magnitude of the second reduction peak will be dependent on the rate of chemical conversion of R to M. In the reverse potential sweep, it is possible to observe the oxidation of P to M and depending on k_{ECE} and the potential scan rate, a second oxidation peak may be seen where R is re-oxidised to O. At faster scan rates there is less time for R to react resulting in a decrease in the M/P redox response and an enhanced back peak in the O/R system. Similarly at slower scan rates, more time is available for R to be converted to M and little to no reverse oxidation peak is observed for the O/R couple.

Figure 1.17. Cyclic voltammograms to illustrate the ECE reaction mechanism. Modified from reference 45.

The ECE reaction mechanism can itself be extended when the species P from the second electrochemical step undergoes a homogeneous chemical reaction in solution (Figure 1.18). This is known as the ECEC electrolysis mechanism that can also be followed by additional E and C processes.

$$\text{E:} \qquad O_{(aq)} + n e^-_{(m)} \;\rightleftharpoons\; R_{(aq)}$$

$$\text{C:} \qquad R_{(aq)} \rightarrow M_{(aq)}$$

$$\text{E:} \qquad M_{(aq)} + n e^-_{(m)} \;\rightleftharpoons\; P_{(aq)}$$

$$\text{C:} \qquad P_{(aq)} \rightarrow Q_{(aq)}$$

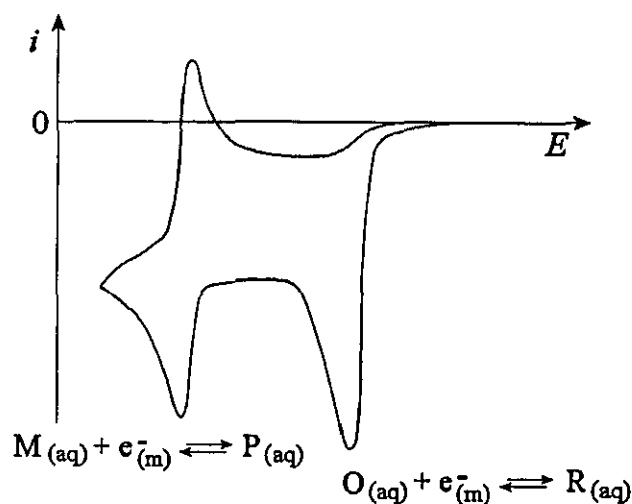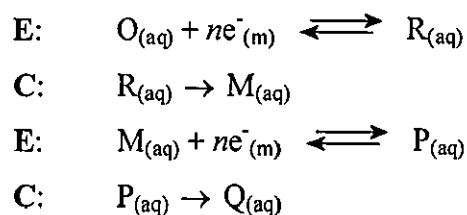**Figure 1.18.** Figure to illustrate an ECEC mechanism in a coupled electrolysis reaction.[44]

1.4.10.3. The EC′Mechanism

A further coupled reaction mechanism of interest is the EC′ reaction (Figure 1.19) where C′ represents a catalytic process, which often corresponds to a clean and efficient means of improving chemical reactivity. The catalytic process takes place as R, the product of the electron transfer step, reacts with the substrate molecule Y in solution, re-oxidising O and forming species N.

$$\text{E:} \qquad O_{(aq)} + n e^-_{(m)} \;\rightleftharpoons\; R_{(aq)}$$

$$\text{C′:} \qquad R_{(aq)} + Y_{(aq)} \rightarrow N_{(aq)} + O_{(aq)}$$
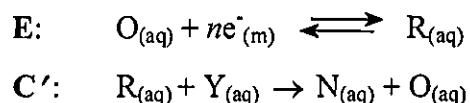
Figure 1.19. Figure to illustrate an EC′ mechanism in a coupled electrolysis reaction.[44]

A typical cyclic voltammogram for an EC′ reaction is shown in Figure 1.20 where increasing concentrations of Y are present in solution. As the level of substrate Y increases, an enhancement in the current response is seen (as O is regenerated and able to be re-reduced) compared to the voltammetric behaviour when no substrate is present. The size of the catalytic current is consequently dependent on the rate of reaction of the catalytic step and the quantity of substrate present in solution.
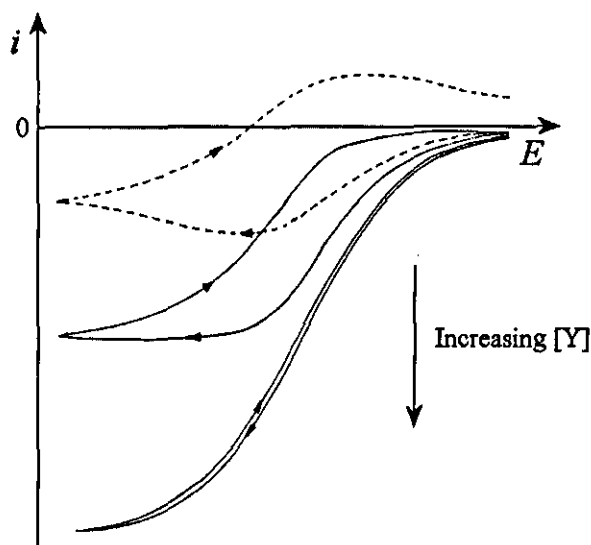
Figure 1.20. Cyclic voltammograms to illustrate the EC' reaction mechanism. Modified from reference 45.

1.4.10.4. The EE Mechanism

Section 1.4.10.2 illustrated that it is possible for multiple electron transfer steps to occur coupled by a homogeneous chemical reaction. However the transfer of multiple electrons can also be observed where a reactant is able to change oxidation state by more than one without the need for a chemical reaction intermediate step. The simplest example of a multiple electron transfer mechanism is the EE reaction where two electrons are transferred. This ability to alter the oxidation state of a molecule by more than one is typically seen in the electrochemistry of inorganic metals or organic electrochemistry.[45] The EE reaction can either consist of one step involving the transfer of two electrons (Figure 1.21a) or alternatively it may proceed via two consecutive single electron steps (Figure 1.21b).

(a)   **EE:** $O_{(aq)} + 2e^-_{(m)} \rightleftharpoons R_{(aq)}$

(b)   **E:** $O_{(aq)} + e^-_{(m)} \rightleftharpoons P_{(aq)} \quad (E = E_1^o)$

              E: $P_{(aq)} + e^-_{(m)} \rightleftharpoons R_{(aq)} \quad (E = E_2^o)$
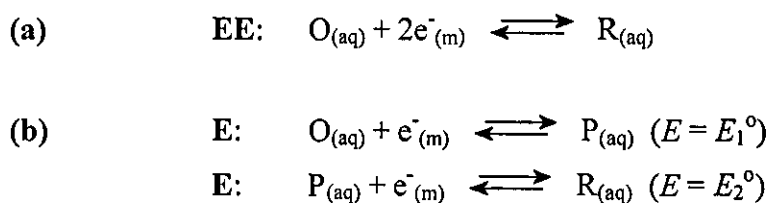
Figure 1.21. Figure to illustrate a CE mechanism in a coupled electrolysis reaction.[45]

The consecutive reaction pathway is most common due to the relative ease in overcoming two small activation barriers compared to a single large energy barrier. The difference in the potential values $E_1^{\,0}$ and $E_2^{\,0}$ will influence the voltammetric response meaning the electron transfer steps can either occur at similar or distinct potentials. Figure 1.22 shows the voltammogram obtained for a molecule undergoing two single, reversible electron transfer reactions.
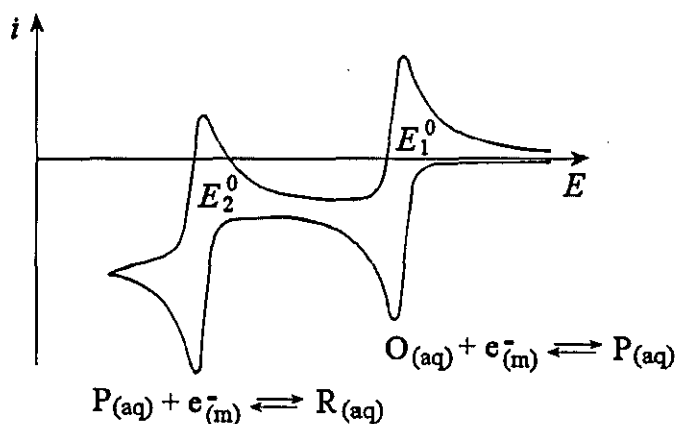
Figure 1.22. Cyclic voltammograms to illustrate an EE two-electron transfer reaction mechanism. Modified from reference 45.

1.4.10.5. The CE Mechanism

A final example of a coupled reaction mechanism is the CE electrolysis mechanism (Figure 1.23), where the electroactive species is not initially present in the bulk solution. However species Q, may be able to undergo a chemical reaction to form O (the electroactive species) prior to undergoing the electron transfer step to give R.

$$C: \quad Q_{(aq)} \longrightarrow O_{(aq)}$$

$$E: \quad O_{(aq)} + ne^{-}{}_{(m)} \rightleftharpoons R_{(aq)}$$
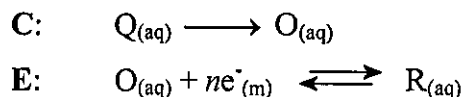
Figure 1.23. Figure to illustrate a CE mechanism in a coupled electrolysis reaction.[44]

1.4.11. Voltammetry of Surface Adsorbed Species

An electrode reaction involving the electron transfer of a uniformly adsorbed surface layer of the electroactive couple O/R (equation 1.31) will have different voltammetric behaviour, compared to the solution-phase voltammogram for a stable, reversible electron transfer reaction.

$$O_{(ads)} + ne^-_{(m)} \rightleftharpoons R_{(ads)} \tag{1.31}$$

Figure 1.24 shows the resulting ideal cyclic voltammogram for a surface adsorbed species that remains adsorbed to the electrode surface after reduction, and is consequently able to be reconverted to O in the reverse potential sweep.
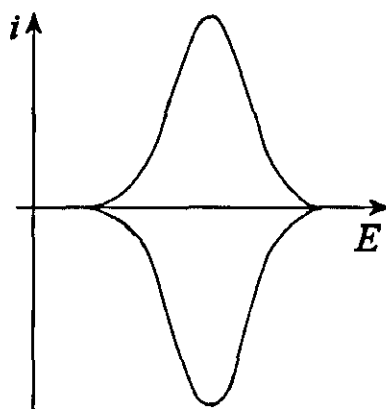
**Figure 1.24.** The ideal cyclic voltammogram for the reversible electron transfer reaction of a surface-adsorbed layer of reactant where the coverage of the adsorbed species follows a Langmuir isotherm.[45]

Both the reduction and oxidation peaks are symmetrical, with the current response dropping to zero after reaching a maximum, as the reactant is fully converted due to the absence of diffusional mass transport supplying fresh reactant from bulk solution. The number of sites available on the electrode surface where adsorption can occur will therefore control the properties of the voltammogram observed. The areas under the redox peaks are equal and a measure of the charge required for the electrochemical reaction allowing the quantity of electroactive material adsorbed on the electrode surface to be estimated.

Adsorption isotherms are used to quantify the relationship (at constant temperature), between the fraction of the surface covered by adsorbate in solution (θ), its free energy of adsorption (ΔG_{ADS}) and the concentration of adsorbate in solution (c). The Langmuir adsorption isotherm (equation 1.32) assumes that adsorption cannot proceed beyond mono-layer coverage, that all binding sites are equivalent and that the electrode surface is uniform (where K is the equilibrium constant).

$$\theta = \frac{K \times c}{1 + (K \times c)} \tag{1.32}$$

Further assumptions of the Langmuir isotherm include that the ability of a molecule to adsorb at a given site is independent of the occupation of neighbouring sites and that there are no lateral interactions between adjacent adsorbed species and therefore the free energy of adsorption is independent of coverage (equation 1.33).[44]

$$\frac{\theta}{1-\theta} = c \exp\left(\frac{-\Delta G^0_{ADS}}{RT}\right) \tag{1.33}$$

The following points can be used as diagnostic criteria for cyclic voltammograms for a redox couple adsorbed on the electrode surface with reversible electron transfer kinetics, where q is the charge density (C m^{-2}).

1. $\Delta E_p = 0$ mV

2. $\left|\dfrac{i_p^{ox}}{i_p^{red}}\right| = 1$

3. $i_p \propto v$

4. E_p are independent of v

5. $q_A = q_C \leq q_{monolayer}$

Digression from ideal behaviour occurs when the surface-adsorbed species is unstable in either its charged or uncharged forms, or is desorbed during the potential

sweep. Any difference in the voltammetric behaviour can therefore be used to investigate the stability and nature of the adsorbed species interaction with the electrode surface. If the adsorbed species is slowly lost from the electrode surface after the initial electrochemical reaction, a decrease in the reverse peak current is expected, allowing the desorption kinetics to be probed by varying the scan rate.

1.4.12. A.C. Impedance Spectroscopy

Impedance is a measure of the ability of a circuit to resist the flow of electrical current[50] similar to resistance (R). However, impedance is not limited by simplifying assumptions of obeying Ohm's law (equation 1.34) at all current (I) and voltage (E) levels and being independent of frequency.

$$R = \frac{E}{I} \tag{1.34}$$

Electrochemical impedance is typically measured by applying an oscillating sinusoidal A.C. potential (equation 1.35) to an electrochemical cell and recording the A.C. current response (equation 1.36) that contains the excitation frequency and harmonics.[45]

$$E(t) = E_m \sin(2\pi f t) \tag{1.35}$$

$$i(t) = i_m \sin(2\pi f t + \theta) \tag{1.36}$$

Where $E_{(t)}$ is the applied sinusoidal potential, f is the frequency measured, E_m is the maximum amplitude, $i_{(t)}$ is the current response, i_m is the maximum current amplitude, t is time and θ is the phase difference between $E_{(t)}$ and $i_{(t)}$. Normally a small (1-10 mV) amplitude excitation signal is used in impedance measurements so that the cell's response is pseudo-linear and the current response is shifted in phase.

Figure 1.25 shows a phase difference between the applied potential and the current

response of $\pi/2$ for a capacitor. In the case of a resistor, no phase shift would be seen and the lines would overlap, i.e. $\theta = 0$.
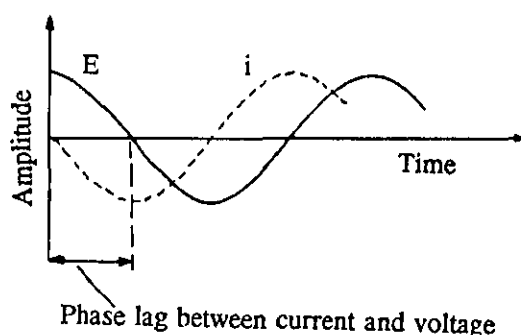

Phase lag between current and voltage

Figure 1.25. The form of the applied potential used in A.C. impedance spectroscopy and the current response with a phase shift of $\pi/2$. [45]

The response of electrical circuits to A.C. potentials can be described in terms of the impedance (Z) defined by equation 1.37, analogous to Ohm's law.

$$Z(f) = \frac{E_{(t)}}{i_{(t)}}$$ (1.37)

As the phase difference between current and voltage can take any value and is dependent on the frequency, the impedance can be calculated using equation 1.38.

$$Z(f) = Z' \sin(2\pi ft) - Z'' \cos(2\pi ft)$$ (1.38)

Traditionally, complex impedance measurements are plotted with Z' (the real part) on the x-axis and $-Z''$ (the imaginary part) on the y-axis for each frequency (Figure 1.26). The vector from the origin to a point with coordinates (Z', $-Z''$) has a length equal to the impedance at an angle of θ, the phase shift with the x-axis. Modern experimental methods allow the electrochemical cell to be connected directly to a frequency response analyser that automatically draws the impedance plots. The use of a three-electrode system and suitable reference electrode allows the impedance of a specific electrode/solution interface to be investigated. [45]
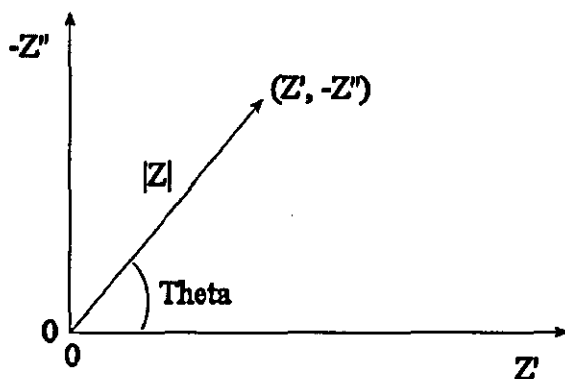
Figure 1.26. Impedance plot with the impedance vector and θ shown.

The shape of the impedance plot will depend on the properties of the cell. For a capacitor, the impedance plot (Figure 1.27) takes the form of a vertical line along the y-axis, as $Z' = 0$ and $-Z'' = \dfrac{1}{\left(2\pi f C_d\right)}$ where C_d is the differential capacitance.
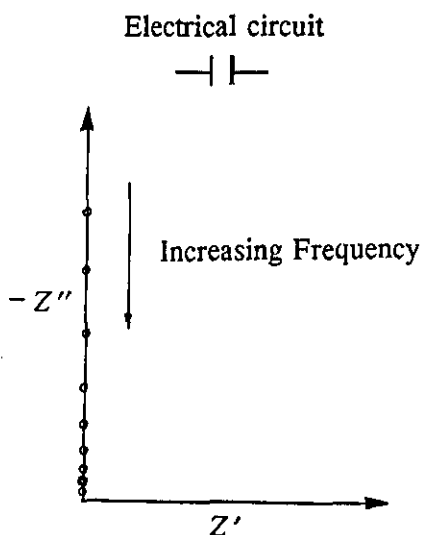
Figure 1.27. Impedance plot for an electrical circuit containing a single electrolytic capacitor.[45]

For the case of a resistor and capacitor in series, a line is seen at $Z' = R$ and $-Z'' = \dfrac{1}{2\pi f C_d}$ (Figure 1.28). This is the type of plot expected for the metal oxide films on an ITO surface where the film acts as the capacitor and the ITO as a resistor.

Electrical circuit

Figure 1.28. Impedance plot for an electrical circuit containing a resistor and capacitor in series.[45]

Another way of presenting the results from impedance measurements is shown in Figure 1.29 where the impedance and θ are plotted as a function of the frequency applied.

Figure 1.29. Bode plot showing the effect of frequency (Hz) on the impedance and phase difference.
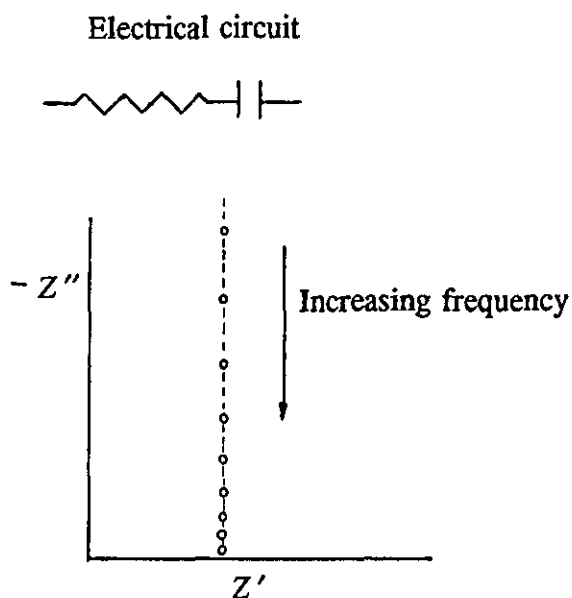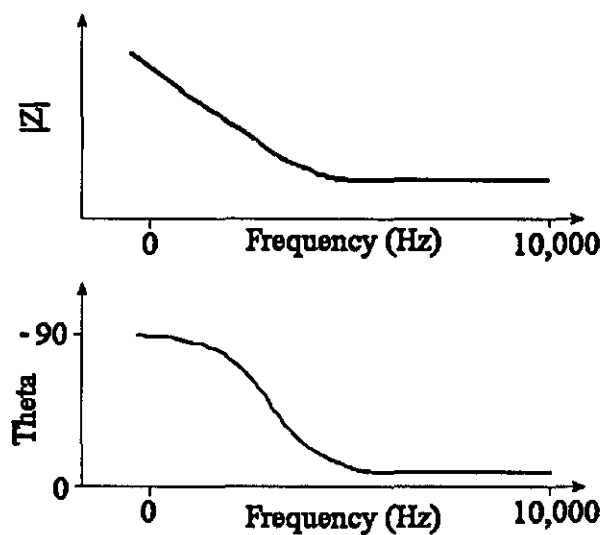
1.5. Electron Movement in Nanoparticles

As previously stated in section 1.2, nanoparticles can be formed with a variety of conducting properties that will affect the processes taking place in the metal oxide films. In order to understand the electron transfer between particles in the metal oxide films, it is necessary to look at the band theory and the energy levels of particles.

Figure 1.30 demonstrates how a metallic state can be generated using the molecular orbital diagrams for the simplified example of lithium atoms. Figure 1.30a shows how two lithium atoms combine through the single $2s^1$ electrons to form a doubly occupied binding molecular orbital (σ) and an unoccupied anti-bonding orbital (σ^*). The combination of ten lithium atoms behaves in a similar way forming five doubly occupied binding molecular orbitals and five unoccupied anti-bonding orbitals (Figure 1.30b). The Pauli exclusion principle describes how the energy levels of identical overlapping electronic orbitals cannot be equal,[51] and Figure 1.30c illustrates how the combination of an infinite number of lithium atoms leads to the formation of extended molecular orbitals, as the quasi-equivalent molecular orbitals can no longer be separated from each other.

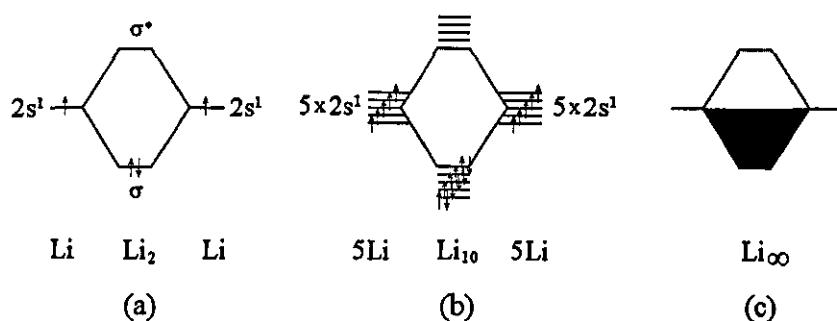**Figure 1.30.** Formation of a metallic state, exemplified by lithium.[3]

In an ideal crystal, where there are far too many atoms to build up a molecular orbital diagram as in Figure 1.30c, the energy levels broaden into 2 distinct bands. The first is the valence band or highest occupied molecular orbital (HOMO). The second energy band is the conduction band or lowest unoccupied molecular orbital

(LUMO). Typically it is either holes in the valence band or mobile electrons in the conduction band that move electrical current around the solid. In semiconductors and insulators there is a band gap between the valence band and the conduction band (Figure 1.31). The application of an electrical potential acts to increase the energy of the electrons such that they have a higher energy than in the LUMO, and electron transfer becomes thermodynamically favourable.
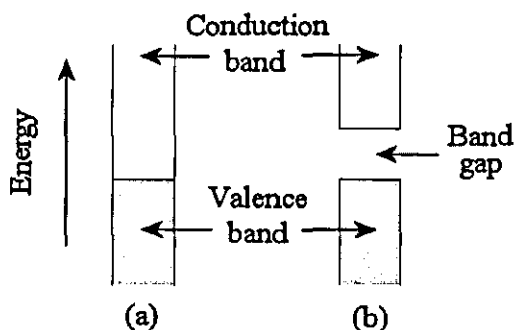
Figure 1.31. Band theory of solids for (a) metals, and (b) semiconductor/ insulator

In non-ideal situations, the conduction of electrons will change as impurities or dopants are introduced. Where an impurity accepts an electron from the valence band, a positive hole is generated in the valence band and the material is classified as a p-type semiconductor. It is also possible for an impurity to donate an electron to the conduction band, where the impurity electrons conduct to give an n-type semiconductor.

The relation between the molecular orbital description of a finite molecular system and the infinite situation in a bulk metal is that the HOMO is now called the Fermi energy (E_F), which is dependent on the density of the electrons and is therefore independent of the particle size. However the distance between energy levels is known to increase with decreasing particle size. Figure 1.32 shows the relationship between E_F and the development of the density of states (DOS) as a function of energy from a molecular system to a bulk metal. In Figure 1.32a only well separated energy levels are present for a typical molecular state, whereas in Figure 1.32c, a characteristic band structure is observed, corresponding to an infinite number of non-differentiated electrons in bulk materials. Figure 1.32b illustrates the electronic

configuration of nanosized particles where there are near-degenerate electronic levels, i.e. the unstructured energy bands in a bulk material begin to split but without forming the truly discrete levels observed at the molecular level.

(a)   (b)   (c)
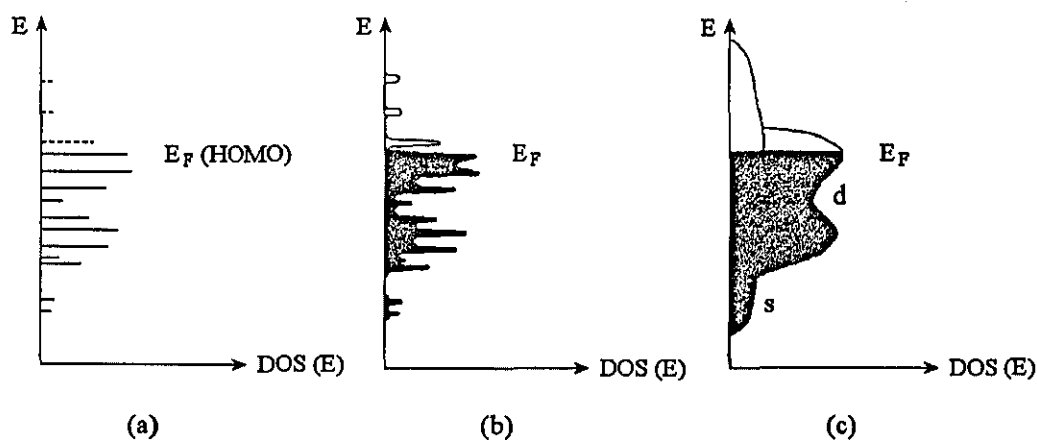
Figure 1.32. Formation of band structure for (a) a molecular state, (b) a nanoparticle with broadened energy states, and (c) a fully developed band structure consisting of s and d band.[3]

The physical properties of semi-conductor particles have been shown to depend very sensitively on the particle size in a similar way to metals, where the spatial confinement of electronic (and vibrational) excitations dominates. The quantisation of electronic energy levels occurs with decreasing particle size (<10 nm) manifesting in the widening of the bandgap between the valence band and the conduction band.[52] The restriction of electron mobility can therefore be reached by reducing the volume of the particle from a three-dimensional bulk material, to a two-dimensional quantum well, a one-dimensional quantum wire, and finally to the minute size of a "zero-dimensional" quantum dot.

Titanium (IV) oxide and cerium (IV) oxide are both semi-conductors[53,54] however the worse inter-particle electron transfer in mesoporous films means that movement of electrons through the films are slower than that recorded for a compact crystalline material.[55] It is assumed in nano-structured thin films that electron transport proceeds primarily via diffusion. A model where electrons move between localised band gap states by hopping between nanoparticles has been suggested.[56]

1.6. Surface Imaging & Analysis Techniques

1.6.1. Scanning Electron Microscopy

Scanning Electron Microscopy (SEM) is a popular technique used to study the surface topography of samples[57] where the first SEM was built in the 1960's. A typical SEM is capable of magnifications 1000 times greater than the best optical microscopes allowing sample imaging in the 10 nm range.

Figure 1.33 shows a schematic of an SEM. It works by focusing a high-energy (typically 10 keV) beam of electrons across the surface of the sample held in a vacuum. The electrons are produced at the electron gun (usually a tungsten filament) by passing a large current through it, heating the filament to the thermionic emission temperature of electrons (approximately 2700 K). In a Field Emission Gun Scanning Electron Microscope (FEGSEM) the tungsten filament is replaced by a single crystal tungsten wire sharpened to a point. The wire cathode tip is surrounded by a high electric field that attracts electrons from the cathode. The FEG is able to generate much larger electron densities compared to the conventional tungsten filament. The increase in electron density allows a reduction in the beam diameter and therefore better resolution. The FEG system has been used in this investigation to obtain high resolution images of the nanoparticle film surfaces.
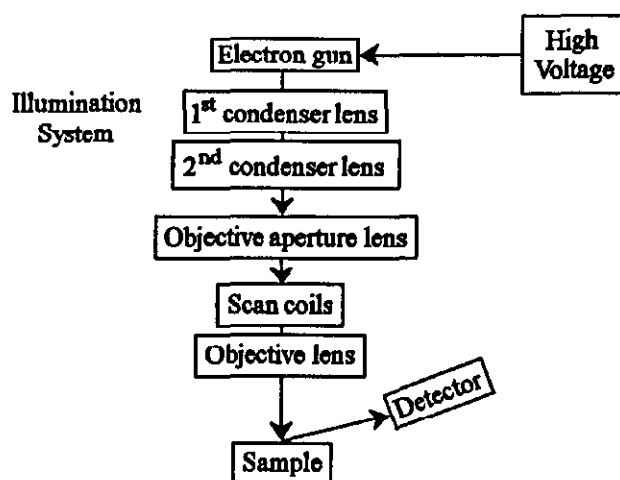
Figure 1.33. Schematic of a typical Scanning Electron Microscope

When the incident beam of electrons hit the sample surface, a number of energetic emissions can be recorded.

1. The incident electrons cause low energy secondary electrons to be generated some of which escape from the surface. The secondary electrons emitted from the sample, are detected for example by attracting them onto a phosphor screen. This screen will glow and the intensity of the light is measured with a photo-multiplier.

2. The incident electrons will also cause X-rays to be generated, which is the basis of the energy-dispersive X-ray analysis (EDX) technique providing information on the chemistry of individual particles.

3. Some of the incident electrons may strike an atomic nucleus and bounce back into the vacuum. These electrons are known as primary backscattered electrons and can be detected with a backscattered electron detector. Backscattered electrons can also give information on the surface topography and the average atomic number of the area under the electron beam.

Reducing the energy of the incident beam can increase the surface sensitivity of the SEM. This can be achieved by increasing the voltage on the sample to just below the incident beam energy.

1.6.2. Transmission Electron Microscopy

Transmission electron microscopy (TEM) is used widely for the micro-structural characterisation of materials.[58] Using concepts developed by Knoll and Ruska, the first practical transmission electron microscope was built at the University of Toronto in 1938 by Prebus and Hillier.

Similar to SEM, TEM utilises a focused high-energy (200 keV) beam of electrons. Instead of being focused on the surface of the sample, the electron beam passes through the sample. These electrons are scattered at different angles depending on

the density of the atom it encounters and can either be un-deflected, deflected but loses no energy (elastically deflected), or loses a significant amount of energy and is probably deflected (inelastically scattered). The system of lens and apertures below the sample allows a contrasting image to be produced from the different scattered angles. The image is then formed as a shadow on a fluorescent screen, layer of photographic film or detected by a CCD camera. A schematic of a TEM is shown in Figure 1.34. A modern transmission electron microscope may have the capability to use 6 main techniques.

1. Conventional imaging using bright-field (using only transmitted electrons) and dark-field (using only diffracted electrons) TEM.

2. Measuring electron diffraction from selected areas of the sample using selective area electron diffraction, (SAD) allows the crystallography of specific areas in the sample to be studied.

3. With a high resolution TEM it is possible to carry out phase-contrast imaging and atomic scale resolution.

4. Elemental determination is possible using energy-dispersive X-ray spectroscopy (EDX) as in SEM.

5. Electron energy-loss spectroscopy (EELS) can be used to measure the energy lost from the incident electrons to plasmons or core excitations. This enables information on the local chemistry and structure to be gathered.

6. In scanning transmission electron microscopy or STEM, the narrow beam of electrons is moved in a raster pattern across the sample. At the same time it is possible to detect emitted X-rays, secondary electrons (SED) or backscattered electrons (BSE).
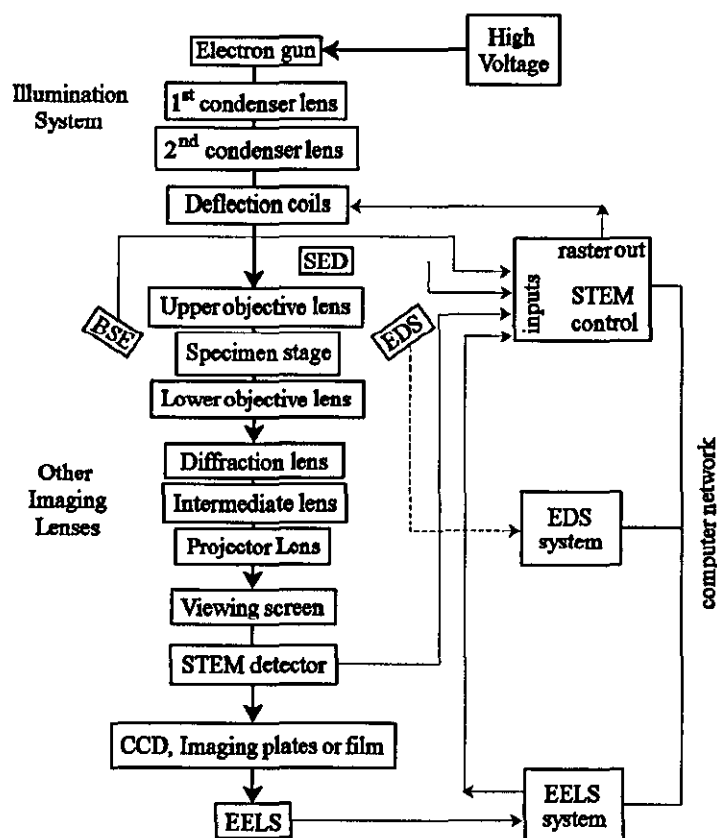
Figure 1.34. Schematic of a typical Transmission Electron Microscope with STEM capability.[58]

To enable the electrons to pass through the sample, it must be very thin (typically less than 100 nm). The limitation on sample size can result in a large amount of sample preparation being necessary. TEM images were obtained of the partially oxidised TiC nanoparticles.

1.6.3. X-Ray Powder Diffraction

XRD or X-ray diffraction is a technique for the analysis of crystalline materials.[59] This is possible due to the elastic scattering (diffraction) of X-rays of known wavelength, λ, from the electron clouds in atomic planes in the sample. The position of the diffraction peaks produced is a measure of the distance between discrete crystallographic planes within the sample while their intensity is directly proportional to the number of electrons (atoms) that are found in the atomic planes.

The condition for constructive wave interference and therefore strong diffraction from planes with spacing, d, is given by Bragg's law (equation 1.39).

$$n\lambda = 2d \sin (\theta) \hspace{4cm} (1.39)$$

Where θ is the angle between the atomic planes and the incident X-ray beam and n is an integer. Every crystalline solid will have a unique pattern of d-spacings (diffraction pattern) and the resultant diffraction pattern can be used to identify unknown crystalline phases, determine residual stresses, preferred orientation or grain size. It is therefore possible to identify solids with the same chemical composition, but different crystalline structure by their pattern of d-spacings.

The Scherrer formula (equation 1.40) relates the thickness of a crystallite to the width of its diffraction peaks and is widely used to determine particle size distributions in clays and polymers:

$$t = \frac{0.9\lambda}{\sqrt{B_m^2 - B_s^2}\cos\theta} \hspace{4cm} (1.40)$$

Where t = crystallite thickness (Å), B_m and B_s = width in radians of the diffraction peaks (at half maximum height) of the test sample and a highly crystalline standard (0.1) sample respectively, and λ = wavelength of the X-ray beam (Å).

XRD was used to determine the size and structure of the TiO_2 and CeO_2 metal oxide nanoparticles before and after heat treating at 500°C. The XRD technique was also used to determine the size and structure of the TiC nanoparticles before and after thermal oxidation over a range of temperatures.

1.6.4. Simultaneous Small-Angle X-Ray Scattering and Wide-Angle X-Ray Scattering (SAXS-WAXS)

SAXS/WAXS or simultaneous small-angle X-ray scattering and wide-angle X-ray scattering is a similar technique to XRD, where the elastic scattering of X-rays is measured at both very low (0.1 - 10°) and wide angles (up to 40°). In the small angle range information about the average shape and size of macromolecules, distances in partially ordered materials, and pore sizes can be obtained. SAXS is able to determine structural information of molecules between approximately 5 and 25 nm in size. The SAXS technique has been applied to a large number of areas including colloids, metals, polymers, proteins and pharmaceuticals. The scattering angle is represented by Q, tangent of half the scattering angle, θ, (see equation 1.41) due to the small angular range in SAXS.[60]

$$Q = \frac{4\pi \sin \theta}{\lambda} \qquad (1.41)$$

Wide angle X-ray scattering is the same technique as SAXS only the distance from the sample to the detector is shorter allowing the diffraction at larger angles to be observed. WAXS is often used to determine the crystalline structure of polymers where the diffraction pattern generated allows the calculation of the chemical or phase composition, texture, and crystallite size. Modern instruments are capable of measuring small, intermediate and wide angle X-ray scattering.

1.7. The Quartz Crystal Microbalance Technique

QCM or quartz crystal microbalance is an analytical tool typically comprised of a thin AT-cut alpha quartz crystal with an electrode plated on each side (Figure 1.35). AT-cut crystals are often used as they can be cut to give a temperature coefficient close to zero at one or two temperatures. By connecting the electrodes to an oscillator and applying an AC voltage, the quartz crystal starts to oscillate at its resonance frequency due to the piezoelectric effect.[61]
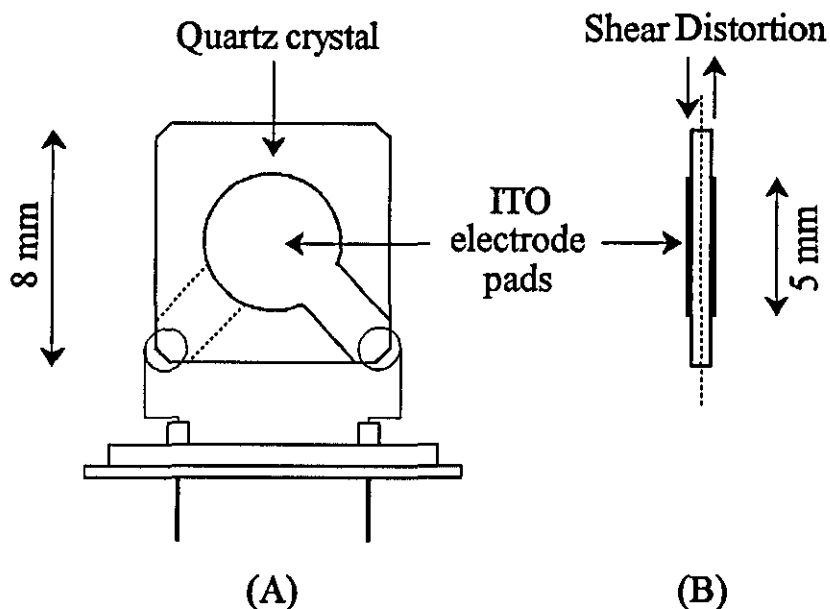
Figure 1.35. Schematic drawing of (A) a quartz crystal resonator with ITO electrodes evaporated onto the surface and (B) the movement of a quartz disk with applied potential. The type of resonator used here operates at 9.1 MHz in air.

Jacques and Pierre Curie were the first to discover the piezoelectric effect.[62] In 1880 they applied a mechanical stress to the surface of various crystals (including quartz) and noted an electrical potential across the crystal with a magnitude proportional to the applied stress. The Curies also experimentally verified the 'converse piezoelectric effect' where an applied voltage across the surface of these crystals resulted in a corresponding mechanical strain. The converse piezoelectric effect is the basis of the QCM technique.

Application of an electric potential across the AT-cut quartz crystal produces lattice strain and shear deformation proportional to the applied potential as the dipoles in the acentric material re-orientate (Figure 1.36).
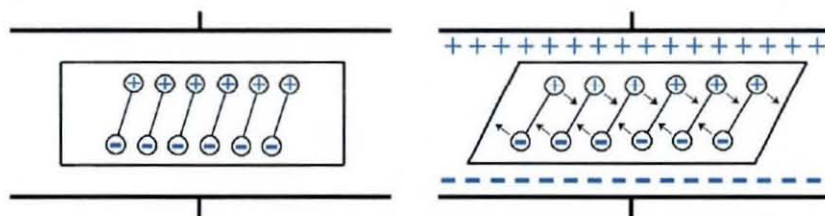
Figure 1.36. Schematic representation of the converse piezoelectric effect for shear motion.[62]

This deformation is elastic in quartz. An identical strain is produced on application of the opposite polarity. By alternating the direction of the potential across the crystal surface it is possible to generate a transverse shear wave in the quartz crystal. This oscillation is generally very stable, Figure 1.37 shows a schematic of the transverse shear wave in a quartz crystal and a composite resonator where a layer of foreign material has been deposited onto the crystal. The wavelength is longer in the composite resonator due to the increase in thickness. This reduces the resonant frequency compared to the clean quartz crystal.
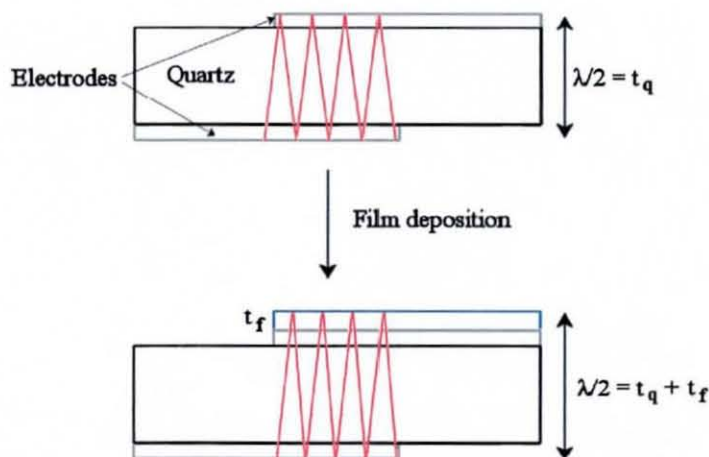

Figure 1.37. Schematic representation of the transverse shear wave in quartz crystal and a quartz crystal and a layer of film.[62]

If a rigid layer is deposited evenly onto one or both of the electrodes the resonant frequency will decrease proportionally to the mass of the adsorbed layer according to the Sauerbrey equation (equation 1.42).

$$\Delta f = \frac{-2f_0^2 \Delta m}{A\sqrt{\rho_q \mu_q}} \tag{1.42}$$

Where Δf = measured frequency shift, f_0 = resonant frequency of the fundamental mode of the crystal, Δm = mass change per unit area (g/cm^2), A = piezo-electrically active area, ρ_q = density of quartz, 2.648 g/cm^3, and μ_q = shear modulus of quartz, 2.947 x 10^{11} g cm^{-1} s^2.

The limitations of the Sauerbrey equation in general are due to non-ideal behaviour of the film deposited on the resonator surface, including non-uniformity and non-rigidity of the added film.

The QCM system is very versatile and has been used in vacuum systems, in air and can also be made to resonate in liquids. This allows the QCM to have numerous applications including gas phase analysis, immunosensors and drug analysis.[63] The QCM system is used in this investigation to monitor the formation of the nanoparticle films on one side of the crystal in air.

1.8. Biphasic Electrochemical Systems

1.8.1. Introduction

When two or more phases that are highly immiscible with each other come into contact, a phase boundary is created. For example if a hydrophobic organic phase comes into contact with an aqueous phase, a liquid | liquid interface is produced.

The first direct electrochemical study of the interface between two immiscible electrolyte solutions (ITIES) was carried out in 1902 by Nernst and Riesenfeld[64] where they observed the transfer of coloured inorganic ions between water and phenol on application of a voltage.

There are many important processes in nature and technology that occur at liquid | liquid interfaces such as membrane processes or phase transfer catalysis. The behaviour of both neutral and charged species at liquid | liquid interfaces can be examined and utilised in various studies.[65,66]

1.8.2. Partitioning of Neutral Molecules at Liquid | Liquid Interfaces

It is possible to define the chemical potential (μ_i) of a neutral species in a biphasic medium using equation 1.43, where μ_i^0 is the standard chemical potential and a_i is the activity.

$$\mu_i = \mu_i^0 + RT \ln a_i \qquad (1.43)$$

After a time the species will come to equilibrium in the 2 phases so it is possible to assume the sum of the chemical potentials in the water phase are equal to the sum of the chemical potentials in the organic phase.

The potential difference ($\Delta^{O\text{-}W}\mu^0$) can be determined by the ratio of activity of the neutral species in each phase. The ratio gives the equilibrium coefficient ($K_{partitioning}$).

$$\Delta^{O\text{-}W}\mu^0 = RT \ln \frac{a_{organic}}{a_{water}} = RT \ln K_{partitioning} \qquad (1.44)$$

The higher the value of log K_{ow} the more the compound prefers to be in the organic phase. This allows the behaviour of various compounds to be compared.

1.8.3. Partitioning of Ionic Molecules at Liquid | Liquid Interfaces

It is also possible to study the partitioning of ions at liquid | liquid interfaces, in particular what happens if a salt is added to a biphasic system. Cations and anions

will have different preferences of which phase they distribute in. This creates a charge imbalance between phases resulting in ions distributing characteristically at the interface.

As with the neutral species it is possible to define the potential for each component. However in the case of charged species it is the electrochemical potential ($\tilde{\mu}_i$) that is calculated not the chemical potential as shown in equation 1.45, where z_i is the charge of the ion and Φ_i is the electrical potential of the ion.

$$\tilde{\mu}_i = \mu_i^0 + RT \ln a_i + z_i F \phi_i \qquad (1.45)$$

Again at equilibrium state, the sum of the potentials in each phase is equal. This can be shown for the cation and anion in each phase. The potential terms add up resulting in the potential term across the interface being relative to the ratio of ions in the biphasic system as shown below (assuming that the cation and anion have the same charge).

$$F\phi_{+water} - F\phi_{-water} - F\phi_{+organic} + F\phi_{-organic} = F\Delta\phi$$
$$= \Delta^{o-w}\mu_+^0 + RT \ln \frac{a_{+organic}}{a_{+water}} + \Delta^{o-w}\mu_-^0 + RT \ln \frac{a_{-organic}}{a_{-water}} \qquad (1.46)$$

By imposing electroneutrality equation 1.46 can be simplified, as there is no need to identify the positive and negative ions individually:

$$F\Delta\phi = \Delta^{o-w}\mu_+^0 + \Delta^{o-w}\mu_-^0 + 2RT \ln \frac{a_{organic}}{a_{water}} \qquad (1.47)$$

The potential difference is determined by the ratio of the activities and this ratio in turn is dependent on the individual preferences of ions. In the rare case of the Gibb's energy for transfer for both cation and anion being the same, there is no potential across the interface. This means that any imbalance will create a potential difference across the liquid | liquid interface.

The composition of the two solvent phases can be represented as a high concentration of one phase with a small concentration of the other that switches round at the interface (see Figure 1.38). The size of the interfacial region is about 1 nm. The lower the solubility of one solvent in the other, the thinner this interfacial region should be.
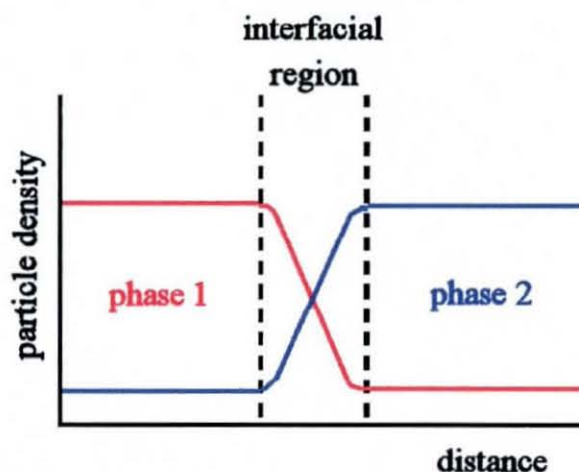
Figure 1.38. Figure representing the composition of the solvent phases and at the liquid | liquid interface.[66]

As previously stated the orientation of the ions in each phase creates a potential difference across the interface. However at the interface electroneutrality does not hold and the ions distribute as shown in Figure 1.39 below, with the cations in the organic phase and the anions in the aqueous phase.

Figure 1.39. Schematic of the ion pairs present in the interfacial region and a plot of the charge density across the interface demonstrate there is a definite positive and negative region.[64,66]

1.8.4. Biphasic Voltammetry

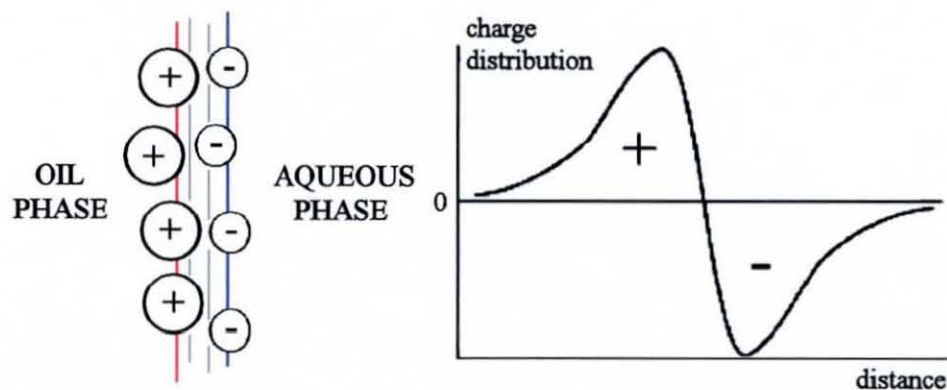The potential across the interface can be controlled electrochemically. In a very simple case, it is possible to introduce two electrodes to the system (Figure 1.40A). When a potential is applied between the two electrodes, charge propagates to the liquid | liquid interface. If a redox couple is present in each phase, electron transfer can be driven at the liquid | liquid interface (equation 1.48).

$$O_1 + R_2 \rightleftharpoons R_1 + O_2 \qquad\qquad (1.48)$$

The basic scheme for electron transfer at the liquid | liquid interface is shown in Figure 1.40B where O_1 and R_1 are in phase 1, and O_2 and R_2 are in phase 2. The reduction of the species in phase 1 by the redox couple in phase 2 requires the movement of both species to the interfacial reaction planes located at a distance a and b from the liquid | liquid interface, respectively.[65]
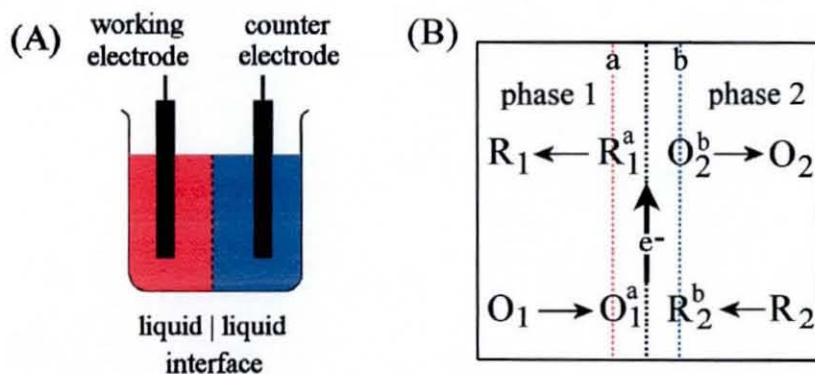
Figure 1.40. (A) Two electrode configuration for the study of the interface between two immiscible solutions (ITIES) and (B) a schematic representation of the heterogeneous electron transfer reaction driven at the liquid | liquid interface.[65]

A requirement for the study of electron transfer processes is the ability of the two phases to conduct electrical charge. This can be achieved typically by adding dissociating salts (similar to the addition of the supporting electrolyte described in section 1.4.7).

Alternatively it is possible to drive the transfer of ions at the interface between the two immiscible phases. For example, when a redox couple in the organic phase undergoes oxidation, the transfer of anions across the liquid | liquid interface can occur simultaneously to maintain the overall electroneutrality of the oil phase (equation 1.49). In the reverse reduction step, the anion is expelled back into the aqueous phase.[67]

$$A_{(organic)} + X^-_{(aq)} \rightleftharpoons [A^+X^-]_{(organic)} + e^- \qquad (1.49)$$
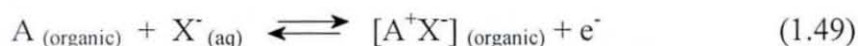
By positioning two electrodes (one counter and one reference) in each phase, it is possible to expand on the simple system in Figure 1.40A and apply a potential directly to the interface (Figure 1.41). The potential can be scanned and the potential difference between the two reference electrodes measured. This allows the electrochemical response or cyclic voltammogram for the biphasic ion transfer reaction under investigation to be probed.
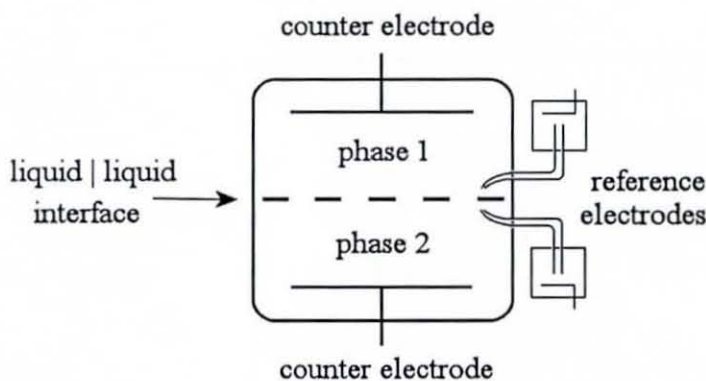
Figure 1.41. Schematic of the electrolytic cell with a four-electrode configuration for the study of the ITIES.[66]

The resulting cyclic voltammogram looks like a typical cyclic voltammogram (Figure 1.42) produced in a conventional electrochemical experiment in that if you change the scan rate, the peak current will change allowing the partition coefficient to be determined. Characteristic voltammetric responses can be recorded in the presence of different species due to the variation in transfer potential.

Figure 1.42. Dotted line is the typical cyclic voltammogram for the base electrolytes (aqueous phase = 0.01M Li_2SO_4 and organic phase = 0.01M crystal violet tetraphenylborate) only at a nitrobenzene | water interface, and the solid line is the typical cyclic voltammogram for the transfer of ClO_4^- ions at the nitrobenzene | water interface.[64]

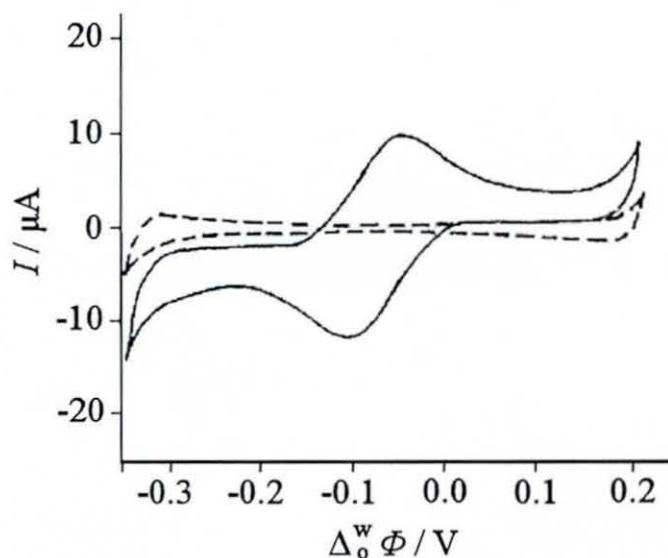The first experiments to be carried out in this area were reported towards the end of the 19th century, however, it was not until the work of Gavach in 1968 that interest in this area started to increase.[66] This type of experiment can be utilised in many other types of studies allowing binding constants to be calculated[64] and metal deposits to be formed.[68]

It is also possible to use a similar biphasic system with oil/water/electrode where the triple interface is the site of electron/ion transfer.[67,69] In these experiments, the working electrode surface is modified with the insoluble organic phase, which is then immersed into an aqueous electrolyte solution where the reference and counter electrode are located. Biphasic voltammetric measurements can then be carried out using a classical three-electrode potentiostat instead of the four-electrode potentiostat. The working electrode can be modified in a number of ways, with investigations frequently reported for single droplet and random microdroplet array configurations. Experiments at droplet-modified electrodes are normally undertaken using unsupported organic material, thus enabling the site of electron/ion transfer to

be localised initially at the triple phase boundary with the reaction advancing toward the centre of the droplet. In chapter 4, this technique was utilised to study the transfer of ions such as perchlorate, phosphate and protons between an aqueous phase and organic phase immobilised on an electrode surface.

1.9. References

[1] J. Perez-Juste, I. Pastoriza-Santos, L.M. Liz-Marzan, P. Mulvaney, *Coord. Chem. Rev.* 249 (2005) 1870

[2] M.J. Pitkethly, *Mater. Today* 6 (2003) 36

[3] K.J. Klabunde (Ed.), *Nanoscale Materials in Chemistry* John Wiley & Sons, 2001

[4] P. Dobson, "*Nanoparticles & Nanocomposites*" paper in 'Commercial and Industrial Applications for Microengineering and Nanotechnology', 26th April 1999, London

[5] Y. Miyazaki, S. Shiratori, *Thin Solid Films* 499 (2006) 29

[6] W.Y. Wang, Y.P. Xu, D.F. Zhang, X.L. Chen, *Mater. Res. Bull.* 36 (2001) 2155

[7] D. Zuliang, Z. Weifeng, H. Yabin, M. Guohong, Z. Weill, Z. Ziqiang, N. Gu, L. Zuhong, *Supramol. Sci.* 5 (1998) 453

[8] L. Chen, M. Subirade, *Biomaterials* 26 (2005) 6041

[9] S.M. Prokes, W.E. Carlos, L. Seals, S. Lewis, J.L. Gole, *Mater. Lett.* 54 (2002) 85

[10] L. Li, Y. Li, *Mater. Chem. Phys.* 94 (2005) 1

[11] S. Chen, M. Paulose, C. Ruan, G.K. Mor, O.K. Varghese, D. Kouzoudis, C.A. Grimes, *J. Photochem. Photobiol. A* 177 (2006) 177

[12] L. Feng, X. Kong, K. Chao, Y. Sun, Q. Zeng, Y. Zhang, *Mater. Chem. Phys.* 93 (2005) 310

[13] H.Y. Wang, X.J. Li, *Sens. Actuators B* 110 (2005) 260

[14] H.L. Tang, M. Pan, S.P. Jiang, R.Z. Yuan, *Mater. Lett.* 59 (2005) 3766

[15] A.K. Gupta, M. Gupta, *Biomaterials* 26 (2005) 3995

[16] P.M. Jenneson, R.D. Luggar, E.J. Morton, O. Gundogdu, U. Tuzun, *J. App. Phys.* 96 (2004) 2889

[17] M. Avella, J.J. De Vlieger, M.E. Errico, S. Fischer, P. Vacca, M.G. Volpe, *Food Chem.* 93 (2005) 467

[18] L. Cumbal, J. Greenleaf, D. Leun, A.K. SenGupta, *React. Funct. Polym.* 54 (2003) 167

[19] A.N. Shipway, E. Katz, I. Willner, *Chem. Phys. Chem.* 1 (2000) 18

[20] C. Lee, Y. Kang, K. Lee, S.R. Kim, D-J. Won, J.S. Noh, H.K. Shin, C.K. Song, Y.S. Kwon, H-M. So, J. Kim, *Curr. Appl. Phys.* 2 (2002) 39

[21] T. Tanase, Y. Kobayashi, T. Miwa, M. Konno, *Thin Solid Films* 485 (2005) 22

[22] X.M. Cai, K.W. Cheng, C.O. Oey, A.B. Djurisic, W.K. Chan, M.H. Xie, P.C. Chui, *Thin Solid Films* 491 (2005) 66

[23] P. Thilakan, S. Kalainathan, J. Kumar, P. Ramasamy, *J. Electron. Mater.* 24 (1995) 719

[24] Y. Maehara, S. Takenaka, K. Shimizu, M. Yoshikawa, S. Shiratori, *Thin Solid Films* 438 (2003) 65

[25] A. Ulman, *Chem. Rev.* 96 (1996) 1533

[26] S. Ito, K. Kawano, M. Yamamoto, H. Hasegawa, T. Hashimoto, *Macromolecules* 28 (1995) 3736

[27] Y.M. Lvov, 'Thin Film Nanofabrication by Alternate Adsorption of Polyions, Nanoparticles and Proteins' Institute for Micromanufacturing, Louisiana Tech University, Ruston, LA in *Handbook for Surfaces & Interfaces, Volume 3: Nanostructured Materials*, H. Nalwa (Ed.) Academic Press, NY, 2001

[28] C. Papenfuss, W. Muschik, *Thin Solid Films* 284-285 (1996) 484

[29] K.B. Blodgett, I. Langmuir, *Phys. Rev.* 51 (1937) 964

[30] B.P. Binks, *Adv. Colloid Interface Sci.* 34 (1991) 343

[31] A.P. Girard-Egrot, S. Godoy, L.J. Blum, *Adv. Colloid Interface Sci.* 116 (2005) 205

[32] F. Davies, S.P.J. Higson, *Biosens. Bioelectron.* 21 (2005) 1

[33] M. Brust, C.J. Kiely, *Colloids Surf. A* 202 (2002) 175

[34] Z. Wang, X. Hu, *Thin Solid Films* 352 (1999) 62

[35] B.J. Chen, X.W. Sun, C.X. Xu, *Ceram. Int.* 30 (2004) 1725

[36] S. Fujita, S. Shiratori, *Thin Solid Films* 506 (2006) 545

[37] J-H. Kim, S. Fujita, S. Shiratori, *Thin Solid Films* 499 (2006) 83

[38] K. Cai, A. Rechtenbach, J. Hao, J. Bossert, K.D. Jandt, *Biomaterials* 26 (2005) 5960

[39] G. Decher, J.D. Hong, *Macromol. Symp.* 46 (1991) 321

[40] M.A. Correa-Duarte, M. Gierig, N.A. Kotov, L.M. Liz-Marzan, *Langmuir* 14 (1998) 6430

[41] D.J. Neivandt, M.I. Gee, C.P. Tripp, M.L. Hair, *Langmuir* 13 (1997) 2519

[42] T. Serizawa, K. Yamamoto, M. Akashi, *Langmuir* 15 (1999) 4682

[43] A.J. Bard, L.R. Faulkner, *Electrochemical Methods: Fundamentals & Applications*, John Wiley & Sons, 2nd edition 2001

[44] D. Pletcher, *A First Course in Electrode Processes*, Alresford Press Ltd, Alresford 1991

[45] A.C. Fisher, *Electrode Dynamics*, Oxford University Press, Oxford 1996

[46] T.E. Edmonds, *Chemical Sensors*, Blackie & Son Ltd 1988

[47] D.R. Crow, *Principles & Applications of Electrochemistry*, Stanley Thornes (Publishers) Ltd, 4th edition 1994

[48] R.W. Cattrall, *Chemical Sensors*, Oxford University Press, Oxford 1997

[49] A.M. Bond, *Broadening Electrochemical Horizons: Principles & Illustration of Voltammetric & Related Techniques*, Oxford University Press, Oxford 2002

[50] K.B. Oldham, J.C. Myland, *Fundamentals of Electrochemical Science*, Academic Press, INC. San Diego 1994

[51] S. Roy Morrison, *Electrochemistry at semiconductor and oxidised metal electrodes*, Plenum Press, New York, 1980

[52] K.M. Reddy, S.V. Manorama, A.R. Reddy, *Mater. Chem. Phys.* 78 (2002) 239

[53] R. Hengerer, B. Bolliger, M. Erbudak, M. Grätzel, *Surf. Sci.* 460 (2000) 162

[54] M. Mogensen, N.M. Sammes, G.A. Tompsett, *Solid State Ionics* 129 (2000) 63

[55] E.A. Meulenkamp, *J. Phys. Chem.* B 103 (1999) 7831

[56] J. Bisquirt, D. Cahen, G. Hodes, S. Ruhle, A. Zaban, *J. Phys. Chem.* B 108 (2004) 8106

[57] O.C. Wells, *Scanning Electron Microscopy*, McGraw-Hill, New York, 1974

[58] B. Fultz, J.M. Howe, *Transmission Electron Microscopy and Diffractometry of Materials*, Springer, Berlin 2002

[59] S.E. Dann, *Reactions and Characterisation of Solids, Royal Society of Chemistry,* Cambridge 2000

[60] O. Glatter, O. Kratky, *Small Angle X-ray Scattering* Academic Press, London, 1982, p. 105

[61] D.A. Buttry, *Electroanalytical Chemistry,* Marcel Dekker Inc., New York, 17 (1991) 1

[62] D.A. Buttry, M.D. Ward, *Chem. Rev.* 92 (1992) 1355

[63] T-Y. Lin, C-H. Hu, T-C. Chou, *Biosens. Bioelectron.* 20 (2004) 75

[64] H.H. Girault, D.J. Schiffrin, *Electroanalytical Chemistry,* Marcel Dekker Inc., New York, 15 (1989) 1

[65] F. Reymond, D. Fermin, H.J. Lee, H.H. Girault, *Electrochim. Acta* 45 (2000) 2647

[66] W. Schmickler, *Interfacial Electrochemistry*, Oxford University Press, Oxford (1996) Ch 12

[67] C.E. Banks, T.J. Davies, R.G. Evans, G. Hignett, A.j. Wain, N.S. Lawrence, J.D. Wadhawan, F. Marken, R.G. Compton, *Phys. Chem. Chem. Phys.*, 5 (2003) 4053

[68] C. Johans, R. Lahtinen, K. Kontturi, D.J. Schiffrin, *J. Electroanal. Chem.* 488 (2000) 99

[69] R. Gulaboski, F. Scholz, *J. Phys. Chem. B* 107 (2003) 5650

Chapter 2

TiO$_2$ Mono-Layer Film Electrochemistry

2.1. Introduction

Titanium (IV) oxide, TiO$_2$, is an abundant, relatively cheap, versatile material with a high chemical stability and biocompatibility.[1] TiO$_2$ has consequently been used in a wide number of applications, ranging from use in pigments[2] (in paper, cosmetics and paint), as photo-catalysts[3] and to dimensionally stable electrodes.[4] The use of single crystal electrodes for the photoelectrochemical decomposition of water to hydrogen and oxygen[5] in 1972 promoted further interest in the photochemical properties of TiO$_2$. The layer of semiconductor in the dye-sensitised solar cell produced by Grätzel is obtained from a TiO$_2$ colloid.[6]

The surface chemistry of TiO$_2$ has been carefully studied at polycrystalline and at single crystal surfaces.[7] TiO$_2$ has been investigated extensively usually in the form of thin meso- or microporous films at inert electrodes,[8] at titanium surfaces,[9,10,11] but also in the form of single crystals.[12,13]

The electrochemical properties of mesoporous films of TiO$_2$ have been intensely studied[14,15,16,17] and recently models have been developed[18] to describe the capacitive and reactive properties of nanoporous semi-conducting TiO$_2$. A number of studies have also been carried out to investigate the conductivity of nano-structured TiO$_2$ films permeated with electrolyte.[19] However, relatively little is known about the behaviour of individual TiO$_2$ nanoparticles or ensembles of TiO$_2$ nanoparticles assembled into a mono-layer. It is shown here that electrochemical experiments with mono-layer deposits of TiO$_2$ can be readily conducted and provide data complementary to results from thick film and single crystal experiments. When immobilized into a mono-layer of nanoparticles, TiO$_2$ shows features similar to those of polyoxometalate redox systems[20] with surface site reduction (here Ti(IV/III)) and protonation. Experiments were conducted at boron-doped diamond substrates.

Boron-doped diamond[21] as an inert electrode material has found a wide range of applications in electroanalysis,[22] electro-synthesis,[23] and waste treatment.[24] The chemically inert diamond surface combined with a wide accessible potential window and low background current makes boron-doped diamond an ideal substrate material for the immobilisation of sensor probes.[25] Various types of nanoparticles (gold,[26,27] platinum[28] and other metals,[29] hydrous iron oxide,[30] ruthenium oxide,[31] and iridium oxide[32]) have previously been immobilised at boron-doped diamond surfaces and investigated with voltammetric techniques.

In this chapter, experiments are described in which titanium (IV) oxide, TiO_2 (anatase), nanoparticles are adsorbed onto the surface of a polycrystalline boron-doped diamond electrodes (industrially polished to mirror finish) and studied in aqueous solution environments. The reduction response for the TiO_2 nanoparticles is proposed to be associated with the formation of surface Ti(III) and accompanied by the adsorption of protons. Two distinct types of sites for the reduction process associated with proton adsorption are observed.

2.2. Experimental

2.2.1. Chemicals

Demineralised and filtered water was taken from an Elga water purification system (Elga, High Wycombe, Bucks, UK) with a resistivity of not less than 18 MΩ cm. Titanium (IV) oxide sol (anatase, *ca.* 6 nm diameter, 30-35% in aqueous HNO_3, pH 0-3, TKS-202) was obtained from Tayca Corp., Osaka, Japan and diluted with deionised water. $NaClO_4$, KOH, H_3PO_4, $HClO_4$, maleic acid, phytic acid dodecasodium salt hydrate, K_2HPO_4, and KH_2PO_4 were obtained commercially in analytical or the highest purity grade available.

2.2.2. Instrumentation

Voltammetric measurements were performed with a computer controlled Eco Chemie PGSTAT20 Autolab potentiostat system. Experiments were conducted in staircase voltammetry mode with a platinum gauze counter electrode and saturated calomel reference electrode (SCE (saturated KCl), REF401, Radiometer). Polycrystalline boron-doped diamond with mirror-finish polish (mineral acid treated, doping level *ca.* 10^{21} cm^{-3}, Windsor Scientific, Slough, UK) obtained in the form of plates (5 mm × 5 mm × 0.6 mm) for use in electrochemical experiments (mounted with silver epoxy back contact in epoxy) and in the form of 3 mm diameter disks (for FEGSEM experiments). The working electrode surface was modified with a porous metal oxide film. The coating of TiO_2 was removed by polishing with wet alumina (Buehler, 0.3 μm).

The 3-electrode system was set up in a glass cell (refer to Figure 1.9). Prior to conducting electrochemical experiments, all solutions were purged with argon (BOC, UK) to remove O_2. All experiments were carried out at a temperature of 22 ± 2°C.

Scanning electron microscopy images were obtained with a Leo 1530 field emission gun scanning electron microscope (FEGSEM) system. Prior to FEGSEM imaging, the sample surface was scratched with a scalpel blade.

2.3. Reactivity of TiO$_2$ Nanoparticle Mono-layers at Boron-Doped Diamond Electrodes

2.3.1. Adsorption of TiO$_2$ Nanoparticles onto Boron-Doped Diamond Surfaces

Boron-doped diamond surfaces after treatment with mineral acids have oxygen functionalised surfaces and allow some types of positively charged colloids to readily adsorb. It has been shown recently that boron-doped diamond allows nanoparticulate oxides to be adsorbed onto the surface in the form of a very thin

layer. This configuration with an inert and geometrically well-defined boron-doped diamond surface substrate (see Scheme 2.1) allows the electrochemical properties of the nanoparticle deposits to be studied and potential distribution effects within the oxide layer or within the pores of the oxide to be minimised.
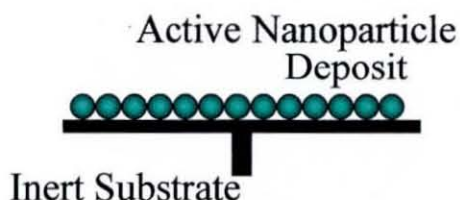
Scheme 2.1. Schematic drawing of an active nanoparticle deposit immobilised at an inert boron-doped diamond electrode surface.

Figure 2.1 shows a FEGSEM image of a boron-doped diamond surface modified with a layer of TiO_2 nanoparticles adsorbed onto the electrode surface after being immersed manually in an aqueous 3 %wt TiO_2 solution for *ca.* 30 seconds and rinsed with deionised water.
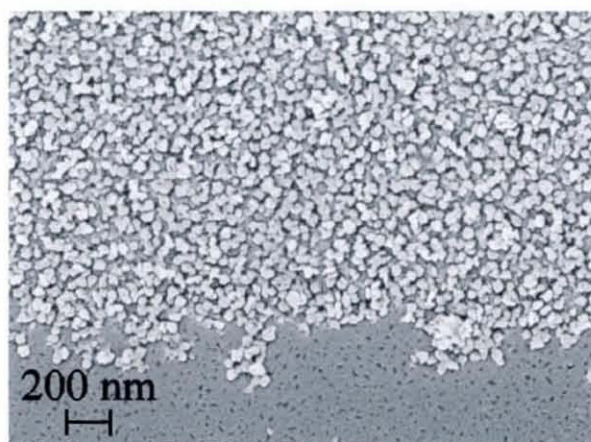

Figure 2.1. FEGSEM image of a mono-layer deposit of TiO_2 nanoparticles (agglomerates of 10-40 nm diameter) on a boron-doped diamond substrate

The diamond is flat and featureless and the TiO_2 nanoparticles appear in the form of aggregates of 10 – 40 nm diameter. In the lower part of the micrograph, the particles have been removed by scratching with a scalpel blade.

2.3.2. Surface Electrochemistry of TiO₂ Nanoparticles at Boron-Doped Diamond Electrode Surfaces

The voltammetric response from a polished boron-doped diamond electrode immersed in aqueous 0.1 M phosphate buffer at pH 7 between +0.5 V and −1.8 V *vs.* SCE is featureless and consistent with a clean background (Figure 2.2).
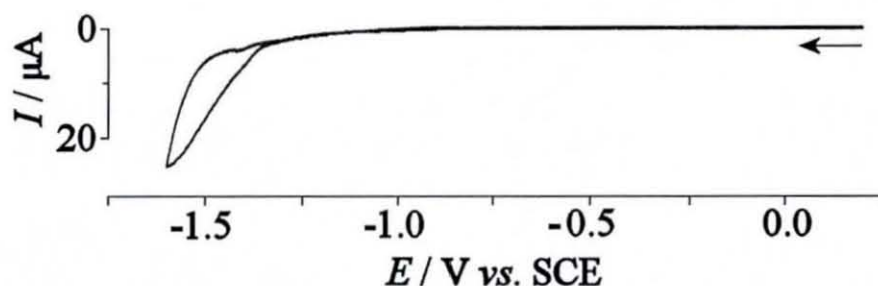

Figure 2.2. Cyclic voltammograms for a clean boron-doped diamond plate electrode immersed in aqueous 0.1 M phosphate buffer pH 7 (scan rate 10 mVs⁻¹).

After adsorption of a TiO₂ mono-layer a new reduction response is detected commencing at a potential of −0.8 V *vs.* SCE. The shape of this voltammetric response (see Figure 2.3Ai) is characteristic for TiO₂ thin films and has been explained in terms of sequential filling electronic states within the oxide.[18] For TiO₂ films more extended than a mono-layer, this voltammetric response is dominating the overall behaviour. However, for the mono-layer deposit new features can be observed. Scanning the potential more negative allows a new peak feature to be observed, which is less broad than the first reduction signal. After reversal of the scan direction (see Figure 2.3Aii) two peak features are observed also during oxidation. Scanning the potential further into the negative potential range causes the oxidation peak to shift positively and a shoulder towards even more positive potentials develops. It is likely that the shift in the oxidation peak potential is associated with a change in the proton binding at the TiO₂ surface.
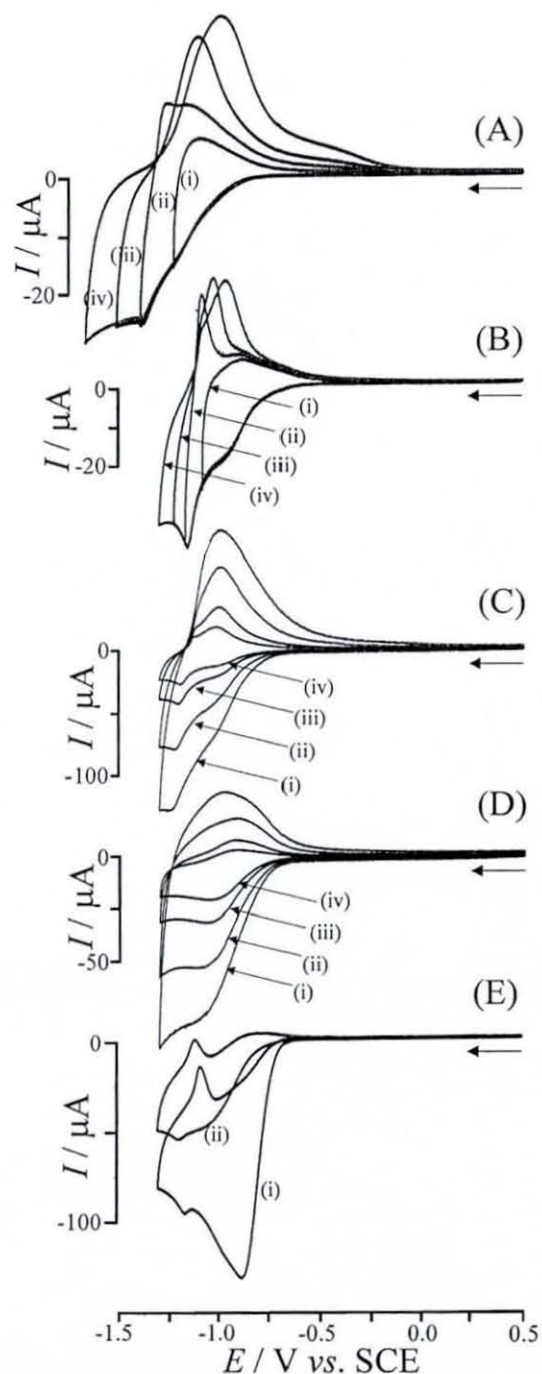
Figure 2.3. Cyclic voltammograms for the reduction of a mono-layer deposit of TiO_2 nanoparticles at a 5 mm × 5 mm boron-doped diamond plate electrode (A) immersed in aqueous 0.1 M phosphate buffer pH 7 with variable reversal potential (scan rate 100 mVs^{-1}), (B) immersed in aqueous 0.1 M $NaClO_4$/ 1 mM $HClO_4$ with variable reversal potential (scan rate 100 mVs^{-1}), (C) immersed in aqueous 0.1 M $NaClO_4$/ 0.5 mM $HClO_4$ with variable scan rate of (i) 1000, (ii) 500, (iii) 200, (iv) 100 mVs^{-1}, (D) immersed in aqueous 0.1 M $NaClO_4$/ 0.1 mM $HClO_4$ with variable scan rate of (i) 1000, (ii) 500, (iii) 200, (iv) 100 mVs^{-1}, and (E) immersed in aqueous 0.1 M $NaClO_4$/ 1 mM $HClO_4$ (i) with 1 mM maleic acid and in (ii) with 1 mM phytic acid added (scan rate 100 mVs^{-1}).

In order to explore the involvement of protons in the TiO_2 reduction and re-oxidation processes, voltammetric experiments were conducted in un-buffered aqueous 0.1 M $NaClO_4$ with small concentrations of protons. Under these conditions, a similar set of voltammetric responses are generated (see Figure 2.3B) and the two reduction peaks are again observed. Both the first and the second reduction signal are highly symmetric (consistent with the presence of reversible surface states) and only when the potential is scanned into more negative potentials, a shift of the oxidation peak occurs (probably associated with a gradual structural re-arrangement at the surface). By reducing the concentration of protons from 1 mM to 0.5 mM and finally to 0.1 mM (see Figures 2.3B, C, and D, respectively) causes the second reduction peak to disappear and the first reduction peak to become smaller. This behaviour is consistent with a proton depletion effect within the aqueous solution phase and proves the direct involvement of protons in the reduction process. The Randles Sevcik equation[33] (equation 2.1) allows the current peak for mass transport controlled depletion of protons to be calculated.

$$i_p = -0.446\, n\, F\, A\, c \sqrt{\frac{nFvD}{RT}} \qquad\qquad (2.1)$$

In this equation, the peak current (i_p) for the reduction, is expressed in terms of n, the number of electrons transferred per proton ($n = 1$), the Faraday constant (F), the geometric electrode area ($A = 2.5 \times 10^{-5}$ m^2), the scan rate ($v = 0.1$ Vs^{-1}), the approximate diffusion coefficient for protons[34] $D = 1 \times 10^{-8}$ m^2s^{-1}, the gas constant (R), and T, the absolute temperature. The calculated peak current for a proton concentration of 0.1 mM is $i_p = 21 \times 10^{-6}$ A, consistent with the voltammetric results (see Figure 2.3D). Therefore, it can be assumed that the reduction of Ti(IV) occurs accompanied by proton adsorption, and that the two reduction peaks observed in Figure 2.3 may be attributed to two distinct binding sites for protons in the vicinity of Ti(III) sites. A schematic drawing (see Scheme 2.2A) illustrates this situation where one binding site is an 'outer' surface position (see Ha) while a second binding site is located further within the nanoparticle surface (see H_b).

The total number of binding sites for both H_a and H_b can be estimated from the

charge under the voltammetric response (*ca.* 150 µC) assuming one electron is transferred for every H^+ bound. Equation 2.2 shows how the total number of electrons transferred during the reduction of Ti(IV) can be calculated, where N_A is the Avogadro constant.

$$number \ of \ e^- = \frac{charge \times N_A}{F}$$ (2.2)

Taking into account the amount of TiO_2 particles on the boron-doped diamond surface (see Figure 2.1, *ca.* 10^{12} particles on 5 mm × 5 mm) this suggests *ca.* 1000 electrons per 6 nm diameter TiO_2 particle, consistent with a surface process (there are approximately 3300 Ti atoms per 6 nm diameter anatase particle).
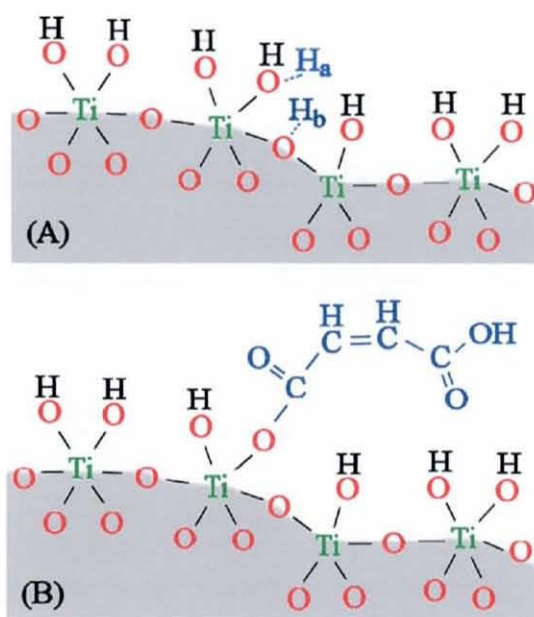
Scheme 2.2. A schematic representation of the TiO_2 nanoparticle surface with potential binding sites for (A) protons and (B) maleic acid.

It is interesting to explore the kinetic effects coupled to proton binding at the TiO_2 surface. At a sufficiently slow scan rate, the reduction process becomes chemically irreversible (see Figure 2.3D) and proton reduction to dihydrogen has been suggested in the literature.[35,36] The oxidation response is diminished at a scan rate of

approximately $v_{transition} = 0.5$ Vs^{-1} and the rate constant for the surface process can be estimated as $k = \dfrac{A_{total} \, F \, v_{transition}}{RT} = 2 \times 10^{-3}$ m^{2}s^{-1} (with $A_{total} \approx 10^{-4}$ m^2). However, in the presence of a higher concentration of protons, when the second reduction process occurs, the voltammetric response becomes more reversible and the dihydrogen evolution process is apparently suppressed. The peak-shape of the second reduction process suggests a process 'deeper' within the surface (see H$_b$) and it may be speculated that this will reduce the availability of electrons for the two-electron reduction of protons to dihydrogen at sites denoted H$_a$ (see Scheme 2.2A). One possible implication of this observation is that small quantities of fully reduced TiO$_2$ nanoparticles will behave chemically different when compared to thicker layers of mesoporous TiO$_2$.

2.3.3. Electron Transfer Processes at TiO$_2$ Nanoparticles Adsorbed onto Boron-Doped Diamond Electrode Surfaces

The availability of electrons within the TiO$_2$ particles and the availability of binding sites at the TiO$_2$ surface poses the question whether selective reduction processes can be driven electrochemically at the TiO$_2$ surface in the presence of the inert boron-doped diamond electrode surface. Electrochemical reduction processes at TiO$_2$ electrodes have been well studied[37] and it has recently been reported that olefins with carboxylate group, such as maleic acid,[38,39] can be reduced electro-catalytically at TiO$_2$ electrodes. This report is confirmed here for the case of a single layer of TiO$_2$ nanoparticles.

Figure 2.3E shows the effect of adding maleic acid (*ca.* 1 mM) into an aqueous solution of 0.1 M NaClO$_4$ and 1 mM HClO$_4$. A new chemically irreversible reduction response is observed at −0.8 V *vs.* SCE consistent with the potential for the first reduction of the TiO$_2$ surface. This process is not observed at a polished boron-doped diamond electrode (not shown) and therefore is entirely due to the presence of TiO$_2$ as 'electrocatalyst' (see Scheme 2.2B). This is supported by the simultaneous disappearance of the anodic peak on addition of maleic acid, indicating a heterogeneous redox catalysis reaction process, where the electro-

generated Ti^{3+} species reduces maleic acid to succinic acid (equation 2.3), and Ti^{4+} is regenerated.[39] Using equation 2.1, the peak current for the two electron two proton reduction of maleic acid to succinic acid can be estimated as 130 μA, consistent with the voltammetric response recorded (see Figure 2.3E).

$$maleic\ acid \xrightarrow{+2H^+,\ +2e^-} succinic\ acid$$

(2.3)
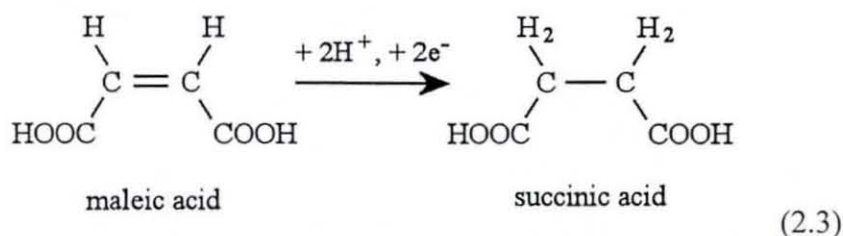
The use of nanoparticulate TiO_2 coated boron doped diamond electrodes allows a greater potential window to be investigated and therefore further insights into the site of the catalytic reduction process have been elucidated, with respect to the reduction of maleic acid at a Ti/ceramic TiO_2 cathode.[39] Additional benefits in this work include the investigation of lower concentrations of maleic acid under less extreme acidic conditions, resulting in a more defined peak for the reduction of maleic acid and safer working conditions respectively.

Finally, addition of a competitive binder, here phytic acid (Figure 2.4), reduces the current for the electrocatalytic reduction process by binding to the TiO_2 surface, decreasing the number of binding sites available for the electrocatalytic reduction of maleic acid (see Figure 2.3Eii) and possibly introduces a novel way of controlling reactivity and selectivity at the TiO_2 surface.
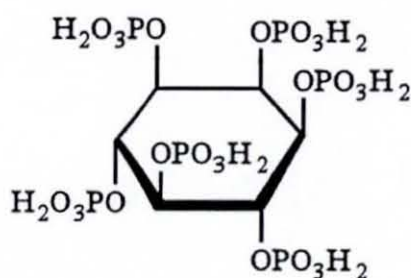

Figure 2.4. Molecular structural unit of the phytate organic binder unit

There are several beneficial features of employing mono-layers or well-defined amounts of TiO_2 electro-catalyst nanoparticles immobilised at boron-doped diamond electrodes. With thick film TiO_2 electrodes, dihydrogen evolution can occur in competition to other beneficial reduction processes, but a thin film TiO_2 electrode and at sufficiently negative potentials, the suppression of the competing dihydrogen evolution process appears to be possible. A catalytic reduction process may be optimised by judicial choice of proton concentration, olefin concentration, catalyst amount, and applied potential. In the future, the presence of a co-binder at the TiO_2 surface may be employed to control the selectivity of the reduction process or to introduce chirality.

2.4. Conclusions

It has been shown that voltammetric experiments with mono-layer films of TiO_2 (anatase) nanoparticles at boron-doped diamond electrodes surfaces give insights into oxide surface processes, the type and availability of binding sites, and the reactivity and the mechanism of surface processes. Boron-doped diamond is a versatile and highly beneficial substrate material and there may be real benefits (in terms of efficiency and selectivity of electron transfer processes) in employing very thin films of nanoparticles on boron-doped diamond substrates

2.5. References

[1] B.S. Ng, I. Annergren, A.M. Soutar, K.A. Khor, A.E.W. Jarfors, *Biomaterials* 26 (2005) 1087

[2] C.S. Fang, Y.W. Chen, *Mater. Chem. Phys.* 78 (2003) 739

[3] A. Fujishima, K. Hashimoto, T. Watanabe, *TiO2 Photocatalysis Fundamentals and Applications*, BKC Inc., Tokyo, 1997

[4] H. Wendt, G. Kreysa, *Electrochemical Engineering*, Springer, Berlin, 1999

[5] A. Fujishima, K. Honda, *Nature* 238 (1972) 37

[6] B. O'Regan, M. Grätzel, *Nature* 353 (1991) 737

[7] U. Diebold, *Surf. Sci. Rep.* 48 (2003) 53

[8] I. Abayev, A. Zaban, F. Fabregat-Santiago, J. Bisquert, *Phys. Stat. Sol. A-Appl. Res.* 196 (2003) R4

[9] C.J. Boxley, H.S. White, C.E. Gardner, J.V. Macpherson, *J. Phys. Chem. B* 107 (2003) 9677

[10] E.M. Oliveira, C.E.B. Marino, S.R. Biaggio, R.C. Rocha-Filho, *Electrochem. Commun.* 2 (2000) 254

[11] O.R. Camara, C.P. De Pauli, M.C. Giordano, *Electrochim. Acta* 29 (1984) 1111

[12] H. Pelouchova, P. Janda, J. Weber, L. Kavan, *J. Electroanal. Chem.* 566 (2004) 73

[13] R. Memming, *Semiconductor Electrochemistry*, Wiley-VCH, Weinheim, 2001

[14] L. Kavan, M. Grätzel, J. Rathousky, A. Zukal, *J. Electrochem. Soc.* 143 (1996) 394

[15] G. Boschloo, D. Fitzmaurice, *J. Electrochem. Soc.* 147 (2000) 1117

[16] J. Bisquert, *J. Phys. Chem. B* 108 (2004) 2323

[17] I. Mora-Sero, J. Bisquert, *Nano Lett.* 3 (2003) 945

[18] F. Fabregat-Santiago, I. Mora-Sero, G. Garcia-Belmonte, J. Bisquert, *J. Phys. Chem. B* 107 (2003) 758

[19] H. Greijer Agrell, G. Boschloo, A. Hagfeldt, *J. Phys. Chem. B* 108 (2004) 12388

[20] See for example T. Yamase, M.T. Pope, *Polyoxometalate Chemistry for Nano-composite Design*, Kluwer Academic, Amsterdam, 2003

[21] Yu. V. Pleskov, *Russ. J. Electrochem.* 38 (2002) 1275

[22] R.G. Compton, J.S. Foord, F. Marken, *Electroanalysis* 15 (2003) 1349

[23] J.D. Wadhawan, F.J. Del Campo, R.G. Compton, J.S. Foord, F. Marken, S.D. Bull, S.G. Davies, D.J. Walton, S. Ryley, *J. Electroanal. Chem.* 507 (2001) 135

[24] L. Ouattara, M.M. Chowdhry, C. Comninellis, *New Diam. Front. Carb. Technol.* 14 (2004) 239

[25] L. Su, X.P. Qiu, L.H. Guo, F.H. Zhang, C.H. Tung, *Sens. Actuators B-Chem.* 99 (2004) 499

[26] Y.R. Zhang, S. Asahina, S. Yoshihara, T. Shirakashi, *Electrochim. Acta* 48 (2003) 741

[27] K.B. Holt, G. Sabin, R.G. Compton, J.S. Foord, F. Marken, *Electroanalysis* 14

(2002) 797

[28] F. Montilla, E. Morallon, I. Duo, C. Comninellis, J.L. Vazquez, *Electrochim. Acta* 48 (2003) 3891

[29] J.S. Gao, T. Arunagiri, J.J. Chen, P. Goodwill, O. Chyan, J. Perez, D. Golden, *Chem. Mater.* 12 (2000) 3495

[30] K.J. McKenzie, D. Asogan, F. Marken, *Electrochem. Commun.* 4 (2002) 820

[31] K.J. McKenzie, F. Marken, *Electrochem. Solid State Lett.* 5 (2002) E47

[32] C. Terashima, T.N. Rao, B.V. Sarada, N. Spataru, A. Fujishima, *J. Electroanal. Chem.* 544 (2003) 65

[33] F. Scholz (ed.), *Electroanalytical Methods*, Springer, Berlin, 2002 p.64

[34] R. Mills, V.M.M. Lobo, *Self-diffusion in Electrolyte Solution* Elsevier, Amsterdam, 1989

[35] Y. Doi, M. Tamaki, *Inorg. Chim. Acta* 64 (1982) L145

[36] M. Ashokkumar, *Int. J. Hydrogen Energy* 23 (1998) 427

[37] V.B. Baez, J.E. Graves, D. Pletcher, *J. Electroanal. Chem.* 340 (1992) 273.

[38] J.S. Gu, D.B. Chu, X.F. Zhou, G.X. Shen, *Acta Chim. Sin.* 61 (2003) 1405

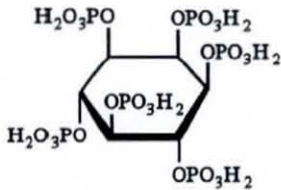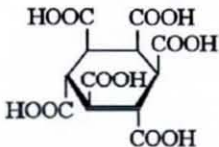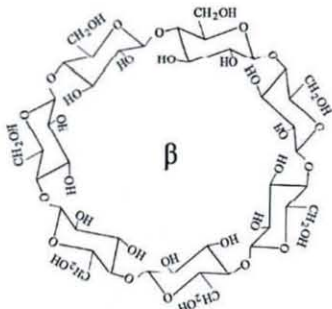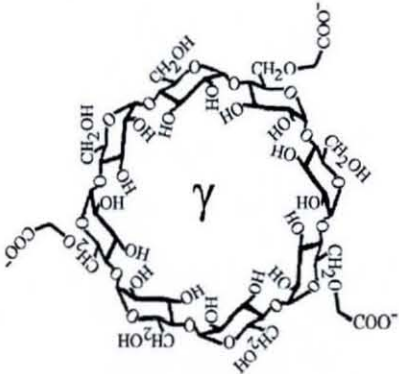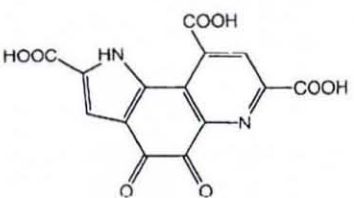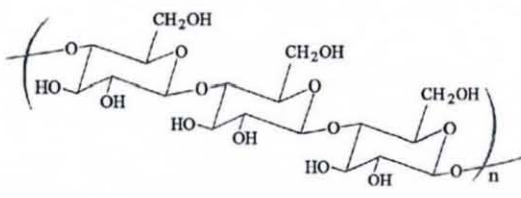[39] D. Vasudevan, *J. Appl. Electrochem.* 25 (1995) 176
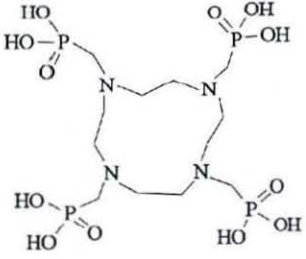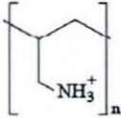
Chapter 3

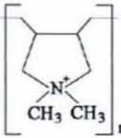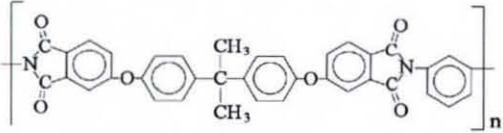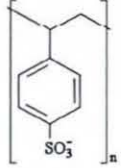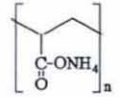# Electrochemical Processes in TiO₂ Multi-Layer Films

3.1. Introduction

The formation and electrochemistry of titanium (IV) oxide nanoparticle multi-layer films using various organic binder molecules are described in this chapter and the role of the binder molecule in the layer-by-layer deposition process is explored.

Several types of binder systems have been employed over recent years to allow nanoparticle deposits to be formed in a layer-by-layer process. The ability of the negatively charge binder to adhere to the TiO₂ surface and to provide new binding sites is most important. Systems used to date are summarised in Table 3.1.

Binder	Description	Ref.
Phytic acid H₂O₃PO OPO₃H₂ OPO₃H₂ OPO₃H₂ H₂O₃PO OPO₃H₂	Phytic acid or phytate has been used in previous studies and is known to bind well to metal oxides including TiO₂ via the six phosphate groups. Applications include the study of cytochrome c and haemoglobin.	This work,[1,2]
1,2,3,4,5,6-cyclohexanehexacarboxylic acid (CHHCA) HOOC COOH COOH COOH HOOC COOH and other isomers	CHHCA has a very similar structure to phytic acid and has again been shown to be a good binder to TiO₂ nanoparticles via the carboxylate groups. Investigations into voltammetry with weakly adsorbed redox systems have been reported.	[3]

β-cyclodextrin CH₂OH structure with β label	The application of β-cyclodextrin as a binder was unsuccessful in this investigation using layer-by-layer deposition. Ultra thin TiO₂ β-cyclodextrin films have been described using a sol-gel deposition process for the detection of aromatic compounds in water.	This work,[4]
Carboxymethyl-γ-cyclodextrin structure with γ label	The use of a carboxymethyl substituted cyclodextrin was more successful in the film formation due to the favourable binding of the carboxylate groups to the TiO₂ nanoparticle surface.	This work,[5]
2,7,9-tricarboxypyrroloquinoline quinone (PQQ) structure	PQQ was another successful binder that binds to the TiO₂ nanoparticle surface via carboxylate groups allowing the formation of novel TiO₂ PQQ mesoporous films. The ortho C=O groups are also possible binding sites.	This work.
Cellulose structure	TiO₂ cellulose nanoparticle films have been reported using layer-by-layer and sol-gel deposition processes. Characterisation was carried out using TEM, SEM and XRD techniques.	[6]

1,4,7,10-tetraazacyclododecane-1,4,7,10-tetrayl-tetrakis(methyl-phosphonic acid) (TAPA) 	TAPA has four identical phosphonate pendant arms that have been shown to be capable of binding to the surface of TiO$_2$ nanoparticles.	This work.
Poly(allylamine) (PAH) **Polydiallyldimethylammonium (PDDA)** **Poly(etherimide) (PEI)** **Poly(styrenesulfonate) (PSS)** **Poly(acrylic acid) (PAA)** 	The use of polyelectrolytes such as PAH, PDDA, PEI, PSS or PAA in layer-by-layer deposition with TiO$_2$ is reported in the literature, describing film manufacture and applications such as gas sensing and noble metal binding.	7,8,9,10,11

Nafion[®]	Previous reports include the use of TiO_2 Nafion[®] single layer films for humidity sensing. Here, Nafion[®] has been shown to be a successful binder in layer-by-layer deposition.	This work,[12]
$- [(CF_2 - CF_2)_n - CF - CF_2]_p -$ $\quad \quad \quad |$ $(OCF_2 - CF)_m - OCF_2 CF_2 - SO_3^- M^+$ $\quad \quad |$ $\quad \quad CF_3$		

Table 3.1. Table to summarise the various binder molecules found in the literature and employed in this study with TiO_2 nanoparticles.

The binder molecules employed in this chapter include carboxymethyl-γ–cyclodextrin, and 1,4,7,10-tetraazacyclododecane- 1,4,7,10-tetrayl- tetrakis (methyl - phosphonic acid) (TAPA) which were used as they have cyclic structures capable of forming inclusion complexes or co-ordinating to metal ions. The incorporation of pyrroloquinoline quinone (PQQ) as a redox active binder within the semi-conducting TiO_2 film is demonstrated. Phytic acid has been previously studied in the directed assembly of TiO_2 mesoporous films. Here the influence of film thickness on the conductivity and electrochemistry are demonstrated. This chapter concludes with the formation and electrochemistry of TiO_2 nanoparticle films using the ionomer Nafion[®] as a highly effective binder.

The multi-layer TiO_2 binder films were deposited onto flat glass substrates coated with a thin layer of tin-doped indium oxide or ITO. ITO is typically composed of indium (III) oxide (In_2O_3) with various amounts of tin (IV) oxide (SnO_2) dopant. ITO has a high (almost metallic) conductivity and high optical transparency, where higher levels of SnO_2 doping results in a greater conductivity but decreased optical transparency. ITO has consequently been employed in a vast number of areas including, transparent conductive coatings for displays (liquid crystal, flat panel, plasma), touch panels, electronic ink applications, solar cells, gas sensors, and antistatic coatings. Due to its chemical inertness over a wide potential window and low background current, ITO has also been widely used in electrochemical investigations. Various types of nanoparticles have been immobilised at ITO surfaces including gold,[13] iron (III) oxide,[14] platinum,[15] titanium (IV) oxide,[16] silver,[17] and silicon (IV) oxide.[18] The high electrical conductivity of ITO coated

glass and the lower cost compared to boron-doped diamond substrates makes ITO an ideal electrode substrate material for the immobilisation of multi-layer titanium (IV) oxide sensor probes.

3.2. Experimental

3.2.1. Chemicals

Demineralised and filtered water was taken from an Elga water purification system (Elga, High Wycombe, Bucks, UK) with a resistivity of not less than 18 MOhm cm. Titanium (IV) oxide sol (anatase, *ca.* 6 nm diameter, 30-35% in aqueous HNO_3, pH 0-3, TKS-202) was obtained from Tayca Corp., Osaka, Japan and diluted with deionised water. β-cyclodextrin, carboxymethyl-γ-cyclodextrin, pyrroloquinoline quinone, 1,4,7,10-tetraazacyclododecane- 1,4,7,10-tetrayl- tetrakis (methyl-phosphonic acid), phytic acid dodecasodium salt hydrate, Nafion® perfluorinated ion-exchange resin (5 %wt solution in a mixture of lower aliphatic alcohols and water), absolute ethanol, methanol, 1,1′-ferrocenedimethanol, dihydronicotinamide adenine dinucleotide, dopamine, $CuSO_4.5H_2O$, $[Ru(NH_3)_6]Cl_3$, $NaClO_4$, NaOH, H_3PO_4, $HClO_4$, KOH, K_2HPO_4, and KH_2PO_4 were obtained commercially in analytical or the highest purity grade available.

3.2.2. Instrumentation

Voltammetric measurements were performed with a computer controlled Eco Chemie PGSTAT20 Autolab potentiostat system. Experiments were conducted in staircase voltammetry mode with a platinum gauze counter electrode and saturated calomel reference electrode (SCE (saturated KCl), REF401, Radiometer). The working electrode was a tin-doped indium oxide (ITO) coated glass (10 mm × 60 mm, resistivity 20 Ohm per square) with approximately 8% tin, obtained from Image Optics Components Ltd. (Basildon, Essex). The ITO electrode surface was modified with a porous metal oxide film giving a geometric working electrode area

of 1 cm^2, defined using Magic tape (Scotch 3D). Prior to conducting electrochemical experiments, all solutions were purged with argon (BOC, UK). All experiments were carried out at a temperature of $22 \pm 2^\circ$C. An Elite tube furnace system was employed for cleaning ITO electrode surfaces (at 500°C in air) and for calcining metal oxide binder films (at 500°C in air).

Scanning electron microscopy images were obtained with a Leo 1530 Field Emission Gun Scanning Electron Microscope (FEGSEM) system. Prior to FEGSEM imaging, the sample surface was scratched with a scalpel blade. Impedance spectroscopy experiments were carried out on a Solartron SI 1260 impedance/ gain-phase analyser and a Solartron SI 1287 electrochemical interface.

A quartz crystal oscillator circuit (Oxford Electrodes) connected to a frequency counter (Fluke, PM6680B) allowed the resonance frequency of the quartz crystal sensor to be monitored simultaneously to conducting voltammetric experiments. A Faraday cage was used to contain the quartz crystal to minimise noise interference. The analogue output of the counter was fed into the ADC input of an Autolab potentiostat system (Eco Chemie, Netherlands) and data processing was possible with GPES software (Eco Chemie, Netherlands). Layer-by-layer deposition processes were monitored with the crystal suspended in air. Droplets of solution were applied to one side of the crystal and after rinsing and drying the frequency measured and monitored step-by-step.

The simultaneous small-angle X-ray scattering and wide-angle X-ray scattering (SAXS/WAXS) pattern of the TiO$_2$ Nafion® and TiO$_2$ nanoparticle films was obtained on a SAXSess system using a PW3830 X-ray generator and the X-ray image plates were observed using a Perkins Elmer Cyclone Storage Phosphor System. A multi-layer film of TiO$_2$ Nafion® and of pure TiO$_2$ was produced on a thin optical microscopy cover plate for SAXS measurements. The patterns were recorded in transmission mode with Cu Kα radiation (λ = 1.5406) at 40 kV and 50 mA over a wide region of 2θ with an exposure time of 20 minutes. A background pattern from a clean cover plate was subtracted and the data corrected for slit smearing before fitting.

3.2.3. Deposition and Electrode Preparation Procedures

Throughout this investigation, the majority of electrodes used were composed of metal oxides and organic binder molecules. Deposition of multi-layer mesoporous films of metal oxide and organic binder on ITO glass electrodes followed a layer-by-layer dip coating method.[14] A clean ITO surface (washed with ethanol, rinsed with deionised water, dried, and 60 minute heat treatment at $500^{\circ}C$ in air) was dipped into a solution of TiO_2 nanoparticles for 30 seconds followed by rinsing with deionised water. The metal oxides form small agglomerates on the hydrophilic ITO surface. By dipping the resulting nanoparticle deposit into a solution of binder molecule such as phytic acid (40 mM in pH 3 aqueous solution) and rinsing, it is possible to reverse the surface charge. The dipping process was undertaken using a robotic Nima dip coating carousel (DSG – Carousel, Nima Technology, Coventry, UK) and repeated to give multi-layer deposits.

Figure 3.1 shows a schematic of the layer-by-layer deposition process, which relies on the electrostatic interaction between the positively charged metal oxide nanoparticle, applied in step one and the negatively charged binder species applied in step two. Two rinse steps follow both step one and step two to remove excess unbound particles from the electrode surface.
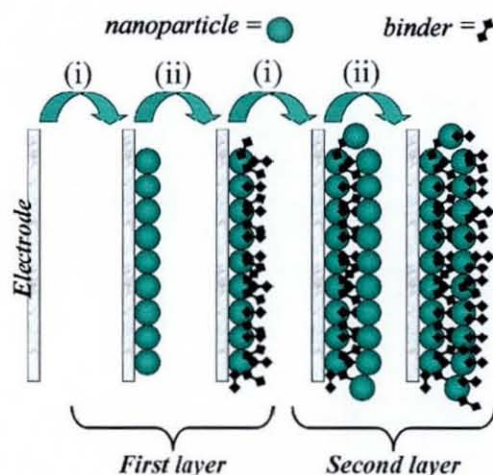

Figure 3.1. Schematic drawing showing the steps involved in the directed assembly multi-layer structures based on the electrostatic interactions between the TiO_2 nanoparticles and a suitable multi-dentate binder molecule such as phytic acid.

The dip coating procedure can therefore be summarised as the ITO coated substrate sequentially being immersed in 6 different pots, where pot 1 contained 3 %wt TiO_2 suspension, pots 2 and 3 contained deionised water, pot 4 contained the organic binder solution and pots 5 and 6 contained deionised water. The ITO was held in solution for 30 seconds in each pot with no drying stage in-between. Each pot of solution is magnetically stirred throughout the deposition procedure. For the layer-by-layer deposition of the TiO_2 Nafion® films, pots 3 and 4 contained methanol instead of deionised water.

The physical and chemical properties of the organic binder molecules allow the structure and surface of the nanoparticle film to be readily modified. The different binders used were phytic acid (40 mM in pH 3 aqueous solution), carboxymethyl-γ-cyclodextrin (0.1 mM in deionised water), pyrroloquinoline quinone (PQQ) (0.1 mM in aqueous solution), 1,4,7,10-tetraazacyclododecane- 1,4,7,10-tetrayl-tetrakis (methyl-phosphonic acid) (TAPA) (1 mM in aqueous solution) and Nafion® (0.5 %wt solution diluted with methanol from 5 %wt commercial solution).

3.3. Formation of TiO_2–1,4,7,10-tetraazacyclododecane-1,4,7,10-tetrayl-tetra-kis(methyl-phosphonic acid) (TAPA) Multi-Layer Films

3.3.1. Introduction

Polyazacycles with co-ordinating pendant arms are known to have many desirable properties such as being good ligands for transition metal[19] and lanthanide ions,[20] forming thermodynamically stable complexes with a high selectivity to metal ions.[21] Polydentate ligands with acetic acid substitutes have been shown to form thermodynamically and kinetically stable complexes with more labile metal ions like the first row-transition metals and trivalent lanthanide ions.[20] The properties of these ligands have been studied for use as magnetic resonance imaging (MRI) contrast agents[22] and diagnostic/therapeutic radiopharmaceuticals.[23] Similar

research has been carried out using azamacrocycles with phosphonic and phosphinic acid groups on pendant arms.[24] The complexes with phosphorus ligands where found to have higher selectivity in complexation compared to those with common acetate derivatives, along with satisfactory thermodynamic stability.[25]

The properties of the tetraphosphonate-substituted polyazacycles make them interesting to look at as potential binders in the layer-by-layer deposition process with metal oxides such as TiO_2.

1,4,7,10-tetraazacyclododecane-1,4,7,10-tetrayl-tetrakis (methyl-phosphonic acid) (TAPA) is a large organic molecule with potential binding sites (phosphate groups) spread over a greater area. Figure 3.2 shows the structure of TAPA, composed of a ring and four identical phosphonate pendant arms.
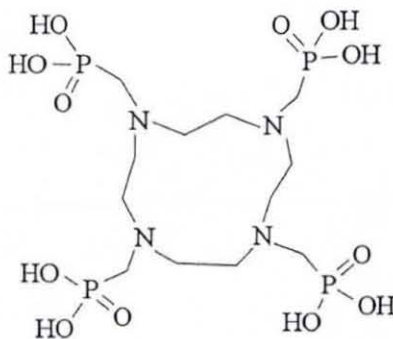

Figure 3.2. The structure of the 1,4,7,10-tetraazacyclododecane-1,4,7,10-tetrayl-tetrakis(methyl-phosphonic acid) (TAPA) ligand.

3.3.2. Formation of Multi-Layer TiO₂ TAPA Films

In order to determine the success of the layer-by-layer deposition process, FEGSEM images of a two layer and 15 layer TiO_2 TAPA film were taken (shown in Figure 3.3). It is clear to see that a mesoporous film was generated on the ITO surface, where the average thickness for a 15 layer film equalled 150 nm.
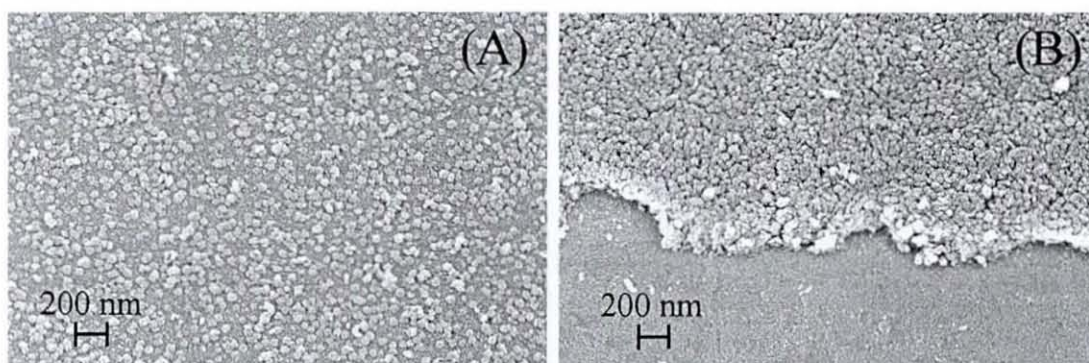
Figure 3.3. FEGSEM images of TiO_2 nanoparticle films deposited layer-by-layer with 1,4,7,10-tetraazacyclododecane- 1,4,7,10-tetrayl-tetrakis (methyl-phosphonic acid) onto the surface of an ITO electrode with (A) a 2 layer TiO_2 TAPA film and (B) a 15 layer TiO_2 TAPA film.

The electron microscopy data can be supported by experiments with quartz crystal oscillator measurements conducted in air. Figure 3.4 shows the subsequent reduction of the resonance frequency of an ITO coated quartz crystal resonator during the manual layer-by-layer deposition process of alternating 3 wt% titanium (IV) oxide sol and 1 mM TAPA (see procedure given in section 3.2.3). Each TiO_2 TAPA layer is consistent with a 700 Hz change corresponding to 734 ng (according to the Sauerbrey equation[26]). Rearranging the Sauerbrey equation gives the expression in equation 3.1.

$$\frac{\Delta m}{\Delta f} = -\frac{A\sqrt{\mu_Q \rho_Q}}{2f_0{}^2} \qquad (3.1)$$

As the geometric resonator area, $A = 0.2$ cm^2, the frequency change corresponds to a mass increase with $\dfrac{\Delta m}{\Delta f}$ = -1.05 ng Hz^{-1} (see experimental).

By taking the particle density for a mono-layer (from the electron micrograph, Figure 3.3A.) and the density of anatase, 3.9 g cm^{-3}, the weight of a mono-layer of TiO_2 particles can be estimated as 266 ng. This results in an estimate for the weight for a mono-layer of TAPA as *ca.* 468 ng (molecular weight 548.3 g mol^{-1}) or 8.5 x 10^{-10} mol per layer (ignoring the presence of water).
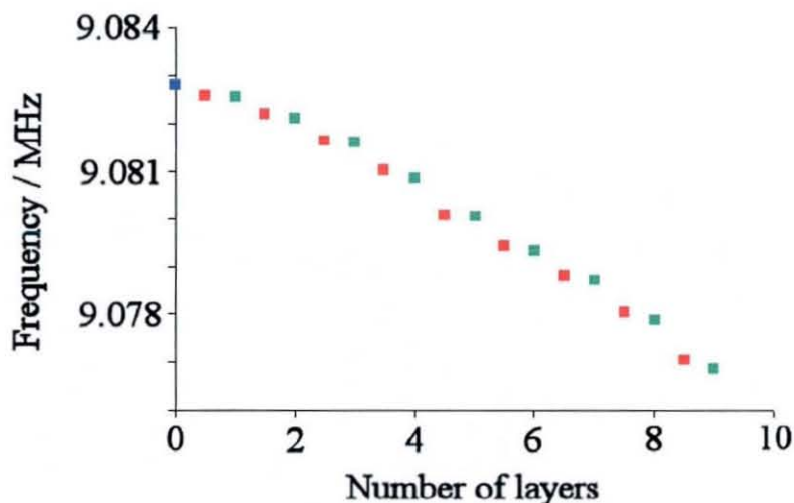
Figure 3.4. Plot of the resonance frequency change for an ITO coated quartz crystal (■) during layer-by-layer deposition of TiO_2 (■) and TAPA (■).

It is possible to see that the deposition process for a multi-layer film of TiO_2-TAPA is successful. In order to investigate the metal binding properties of the TAPA ligand, preliminary Cu^{2+} binding tests have been performed.

3.3.3. Solution Phase Complexation of Cu^{2+} with TAPA

Tetraphosphonate-substituted polyazacycles are known to form stable complexes with metal ions including Cu^{2+}, a readily available metal ion with known electrochemistry. Any complexation of Cu^{2+} with TAPA will influence the voltammetric response recorded. A method of studying a possible TAPA Cu^{2+} complex was investigated using an addition experiment where increasing concentrations of the TAPA ligand were added to 1 mM $CuSO_4$ in 0.1 M $NaClO_4$ electrolyte solution. The solution was degassed with argon for approximately 15 minutes after each addition of TAPA to facilitate the mixing of TAPA throughout the solution.
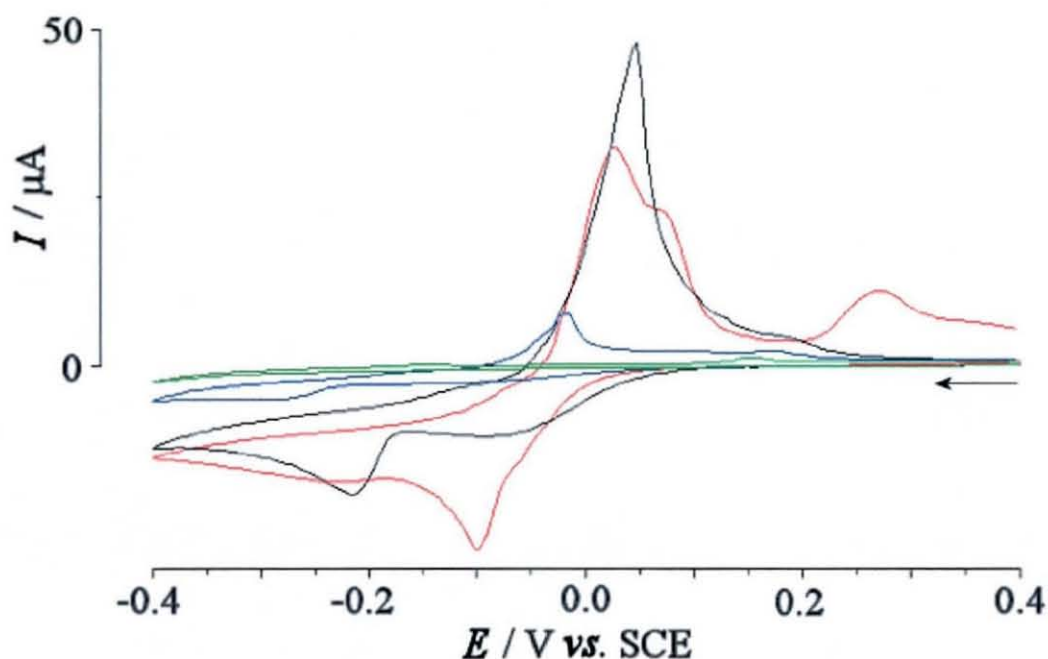
Figure 3.5. Voltammograms recorded for the addition experiment using glassy C working electrode in 1 mM $CuSO_4$ in 0.1 M $NaClO_4$. Red line = plus 0 mM TAPA, black line = plus 0.5 mM TAPA, blue line = plus 1 mM TAPA, and green line = plus 2 mM TAPA. Scan rate 10 mVs^{-1}. Scan 1 is shown in each case.

As increasing amounts of TAPA were added, the colour of the solution changed from colourless with 0 mM TAPA, to intense blue at 2 mM TAPA, indicating a successful complexation process is possible between TAPA and aqueous Cu^{2+}. The background voltammogram in the presence of no TAPA shows a sharp stripping peak as copper (metal) is deposited (equation 3.2a and b). By adding a small amount of TAPA (0.5 mM), the nucleation process is changed and the peak current for oxidation increases. Interestingly, on addition of further TAPA (1 mM), copper has to be removed from the TAPA complex to be oxidised and reduced. This results in a decrease in peak current and a shift to more negative potentials as the overpotential increases. With excess TAPA (2 mM), the copper peak has moved off the potential scale. It is possible in the presence of excess TAPA, that polymerisation between unbound phosphonate ligands and copper ions in adjacent complexes occurs.

3.3.4. Immobilisation & Redox Reactivity of Cu^{2+} in TiO_2 TAPA Films

Before introducing the metal cation to the complex, initial electrochemical testing of multi-layer deposits of TiO_2 TAPA on ITO in 0.1 M pH 7 phosphate buffer solution were carried out, and typical TiO_2 signals were observed. After a 30 second immersion into 0.1 M aqueous Cu^{2+} containing solution, a new but complex and unstable voltammetric response was observed (Figure 3.6).
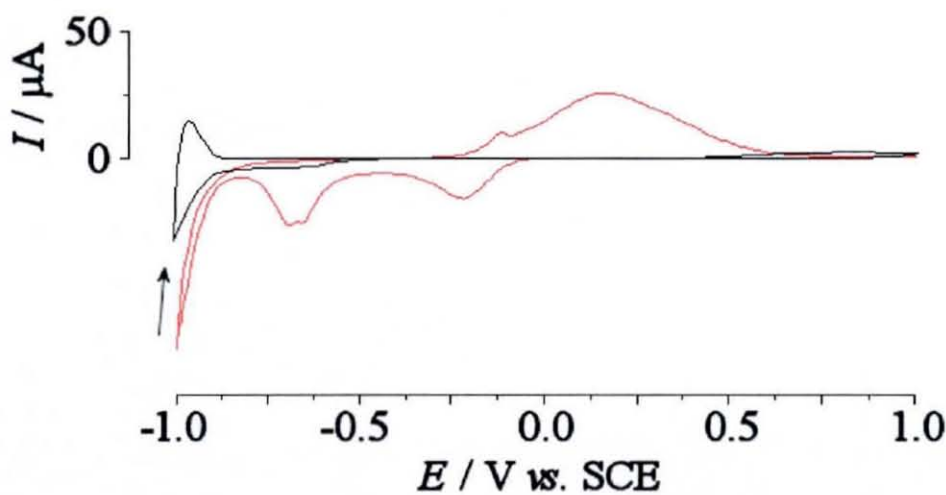

Figure 3.6. Voltammetry for a 15 layer deposit of TiO_2 TAPA film on ITO (i) before (black line) and (ii) after (red line) being dipped into 0.1 M $CuSO_4$ (aq) solution, rinsed and immersed in 0.1 M pH 7 phosphate buffer solution. Scan rate 10 mVs^{-1}. Scan 1 is shown in each case.

The exact electrochemistry associated with each copper redox response is not certain. However both the sharp stripping peak observed in Figure 3.5 at 0.05V and the broader peak at 0.13V in Figure 3.6 have been recorded in a previous study[27] investigating the electrochemical reduction of Cu^{2+} on platinum and diamond electrodes. A model involving a disproportionation mechanism (equation 3.2c) is used to explain the shape of the cyclic voltammogram in Figure 3.6 between – 0.5 V and 1.0 V.

$$Cu^{2+} + e^- \rightleftharpoons Cu^+ \qquad\qquad (3.2a)$$

$$Cu^+ + e^- \rightleftharpoons Cu^0 \qquad\qquad (3.2b)$$

$$2Cu^+ \rightarrow Cu^0 + Cu^{2+} \qquad\qquad (3.2c)$$

However, a similar response was observed for TiO_2 phytate films (Figure 3.7) and simply attributed to binding of Cu^{2+} to phosphate groups. This suggests that only the Cu^{2+} weakly adsorbed to the phosphate on the surface of the mesoporous TiO_2 films is oxidised and reduced.
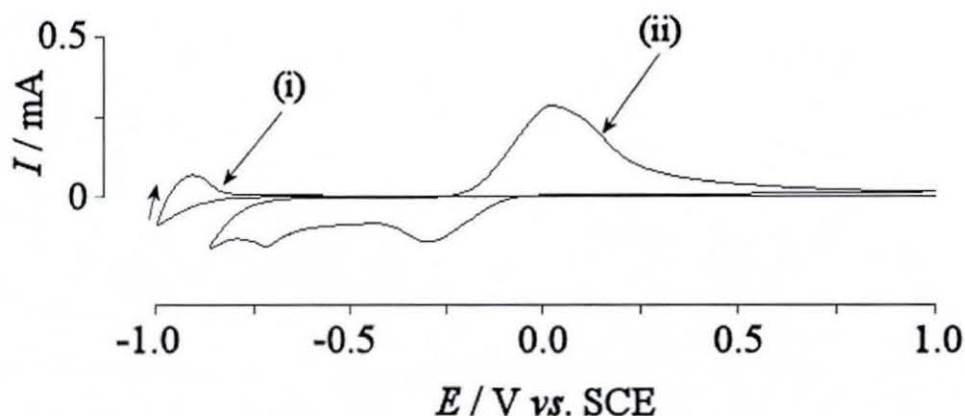

Figure 3.7. Voltammetry for a 15 layer deposit of TiO_2 phytate film on ITO (i) before and (ii) after being dipped into 0.1 M $CuSO_4$ (aq) solution, rinsed and immersed in 0.1 M pH 7 phosphate buffer solution. Scan rate 10 mVs^{-1}. Scan 1 is shown in each case.

In conclusion, either the binding of Cu^{2+} to the immobilised TAPA or the flow of electrons through the semi-conducting film is not sufficient to result in an analytically useful signal. The reactivity and analytical applicability of TiO_2 TAPA films for other metal cations remains to be explored.

3.4. Formation and Electrochemistry of TiO_2– 2,7,9-tricarboxypyrroloquinoline quinone (PQQ) Multi-Layer Films

3.4.1. Introduction

The structure of 2,7,9-tricarboxypyrroloquinoline quinone (pyrroloquinoline quinone, PQQ, or its older name, methoxatin, Figure 3.8) was determined using X-ray diffraction analysis by Salisbury *et al.* in 1979[28,29] and PQQ is now established as a cofactor for many quinoproteins. Quinoproteins are oxidoreductases that

contain an amino acid-derived orthoquinone cofactor, the most common being PQQ, and are recognised as the third class of redox enzyme following pyridine nucleotide- and flavin-dependent dehydrogenases.[29]

Figure 3.8. Molecular structural unit of the PQQ organic binder unit.

Studies into the structure and catalytic mechanism of PQQ and quinoproteins have been conducted[29,30,31,32,33] with the most interest being reported in methanol and glucose dehydrogenases.

The physiological importance of PQQ has been a subject of recent study[34,35,36] and although PQQ is not synthesised in mammals it can be readily absorbed by the lower intestine after ingestion. Nicotinamides and flavins are essential cofactors in enzyme catalysed redox reactions and are classified as vitamins as they must be supplied in the diet. PQQ is found in various foods, including meat and vegetables, and studies using mice[37] fed on a PQQ-deficient diet have been shown to develop poorly leading to interest in PQQ becoming classified as a new B vitamin.

Analytical uses of the coenzyme PQQ include the detection of a range of thiols,[38,39] where changes in thiol levels can be used to study proper physiological functions or in the diagnosis of disease states. This is possible because the PQQ molecule is electrochemically active and able to directly undergo electron transfer with an electrode without the need for a mediator. This allows PQQ to catalyse a number of reactions such as the oxidation of alcohols,[40] glucose[41] and amines.[42] The electrocatalytic oxidation of dihydronicotinamide adenine dinucleotide (NADH) on PQQ modified electrodes has also been reported, particularly in the presence of Ca^{2+} ions.[43]

The electrochemical and chemical properties of PQQ and analogous quinoquinones were first recorded in the 1980's[44] and a single two electron reversible transfer was observed (Figure 3.9).
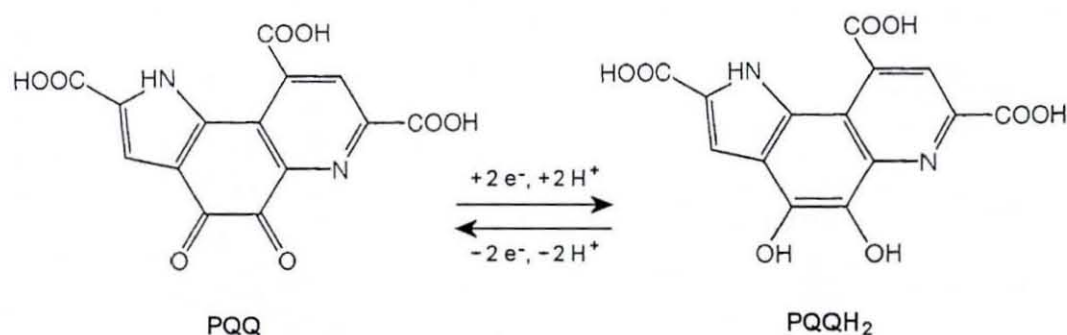

Figure 3.9. Schematic representation of the redox process of PQQ.[45]

More recent studies using PQQ immobilised on silica gel modified with zirconium oxide have also been carried out[45] and the effect of pH on the electrochemistry have been investigated.[45,46,47]

In this chapter, a layer-by-layer deposition process was employed to make TiO_2 PQQ mesoporous films on ITO surfaces where the carboxylate and ortho C=O groups in PQQ act as the binding sites. The electrochemistry of these films was investigated and the effect of film thickness, scan rate, and solution pH studied.

3.4.2. Formation & Reactivity of Multi-Layer TiO_2 PQQ Films

The formation of the TiO_2 PQQ films was characterised using field emission gun scanning electron microscopy (FEGSEM) and a quartz crystal microbalance (QCM) system. Figure 3.10 shows the typical FEGSEM images for a 2 and 15 layer TiO_2 PQQ film. A much thinner film (80 nm) is generated with respect to the TiO_2 TAPA films seen in the previous section.
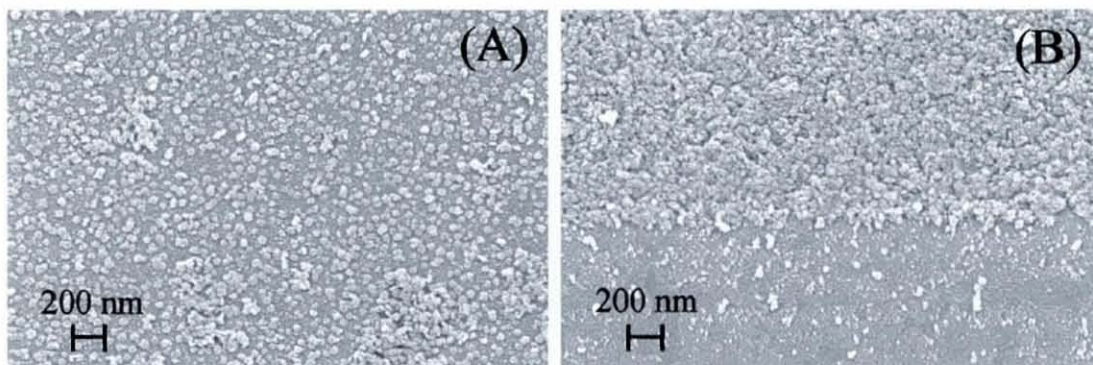
Figure 3.10. FEGSEM images of TiO₂ nanoparticle films deposited layer-by-layer with pyrroloquinoline quinone onto the surface of an ITO electrode with (A) 2 layers TiO₂ PQQ film and (B) 15 layers TiO₂ PQQ.

Figure 3.11 shows the subsequent reduction of the resonance frequency of an ITO coated quartz crystal resonator during the layer-by-layer deposition process of alternating 3 %wt titanium (IV) oxide sol and 0.1 mM PQQ. Each TiO₂ PQQ layer is consistent with a 349 Hz change corresponding to 366 ng. This gives a weight of a mono-layer of TiO₂ particles as 240 ng plus 126 ng PQQ (molecular weight 330.2 g mol^{-1}) or 3.8×10^{-10} mol per layer (on a 0.2 cm^2 area).
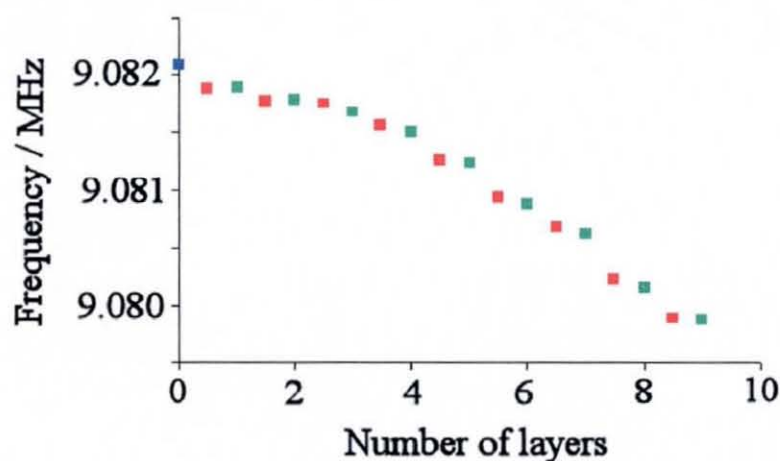

Figure 3.11. Plot of the resonance frequency change for an ITO coated quartz crystal (■) during layer-by-layer deposition of TiO₂ (■) and PQQ (■).

Cyclic voltammetry of PQQ solutions using unmodified gold or platinum electrodes have been reported where irreversible voltammograms are generated due to the difficulties in the direct electron transfer between the electrodes and PQQ. However, the use of modified electrodes (e.g. self assembled thiolate mono-layers on gold electrodes) allows the observation of the reversible redox couple expected for the two-electron transfer process in PQQ, at approximately –0.13 V *vs.* SCE at pH 7. Cyclic voltammograms obtained using carbon paste electrodes modified with a matrix of silica, zirconium oxide and PQQ exhibit the expected redox couple plus a second unexplained anodic peak.[45,47] The composition of the electrode is therefore influential in the PQQ voltammetric response recorded.

The initial electrochemical experiments in this investigation were carried out using cyclic voltammetry in 0.1 M pH 7 phosphate buffer solution for 15, 30 and 45 layer TiO_2 PQQ films on ITO. Figure 3.12 shows the first and fifth scan recorded for the 15 layer TiO_2 PQQ film, however all 3 multi-layer films produced similar responses. In the first potential scan, only a very small oxidation signal in the expected PQQ redox response is observed (process I) plus a new reduction peak at approximately –0.6 V *vs.* SCE (process II). After 5 scans, a more defined oxidation peak and corresponding reduction peak are observed for process I plus a decrease in the magnitude of the process II reduction peak.
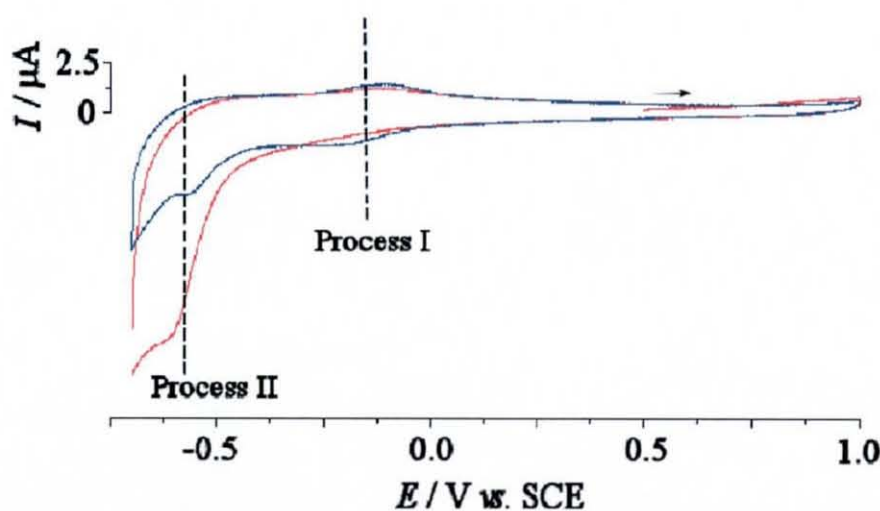

Figure 3.12. Comparison of the first (red line) and fifth (blue line) scan for a 15 layer TiO_2 PQQ film electrode in 0.1 M pH 7 phosphate buffer. Scan rate 100 mVs^{-1}.

Interestingly, after being held at 0.5 V for 15 minutes (Figure 3.13), a clear oxidation and slight reduction response for process I is seen (E_{mid} = approximately - 0.2 V vs. SCE), and the process II reduction peak is similar in size to that initially recorded (Figure 3.12). The electrode was held at 0.5 V to ensure that the PQQ was fully re-oxidised enabling an improved PQQ redox response to be recorded. In the second scan the reduction peak for process I increases and has a greater degree of symmetry, however with repeated cycling the current response for both process I and process II decreases.
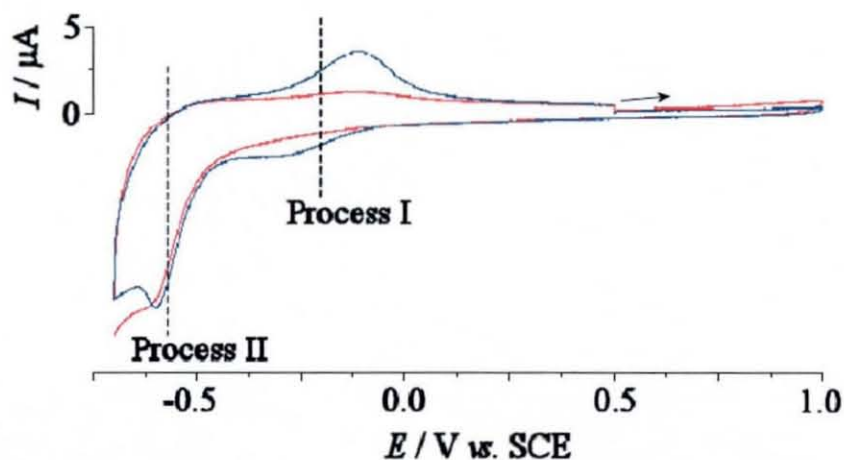

Figure 3.13. Comparison of the first scans for a 15 layer TiO$_2$ PQQ film electrodes before (red line) and after (blue line) being held at 0.5 V for 15 minutes in 0.1 M pH 7 phosphate buffer. Scan rate 100 mVs^{-1}.

The effect of the length of time the TiO$_2$ PQQ electrode was held at 0.5 V for was investigated over a range of 5 to 60 minutes, and a 15 to 30 minute period of time at 0.5 V was seen to be optimum, producing a significant increase in the redox response of PQQ observed.

The process of repeatedly holding the electrode at an oxidising potential of 0.5 V results in an even more defined current response for process I. Figure 3.14 shows the cyclic voltammograms for a 15, 30 and 45 layer TiO$_2$ PQQ film after being repeatedly held at 0.5 V for 15 minutes four times. It is now possible to observe the influence of the film thickness on the PQQ voltammetric response. Firstly, a slight increase in the background capacitive current is seen with increasing film thickness

due to the increase in TiO_2 deposited in the nanoparticle film. Secondly, an increase in the peak current for process II is recorded as the amount of PQQ present increases. Next, an increase in the peak separation for process I is observed, in addition to a shift in the peak potential for process II, to more negative potentials with increasing film thickness. This is most likely due to a decrease in the ease of electron flow trough the TiO_2 PQQ nanoparticle film. By repeatedly holding the electrode at 0.5 V for shorter lengths of time instead of one long holding step, a more defined voltammetric response is generated. A possible explanation for this is that surface relaxation/rearrangement occurs between holding steps facilitating the further re-oxidation of PQQ.
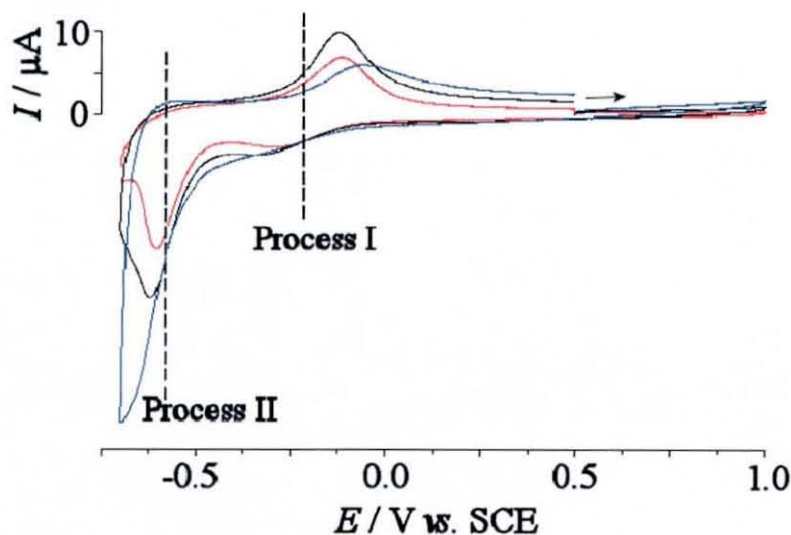

Figure 3.14. Comparison of the first scan for increasing thickness TiO_2 PQQ film electrodes after being held at 0.5 V for 15 minutes for the fourth time in 0.1 M pH 7 phosphate buffer where (i) red line = 15 layers, (ii) black line = 30 layers and (iii) blue line = 45 layers. Scan rate 100 mVs^{-1}.

The effect of scan rate on the electrochemistry of the TiO_2 PQQ electrodes in 0.1 M pH 7 phosphate buffer solution was investigated next. Figure 3.15 shows the linear proportional increase in oxidation peak current with scan rate (1-500 mVs^{-1}) expected for a surface confined process, recorded from the cyclic voltammograms for process I at a 15 layer TiO_2 PQQ electrode. This indicates that the electron transfer process measured for PQQ in the TiO_2 mesoporous film is a surface process dependent on the flow of electrons to the electrode surface. In order to 'renew' the activity of the electrode, it was held at 0.5 V for 15 minutes between each scan rate.
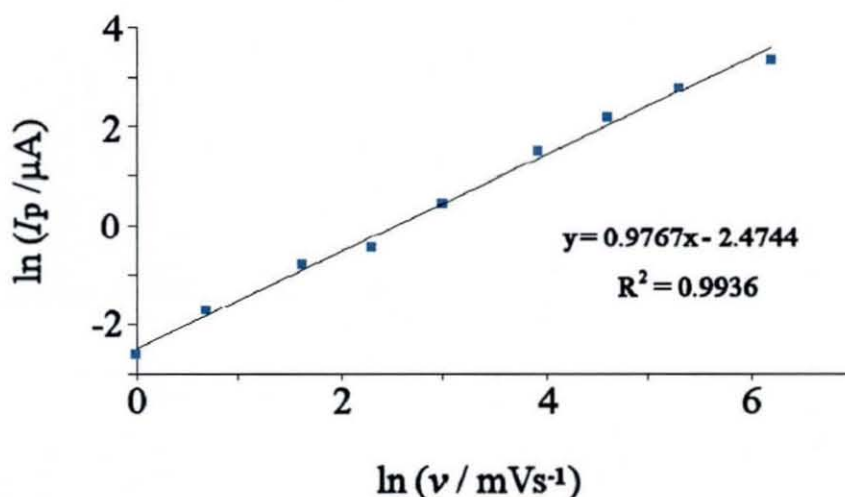
Figure 3.15. Plot of the natural log peak current (μA) for the oxidation peak in Process I against the natural log scan rate (mVs^{-1}) for the first scan for 15 layer TiO$_2$ PQQ film electrode after being held at 0.5 V for 15 minutes for the fourth time in 0.1 M pH 7 phosphate buffer.

It is interesting to compare the charge under the reduction response with the estimated amount of PQQ on the electrode surface. Integration under the voltammetric response obtained at 100 mVs^{-1} for the 15 layer TiO$_2$ PQQ electrode gives approximately 2 μC. In comparison, for a mono-layer of PQQ adsorbed on TiO$_2$ particles an expected charge, for a two-electron process, of 370 μC can be calculated using equation 3.3. The number of electrons (e^-) transferred in the two-electron reduction of PQQ was estimated as follows. The number of moles of PQQ in a mono-layer deposit in a 0.2 cm^2 area, determined from the QCM data (see Figure 3.11), was multiplied to give the number of moles of PQQ deposited in a mono-layer in a 1 cm^2 area. The number of moles in a 1 cm^2 area multiplied by the Avogadro constant (N_A) equals the number of PQQ molecules present. Assuming 100 % of the PQQ molecules are electrochemically active and a two-electron transfer process occurs, the number of electrons is equal to the number of PQQ molecules multiplied by two.

$$charge = \frac{number\ of\ e^- \times F}{N_A} \qquad (3.3)$$

Therefore only around 0.55% of the deposit is electrochemically reduced with a

scan rate of 100 mVs^{-1} and immersed in aqueous 0.1 M pH 7 phosphate buffer. Therefore a substantial amount of molecular binder (PQQ) appears to remain inactive.

The presence of two reduction peaks indicates two different possible electron transport processes, with process I at –0.2 V *vs.* SCE corresponding to electron transfer over the surface of the TiO_2 PQQ film close to the ITO electrode interface (equation 3.4a). The second irreversible process II reduction peak (equation 3.4b) seen at –0.6 V *vs.* SCE could correspond to electron transfer through the TiO_2 nanoparticles away from the ITO interface (Figure 3.16). This would explain (at least in part) the low charge under the reduction peaks.
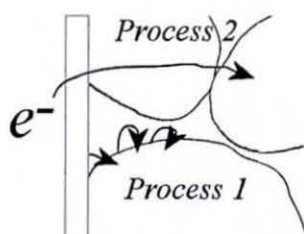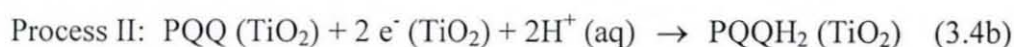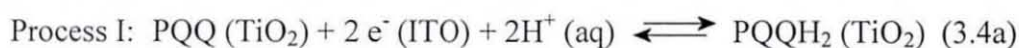

Figure 3.16. Diagram representing the two possible electron transport processes in TiO_2 PQQ films on ITO surfaces.

Process I: $PQQ (TiO_2) + 2 e^- (ITO) + 2H^+ (aq) \rightleftharpoons PQQH_2 (TiO_2)$ (3.4a)

Process II: $PQQ (TiO_2) + 2 e^- (TiO_2) + 2H^+ (aq) \rightarrow PQQH_2 (TiO_2)$ (3.4b)

3.4.3. The Effect of pH on the Reactivity of Multi-Layer TiO_2 PQQ Films.

Next, an investigation into the effect of pH on the redox response in 0.1 M phosphate buffer solution was carried out for 15 layer TiO_2 PQQ electrodes. A new electrode was used for each pH solution. Figure 3.17 shows a comparison of scans 1, 2 and 50 at different pH. In Figure 3.9 the redox reaction of PQQ is shown to involve protons and equation 3.5 illustrates that the state of protonation of the PQQ surface is expected to directly cause the peak potential to shift in a Nernstian manner.
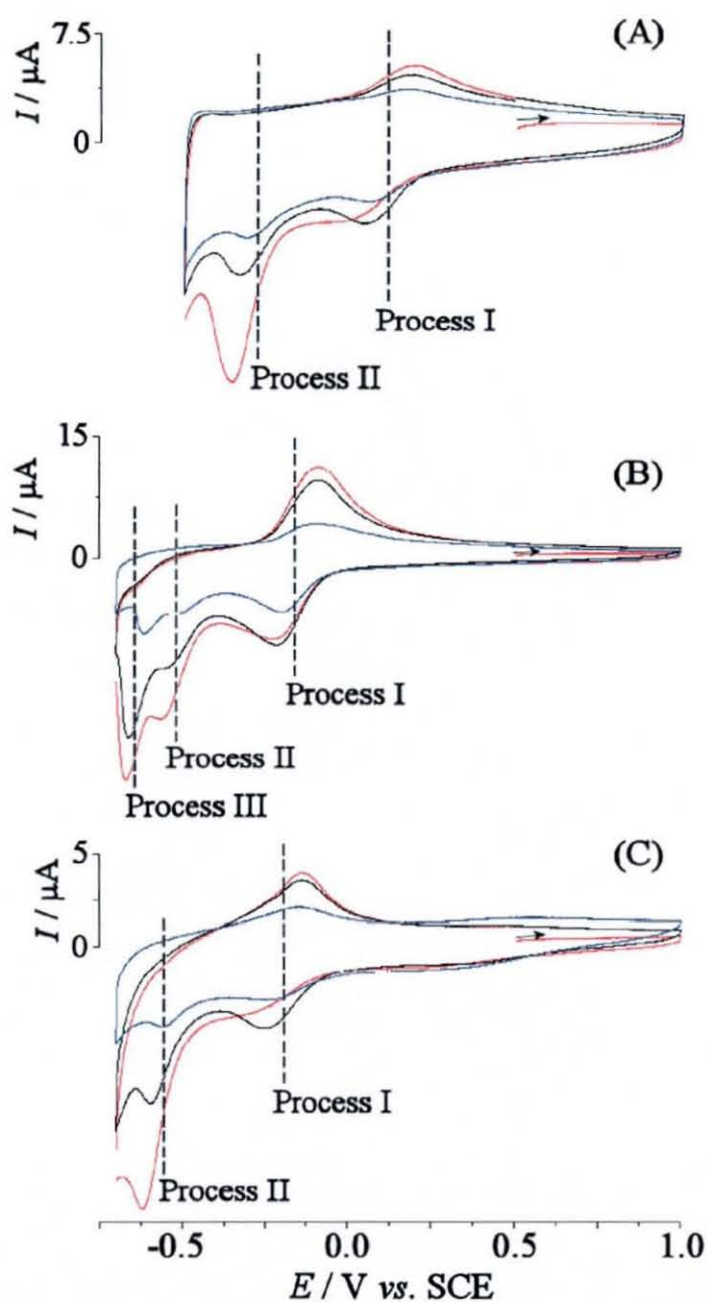
Figure 3.17. Comparison of the (i) first (red line), (ii) second (black line) and (iii) fiftieth (blue line) scan for 15 layer TiO_2 PQQ film electrode in (A) pH 2, (B) pH 5.5, and (C) pH 7 0.1 M phosphate buffer solution. Scan rate 100 mVs^{-1}.

$$E = E^{o'} + \frac{2.3RT}{2F} \log \frac{[PQQ]}{[PQQH_2]} + \frac{2.3RT}{2F} \log[H^+]^2 \qquad (3.5)$$

By increasing the number of protons present, the peak potential for both processes I

and II are seen to shift to more positive potentials. At pH 5.5 it is also possible to see the beginning of another reduction peak associated with the TiO_2 as seen in chapter 2. A reduced potential scan range is use at pH 2 to avoid recording the process III redox response.

The reproducibility of the voltammetry over 50 cycles for a 15 layer TiO_2 PQQ electrode at pH 2, pH 5.5 and pH 7 after the electrode had been held at 0.5 V for 30 minutes three times is shown in Figure 3.17. As mentioned previously, process I becomes more symmetrical and decreases gradually with repeated cycling. Process II shows a large decrease between scans 1 and 2 and a much more gradual decrease in subsequent scans. This could be due to poor reversibility and changes in the TiO_2 PQQ film conductivity, as the surface of nanoparticle film gradually rearranges with repeated potential cycling may increase the difficulties in the direct electron transfer between PQQ and the TiO_2 nanoparticle support on ITO electrodes substrate.

Figure 3.18 shows the shift in peak potential for process I and process II as a function of pH for 15 layer TiO_2 PQQ films. The shift in peak potential observed is consistent with the proton involvement in the PQQ redox reaction shown in Figure 3.9 and described by the Nernst equation for PQQ (equation 3.5).
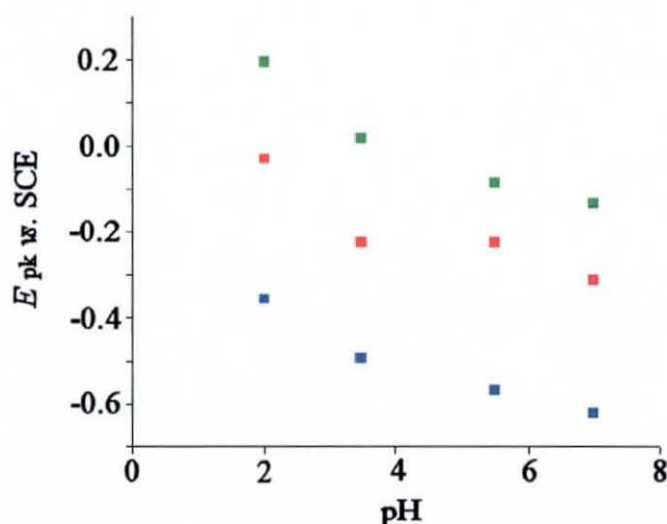

Figure 3.18. Comparison of the peak potential (V) in the first scan for 15 layer TiO_2 PQQ film electrodes after being held at 0.5 V for 30 minutes for the third time. Scan rate 100 mVs^{-1} in various pH 0.1 M phosphate buffer. Process I oxidation: ■. Process I reduction: ■ and Process II reduction: ■.

3.4.4. The Electrocatalytic Oxidation of NADH at Multi-Layer TiO₂ PQQ Films

As previously stated, PQQ is electrochemically active and capable of catalysing many reactions such as the oxidation of NADH. Reports of PQQ modified electrodes and the electrocatalysis of NADH include the use of electro-polymerised aminobenzene isomers and PQQ on various substrates[48] and PQQ immobilized on silica gel modified with zirconium oxide.[45] In this investigation, the ability of TiO₂ PQQ mesoporous films to electro-catalytically oxidise NADH was explored but no coupled process was observed. PQQ immobilised at the TiO₂ surface appears to be catalytically ineffective or the flow of electrons to achieve an anodic process is simply too slow.

3.5. Conductivity Effects in Multi-Layer TiO₂-Phytate Films

3.5.1. Introduction

A small monomeric binder such as phytic acid (Figure 3.19), a naturally occurring cyclic hexaphosphate, has been shown to readily bind to oxide surfaces such as iron oxide[14] or titanium oxide[49] in previous studies and is used here to probe the effect of film thickness on the conductivity.
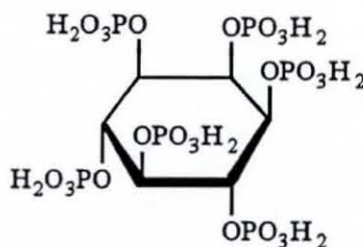

Figure 3.19. Molecular structural unit of the phytate organic binder unit.

3.5.2. Cyclic Voltammetry of Multi-Layer TiO₂-Phytate Films

The electrochemistry of TiO₂ phytate films was examined in aqueous solutions producing a response similar to that described in previous studies[50,51] where a reduction and subsequent oxidation peak accompanied by proton insertion are observed (equation 3.6).

$$Ti^{4+} (TiO_2) + e^- (ITO\ electrode) + H^+ (aq) \rightarrow Ti^{3+} (TiO_2) + H^+ (TiO_2) \quad (3.6)$$
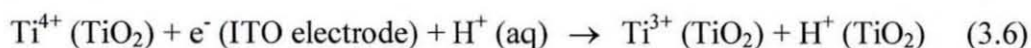
Figure 3.20 shows the effect of increasing the number of layers of TiO₂ phytate present at the electrode surface. It can clearly be seen that the reduction response steadily increases and a new stepped oxidation feature is observed for thicker films. The effect of thickness on the voltammetric behaviour of TiO₂ has not previously been investigated and is certainly important. By changing the number of layers, it is found that the shape of the resulting cyclic voltammograms change dramatically.
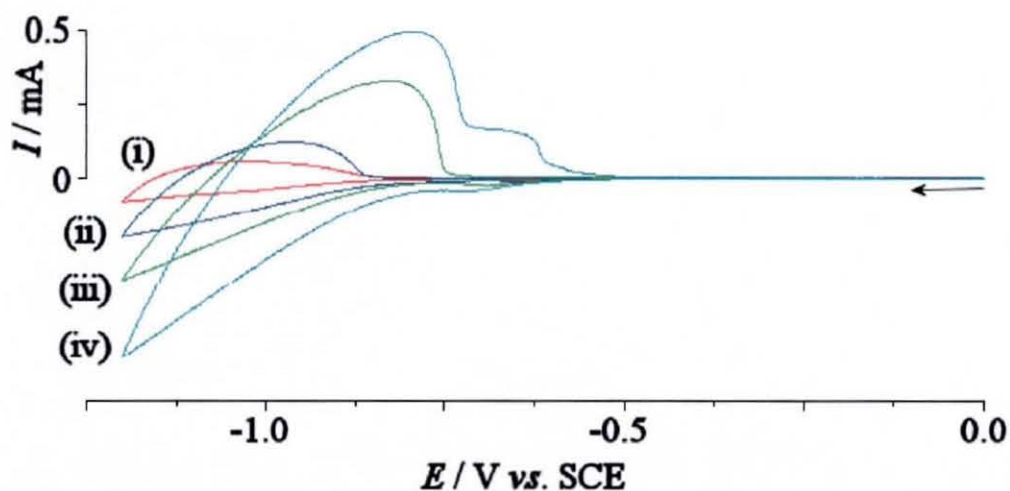
Figure 3.20. Cyclic voltammograms (scan rate 50 mVs⁻¹) for the reduction of TiO₂ phytate nanoparticle films deposited at ITO electrodes and immersed in 0.1 M NaClO₄. Films of TiO₂ phytate were grown with (i) 5, (ii) 10, (iii) 15, and (iv) 20 layers. The first scan is shown in each case.

Using a model of a resistor and a capacitor in series (Figure 3.21) to represent the ITO and TiO₂ film components respectively, it is possible to predict or 'simulate'

the shape of the voltammetric response expected. This allows insights into the diffusion of electrons to be obtained as the electronic states in TiO_2 are charged and discharged.
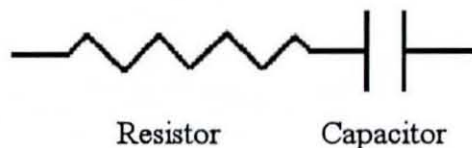

Resistor   Capacitor

Figure 3.21. Schematic of an electric circuit containing a resistor and capacitor in series representing the ITO surface and TiO_2 nanoparticle film components respectively.

In order to simulate the current response (equation 3.7), it is necessary to determine both the capacitance (C) with varying potential (U), and the integral of current with time ($\int I_t dt$).

$$I_t = \frac{U_t}{R} - \frac{\int I_t dt}{RC} \qquad (3.7)$$

The capacitance term required in equation 3.7 can be calculated by fitting a polynomial expression (equation 3.8).

$$C = C_0 + \left\{ a + a_1(x - x_0) + \frac{a_2^2}{2}(x - x_0)^2 + \frac{a_3^3}{6}(x - x_0)^3 + ... \frac{a_m^m}{m!}(x - x_0)^m \right\} \qquad (3.8)$$

In this equation C_0 is the initial capacitance (F), a to a_m are constants, x is the potential (V) and x_o is a constant shift in potential (V).

In a spreadsheet analysis, the initial current point is assumed to be C_o multiplied by the scan rate (Vs^{-1}). This can then be used to calculate the integral of current with time (equation 3.9), where $\int I_0 dt$ is equal to 0.

$$\int I_t dt = \int I_{t-1} dt + I_{t-1}(t_t - t_{t-1}) \qquad (3.9)$$

The product from equations 3.7 and 3.9 are then fed back into each other in a loop and the a_m constants in equation 3.8 manipulated to give the optimum fit to the experimental data recorded, thereby generating the simulated current response.

Figure 3.22 shows the cyclic voltammograms for the experimental and 'simulated' data for a 5 layer deposit of TiO_2 phytate on an ITO substrate. The simulated current response is seen to be a good fit for most of the data points, especially in the region 0 V to -0.6 V and -1.1 V to -1.2 V. The first mismatch between the recorded voltammetry and simulation occurs in the size of the peak current (I_p), possibly due to a degree of irreversibility and hydrogen evolution. The second difference is observed in the steeper decline in current after I_p in the experimental voltammogram, which is not consistent with the simple RC model (see Figure 3.21). This is attributed to a sudden decrease in the number of charged electrons flowing from the TiO_2 nanoparticle surface back to the ITO electrode. Again this is not incorporated into the simplistic 'simulation' and is an indication of the diffusion of electrons through the film potentially allowing the diffusion coefficient to be estimated. In future, a better simulation model needs to be developed to account for electron diffusion effects.
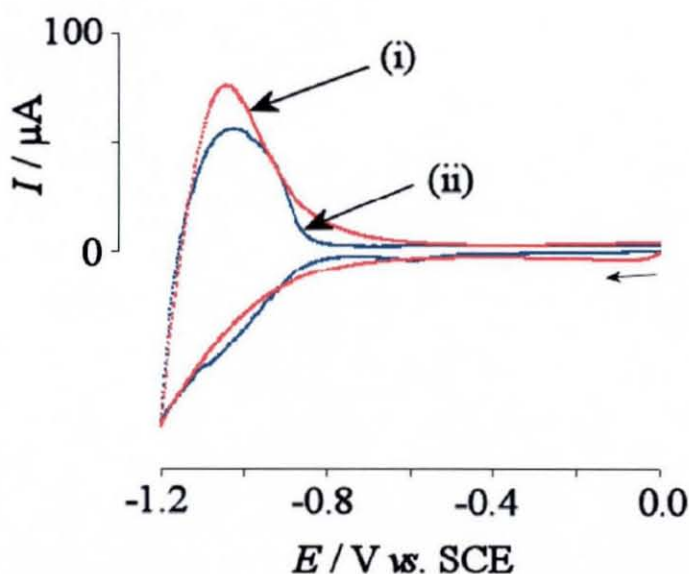

Figure 3.22. Cyclic voltammograms (scan rate 50 mVs^{-1}) for the (i) simulated and (ii) experimental data for the reduction of TiO_2 in a 5 layer TiO_2 phytate film deposited at ITO electrodes and immersed in 0.1 M NaClO$_4$.

This mismatch between the experimental and simulated voltammetric data increases with film thickness as a steep shoulder is seen in the return oxidation potential sweep.

3.5.3. A.C. Impedance Spectroscopy of Multi-Layer TiO_2-Phytate Films

Next, A.C. impedance spectroscopy was used to investigate the resistance and capacitance for a 15 layer TiO_2 phytate film on an ITO electrode in 0.1 M $NaClO_4$ at D.C. potentials of 0.5 V, 0 V, -0.25 V, -0.5 V, -0.75 V and −1 V. The frequency was scanned from 50,000 Hz to 0.5 Hz with an AC amplitude of 10 mV at each potential. Figure 3.23 shows the effect of the frequency on theta, the phase difference and |Z|, the impedance (see section 1.4.12) for the range of set potentials. The changes in impedance and phase shift reflect the changes in the conductivity of the TiO_2 phytate film at more negative potentials as the TiO_2 redox process shown in Figure 3.20 occurs.
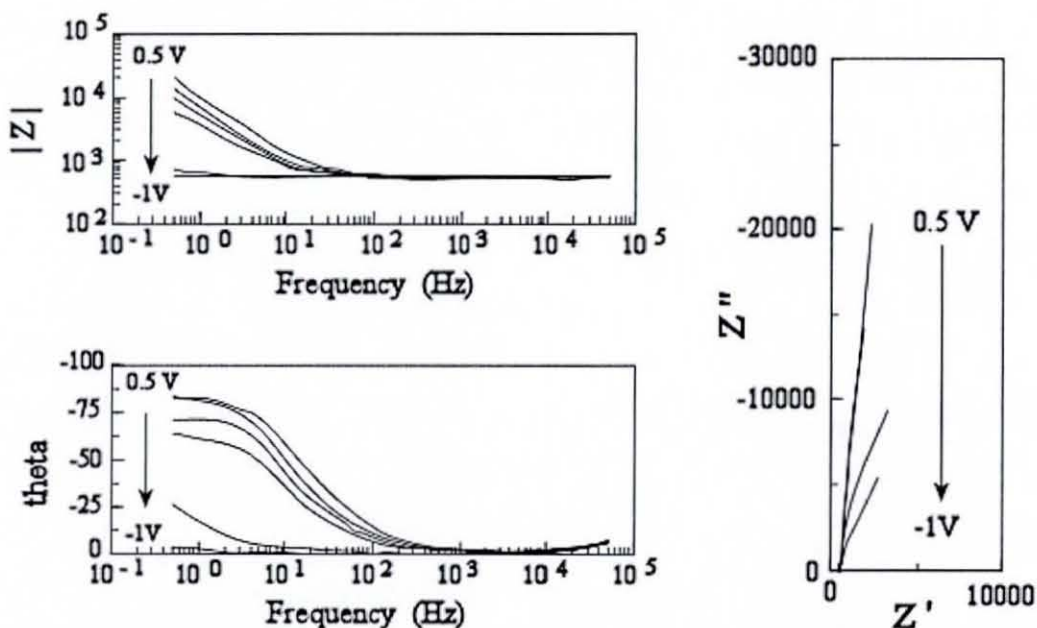

Figure 3.23. Bode plots of |Z| and theta as a function of frequency and plots of Z'' (imaginary) *vs.* Z' (real) (Ω) for a 15 layer TiO_2 phytate film on an ITO electrode over a range of potentials in 0.1 M $NaClO_4$.

Using the same model of a resistor and a capacitor in series (see Figure 3.21), theoretical values can be fitted to the experimental data as seen in Figure 3.24.
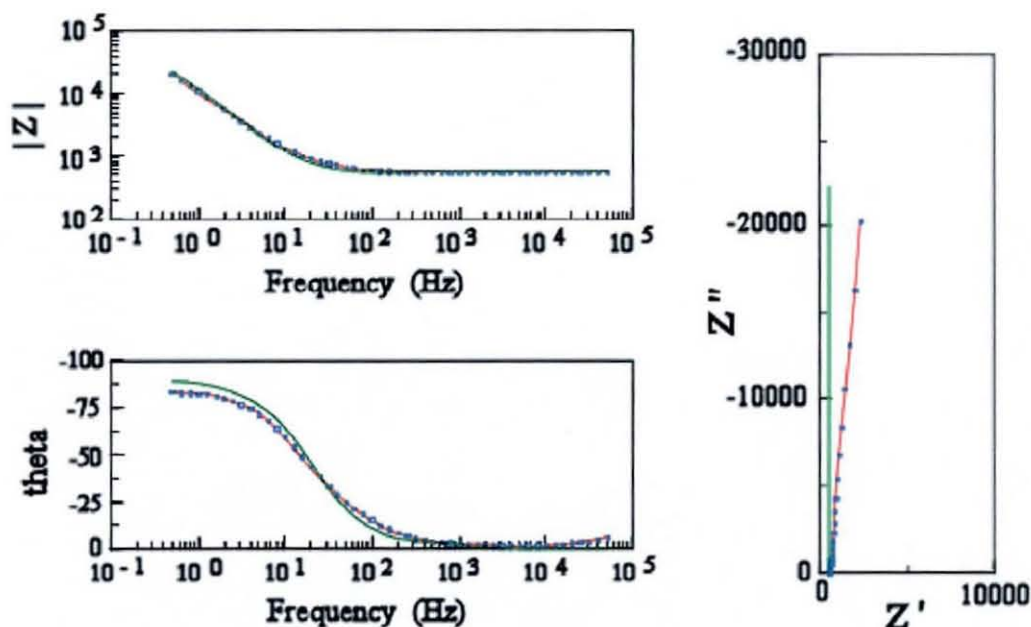

Figure 3.24. Bode plots of fit (green line) and experimental data of |Z| and theta as a function of frequency and plots of Z''(imaginary) *vs.* Z'(real) (Ω) for a 15 layer TiO_2 phytate film on an ITO electrode at a potential of +0.5 V in 0.1 M $NaClO_4$.

By fitting the data, it is possible to calculate the resistance and capacitance at each potential for the TiO_2 phytate film in $NaClO_4$ solution. Interestingly, the resistance only varies by 30 Ω going from 0.5 V to –1.0 V, compared to the 7899 μF difference in capacitance.

Potential (V)	Resistance (Ω)	Capacitance (μF)
0.50	562.3	14.2
0.00	562.4	20.7
-0.25	557.0	27.7
-0.50	555.0	39.9
-0.75	543.9	899.2
-1.00	532.4	7913.4

Figure 3.25. Table of resistance and capacitance values (to one d.p.) for a 15 layer TiO_2 phytate film on an ITO electrode over a range of potentials in 0.1 M $NaClO_4$.

A similar set of impedance measurements were conducted with a clean ITO electrode in 0.1 M NaClO$_4$ solution. Figure 3.26 shows the Bode plot and plot of imaginary impedance *vs.* real impedance. The shape of the plots is similar at each set potential unlike the case of the TiO$_2$ phytate film where the impedance and theta both decreased at more negative potentials.
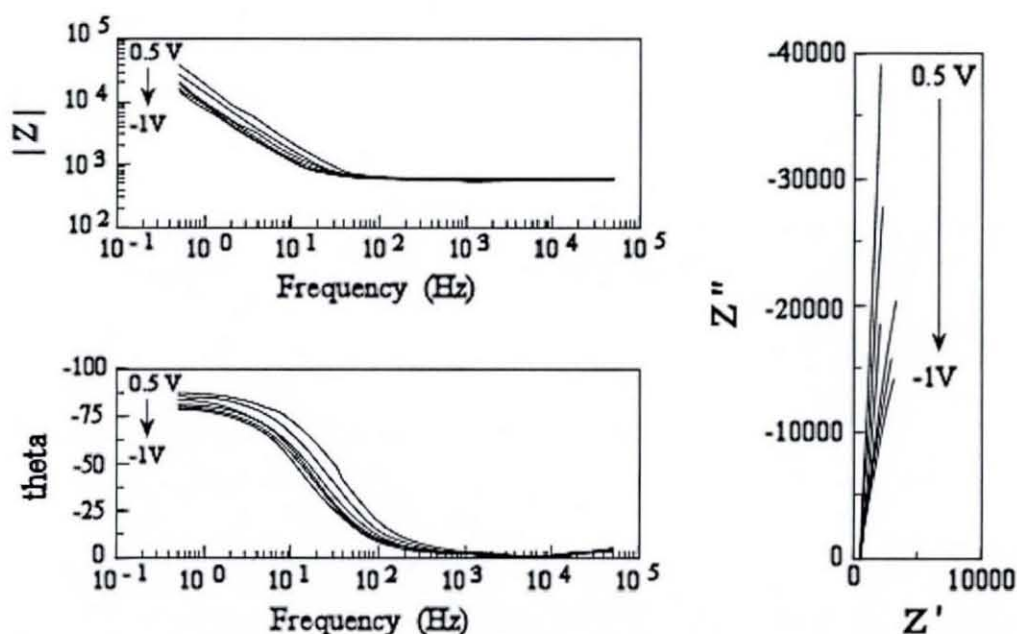

Figure 3.26. Bode plots of |Z| and theta as a function of frequency and plots of Z″(imaginary) *vs.* Z′ (real) (Ω) for an ITO electrode over a range of potentials in 0.1 M NaClO$_4$.

Using the model of a resistor and a capacitor in series, values of resistance and capacitance were calculated for the ITO electrode (Figure 3.27), as before there is little change in resistance with only a 21.5 Ω difference between 0.5 V and −1.0 V. The ITO electrode also shows an 11.7 µF change in capacitance, over the potential range. This indicates that the ITO surface is behaving as a resistor and contributes very little to the change in capacitance of the system.

Potential (V)	Resistance (Ω)	Capacitance (µF)
0.50	582.6	7.8
0.00	602.2	10.7
-0.25	605.9	14.0
-0.50	603.8	15.9
-0.75	604.1	18.0
-1.00	603.8	19.5

Figure 3.27. Table of the resistance and capacitance values (to one d.p.) for an ITO electrode over a range of potentials in 0.1 M NaClO₄.

In summary, the impedance data reveal that only capacitive effects are observed as a function of applied potential. The resistance value is constant and can be identified as mainly due to the ITO film. This analysis is in agreement with the cyclic voltammetric response (see Figure 3.20) and suggests high electrical conductivity and capacitive TiO_2 particle charging at negative potentials.

3.5.4. The Effect of pH on the Reactivity of Multi-Layer TiO₂-Phytate Films

The effect of the proton activity on the TiO_2 based redox system and conductivity is interesting. Figure 3.28 shows cyclic voltammograms obtained for a 15 layer film pre-treated in phosphate buffer solutions at various pH values. This was achieved by dipping the electrode into a 0.1 M phosphate buffer solution of known pH followed by rinsing with water and re-immersing into aqueous 0.1 M NaClO₄. The TiO_2 phytate film itself behaves as a buffer and can store the pH information. In Figure 3.28 it can be seen that the voltammetric response moves systematically to more positive potentials (60 mV per pH unit) with lower pH.
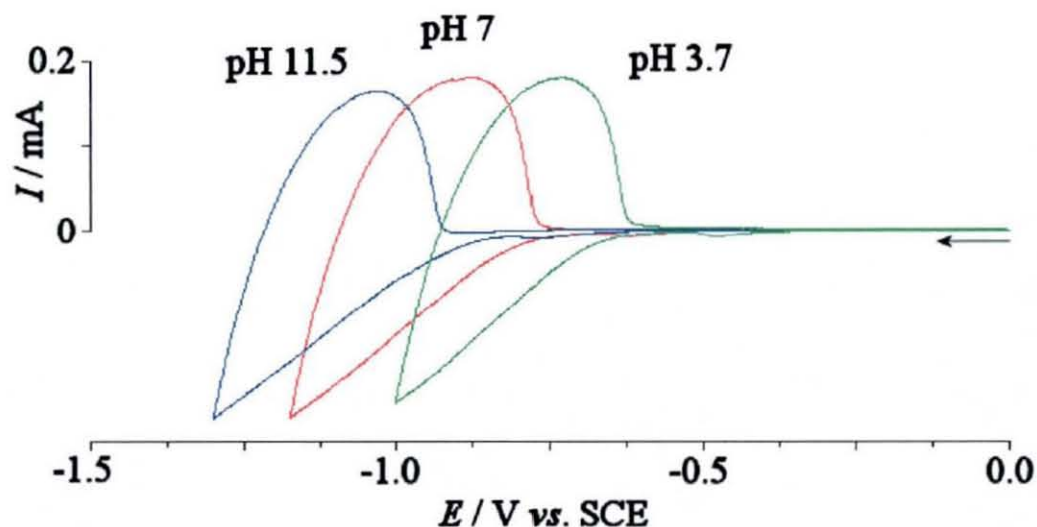
Figure 3.28. Cyclic voltammograms (scan rate 50 mVs^{-1}) for the reduction of a 15 layers TiO$_2$ phytate film on ITO electrodes. The electrode was dipped into 0.1 M phosphate buffer solutions of various pH values and then immersed in aqueous 0.1 M NaClO$_4$ for voltammetric analysis. The first scan is shown in each case.

The state of protonation of the TiO$_2$ surface directly causes energy levels to shift in a Nernstian manner. This can be explained with the surface activity of protons affecting the Ti(IV/III) reduction (equation 3.10).

$$E = E^{o'} + \frac{2.3RT}{nF} \log \left[\frac{Ti^{4+}}{Ti^{3+}} \right] + \frac{2.3RT}{nF} \log \left[H^{+} \right] \tag{3.10}$$

This Nernst equation is consistent with experimental results presented in chapter 2 where the uptake of protons into the TiO$_2$ lattice upon reduction was suggested.

3.6. Processes in TiO₂ Carboxymethyl-γ-cyclodextrin Multi-Layer Films

3.6.1. Introduction

Unlike phytic acid or CHHCA, which have a potential large number of co-ordination sites in a small area i.e. on a cyclohexane ring, larger organic molecules such as cyclodextrins have their potential binding sites (hydroxyl groups) spread over a greater area. Cyclodextrins are also known to have other desirable properties (such as selective binding of analytes) that make them interesting to look at as potential binders in the layer-by-layer deposition process with metal oxides such as TiO₂.

Cyclodextrins (cycloamyloses, cyclomaltoses or Schardinger dextrins) are composed of glucopyranose units linked by α- (1-4) bonds to form cyclic oligosaccharides, where the 3 main types of cyclodextrin differ only by the number of glucopyranose units present. α - cyclodextrin is comprised of 6 units, β - cyclodextrin is comprised of 7 units and γ - cyclodextrin is comprised of 8 units (see Figure 3.29).
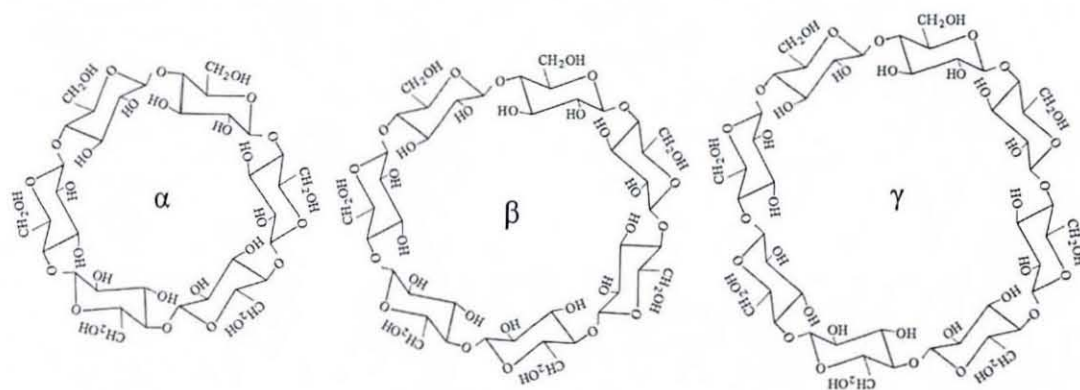

Figure 3.29. Figure to show the structures of the 3 main types of cyclodextrin, α – cyclodextrin, β – cyclodextrin and γ – cyclodextrin.

Apart from these naturally occurring cyclodextrins, many cyclodextrin derivatives have been synthesised, using for example amination, esterification or carboxymethylation of the hydroxyl groups of the cyclodextrins.

Cyclodextrins were first discovered in 1891 by Villiers[52] and work by Schardinger in the following years led to the isolation of several crystalline dextrins from the starch digest produced by certain bacterium. The structures of α and β – cyclodextrin were determined by X-ray crystallography in 1942 and γ – cyclodextrin in 1948.

The ring like structure of the cyclodextrins creates a hydrophobic interior and hydrophilic exterior. Cyclodextrins are known to form inclusion complexes with small compounds (e.g. with drugs)[53] in the centre of the ring structure. The size of the cyclodextrin and the molecule trying to incorporate will determine the orientation of the molecule in the cyclodextrin. The ability of cyclodextrins to form host-guest complexes[54] has resulted in their use in a wide range of areas including cosmetics, foods, pharmaceuticals, and agricultural and chemical industries. Cyclodextrins have also been used as enzyme models due to the resemblance of the hydrophobic cavity to the binding sites of enzymes.[55,56]

Ferrocene derivatives are known to interact with cyclodextrin (see Figure 3.30) to form weak complexes.[57] Ferrocene has been proposed[58] in aqueous media to bind to α-cyclodextrin (with the first formation constant K_{red} = 45 M^{-1}), to β-cyclodextrin (K_{red} = 3200 M^{-1}) and to γ-cyclodextrin (K_{red} = 155 M^{-2}) where the formation of a 2:1 ferrocene to cyclodextrin was suggested. Studies employing a variety of ferrocene derivatives[59] confirmed the weak binding and in particular the binding constant for 1,1´-ferrocenedimethanol to β-cyclodextrin in aqueous 0.2 M NaCl was reported as K_{red} = 1400 M^{-1}.
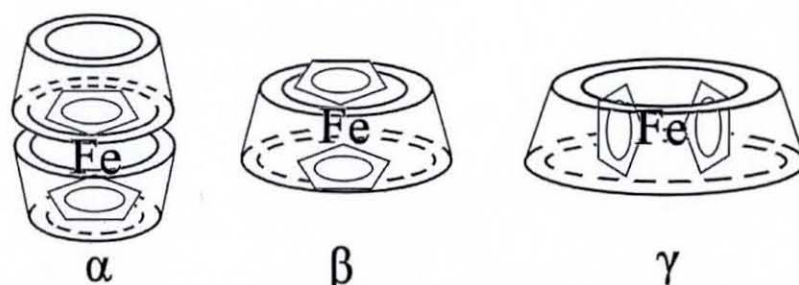

Figure 3.30. Structures of the inclusion complexes formed between ferrocene with α-cyclodextrin, β-cyclodextrin and γ-cyclodextrin.[60]

Figure 3.31 shows the typical dimensions of γ- cyclodextrin, how the subunits are orientated and the structure of 1,1′-ferrocenedimethanol. Only one possible isomer of the carboxymethyl-γ-cyclodextrin is shown.
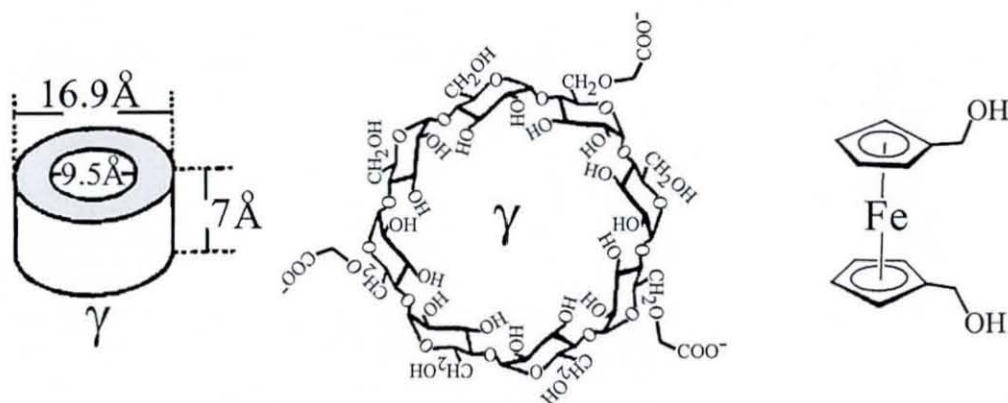

Figure 3.31. A schematic drawing to show the approximate dimensions and structure of carboxymethyl-γ-cyclodextrin and the structure of 1,1′-ferrocenedimethanol.

Here, binding constants for the interaction of 1,1′-ferrocenedimethanol in aqueous 0.1 M phosphate buffer solutions at pH 7 and at pH 2 are determined. Binding of 1,1′-ferrocenedimethanol to the TiO_2 surface immobilised carboxymethyl-γ-cyclodextrin is observed and shown to be consistent with the binding in solution

3.6.2. Formation of Multi-Layer TiO₂ Carboxymethyl-γ-Cyclodextrin Films

Initial deposition studies were carried out using β – cyclodextrin, the most widely used and lowest priced cyclodextrin, however, there was little or no film growth observed even after several deposition cycles due to the poor binding of the alcohol functional groups with the TiO_2 nanoparticle surface. Next, due to the favourable binding of TiO_2 to carboxylate groups, carboxymethyl–γ–cyclodextrin was investigated as a binder molecule. γ–cyclodextrin is larger than β – cyclodextrin, and will therefore have a greater number of functional binding sites present, and carboxymethyl–γ–cyclodextrin combines this increased number of binding sites

with the favourable binding ability of the carboxylate functional groups to the TiO_2 nanoparticle surface.

The layer-by-layer deposition process was much more successful using carboxymethyl-γ–cyclodextrin and it was possible to develop films of various thicknesses. The deposition procedure involved alternately dipping ITO electrode substrates into solutions of 0.3 %wt titanium (IV) oxide sol and aqueous 0.1 mM carboxymethyl-γ–cyclodextrin solution. Two intermittent rinsing dips in distilled water between solution A and B were carried out (see experimental). The immersion time in the TiO_2 sol and the solution of carboxymethyl-γ–cyclodextrin was set to 60 seconds in order to ensure complexation of the adsorption process. However, time parameters for the deposition have not been fully optimised. Typical FEGSEM images of film deposits are shown in Figure 3.32. The layer-by-layer growth is slow but gives rise to a homogeneous film on the electrode surface. A key factor in the slow growth rate is the low concentration of TiO_2 nanoparticles.
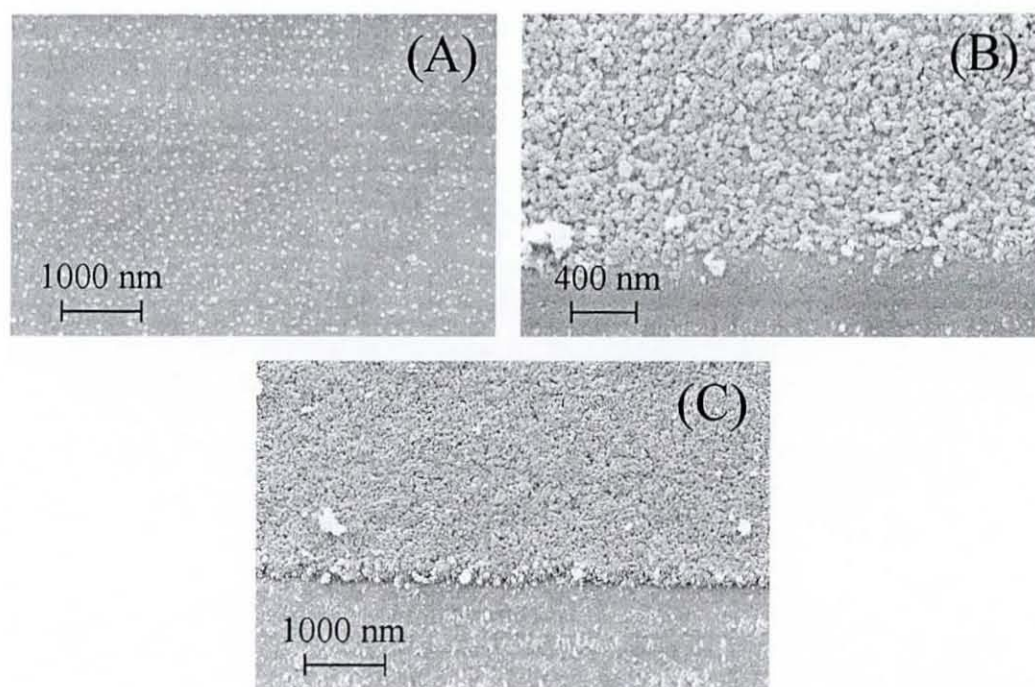

Figure 3.32. FEGSEM images of titanium oxide nanoparticle films (*ca.* 6-10nm diameter) deposited layer-by-layer with carboxymethyl-γ-cyclodextrin onto the surface of an ITO electrode with (A) a single layer of TiO_2 particles, (B) a 10 layer deposit, and (C) a 30 layer deposit of TiO_2 carboxymethyl-γ-cyclodextrin.

The electron microscopy data can be supported by experiments with quartz crystal oscillator measurements conducted in air. Figure 3.33 shows the subsequent reduction of the resonance frequency of an ITO coated quartz crystal resonator during the layer-by-layer deposition process. Each TiO_2 carboxymethyl-γ-cyclodextrin layer is consistent with a 140 Hz change corresponding to 147 ng. The weight of a mono-layer of TiO_2 particles can be estimated as 100 ng, which gives a weight of 47 ng carboxymethyl-γ-cyclodextrin (molecular weight 1471 g mol^{-1}) or 3.2×10^{-11} mol per layer.
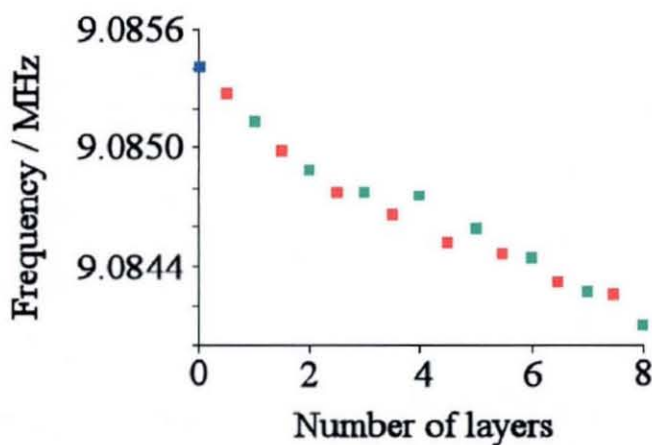

Figure 3.33. Plot of the resonance frequency change for an ITO coated quartz crystal (■) during layer-by-layer deposition of TiO_2 (■) and carboxymethyl-γ-cyclodextrin (■).

3.6.3. Electrochemical Characterisation of Carboxymethyl-γ-Cyclodextrin in Solution and Nanoparticulate TiO_2 Carboxymethyl-γ-Cyclodextrin Films

The binding of ferrocene derivatives into cyclodextrins is well known[61,62,63] and has been attributed to the 'hydrophobic' pocket in the cyclodextrin structure. The binding process can be studied voltammetrically in aqueous solution. A weak complex is formed and as a result the peak current for the oxidation of the ferrocene derivative is expected to decrease. This effect is caused by the decrease in the diffusion coefficient for the 1,1′-ferrocenedimethanol complex upon binding to the cyclodextrin (see Figure 3.34.). This reduction in peak current has been observed and is described quantitatively in the literature.[62,63,64]
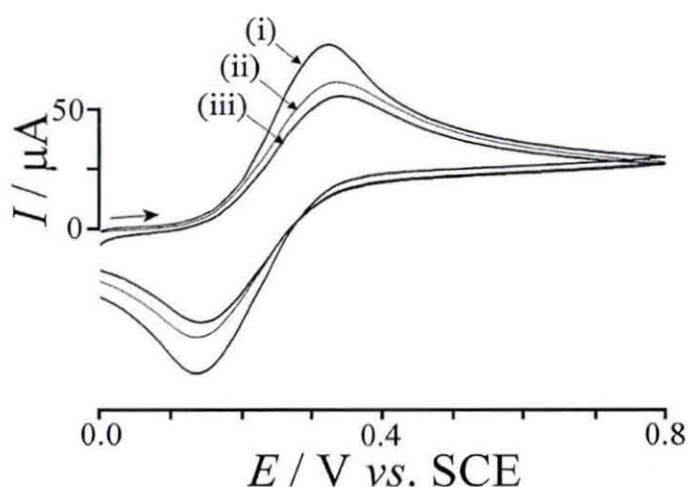
Figure 3.34. Cyclic voltammograms (scan rate 5 mVs^{-1}) obtained at a bare ITO electrode for the oxidation and re-reduction of 1 mM ferrocenedimethanol in aqueous 0.1 M phosphate buffer pH 7 in the presence of (i) 0 mM, (ii) 1 mM, and (iii) 2 mM carboxymethyl-γ-cyclodextrin.

The reaction scheme in Figure 3.35 illustrates the full 'square' reaction scheme resulting from heterogeneous electron transfer and complexation. For the case of 1,1′-ferrocenedimethanol binding to carboxymethyl-γ-cyclodextrin, weak binding (in agreement with the literature[63]) can be suggested. This allows the reaction scheme to be simplified and therefore only part of the mechanism highlighted grey needs to be considered. This corresponds to the electron transfer of the free 1,1′-ferrocenedimethanol and binding of the reduced form of the metal complex.
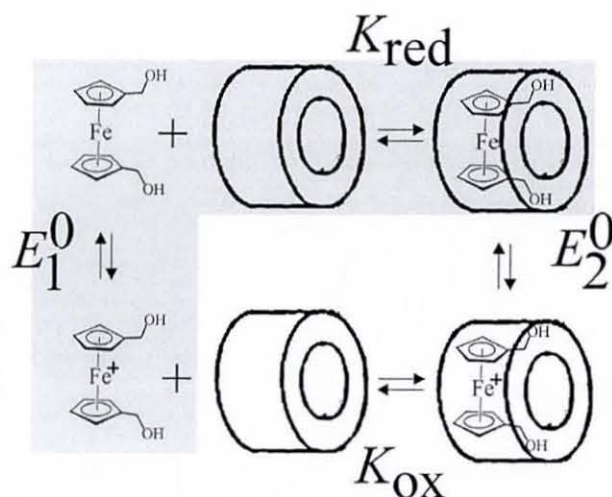

Figure 3.35. 'Square scheme' of the ferrocenedimethanol/carboxymethyl-γ-cyclodextrin redox system.

In order to quantify the effect of the cyclodextrin on the peak currents shown in Figure 3.34, a numerical simulation-based analysis employing the Digisim[TM] software package was applied.[65] For the simplified mechanism shown in Figure 3.35, peak current data were simulated at variable concentrations of carboxymethyl-γ-cyclodextrin. With the approximate diffusion coefficient for 1,1′-ferrocenedimethanol experimentally determined, 1×10^{-9} m^{2}s^{-1},[66] and the diffusion coefficient for carboxymethyl-γ-cyclodextrin estimated, 2.6×10^{-10} m^{2}s^{-1} (from the Stokes-Einstein relationship[67] $D = \dfrac{kT}{6\pi\eta r}$ assuming a diameter of 1.69 nm) it is possible to simulate the effect of 1,1′-ferrocenedimethanol complexation with the carboxymethyl-γ-cyclodextrin based on a simple fast pre-equilibrium step (C$_{rev}$E mechanism).

The rates for complexation and de-complexation were increased to decouple the numerical simulation results from the rate constants and to make the simulated I_p dependent on the equilibrium constant K_{red} only. Figure 3.36 shows simulated normalised peak currents as a function of the concentration of carboxymethyl-γ-cyclodextrin. The equilibrium binding constant for a 0.1 M phosphate buffer solution at pH 7 can be determined as $K_{red} = 1300 \pm 200$ M^{-1}. Similarly, the equilibrium binding constant for a 0.1 M phosphate buffer at pH 2 was determined as $K_{red} = 1000 \pm 200$ M^{-1} (data not shown) assuming 1:1 complex formation. In this data analysis approach the possible formation of complexes and aggregates other than the 1:1 complex are ignored. The assumption of the formation of a 1:1 complex is plausible based on the bigger size of 1,1′-ferrocenedimethanol compared to ferrocene.
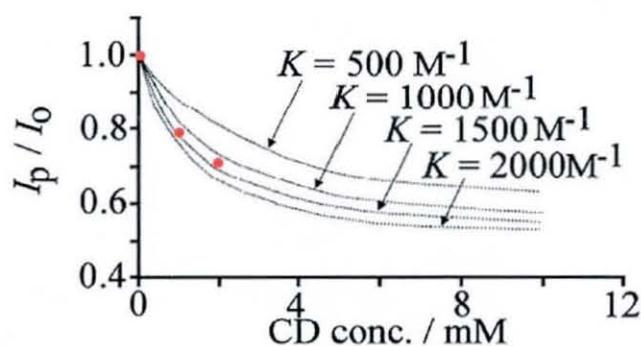
Figure 3.36. A plot of the normalised peak current versus the concentration of carboxymethyl-γ-cyclodextrin (●) together with data generated by simulation with Digisim^{TM} (black lines).

Next, the effect of the TiO$_2$ carboxymethyl-γ-cyclodextrin film on voltammetric response of ferrocenedimethanol was investigated. Figure 3.37 shows cyclic voltammograms obtained in aqueous 0.1 M phosphate buffer solutions at pH 7 and at pH 2 for the oxidation of 1,1′-ferrocenedimethanol at a 10-layer modified ITO electrode.
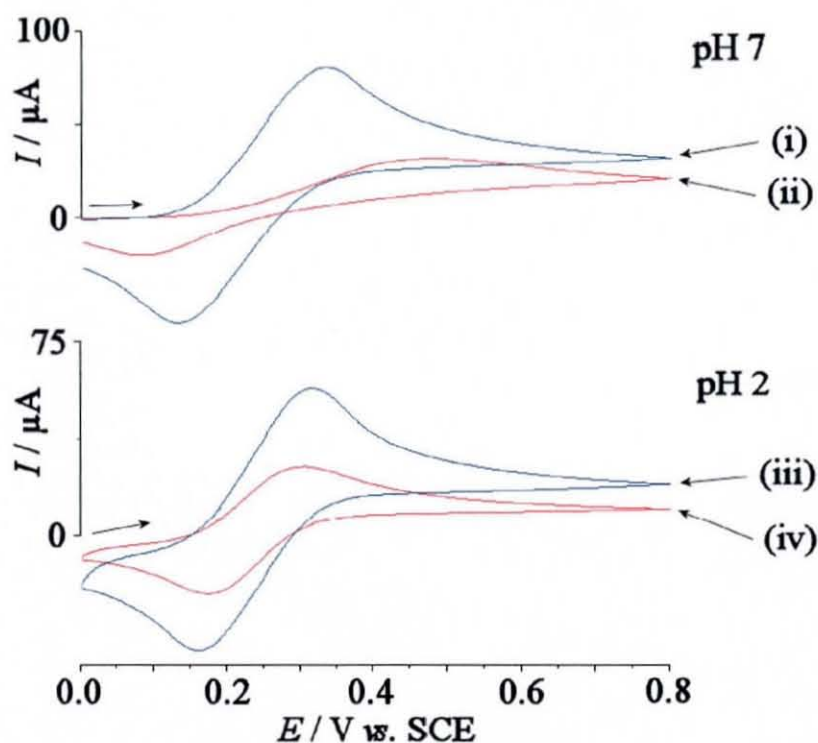

Figure 3.37. Cyclic voltammograms (scan rate 5 mVs^{-1}) obtained for the oxidation and re-reduction of (i and ii) 1 mM ferrocenedimethanol in 0.1 M phosphate buffer pH 7 and (iii and iv) 0.5 mM ferrocenedimethanol in 0.1 M phosphate buffer pH 2. A clean ITO electrode (i and iii) and a 10 layer TiO$_2$ carboxymethyl-γ-cyclodextrin film modified electrode (ii and iv) were used.

The voltammetric response observed for the oxidation and reduction of 1,1′-ferrocenedimethanol at a TiO_2 carboxymethyl-γ-cyclodextrin film at pH 7 (Figure 3.37ii), shows a reduction in the peak current and a widening of the peak-to-peak separation compared to the oxidation and reduction of 1,1′-ferrocenedimethanol at a blank ITO electrode (Figure 3.37i). In spite of the thin nature of the film, diffusion to the electrode surface is clearly obstructed and a further decrease in the peak current is observed for thicker films. It is possible that the carboxymethyl-γ-cyclodextrin unit very effectively fills the pores in the TiO_2 structure and limits access to the electrode surface. Trapping of the 1,1′-ferrocenedimethanol molecule might also contribute to this effect.

In pH 2 phosphate buffer solution, the voltammetric response observed for the oxidation and reduction of 1,1′-ferrocenedimethanol at a TiO_2 carboxymethyl-γ-cyclodextrin film shows a pronounced reduction in peak current (Figure 3.37iv) compared to the oxidation and reduction of 1,1′-ferrocenedimethanol at a blank ITO electrode (Figure 3.37iii). The carboxylic acid functionalities in carboxymethyl-γ-cyclodextrin are likely to be protonated/uncharged under these conditions (pH 2), which might improve film permeability and conductivity. Alternatively, it is necessary to consider that the carboxymethyl-γ-cyclodextrin ring may have decomposed, leaving a TiO_2 film. It is interesting to note that calcination of the TiO_2 films (at 500°C in air to remove all organic components) produces fully permeable films that behave essentially like a bare ITO electrode therefore the interaction of 1,1′-ferrocenedimethanol with the cyclodextrin unit is important.

3.6.4. Adsorption and Reactivity of Ferrocenedimethanol in Nanoparticulate TiO_2 Carboxymethyl-γ-Cyclodextrin Multi-Layer Films

Next, the adsorption of 1,1′-ferrocenedimethanol into TiO_2 carboxymethyl-γ-cyclodextrin host films was investigated. There was no obvious direct signature of surface adsorption in voltammetric data shown in Figure 3.37, but the weak binding characteristics of the carboxymethyl-γ-cyclodextrin towards the redox active 1,1′-

ferrocenedimethanol molecule is expected. Dipping an ITO electrode with a multi-layer deposit of TiO_2 carboxymethyl-γ-cyclodextrin into 1 mM 1,1´-ferrocenedimethanol for 30 seconds, rinsing with distilled water, and immersion into a clean 0.1 M phosphate buffer solution at pH 7, allows the bound 1,1´-ferrocenedimethanol to be observed voltammetrically. Figure 3.38 shows typical voltammetric responses obtained for (i) a 30 layer TiO_2 carboxymethyl-γ-cyclodextrin film and (ii) a 10 layer TiO_2 carboxymethyl-γ-cyclodextrin film modified ITO electrode. It can be seen that the voltammetric response for the oxidation of 1,1´-ferrocenedimethanol increases with layer thickness, however the loss of 1,1´-ferriciniumdimethanol from the electrode surface after oxidation results in a diminished peak current response for the re-reduction process.

The charge under the voltammetric oxidation peaks for the 10 layer and the 30 layer electrodes, 1 μC and 3 μC respectively, demonstrates that the voltammetric signal is correlated to the film thickness. However, additional factors such as the rinsing step and the immersion time before the experiment also affect the magnitude of the voltammetric signal due to the weak adsorption of 1,1´-ferrocenedimethanol. The maximum charge expected (for strong binding) based on quartz crystal microbalance experiments is 9 μC per TiO_2 carboxymethyl-γ-cyclodextrin layer.
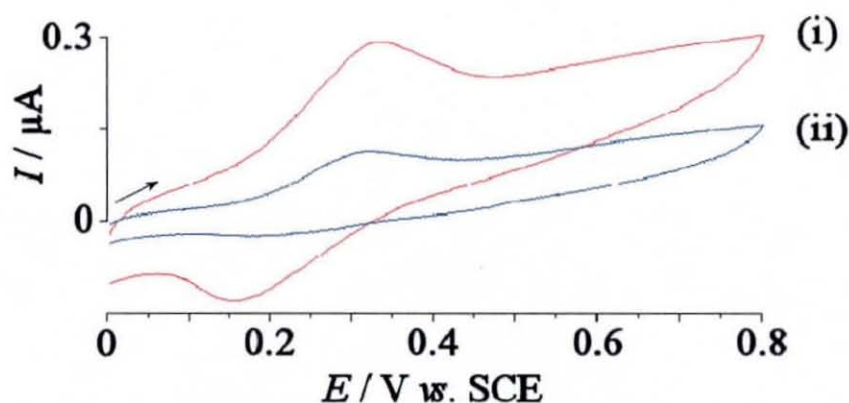

Figure 3.38. Cyclic voltammograms (scan rate 10 mVs^{-1}) for the oxidation and re-reduction of 1,1´-ferrocenedimethanol adsorbed onto (i) a 30 layer and (ii) a 10 layer TiO_2 carboxymethyl-γ-cyclodextrin film on an ITO electrode immersed in aqueous 0.1 M phosphate buffer at pH 7 after adsorption of 1.0 mM 1,1´-ferrocenedimethanol in aqueous 0.1 M phosphate buffer at pH 7.

The stability of the complex formed between 1,1′-ferrocenedimethanol and carboxymethyl-γ-cyclodextrin over repeated cycling of a 30 layer deposit TiO_2 carboxymethyl-γ-cyclodextrin film can be seen in Figure 3.39. During the repeated oxidation and re-reduction, a decrease in the peak current is observed connected to the loss of the 1,1′-ferriciniumdimethanol away from the electrode surface.
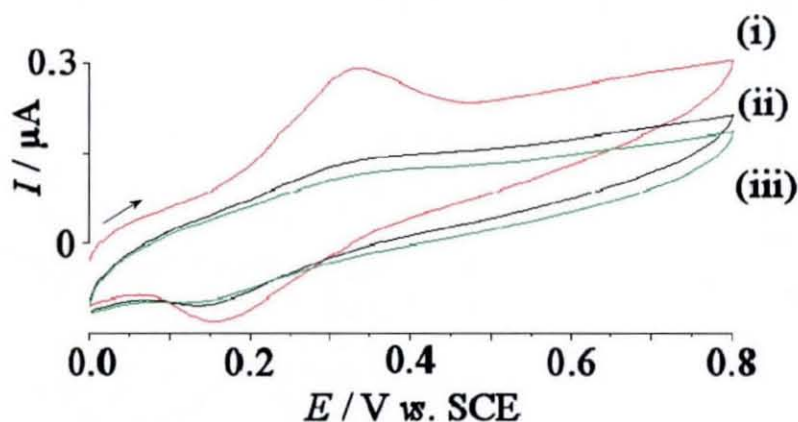

Figure 3.39. Cyclic voltammograms (scan rate 10 mVs⁻¹) obtained for the oxidation and re-reduction of 1,1′-ferrocenedimethanol adsorbed onto a 30 layer deposit TiO_2 carboxymethyl-γ-cyclodextrin film on ITO and immersed in aqueous 0.1 M phosphate buffer at pH 7 after immersion in 1.0 mM 1,1′-ferrocenedimethanol in aqueous 0.1 M phosphate buffer at pH 7 (i) scan 1 (ii) scan 5 and (iii) scan 10.

Next, the effect of the concentration of 1,1′-ferrocenedimethanol during the adsorption process is investigated. If the binding constant at pH 7, $K_{red} = 1300 \pm 200$ M^{-1}, is employed in a Langmuirian binding model, an approximately linear relationship between the concentration of 1,1′-ferrocenedimethanol during the adsorption step and the voltammetric response in buffer solution is expected. Figure 3.40 shows that this is indeed the case.
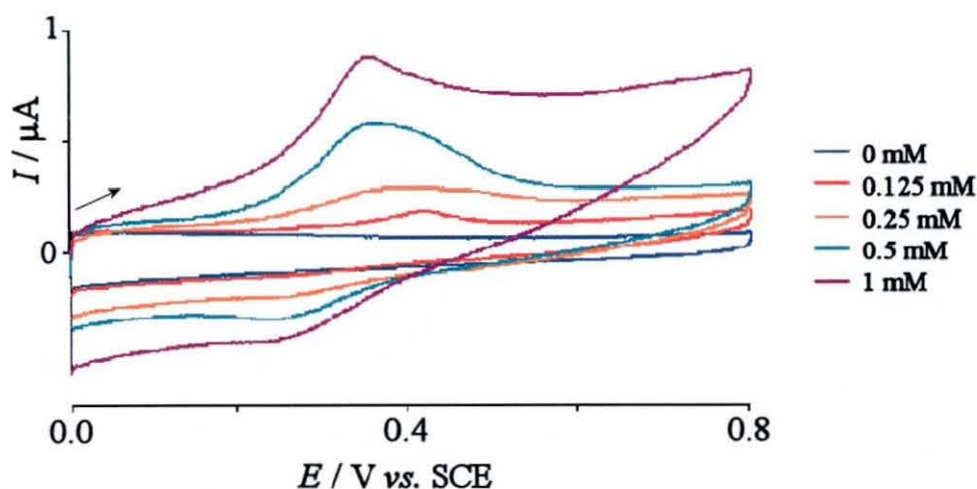
Figure 3.40. Cyclic voltammograms (scan rate 50 mVs^{-1}) for the oxidation and re-reduction of 1,1′-ferrocenedimethanol adsorbed onto a 10 layer deposit TiO$_2$ carboxymethyl-γ-cyclodextrin film on ITO in aqueous 0.1 M phosphate buffer at pH 7 after immersion in (i) 0 mM, (ii) 0.125 mM, (iii) 0.25, (iv) 0.5 mM, and (v) 1.0 mM 1,1′-ferrocenedimethanol in aqueous 0.1 M phosphate buffer at pH 7.

Increasing the concentration of 1,1′-ferrocenedimethanol from 0.125 mM to 1 mM clearly increases the voltammetric response. Furthermore, two distinct oxidation potentials can be identified, with peaks at *ca.* 0.4 V *vs.* SCE and at 0.3 V *vs.* SCE. The two peaks must relate to different binding sites in the TiO$_2$ carboxymethyl-γ-cyclodextrin films. Whether these correspond to differences in binding with the bulk of the film relative to interaction at the edge of the nanoparticle film deposit, or different orientations of the carboxymethyl-γ-cyclodextrin on the TiO$_2$ surface is yet to be determined. Both voltammetric responses are observed at a potential positive compared to the reversible potential of 1,1′-ferrocenedimethanol in homogeneous solution and this is indicative of weaker binding of the 1,1′-ferriciniumdimethanol oxidation product.[68]
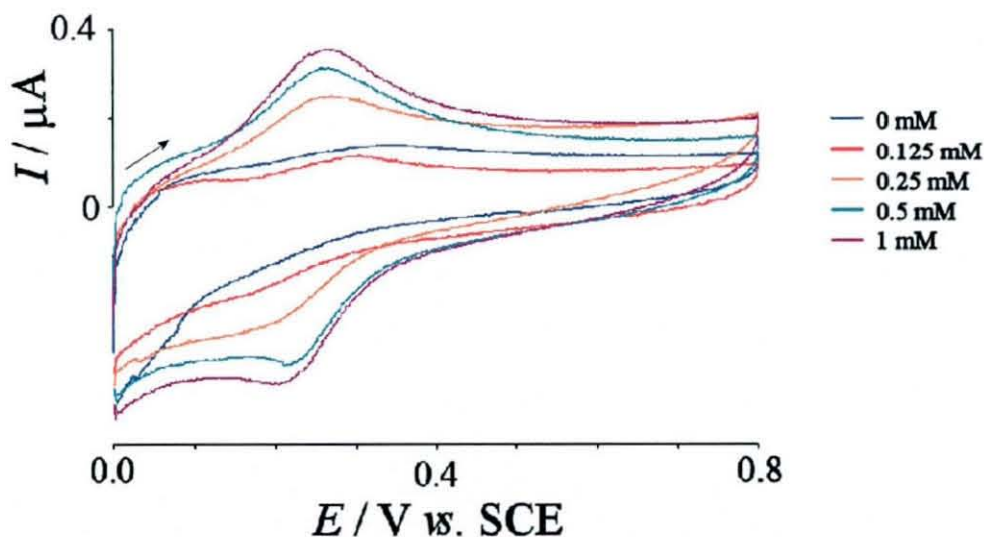
Figure 3.41. Cyclic voltammograms (scan rate 50 mV s^{-1}) obtained for the oxidation and re-reduction of 1,1'-ferrocenedimethanol adsorbed onto a 10 layer deposit TiO$_2$ carboxymethyl-γ-cyclodextrin film on ITO and immersed in aqueous 0.1 M phosphate buffer at pH 2.1 after immersion in (i) 0 mM, (ii) 0.125 mM, (iii) 0.25, (iv) 0.5 mM, and (v) 1.0 mM 1,1'-ferrocenedimethanol in aqueous 0.1 M phosphate buffer at pH 7.

Similar experiments were conducted in phosphate buffer at pH 2 (see Figure 3.41). Again it is possible to see two oxidation peaks for the voltammetric processes for the immobilized 1,1'-ferrocenedimethanol at 0.26 V *vs.* SCE and 0.29 V *vs.* SCE, more negative compared to the processes observed at pH 7. This suggests that the 1,1'-ferriciniumdimethanol oxidation product remains bound at pH 2 (at pH 7 ion pairing with the anionic carboxymethyl group might play a role in the de-complexation). The nature of the two distinct binding sites is again believed to be associated with either the mode of binding of carboxymethyl-γ-cyclodextrin onto the TiO$_2$ surface, e.g. side-on versus face-on, or due to edge effects within the film. However, further experimental work with other guest species and new experimental approaches will be required to gain further insights into the mechanistic effects of the complexation/de-complexation process in TiO$_2$ films.

In summary, TiO$_2$ - carboxymethyl-γ-cyclodextrin nanoparticle films have been successfully deposited using a layer-by-layer technique onto ITO substrates. The

binding of 1,1´-ferrocenedimethanol to the TiO₂ surface immobilised carboxymethyl-γ-cyclodextrin is observed and shown to be consistent with binding in solution

3.7. Charge Transport in TiO₂ Nafion® Multi-Layer Films

3.7.1. Introduction

Nafion® is a copolymer with a tetrafluoroethylene backbone functionalised with perfluorovinyl groups terminated with sulfonate groups (Figure 3.42) and was synthesised in 1962 by Walther Grot of Du Pont de Nemours.[69] Nafion® is the first class of commercial polymers with ionic properties and has a number of advantageous properties including its ionic nature and chemical stability. Another beneficial property of Nafion® is an operating temperature range up to 190°C due to the Teflon® backbone of the polymer, which itself is used as a non-stick coating particularly on pans where a high thermal stability is desired.

$$- [(CF_2 - CF_2)_n - CF - CF_2]_p -$$
$$|$$
$$(OCF_2 - CF)_m - OCF_2 CF_2 - SO_3^- M^+$$
$$|$$
$$CF_3$$
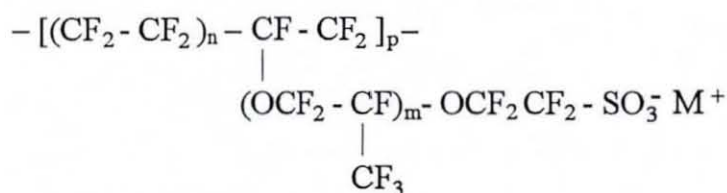
Figure 3.42. Structure of Nafion® repeat unit where the cation M is Na, n varies between 5 and 14, p varies between 200 and 600, and m typically equals 1. [70]

The ionic nature of Nafion® means it is highly conducting to cations, specifically to protons and water. The level of hydration in the membrane can directly affect the ion permeability.[71]

Nafion® has found many applications that utilise its ion selectivity. These include in industry for the electrolysis of NaCl solutions,[72] in energy production in fuel cells

and batteries,[73,74] and in electrochemical sensors.[75,76,77] The fluorinated carbons combined with the already withdrawing sulfonate groups and the stabilising effect of the polymer matrix make Nafion® an extremely strong acid. This has lead to Nafion® being used as a super-acid catalyst especially in organic chemistry,[78] with new possibilities being currently investigated.[79]

Nafion® modified electrodes were originally introduced by Rubinstein and Bard in 1980[80] and are able to incorporate a wide range of electroactive cations onto the electrode surface by electrostatic binding. Charge transport in Nafion® coated electrodes can occur by electron self-exchange, physical diffusion or a combination of the two mechanisms, depending on the nature of the electroactive cations.[81]

The use of nano-TiO$_2$/Nafion® modified electrodes has been reported for a range of applications including, NO sensors,[82] humidity sensors,[12] photocatalysis,[83,84] and sensing trace levels of dopamine.[85]

The overall negative charge and availability of Nafion® in a solution of lower aliphatic alcohols and water are ideal for the use of Nafion® as a binder molecule. This investigation looks at the formation of TiO$_2$ and Nafion® multi-layer films on ITO substrates using the layer-by-layer deposition process. The ability of Nafion® to act as an ion exchange substrate allowed the charge transport of positive analytes in TiO$_2$ Nafion® films in aqueous solution to be studied.

3.7.2. Formation of TiO$_2$ Nafion® Multi-Layer Films

Using the layer-by-layer deposition process described previously in the experimental section, TiO$_2$ Nafion® multi-layer films were generated on ITO substrates. Figure 3.43 shows the typical FEGSEM images for 2 and 15 layer TiO$_2$ Nafion® films. It is possible to see that the TiO$_2$ and Nafion® nanoparticles initially form small clusters of aggregates of approximately 40 nm diameter on the ITO surface and after further deposition cycles, a mesoporous film is observed where a 15 layer TiO$_2$ Nafion® film is approximately 300 nm thick.
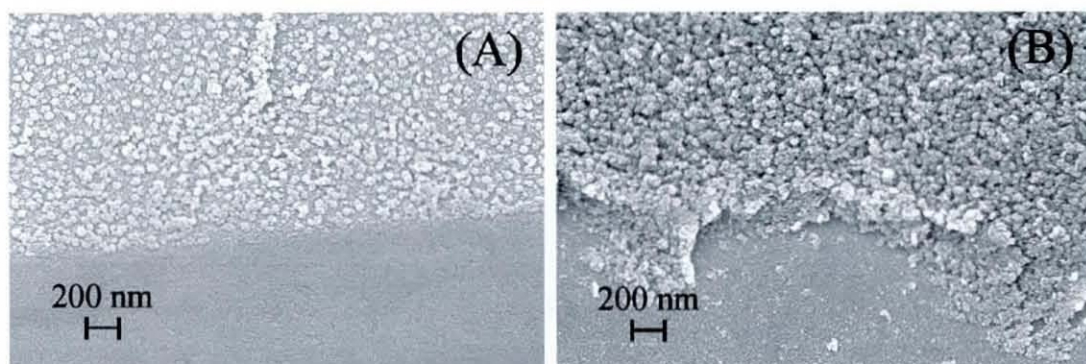
Figure 3.43. FEGSEM images of TiO$_2$ nanoparticle films deposited layer-by-layer with Nafion®
onto the surface of an ITO electrode with (A) a 2 layer TiO$_2$ Nafion® film and (B) a 15 layers TiO$_2$
Nafion® film.

The electron microscopy data again can be supported by experiments with quartz
crystal oscillator measurements conducted in air. Figure 3.44 shows the subsequent
reduction of the resonance frequency of an ITO coated quartz crystal resonator
during the layer-by-layer deposition process. This consisted of alternating 3 wt%
titanium (IV) oxide sol and 0.5 wt% Nafion®. Each TiO$_2$ Nafion® layer is consistent
with a 560 Hz change corresponding to 588 ng. This gives a weight of 443 ng TiO$_2$
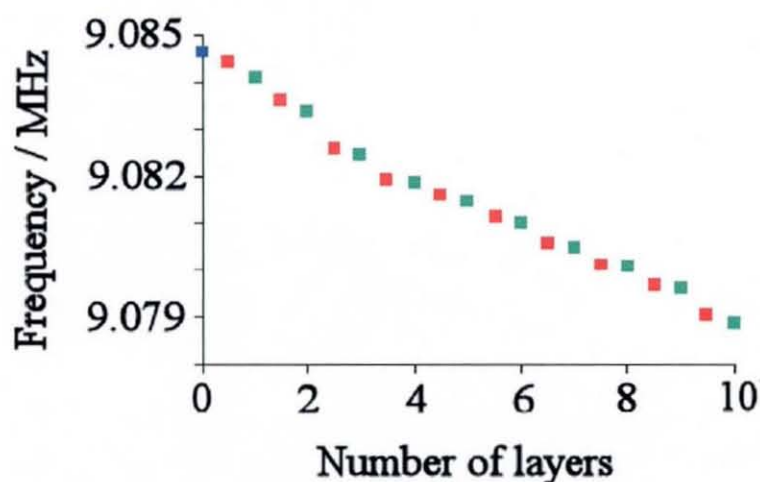and 145 ng Nafion®.

Figure 3.44. A plot of the resonance frequency change for an ITO coated quartz crystal (■) during
layer-by-layer deposition of TiO$_2$ (■) and Nafion® (■).

3.7.3. SAXS-WAXS Characterisation of Mesoporous TiO_2 Nafion® Films

The further characterisation of the TiO_2 Nafion® nanoparticle films was obtained using the simultaneous small-angle X-ray scattering and wide-angle X-ray scattering (SAXS/WAXS) technique. Figure 3.45 shows the intensity of the scattered X-ray diffraction pattern for both TiO_2 Nafion® and pure TiO_2 nanoparticle films. The experimental data can be fitted to a model to determine the structure of the nanoparticle films.
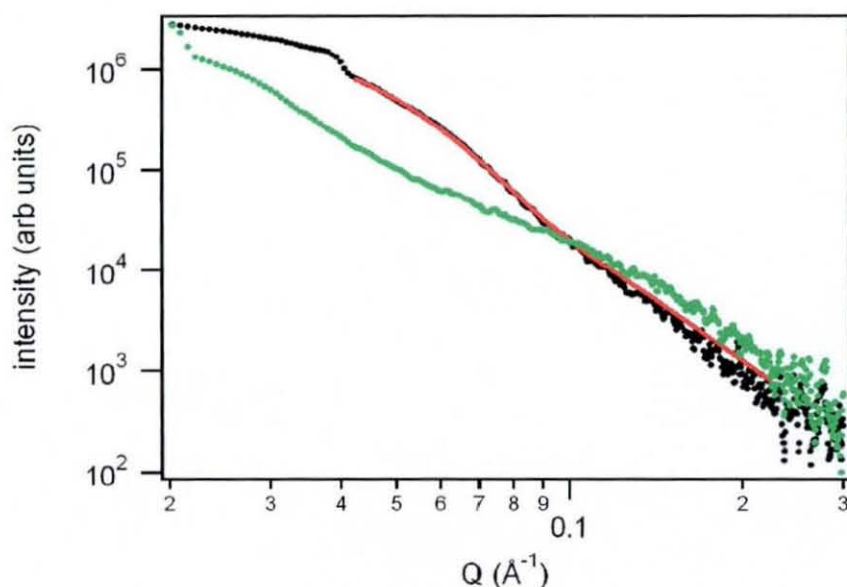

Figure 3.45. Experimental data for (i) TiO_2 film only (black dots), and (ii) TiO_2 Nafion ® (green dots) and theoretical fit for (iii) TiO_2 (red line).

The model is that of isolated polydisperse spheres (polydispersity 0.295) with a mean radius of 39 Å ± 1Å (assuming no interaction between each sphere) and is seen to be a good fit for the TiO_2 film between 0.04 and 0.1 Å^{-1} indicating that there is no colloidal crystallinity. The divergence between the fit and experimental data at greater values of Q suggests possible interaction between spheres. A step in the intensity level is observed in the TiO_2 Nafion® and pure TiO_2 film at 0.04 Å^{-1} and 0.08 Å^{-1} respectively that relates to the size of the particle or aggregate spheres. It is possible to establish that the TiO_2 Nafion® spheres are almost double the size of pure TiO_2 nanoparticles however a more complex structure is present which is not

easily modelled with conventional approaches. From FEGSEM images (see Figure 3.43) a raspberry-type packing or hierarchical clustering seems to occur. The step in intensity level at 0.02 Å^{-1} and 0.04 Å^{-1} in the TiO$_2$ Nafion® and pure TiO$_2$ film respectively, can be attributed to an artefact generated after the subtraction of the background scattering pattern.

3.7.4. Electrochemistry of Mesoporous TiO$_2$ Nafion® Films

The electrochemistry of the TiO$_2$ Nafion® films was investigated in 0.1 M pH 7 phosphate buffer solution over a wide potential window. Figure 3.46 shows the change in voltammetric response over six potential cycles, where the redox response for Ti(IV) becomes more apparent. In chapter 2, the reduction of TiO$_2$ nanoparticles was shown to be accompanied by proton insertion. The ability of Nafion® to transport protons could influence the reduction of TiO$_2$.
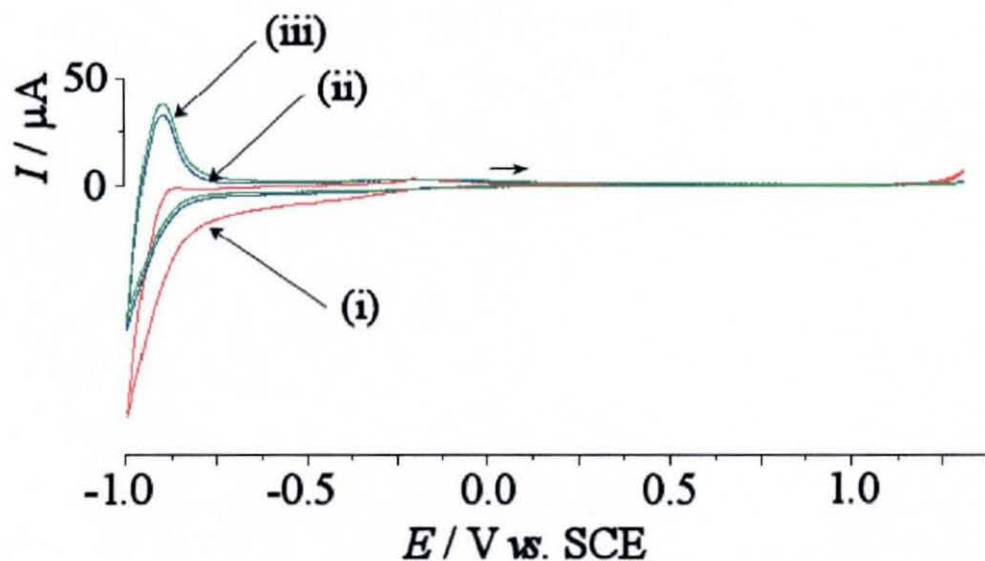

Figure 3.46. Cyclic voltammetry for 10 layers TiO$_2$ Nafion® where (i) scan 1 (ii) scan 2 and (iii) scan 6 in 0.1 M pH 7 phosphate buffer solution. Scan rate 50 mVs^{-1}.

The sixth scan shown above in Figure 3.46iii is typical for what is expected in TiO$_2$ films with and without binder molecules.

3.7.5. Electrochemistry of Mesoporous TiO_2 Nafion® Films with Dopamine

Next the electrochemistry of multi-layer TiO_2 Nafion® films was investigated in the presence of dopamine cations. Dopamine undergoes a two-electron oxidation as shown in equation 3.11.

$$\tag{3.11}$$
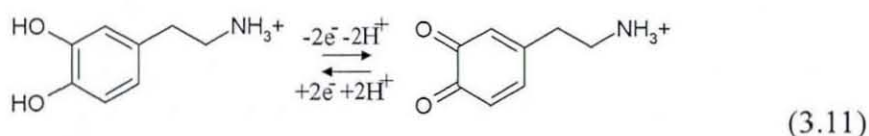
The TiO_2 Nafion® films were dipped into a 2 mM solution of dopamine in 0.1 M pH 7 phosphate buffer for 60 seconds, rinsed with deionised water and then immersed in 0.1 M pH 7 phosphate buffer solution. The resulting cyclic voltammogram is shown in Figure 3.47i.

A similar investigation was carried out using a modified 10 layer TiO_2 Nafion® film. The modification process entailed the calcination of the TiO_2 Nafion® films at $500°C$ to remove the Nafion® particles initially deposited and to bring the remaining TiO_2 particles closer together. The calcined electrode was then soaked in Nafion® solution for three hours to reintroduce a negative surface charge and ion selectivity. This allowed the influence of the film structure on the diffusion of the dopamine through the film to be observed.

The shape of the voltammetry in Figure 3.47 is very different from that expected for a surface-confined species (i.e. symmetrical narrow peaks with a peak separation near to zero). Instead, the peaks are broader and more diffusion-like with a peak separation of 0.7 V (non-calcined film) or 1.1 V (calcined film) at a scan rate of 100 mVs^{-1}. A large peak separation typically indicates a slow heterogeneous electron transfer.[86] The relative size of the oxidation peak to the following reduction peak at 100 mVs^{-1} indicates that either the oxidation product is lost from the TiO_2 Nafion® film during the experiment, or more likely, that the oxidation product polymerises irreversibly.[87] A more symmetrical voltammetric response is observed at faster scan rates, as less time is available for the chemical reaction and polymerisation steps, leaving a greater concentration of dopamine able to be re-reduced.
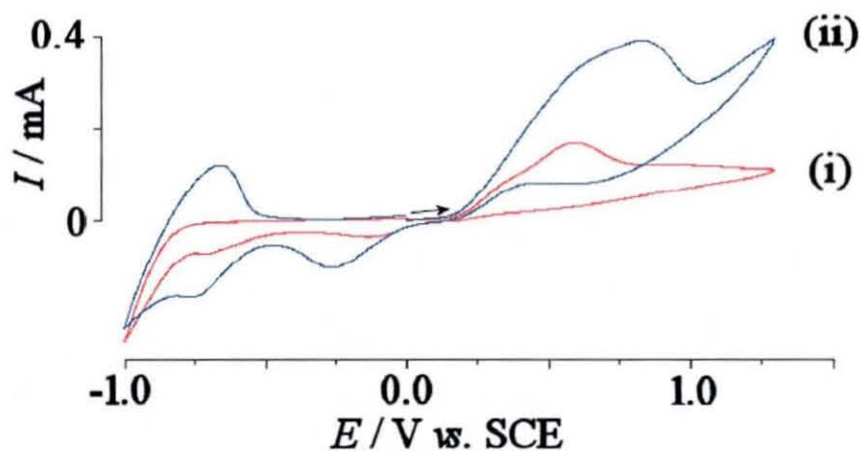
Figure 3.47. Cyclic voltammetry for (i) a 10 layer TiO_2 Nafion® film and (ii) a modified 10 layer TiO_2 Nafion® film, in 0.1 M pH 7 phosphate buffer solution after a 60 second dip in 0.1 M pH 7 phosphate buffer solution + 2 mM dopamine. Scan rate 50 mVs⁻¹. Scan 1 shown in each case.

The electrochemical oxidation of dopamine has been suggested to proceed via an ECC reaction process (shown in Figure 3.48), where the protonated dopamine species (molecule 1) undergoes two consecutive one-electron transfer steps to produce the dopamine ortho-quinone (molecule 2). If molecule 2 loses a proton, two chemical reactions can occur. Figure 3.48c illustrates the intra-molecular cyclisation reaction that generates 5,5-dihydroxyindoline (molecule 3) and Figure 3.48d shows the formation of an aminochrome (molecule 4). Molecule 4 is able to polymerise readily to melanin-like products on the electrode surface (Figure 3.48e), inhibiting the reverse reduction electron transfer reaction of molecule 2 back to molecule 1.[87]

Figure 3.47 indicates that both the calcined and non-calcined electrodes behave in a similar way with the greater amount of Nafion® present in the calcined film giving rise to the larger peak current (I_p) response in Figure 3.47ii.
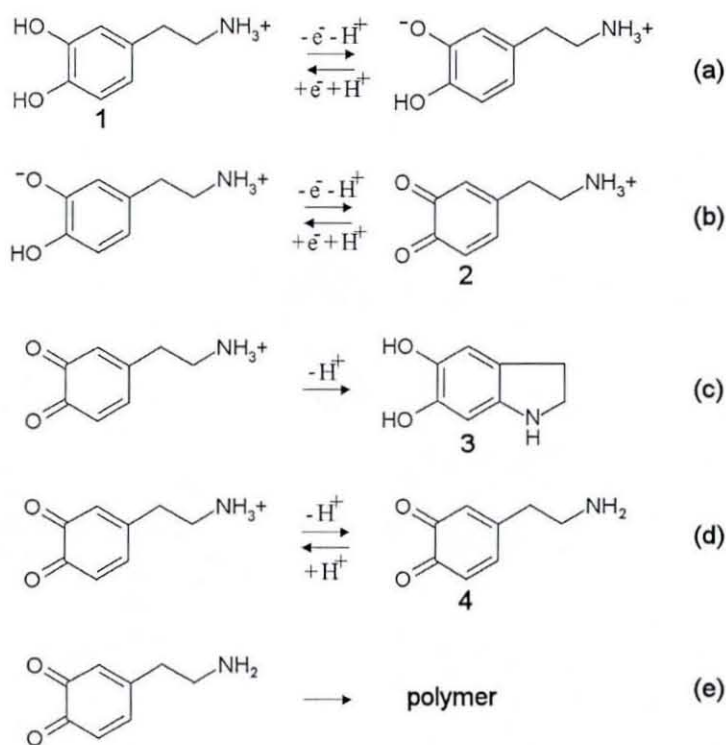
Figure 3.48. The ECC electrochemical process suggested for the oxidation of dopamine.[87]

The number of dopamine ions incorporated into the TiO_2 Nafion® film is dependent on a number of factors. These include the size and charge of the dopamine cation, its concentration in the electrolyte solution, and on the concentration of competing Na^+ ions. The incorporation of dopamine will also depend on the Nafion® film thickness, which will determine the amount of sulfonate groups present and the dopamine diffusion in the film.[88]

The apparent diffusion coefficients for charge transport of dopamine were calculated to determine how fast the dopamine diffuses through the mesoporous TiO_2 Nafion® film. Dopamine only has a low positive charge potentially hindering its transport through the Nafion® film. However this can be overcome due to the hydrophobic nature of dopamine and the affinity of Nafion® for hydrophobic cations.[89]

A 10 layer TiO$_2$ Nafion® film was dipped in 2 mM dopamine in 0.1 M pH 7 phosphate buffer and cycled over a range of potential scan rates (500, 200, 100, 50, 20, 10, 5, 2, and 1 mVs^{-1}) in 0.1 M pH 7 phosphate buffer. The same process was applied to the modified 10 layer TiO$_2$ Nafion® film. By plotting the natural log of the oxidation peak current height against the natural log of the scan rate (v) (Figure 3.49) a transition between a slope of 1 and slope of 0.5 can be calculated (v_{trans}).
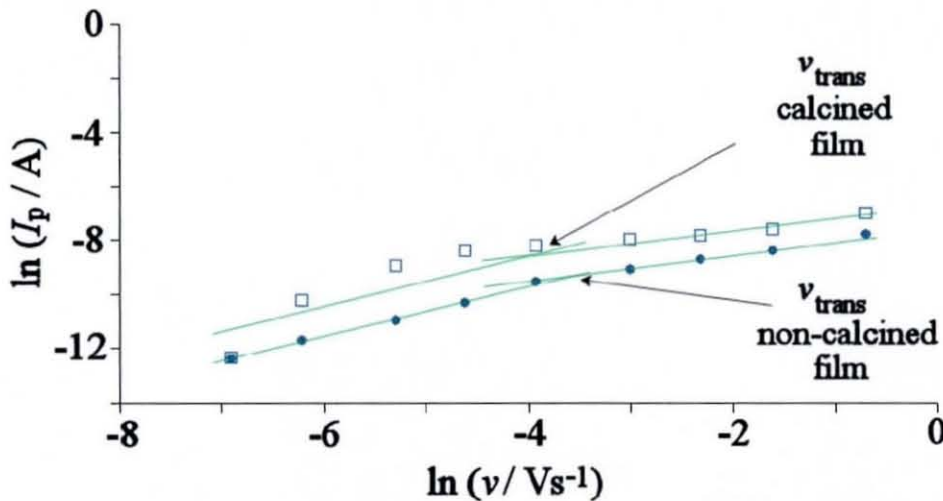
Figure 3.49. A plot of the natural log of the oxidation peak height for the dopamine redox system as a function of the natural log of the scan rate for (i) a 10 layer TiO$_2$ Nafion® film and (ii) a modified 10 layer TiO$_2$ Nafion® film, in 0.1 M pH 7 phosphate buffer solution.

This transition point corresponds to the change from fast scan rates, where I_p is proportional to $\sqrt{v}$ (equation 3.12) to the case of slow scan rates, where I_p is proportional to v (equation 3.13). By combining these two equations, equation 3.14 is obtained for the "transition point" and used to calculate the apparent diffusion coefficient (D_{app}) for both films.

$$I_p = 0.446nFAc\sqrt{\frac{nFvD}{RT}} \tag{3.12}$$

$$I_p = \frac{n^2F^2}{4RT}vVc = \frac{n^2F^2}{4RT}vA\delta c \tag{3.13}$$

$$D_{app} = \frac{nv_{trans}F}{RT}\left(\frac{\delta}{1.784}\right)^2 \tag{3.14}$$

Where I_p is the peak current (A), n is the number of electrons, F is the Faraday constant (96485 Cmol^{-1}), A is the electrode area, c is the concentration of dopamine in the film, v is the scan rate, D is the diffusion coefficient (cm^{2}s^{-1}), R is the gas constant (8.314 JK^{-1}mol^{-1}), T is the temperature (K), and $V = A$ x δ or electrode volume = area x film thickness. The thickness of the 10 layer films is assumed to be 150nm.

Using equation 3.14, D_{app} is estimated as 2.5x10^{-8} cm^{2}s^{-1} for the non-calcined film and 2.0x10^{-8} cm^{2}s^{-1} for the calcined film. The values for the apparent diffusion coefficients are similar to those reported for the oxidation of dopamine at Nafion® coated glassy carbon electrodes[89] where D_{app} = 1.5x10^{-9}cm^{2}s^{-1}. This suggests that D_{app} depends on the diffusion of dopamine in the Nafion® films or (less likely) electrons hopping between dopamine molecules.

3.7.6. Electrochemistry of Mesoporous TiO$_2$ Nafion® Films with Ru(NH$_3$)$_6$$^{3+}$

Next, a similar set of experiments were carried out in the presence of 0.3 mM Ru(NH$_3$)$_6$$^{3+}$ ions which undergo a single electron oxidation as shown in equation 3.15.

$$Ru(NH_3)_6^{3+} + e^- \rightleftharpoons Ru(NH_3)_6^{2+} \tag{3.15}$$
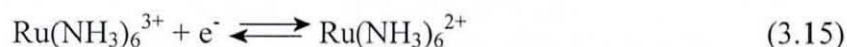
Figure 3.50 shows the voltammetric response for a 10 layer TiO$_2$ Nafion® film after being dipped into a 0.3 mM solution of Ru(NH$_3$)$_6$$^{3+}$ for 60 seconds and then immersed in 0.1 M pH 7 phosphate buffer solution. A modified 10 layer TiO$_2$ Nafion® film (after calcining at 500°C and reintroduction of the Nafion®) was studied in comparison. As seen in section 3.7.5, the modified TiO$_2$ Nafion® film produced a greater voltammetric response as well as a larger background capacitive current.

Figure 3.50. Voltammetry for (i) 10 layers TiO_2 Nafion® and (ii) 10 layers TiO_2 Nafion® calcined at 500°C and soaked in Nafion®, in 0.1 M pH 7 phosphate buffer solution after a 60 second dip in 0.1 M pH 7 phosphate buffer solution + 0.3 mM $Ru(NH_3)_6^{3+}$. Scan rate 50 mVs^{-1}. Scan 1 shown in each case.
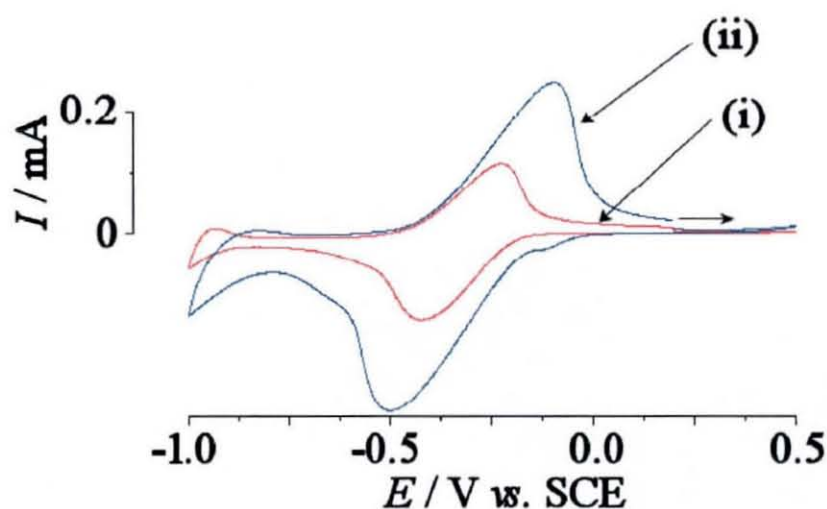
The apparent diffusion coefficient for charge transport of $Ru(NH_3)_6^{3+}$ was calculated as before to determine how fast the cation diffuses through the TiO_2 Nafion® film. Figure 3.51 shows v_{trans} for both electrodes and using equation 3.14, D_{app} was estimated as 2.1 x 10^{-8} cm^{2}s^{-1} and 1.1 x 10^{-8} cm^{2}s^{-1} for the non-calcined film and the calcined film respectively.
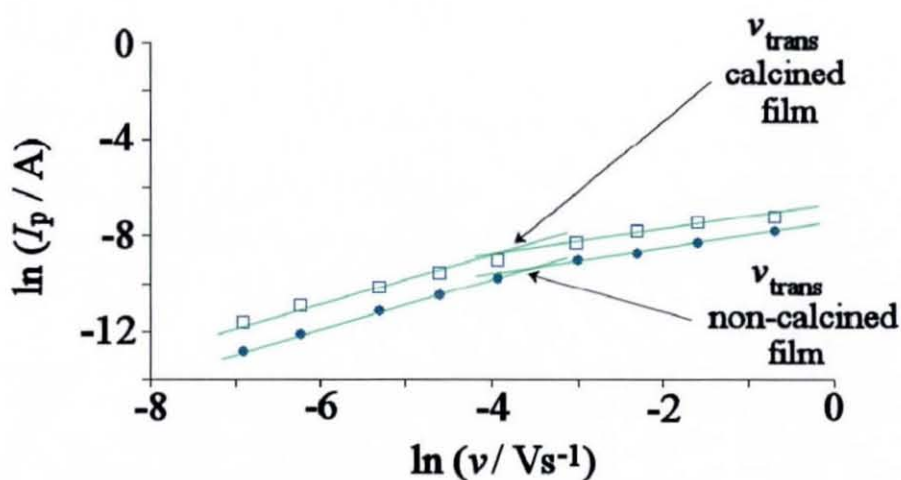

Figure 3.51. A plot of the natural log of the oxidation peak height for the $Ru(NH_3)_6^{3+}$ redox system as a function of the natural log of the scan rate for (i) a 10 layer TiO_2 Nafion® film and (ii) a modified 10 layer TiO_2 Nafion® film, in 0.1 M pH 7 phosphate buffer solution.

The similarity in D_{app} calculated for dopamine and $Ru(NH_3)_6^{3+}$ illustrates that the physical processes involved in diffusion must be the same and due to the presence of Nafion®.

3.8. Conclusions

It has been shown that multi-layer films of TiO_2 nanoparticles (as structure provider and as electrical conduit) are readily formed with a range of binder molecules, with novel multi-layer films containing TiO_2 and TAPA units (as functional part and organic binder) being formed in a layer-by-layer process. The redox reactivity of TAPA with Cu^{2+} in the solution phase has been investigated and it is possible to see that TAPA forms stable complexes with Cu^{2+} ions in solution. However when the TAPA is immobilised on an electrode surface, the electrochemistry changes indicating that the Cu^{2+} complex is forming in a less stable fashion. Binding of Cu^{2+} to phosphonate without incorporation into TAPA is likely.

Novel multi-layer films containing TiO_2 nanoparticles (as structure provider and as electrical conduit) and PQQ units (as functional part and organic binder) were formed in a layer-by-layer process. The influences of film thickness, scan rate, and pH on the electrochemistry of PQQ have been investigated with two possible electron transport processes observed.

Both the film thickness and the solution pH have a considerable effect on the electrochemical response and simplified models for this type of process have been developed for TiO_2 phytate multi-layer films. Impedance spectroscopy has been used to measure the conductivity of multi-layers of TiO_2 films in aqueous solution.

It has been shown that novel multi-layer films containing TiO_2 nanoparticles (as structure provider and as electrical conduit) and cyclodextrin units (as functional part and organic binder) can be formed in a layer-by-layer process. The cyclodextrin remains intact and weak complexation of 1,1'-ferrocenedimethanol is clearly

detected in homogeneous solution at pH 7 and at pH 2 with the associated binding constants, K_{red} = 1300 ± 200 M^{-1} and K_{red} = 1000 ± 200 M^{-1}, respectively. When immobilised onto the surface of TiO$_2$, the carboxymethyl-γ-cyclodextrin retains its binding ability and the Langmuir constant has been shown to be approximately consistent with the homogeneous binding constant. Two distinct types of binding are observed possibly due to geometry or environmental effects. In future this kind of film can be formed with a stronger binding interaction or combined in a multi-layer sensor system based on the electronic effects of binding.

Finally, the ability to form TiO$_2$ nanoparticulate films with Nafion® using a layer-by-layer process has been demonstrated and the apparent transport coefficients for dopamine and Ru(NH$_3$)$_6$$^{3+}$ have been estimated. It has been shown that transport is completely independent of the inert TiO$_2$ host matrix.

3.9. References

[1] K.J. McKenzie, F. Marken, M. Opallo, *Bioelectrochem.* 66 (2005) 41

[2] C.A. Paddon, F. Marken, *Electrochem. Commun.* 6 (2004) 1249

[3] K.J. McKenzie, P.M. King, F. Marken, C.E. Gardner, J.V. Macpherson, *J. Electroanal. Chem.* 579 (2005) 267

[4] D.-H. Yang, M.-J. Ju, A. Maeda, K. Hayashi, K. Toko, S.-W. Lee, T. Kunitake, *Biosens. Bioelectron.* 22 (2006) 388

[5] S.J. Stott, R.J. Mortimer, K.J. McKenzie, F. Marken, *Analyst* 130 (2005) 358

[6] K. Nelson, Y. Deng, *Nanotechnology* 17 (2006) 3219

[7] J.H. Kim, S.H. Kim, S. Shitatori, *Sens. Actuators B* 102 (2004) 241

[8] M. Miyauchi, H. Tokudome, *Thin Solid Films* (2006) Article in press

[9] Y. Miyazaki, S. Shiratori, *Thin Solid Films* 499 (2006) 29

[10] Z.-S. Wang, T. Sasaki, M. Muramatsu, Y. Ebina, T. Tanaka, L. Wng, M. Watanabe, *Chem. Mater.* 15 (2003) 807

[11] B. Ding, J. Kim, E. Kimura, S. Shiratori, *Nanotechnology* 15 (2004) 913

[12] R.-J. Wu, Y.-L. Sun, C.-C. Lin, H.-W. Chen, M. Chavali, *Sens. Actuators B* 115 (2006) 198

[13] R.N. Goyal, M. Oyama, A. Tyagi, S.P. Singh, *Talenta* 72 (2007) 140

[14] K.J. McKenzie, F. Marken, M. Hyde, R.G. Compton, *New J. Chem.* 26 (2002) 625

[15] D.V. Ca, L.Sun, J.A. Cox, *Electrochim. Acta* 51 (2006) 2188

[16] K.J. McKenzie, F. Marken, *Langmuir* 19 (2003) 4327

[17] G. Sandmann, H. Dietz, W. Plieth, *J. Electroanal. Chem.* 491 (2000) 78

[18] Z. Guo, Y. Shen, M. Wang, F. Zhao, S. Dong, A*nal. Chem.* 76 (2004) 184

[19] K.P. Wainwright, *Coord. Chem. Rev.* 166 (1997) 35 and refs. therein

[20] M. Meyer, V. Dahaoui-Gindrey, C. Lecomte, R. Guilard, *Coord. Chem. Rev.* 178-180 (1998) 1313 and refs. therein

[21] I. Lukes, J. Kotek, P. Vojtisek, P. Hermann, *Coord. Chem. Rev.* 216-217 (2001) 287 and refs. therein

[22] P. Caravan, J.J. Ellison, T.J. Mc Murray, R.B. Laufer, *Chem. Rev.* 99 (1999) 2293 and refs. therein

[23] D.E. Reichert, J.S. Lewis, C.J. Anderson, *Coord. Chem. Rev.* 184 (1999) 3 and refs. therein

[24] A.D. Sherry, *J. Alloys Compd.* 249 (1997) 153

[25] A.D. Sherry, J. Ren, J. Huskens, E. Brucher, E. Toth, C.F.C.G. Geraldes, M.M.C.A. Castro, W.P. Cacheris, *Inorg. Chem.* 35 (1996) 4604

[26] M.D. Ward, in I. Rubinstein (ed.), *Physical Electrochemistry*, Marcel Dekker, New York, 1995, p. 293

[27] S. Nakabayashi, D.A. Tryk, A. Fujishima, N. Ohta, *Chemical Physics Letters* 300 (1999) 409

[28] T. Mincey, J.A. Bell, A.S. Mildvan, R.H. Abeles, *Biochemistry* 20 (1981) 7502

[29] C. Anthony, M. Ghosh, *Prog. Biophys. Mol. Biol.* 69 (1998) 1

[30] Y.-J. Zheng, T.C. Bruice, *Proc. Natl. Acad. Sci. USA* 94 (1997) 11881

[31] Y.-J. Zheng, Z.-X. Xia, Z.-W. Chen, F.S. Mathews, T.C. Bruice, *PNAS* 98 No. 2 (2001) 432

[32] A. Oubrie, H.J. Rozeboom, K.H. Kalk, A.J.J. Olsthoorn, J.A. Duine, B.W. Dijkstra, *The EMBO Journal* 18 No. 19 (1999) 5187

[33] K. Matsushita, H. Toyama, M. Yamada, O. Adachi, *Appl. Microbiol. Biotechnol.* 58 (2002) 13

[34] R. Rucker, T. Stites, F. Steinberg, A. Mitchell, *Physiological Importance of PQQ*

from Biological & Molecular Biology of Vitamin B6 & PQQ-dependent Proteins.
Ed. by A. Iriarte, H.M. Kagan & M. Martinez-Carrion (2000) Birkhauser Verlag
Basel/Switzerland

[35] K. He, H. Nukada, T. Urakami, M.P. Murphy, *Biochem. Pharmacol.* 65 (2003) 67

[36] N.P. Khairnar, H.S Misra, S.K. Apte, *Biochem. Biophys. Res. Commun.* 312
(2003) 303

[37] T. Kasahara, T. Kato, *Nature* 422 (2003) 832

[38] T. Inoue, J.R. Kirchhoff, *Anal. Chem.* 74 (2002) 1349

[39] T. Inoue, J.R. Kirchhoff, *Anal. Chem.* 72 (2000) 5755

[40] J. Razumiene, A. Vilkanauskyte, V. Gureviciene, V. Laurinavicius, N.V.
Roznyatovskaya, Y.V. Ageeva, M.D. Reshetova, A.D. Ryabov, *J. Organomet.
Chem.* 668 (2003) 83

[41] M. Yamada, M.D. Elias, K. Matsushita, C.T. Migita, O. Adachi, *Biochim.
Biophys. Acta* 1647 (2003) 185

[42] Y. Ohshiro, S. Itoh, K. Kurokawa, J. Kato, T. Hirao, T. Agawa, *Tetrahedron Lett.*
24 (1983) 3465

[43] E. Katz, T. Lotzbeyer, D.D. Schlereth, W. Schuhmann, H-L. Schmidt, *J.
Electroanal. Chem.* 373 (1994) 189

[44] T.S. Eckert, T.C. Bruice, J.A. Gainor, S.M. Weinreb, *Proc. Natl. Acad. Sci. USA*
79 (1982) 2533

[45] M. Yamashita, C.A. Pessoa, L.T. Kubota, *J. Colloid Interface Sci.* 263 (2003) 99
and refs. therein

[46] Z. Zhang, L.M.V. Tillekeratne, J.R. Kirchhoff, R.A. Hudson, *Biochem. Biophys.
Res. Commun.* 212 (1995) 41

[47] E. Katz, M. Lion-Dagan, I. Willner, *J. Electroanal. Chem.* 408 (1996) 107

[48] A. Curulli, I. Carelli, O. Trischitta, G. Palleschi, *Biosens. Bioelectron.* 12 (1997)
1043

[49] K.J. McKenzie, F. Marken, X. Gao, S.C. Tsang, K.Y. Tam, *Electrochem.
Commun.* 5 (2003) 286

[50] F. Fabregat-Santiago, I. Mora-Sero, G. Garcia-Belmonte, J. Bisquert, *J. Phys.
Chem. B* 107 (2003) 758

[51] G. Boschloo, D. Fitzmaurice, *J. Phys. Chem. B* 103 (1999) 7860

[52] E.M. Martin Del Valle, *Process Biochem.* 39 (2004) 1033

[53] X. Wen, Z. Liu, T. Zhu, M. Zhu, K. Jiang, Q. Huang, *Bioorg. Chem.* 32 (2004) 223

[54] D.J. Cram, J.M. Cram, '*Container Molecules and their Guests*' in J.F. Stoddard (Ed.), *Monographs in Supramolecular Chemistry*, Vol. 4, The Royal Society of Chemistry, Cambridge, 1994.

[55] I. Tabushi, *Acc. Chem. Res.* 15 (1982) 66

[56] R. Breslow, S.D. Dong, *Chem. Rev.* 98 (1998) 1997

[57] A. Ueno, F. Moriwaki, T. Osa, F. Hamada, K. Murai, *Chem. Pharm. Bull.*, 34 (1986) 438

[58] V.V. Strelets, I.A. Mamadjarova, M.N. Nedfedova, N.I. Pysnograeva, V.I. Sokolov, L. Pospisil, J. Hanzlik, *J. Electroanal. Chem.* 310 (1991) 179

[59] T. Komura, T. Yamaguchi, K. Kura, J. Tanabe, *J. Electroanal. Chem.* 523 (2002) 126

[60] A. Harada, *Acc. Chem. Res.* 34 (2001) 456

[61] R. Isnin, C. Salam, A.E. Kaifer, *J. Org. Chem.* 56 (1991) 35

[62] T. Komura, T. Yamaguchi, K. Noda, S. Hayashi, *Electrochim. Acta* 47 (2002) 3315

[63] A.E. Kaifer, M. Gomez- Kaifer, *Supramolecular electrochemistry*, Wiley-VCH, Weinheim, 1991

[64] T. Komura, T. Yamaguchi, K. Kura, J. Tanabe, *J. Electroanal. Chem.* 523 (2002) 126

[65] M. Rudolph, D.P. Reddy, S.W. Feldberg, *Anal. Chem.* 66 (1994) A589

[66] K.J. McKenzie, J. Niedziolka, C.A. Paddon, F. Marken, E. Rozniecka, M. Opallo, *Analyst* 129 (2004) 1181

[67] K.J. Laidler, J.H. Meiser, *Physical Chemistry*, Houghton Mifflin, Boston (1999), p. 906

[68] A. Harada, *Acc. Chem. Res.*, 34 (2001) 456

[69] C. Heitner-Wiguin, *J. Membr. Sci.*, 120 (1996) 1

[70] N.P. Blake, M.K. Peterson, G.A. Voth, H. Metiu, *J. Phys. Chem. B* 109 (2005) 24244

[71] T.A. Zawodzinski Jr., M. Neeman, L.O. Sillerud, S. Gottesfeld, *J. Phys. Chem.* 95 (1991) 6040

[72] R.K. Nagarale, G.S. Gohil, V.K. Shahi, *Adv. Colloid Interface Sci.* 119 (2006) 97

[73] O.J. Murphy, G.D. Hitchens, D.J. Manko, *J. Power Sources* 47 (1994) 353

[74] M. Lopez-Atalaya, G. Codina, J.R. Perez, J.L. Vazquez, A. Aldaz, *J. Power Sources* 39 (1992) 147

[75] P.-G. Su, Y.-L. Sun, C.-C. Lin, *Sens. Actuators B.* 115 (2006) 338

[76] T. Matsumoto, S. Saito, S. Ikeda, *J. Biotechnol.* 122 (2006) 267

[77] B. Adhikari, S. Majumdar, *Prog. Polym. Sci.* 29 (2004) 699

[78] G.O. Olah, D. Meidar, R. Malhotra, J.A. Olah, S.C. Narang, *J. Catal.* 61 (1980) 96

[79] G. Gelbard, *Ind Eng. Chem Res.,* 44 (2005) 8468

[80] I. Rubinstein, A.J. Bard, *J. Am. Chem. Soc.* 102 (1980) 6642

[81] R.J. Mortimer, *J. Electroanal. Chem.* 397 (1995) 79

[82] Y. Wang, C. Li, S. Hu, *J. Solid State Electrochem.* 10 (2006) 383

[83] R. Dabestani, X. Wang, A.J. Bard, A. Campion, M.A. Fox, S.E. Webber, J.M. White, *J. Phys. Chem.* 90 (1986) 2739

[84] E.A. Lund, E. Blatt, D.N. Furlong, A.W.-H. Mau, W.H.F. Sasse, *Aust. J. Chem.* 42 (1989) 1367

[85] S. Yuan, W. Chen, S. Hu, *Mater. Sci. Eng. C* 25 (2005) 479

[86] I. Rubinstein, A.J. Bard, *J. Am. Chem. Soc.* 103 (1981) 5007

[87] X-L. Wen, Y-H. Jia, Z-L. Liu, *Talanta* 50 (1999) 1027 & refs. therein

[88] L.S.Rocha, H.M. Carapuca, *Bioelectrochemistry* 69 (2006) 258

[89] M.N. Szentirmay, C.R. Martin, *Anal. Chem.* 56 (1984) 1898

Chapter 4

Electrochemical Processes at Biphasic Electrodes Immobilised in Mesoporous Nanoparticle Films

4.1. Introduction

Biphasic electrochemical processes are of interest in a wide number of areas such as ion partitioning and sensing, biological membrane processes, and phase transfer catalysis.[1] This means that the development of novel biphasic electrode systems is important. Biphasic electrodes consist of an organic (or oil) phase in contact with an aqueous electrolyte phase and in simultaneous contact with the electrode surface. The benefits of electrodes based on single droplets[2,3] or arrays of microdroplets[4] of water-insoluble liquids have been the subject of recent reports. The electrochemical polarisation of arrays comprised of microdroplet phases containing a femtolitre volume of redox active material has been described.[5] Benefits demonstrated include (i) the elimination for the need of a supporting electrolyte intentionally added to the organic phase, (ii) no electrolyte limitation to the potential for ion transfer reactions, and (iii) very small electrode or droplet size.[6]

Initial studies on microdroplet redox systems based on tetraalkylphenylenediamines were reported in 1997.[7] The electrochemical properties of a wider range of systems have been investigated in subsequent years.[8]

Applications for the microdroplet systems include electroanalysis,[9] electrocatalysis,[10] and photoelectrochemical processes in microenvironments.[11] The detection of liquid | liquid ion transfer processes at the triple phase boundary (electrode | oil | aqueous electrolyte) has attracted attention for the determination of Gibbs free energies[12] with applications especially in pharmaceutical research.[13,14] Microdroplet redox systems have been investigated on a range of electrode materials including the immobilisation of electrochemically active liquids within

hydrophobic silicate-carbon matrices[15,16,17,18,19] and in hydrophobic silicate thin films.[20] This indicates that porous host materials are suitable substrates for the study of biphasic electrochemical processes.

In order to study biphasic electrode systems, different types of experiments may be envisaged. A microdroplet system could be formed on a flat electrode (see Figure 4.1A), e.g. made of basal plane pyrolytic graphite. Alternatively, the organic phase can be deposited onto a thin mesoporous film of metal oxide particles (see Figure 4.1B). Finally, the metal oxide host structure can be coated with a metal (e.g. by gold sputter coating) and the resulting electrode might offer an even more extended triple phase boundary (see Figure 4.1C). All three types of experiments are described and compared here.
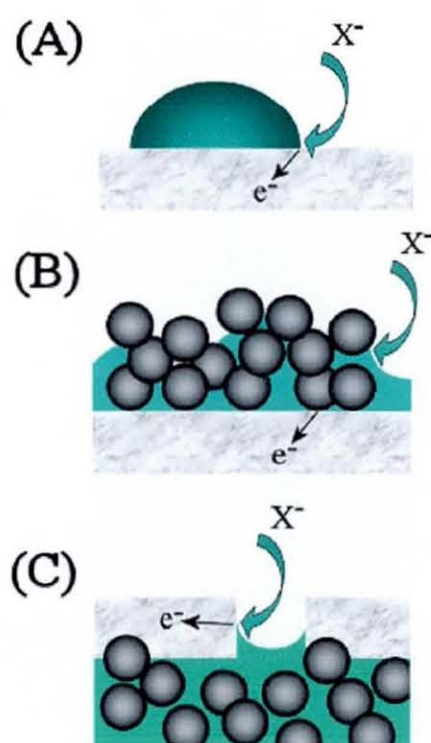

Figure 4.1. A schematic representing the triple interface on (A) a bppg electrode surface (B) a thin metal oxide film on an ITO surface and (C) a thin metal oxide film on an ITO surface with a 20 nm sputter coated layer of gold.

The aim of the novel electrode designs in Figure 4.1B and C, was to allow the deposition of the organic phase onto an electrode with a more defined surface structure and porosity (i.e. removal of the random crevices and microdroplet array seen in bppg). A further potential benefit of the metal oxide mesoporous film electrodes is the improvement in the extent of the triple interface, and consequently an increase in the current response observed.

4.2. Experimental

4.2.1. Chemicals

Demineralised and filtered water was taken from an Elga water purification system (Elga, High Wycombe, Bucks, UK) with a resistivity of not less than 18 MΩ cm. Titanium (IV) oxide sol (anatase, *ca.* 6 nm diameter, 30-35% in aqueous HNO_3, pH 0-3, TKS-202) was obtained from Tayca Corp., Osaka, Japan and diluted with deionised water. *N,N*-Didodecyl-*NN'* – diethyl-benzene-1,4-diamine (DDPD) was prepared by Colin Hayman following a literature method.[21] Di-(2-ethyl-hexyl)phosphate (HDOP), anhydrous acetonitrile, $NaClO_4$, NaOH, H_3PO_4, $HClO_4$, KOH, K_2HPO_4, and KH_2PO_4 were obtained commercially in analytical or the highest purity grade available.

4.2.2. Instrumentation

Voltammetric measurements were performed with a computer controlled Eco Chemie PGSTAT20 Autolab potentiostat system. Experiments were conducted in staircase voltammetry mode with a platinum gauze counter electrode and saturated calomel reference electrode (SCE (saturated KCl), REF401, Radiometer). The working electrode was either a carbon working electrode made from a 4.9 mm diameter basal plane pyrolytic graphite disc (Le Carbon, UK) or a tin-doped indium oxide (ITO) coated glass (10 mm × 60 mm, resistivity 20 Ω per square) with approximately 8% tin, obtained from Image Optics Components Ltd. (Basildon,

Essex). The ITO electrode surface was modified with a porous metal oxide film giving a geometric working electrode area of 1 cm^2.

Prior to conducting electrochemical experiments, all solutions were purged with argon (BOC, UK). All experiments were carried out at a temperature of $22 \pm 2^{\circ}C$. An Elite tube furnace system was employed for cleaning ITO electrode surfaces (at $500^{\circ}C$ in air) and for calcining metal oxide binder films (at $500^{\circ}C$ in air) prior to gold coating in a Polaron sputter coating unit.

Scanning electron microscopy images were obtained with a Leo 1530 Field Emission Gun Scanning Electron Microscope (FEGSEM) system. Prior to FEGSEM imaging, the sample surface was scratched with a scalpel blade.

4.2.3. Deposition and Electrode Preparation Procedures

The DDPD and HDOP liquids were deposited onto three types of working electrode surface by evaporation from an acetonitrile solution using a micropipette. The majority of experimental work was carried out using a 4.9 mm diameter basal plane pyrolytic graphite electrode. The graphite electrode surface was renewed by polishing on a fine (P1000) grade carborundum paper. Two further types of working electrode were fabricated using the layer-by-layer deposition technique described in section 3.2.3, where mesoporous films of TiO_2 phytate were deposited on ITO coated glass electrodes. After the deposition of 15 layers, the TiO_2 phytate films were dried (in air, at room temperature) and calcined (for 60 minutes) to remove the organic phytate material. The second working electrode substrate consisted of this calcined porous TiO_2 film, whereas the third working electrode investigated consisted of the calcined porous TiO_2 film plus a sputter coated 20 nm thick porous gold layer on top of the TiO_2 film surface.

4.3. The Oxidation of *N,N*-Didodecyl-*N′,N′* – diethyl-benzene-1,4-diamine (DDPD) Deposited as Microdroplets onto Basal Plane Pyrolytic Graphite Electrodes

N,N-didodecyl-*N′,N′*-diethylphenylenediamine (DDPD) is a highly water insoluble organic substance. It is this hydrophobicity that allows the study of the oxidation of the phenylenediamine derivative coupled to ion transfer from the aqueous phase into the organic phase. The DDPD liquid was deposited onto a basal plane pyrolytic graphite (bppg) electrode by evaporation of an acetonitrile solution. This resulted in the formation of a random array of microdroplets of the organic phase on the electrode surface, with the triple interface shown in Figure 4.1A. Figure 4.2 shows a typical FEGSEM image of a bppg electrode surface. It is possible to explain the tendency of the droplet deposits to form microdroplet arrays and to penetrate into the crevices and imperfections of the electrode surface.[8]
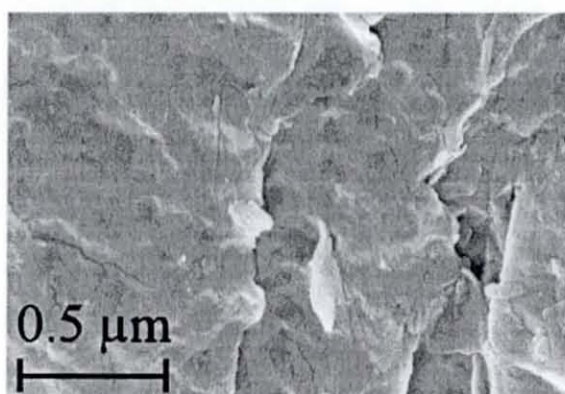

0.5 µm

Figure 4.2. FEGSEM images for a basal plane pyrolytic graphite electrode.

When the DDPD microdroplet array is immersed into aqueous 0.1 M NaClO$_4$ it is possible to observe the electrochemical oxidation coupled to the transfer of ClO$_4^-$ using cyclic voltammetry. The voltammograms produced (see Figure 4.3) have a characteristic sharp and well defined peak with a midpoint potential (E_{mid}) of 0.12 V *vs.* SCE, that is consistent with previous investigations using tetraoctlyphenylenediamines.[21] The process is chemically highly reversible and

changing the scan rate produces an approximately linear increase in peak current indicative of the absence of diffusion control.
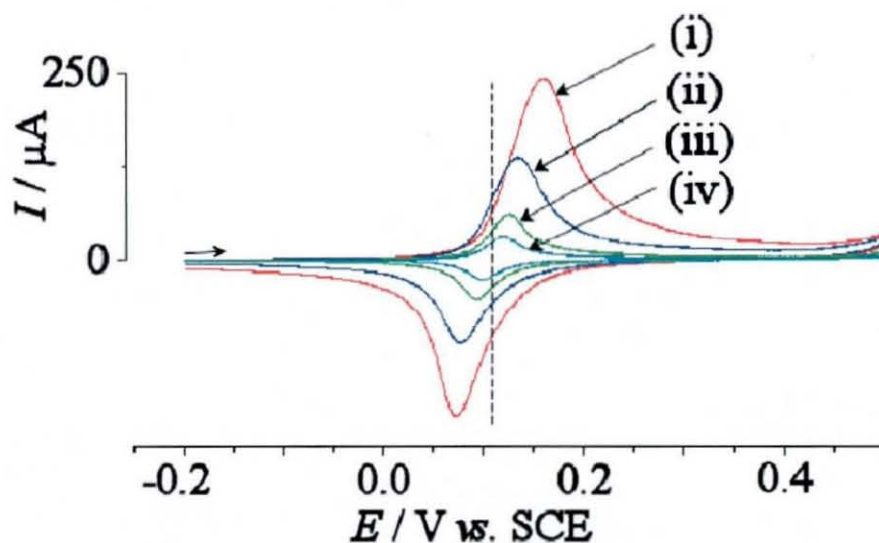

Figure 4.3. Cyclic voltammograms obtained for the oxidation and re-reduction of microdroplets of 1.3 µg DDPD (2.6 nmol) on a 4.9 mm diameter basal plane pyrolytic graphite electrode, scan rates (i) 100, (ii) 50, (iii) 20, and (iv) 10 mVs⁻¹ in 0.1 M NaClO₄.

A proposed equation for the overall electrochemical reaction coupled to ion transfer process is given below, process I. The product formed after completion of the oxidation process can be thought of as an ionic liquid.[6]

$$\text{Process I}\qquad DDPD_{(oil)} + ClO_{4\ (aq)}^{-} \;\rightarrow\; [DDPD^{+}ClO_{4}^{-}]_{(oil)} + e^{-} \qquad (4.1)$$
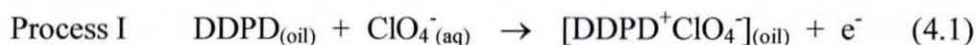
For a deposit of 1.3 µg (2.6 nmol) of DDPD a charge under the oxidation peak of *ca.* 180 µC can be detected. This suggests a *ca.* 70% conversion of the deposit. The efficiency of the process tends to improve at lower scan rates and with low amounts of deposit. However, complete conversion is observed rarely, presumably due to material trapped in crevices at the electrode surface.

Figure 4.4 illustrates the increase in peak current with increasing volumes of DDPD deposited on the graphite electrode where each 10 µl deposit contains 1.3 µg

DDPD. However, a saturation point is reached at approximately 60 μl DDPD (7.8 μg, 15.6 nmol) and any further increase in volume results in a lower peak current. For example, the voltammetry for a 70 μl deposit of DDPD resembles that for a 50 μl deposit of DDPD (not shown). This indicates that with larger volumes of DDPD deposit, the microdroplet array is disrupted reducing the available electroactive surface area at the liquid | liquid interface.
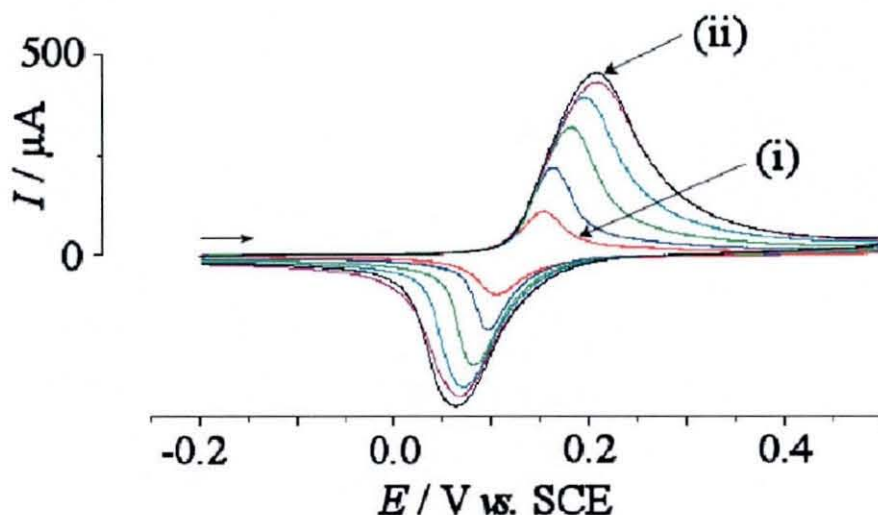

Figure 4.4. Figure to show the voltammetric response of the oxidation and re-reduction of increasing amounts of DDPD deposits, from (i) 10 μl to (ii) 60 μl in 10 μl aliquots on 4.9 mm diameter bppg electrode in 0.1 M NaClO$_4$. Scan rate 100 mVs^{-1}.

4.4. The Oxidation of DDPD within Microdroplets of Dioctylphosphoric Acid (HDOP) Deposited as Microdroplets onto Basal Plane Pyrolytic Graphite Electrodes

In previous investigations it has been observed that the derivatives of phenylenediamines can be easily protonated in the presence of hydrophobic anions.[22] A change from anion transfer (process I) to proton transfer occurred as a function of the anion hydrophobicity and pH. Here it is shown that the limiting case of a water insoluble acid can be chosen to switch the anion transfer entirely to proton transfer over a range of pH. This was achieved by depositing the virtually

water insoluble liquid di-(2-ethyl-hexyl)phosphate (HDOP) from acetonitrile onto the DDPD microdroplets on the bppg electrode surface. HDOP can be thought of as a extremely hydrophobic acid and the interaction of this acid with the DDPD base produces an unusual liquid acid-base complex in the organic phase (see Figure 4.5).
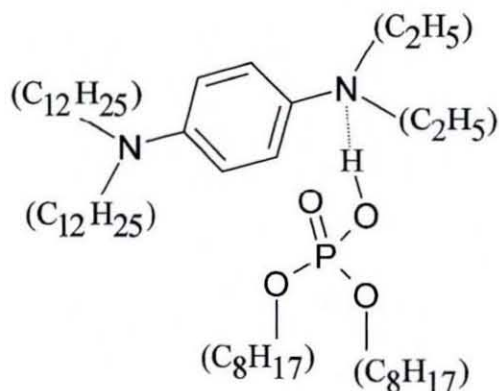

Figure 4.5. Structure of the acid-base complex formed between HDOP and DDPD.

By immersing the deposits of the acid-base complex deposited onto a bppg electrode into an aqueous 0.1 M solution of $NaClO_4$ and applying a potential, a new voltammetric response is observed. The new oxidation process is seen at a more positive potential with an E_{mid} of 0.34 V *vs.* SCE (see Figure 4.6B).
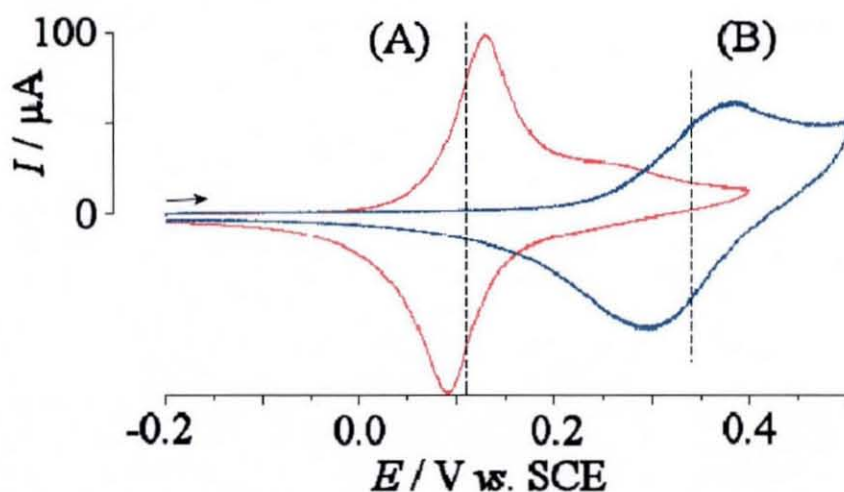

Figure 4.6. The cyclic voltammograms (scan rate 100 mVs^{-1}) for the oxidation and re-reduction of microdroplets of (A) 1.3 µg DDPD (2.6 nmol) and (B) 1.3 µg DDPD plus 4.3 µg HDOP (13 nmol) on a 4.9 mm diameter bppg electrode in aqueous 0.1 M $NaClO_4$.

In the presence of HDOP, process I is not seen even though it would occur at a more negative potential to the new process observed. It is possible to identify the new process based on the voltammetric data as a one-electron oxidation of the HDOP-DDPD complex. This is accompanied by the expulsion of a proton from the organic phase to the un-buffered aqueous phase (see below).

Process II: $[HDOP\text{-}DDPD]_{(oil)}$ $\rightarrow$ $[DPO^-\text{-}DDPD^+] + H^+_{(aq)} + e^-$ (4.2)

For a 1:1 acid to base ratio deposit, process I is reduced and process II is dominating. The absence of the response for process I in the presence of HDOP supports the acid-base complex formation theory. However, during repeated cycling of the potential, the depletion of the Process II signal is observed along with the re-emergence of the Process I signal (see Figure 4.7). This could be caused by the depletion of HDOP at the liquid | liquid interface by loss or slow hydrolysis.
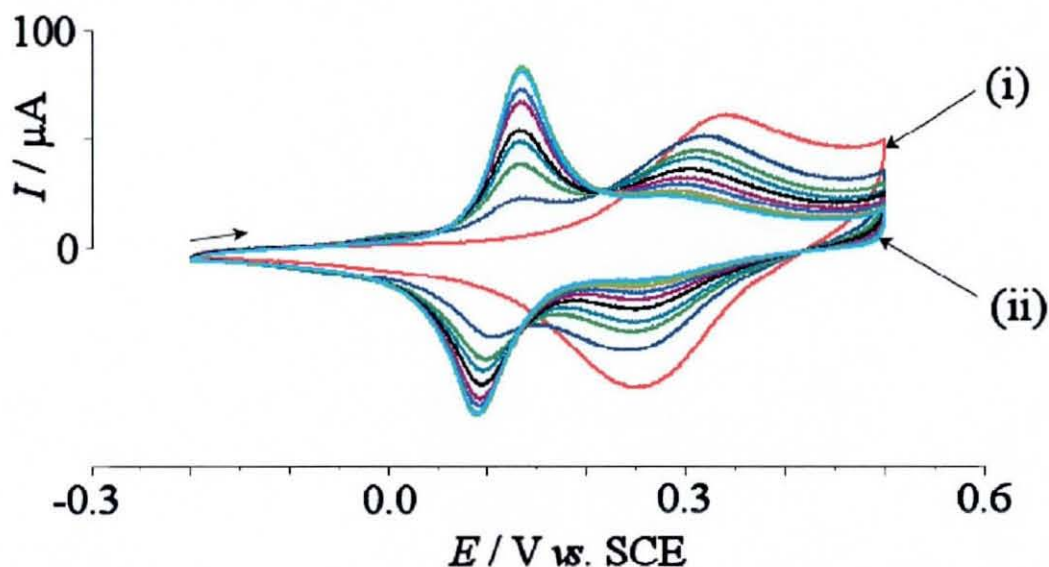

Figure 4.7. The cyclic voltammograms (scan rate 100 mVs^{-1}) for the repeated cycling of the oxidation and re-reduction of microdroplets of a 1:1 acid to base mole ratio deposit on a 4.9 mm diameter bppg electrode in aqueous 0.1 M NaClO$_4$ where (i) scan 1 (red line) and (ii) scan 15 (very light blue line).

Experiments using a higher acid: base ratio determined that there was no significant change in the electrochemical process on increasing the amount of HDOP deposited. However a systematic shift in the voltammetric response to more positive potentials was observed (see Figure 4.8).
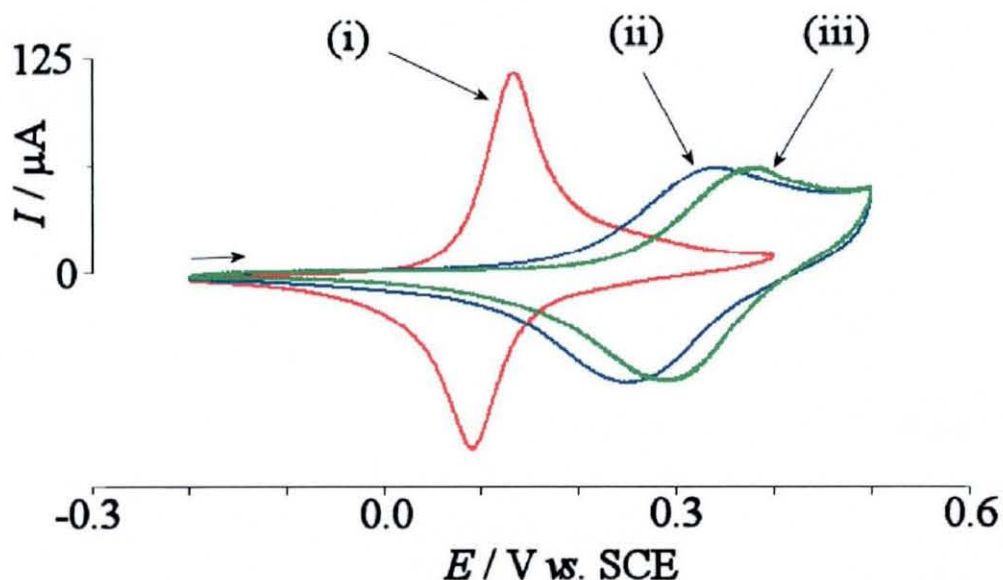

Figure 4.8. The cyclic voltammograms (scan rate 100 mVs^{-1}) for oxidation and re-reduction of microdroplets of various DDPD:HDOP mole ratios deposited on a 4.9 mm diameter bppg electrode in aqueous 0.1 M NaClO$_4$ for (i) 1:0, (ii) 1:1 and (iii) 1:5.

Next, experiments were carried out in aqueous buffer solutions. Figure 4.9 shows a typical voltammogram for the oxidation of microdroplets of DDPD deposited onto a bppg electrode surface and immersed in 0.1 M pH 7 phosphate buffer solution. It is possible to observe the electro-insertion reaction for phosphate (Process III) at E_{mid} = 0.35 V *vs.* SCE.
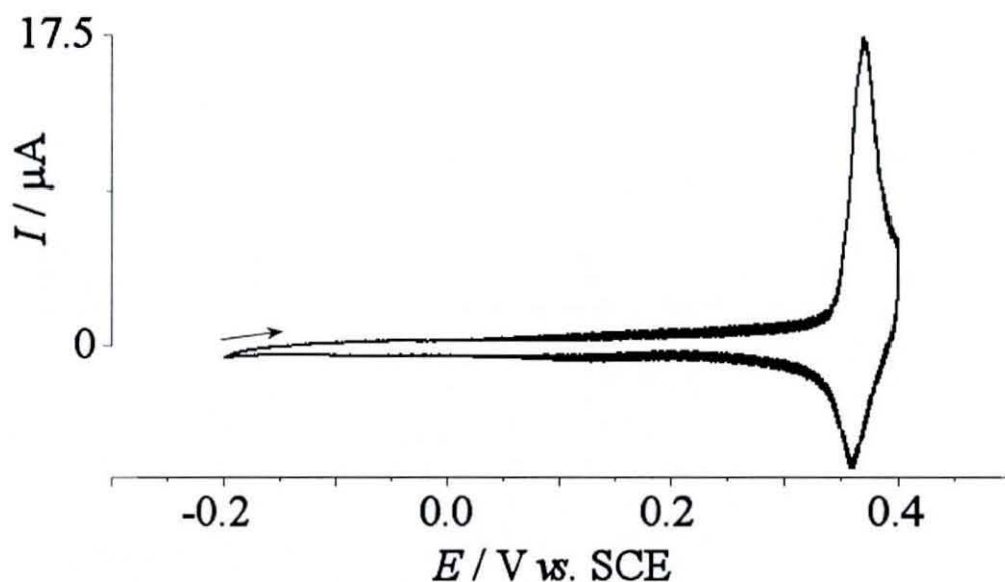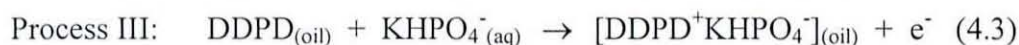
Figure 4.9. Cyclic voltammograms (scan rate 10 mVs^{-1}) obtained for the oxidation and re-reduction of microdroplets of 1.3 μg DDPD (2.6 nmol) deposited onto a 4.9 mm diameter bppg immersed in 0.1 M pH 7 phosphate buffer.

This process is more complex than the DDPD in NaClO$_4$ and it is only cautiously[23] believed to be associated with the co-insertion of potassium (see Process III).

Process III: DDPD$_{(oil)}$ + KHPO$_4^-$$_{(aq)}$ → [DDPD$^+$KHPO$_4^-$]$_{(oil)}$ + e$^-$ (4.3)

In the presence of HDOP, the voltammetric characteristics observed change dramatically. Figure 4.10 shows the voltammograms obtained for DDPD to HDOP mass ratios of 1:0, 1:3, and 1:12. The response for process II is again seen, and a small shift in E_{mid} to more negative values is observed with increasing amounts of HDOP. The trend is consistent with that predicted based on the appropriate Nernst equation derived for Process II (equation 4.4).

$$E = E^{0'} + \frac{RT}{F} \ln \frac{[DPO^- \, DDPD^+](oil)}{[HDOP \, DDPD](oil)} - 2.3 \frac{RT}{F} pH \qquad (4.4)$$

Where R denotes the gas constant, T the absolute temperature, F the Faraday constant, and the reversible half-cell potential is related to activities in both the aqueous and the organic phase.
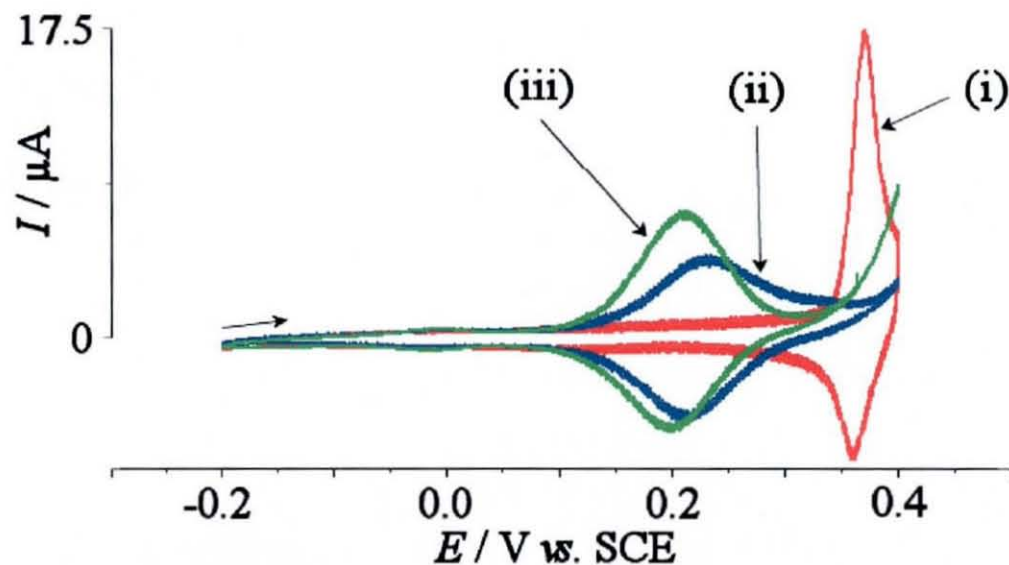

Figure 4.10. Cyclic voltammograms (scan rate 10 mVs^{-1}) obtained for the oxidation and re-reduction of microdroplets of 1.3 μg DDPD (2.6 nmol) with (i) 0 μg HDOP (0 nmol), (ii) 3.9 μg HDOP (10.4 nmol), and (iii) 15.6 μg HDOP (46.8 nmol) deposited onto a 4.9 mm diameter bppg immersed in 0.1 M pH 7 phosphate buffer.

The addition of a 1:1 DDPD:HDOP deposit results in an incomplete complexation process and both Process II and Process III redox responses are observed. The addition of further HDOP to the electrode surface (1:3 DDPD:HDOP mass ratio) results in the observation of Process II only. The charge under the voltammetric oxidation response increases with the addition of more HDOP up to a mass ratio of 1:12 DDPD:HDOP. However, the addition of further amounts of HDOP results in the decrease in charge under both the oxidation and reduction voltammetric peaks. This could be explained by the addition of further HDOP increasing the droplet size, decreasing the concentration of DDPD and consequently resulting in reduced currents and reactant conversion. The features of the voltammograms produced suggest that the addition of HDOP up to a critical amount of approximately 15.6 μg HDOP improves mass transport via diffusion in the organic phase.

Integration of the current under the oxidation peak in Figure 4.10iii gives a total charge of *ca.* 70 μC. This result is consistent with a one-electron electrolysis of *ca.* 30% of the 2.6 nmol DDPD present at the electrode surface (process II).

Next, the effect of the proton activity on the voltammetric response was examined. Figure 4.11 shows typical voltammetric responses obtained for the oxidation of microdroplets containing a 1:16 mixture of DDPD to HDOP (by mass) deposited onto a bppg electrode and immersed in aqueous phosphate buffer solution.
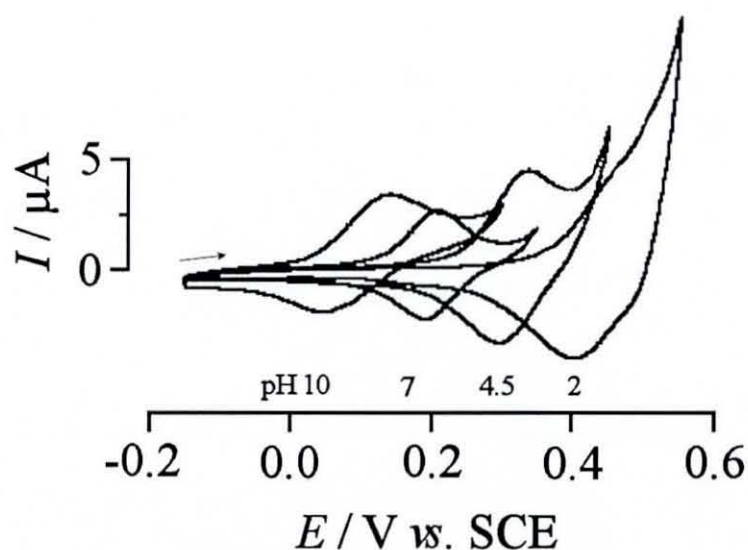

Figure 4.11. The oxidation and re-reduction of microdroplets of 1:16 DDPD to HDOP deposited onto 4.9 mm diameter bppg electrode immersed in aqueous 0.1 M phosphate buffer at various proton activities.

The midpoint potential for the voltammogram is systematically shifted to more positive potentials with increasing proton activity (see Figure 4.11). By changing the pH of the phosphate buffer solution causes a clear shift in midpoint potential of 41 ± 6 mV per pH unit. The exact cause of the sub-Nernstian behaviour remains open, however the sub-Nernstian shift in response is consistent with that reported for DDPD: HDOP deposits on gold electrodes[24] and has been tentatively attributed to the weak coupling of the proton activities in the aqueous and organic phases. If the proton activities in the organic droplets and in the aqueous electrolyte solution were independent, all the protons from inside the droplets would be expected to

move into the aqueous phase during the electrochemical process, and the shift in midpoint potential would have been 59 mV. Conversely, if the proton concentration did not change during the reaction process, no shift in midpoint potential would be observed. Coupling of the proton concentrations inside and outside of the droplets could occur if the surfaces of the droplets become charged during the electrochemical process. In this situation, a part of the protons will not participate in the phase transfer process resulting in the sub-Nernstian shift in the response for Process II. The size of the organic droplet deposits may influence the shift in midpoint potential, where smaller droplets cause a greater degree of surface charging, decreasing the shift in potential.

4.5. The Oxidation of DDPD Deposited as a Liquid Film into Mesoporous TiO_2

In order to improve the experimental design of the biphasic electrodes and to go away from random arrays of microdroplets on graphite, new mesoporous oxide based structures were investigated. The films are composed of TiO_2 nanoparticles of *ca.* 6 nm diameter which are deposited as a 300-400 nm film on ITO glass electrodes as described in the experimental section. The purpose of the TiO_2 nanoparticles was to stabilise the liquid | liquid interface and acid-base complex deposited, and facilitate electron conduction by behaving as interfacial conduits for electrons. The ITO electrode substrate provides a stable, conducting material that is electrochemically inert in the potential window of interest that readily binds to the metal oxide nanoparticles. Figure 4.12 shows a FEGSEM image of a typical calcined TiO_2 film deposit after scratching the surface of the film with a clean scalpel.
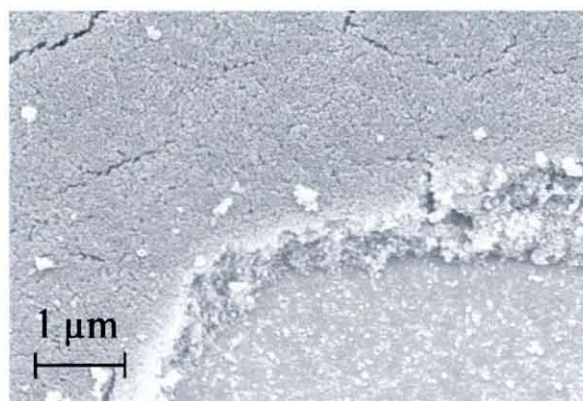
Figure 4.12. FEGSEM image for TiO$_2$ film (300-400 nm thickness) on an ITO electrode.

A DDPD deposit on a clean ITO electrode immersed in aqueous 0.1 M NaClO$_4$, shows no clear voltammetric response associated with Process I. It is possible that the lack of redox response may be due to the bare ITO substrate being insufficiently conducting to effectively catalyse the simultaneous electron transfer and ion transfer process. Alternatively, the DDPD deposit may be unstable on the bare ITO electrode surface and therefore dissociates in the bulk electrolyte solution on immersion in aqueous solution.
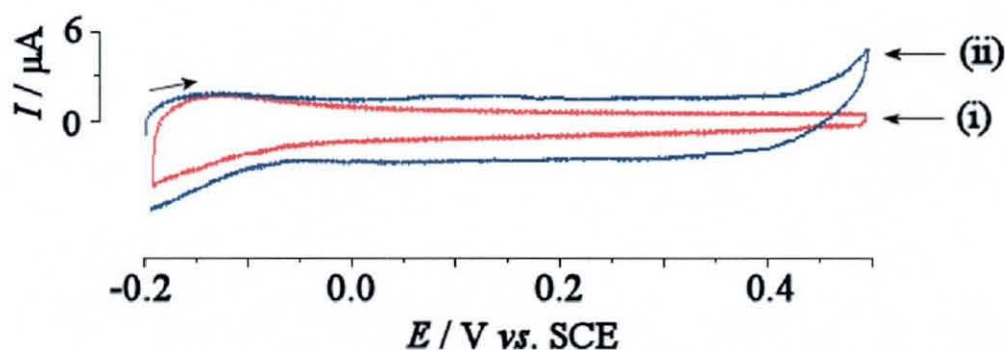

Figure 4.13. Cyclic voltammograms obtained for (i) a blank ITO, and (ii) the oxidation and re-reduction of microdroplets of 1.3 μg DDPD (2.6 nmol) on a blank ITO (scan rates 100 mVs^{-1}) immersed in 0.1 M NaClO$_4$.

In contrast, using a similar deposit of DDPD on a mesoporous TiO$_2$ film electrode immersed in aqueous 0.1 M NaClO$_4$, it is possible to clearly see both the oxidation

and the re-reduction of DDPD (Process I). In Figure 4.14 the oxidation of 1.3 µg DDPD (2.6 nmol) deposited onto a 10 mm^2 TiO$_2$ coated electrode is shown at various scan rates. Changing the scan rate causes an approximately linear increase in the peak current expected for a surface confined process.
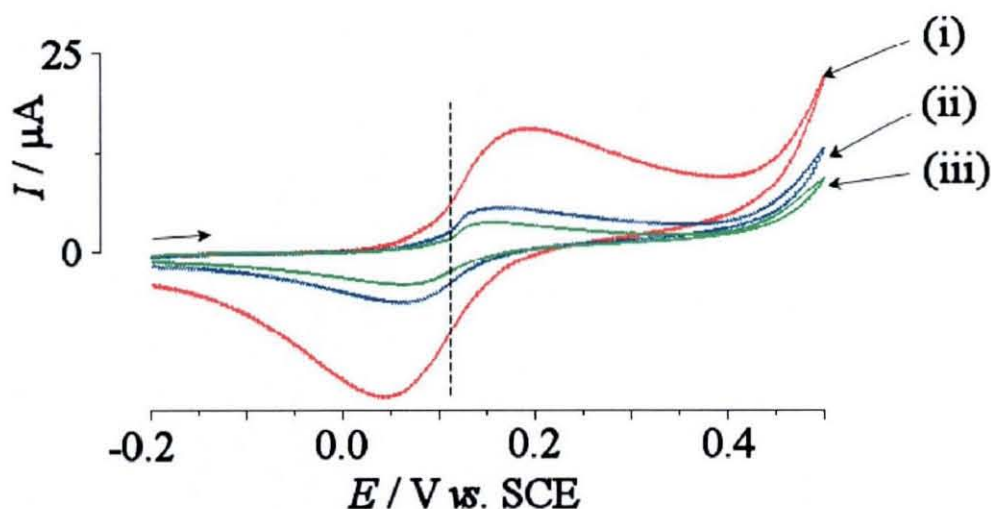

Figure 4.14. Cyclic voltammograms obtained for the oxidation and re-reduction of microdroplets of 1.3 µg DDPD (2.6 nmol) on a 15 layer TiO$_2$ film on ITO (scan rates (i) 50, (ii) 20, and (iii) 10 mVs^{-1}) immersed in 0.1 M NaClO$_4$.

Integration of the area under the oxidation peak at 50 mVs^{-1} gives a charge of *ca.* 50 µC that corresponds to a conversion of *ca.* 20%. This is low when compared to the result seen on the graphite electrode, signifying a lower, less efficient site of reaction (triple phase boundary). Also there is a much greater peak-to-peak separation produced that increases with scan rate, indicating there is a slow kinetic step in the oxidation and re-reduction of DDPD on the TiO$_2$ film electrodes. However, the mesoporous TiO$_2$ based electrode is clearly working and suitable for biphasic processes. A way of improving the efficiency may be found by optimising the film thickness and composition. TiO$_2$ is known to be electrically conducting to a small degree[25,26] and therefore a possible electrode process could involve electron transfer between the TiO$_2$ nanoparticles and the liquid | liquid interface followed by electron conduction in the ITO surface (the triple interface is illustrated in Figure 4.1B).

Next, an electrode coated with a mesoporous TiO_2 film as used above was sputter-coated with a *ca.* 20 nm layer of gold and investigated. The role of the gold layer is to increase the efficiency of the electrode process due to a greater conductivity than TiO_2 and to further extend the three phase boundary (shown in Figure 4.1C). The TiO_2 film acts as a reservoir of a continuous phase of the redox liquid and as a support for the liquid | liquid interface. A typical FEGSEM of the electrode surface is shown in Figure 4.15 where it is possible to see the porous nature of the gold layer conveyed by the porous nature of the under-lying metal oxide layer.
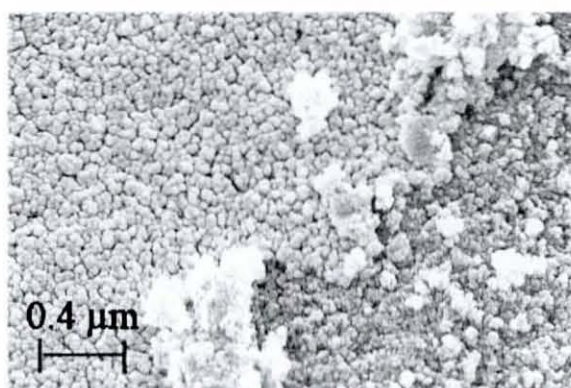

Figure 4.15. FEGSEM image for TiO_2 film (300-400 nm thickness) plus a sputter-coated gold layer (*ca.* 20 nm) on an ITO electrode.

Using similar conditions to the experiments carried out in the absence of a gold layer, the voltammetric response of a 1.3 μg (2.6 nmol) deposit of DDPD was recorded (see Figure 4.16).
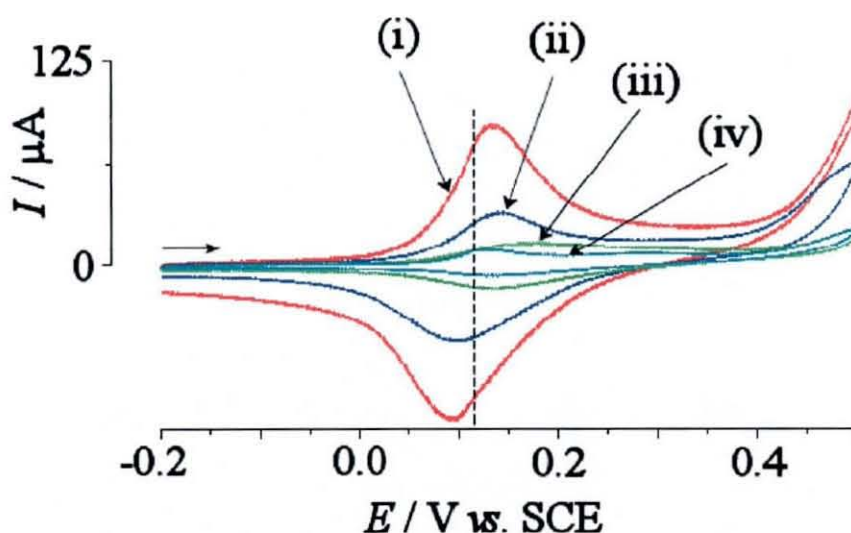
Figure 4.16. Cyclic voltammograms obtained for the oxidation and re-reduction of microdroplets of 1.3 μg DDPD (2.6 nmol) on a 15 layer TiO_2 film with a 20 nm gold layer on ITO immersed in 0.1 M $NaClO_4$. Scan rates of (i) 100, (ii) 50, (iii) 20, and (iv) 10 mVs^{-1} were investigated.

The voltammetric response is greatly improved compared to the TiO_2 with no gold layer, with the conversion reaching 64% (at 100 mVs^{-1}) and a much smaller peak-to-peak separation. This indicates that the metal oxide film with the gold layer gives a better composition for the electrode for the purpose of providing a contact between a redox liquid (DDPD) with a conductive substrate. Increasing the potential scan rate results in an increase in the peak current as well as improving the quality of the voltammetric response observed. Again the redox conversion could be greatly improved by methodically changing the membrane thickness, hydrophobicity, or the amount of oil phase deposited onto the electrode surface.

The oxidative current seen at approximately 0.45 V *vs.* SCE is observed for the blank ITO substrate and all three of the working electrode configurations, and is believed to be a combination of the limit of the electrolyte solution and the second DDPD oxidation reaction. However, in order to verify this it is necessary to increase the potential window to include more positive potentials. If the potential scan range is increased too far for the gold coated TiO_2 modified electrode, the redox activity of the gold sputter coated layer may be observed at approximately 0.5 V *vs.* SCE.

4.6. The Oxidation of DDPD within a Liquid Film of HDOP Deposited into Mesoporous TiO$_2$

As with the bppg electrode, voltammetric responses were recorded using the DDPD: HDOP system. First, the behaviour of the DDPD: HDOP deposited on a clean ITO electrode immersed in 0.1 M pH 7 phosphate buffer solution was investigated. Figure 4.17 shows the voltammetric response for an unmodified ITO electrode before and after the deposition of the acid: base complex, with only a very small, broad response associated with Process II and a small oxidation peak for Process III observed. This indicates that the DDPD is not 100% complexed by the HDOP similar to the bppg voltammetry and therefore a larger deposit of HDOP is required to eliminate the Process III peak. The lack of redox response may again be due to an insufficient conductivity or an unstable organic deposit.
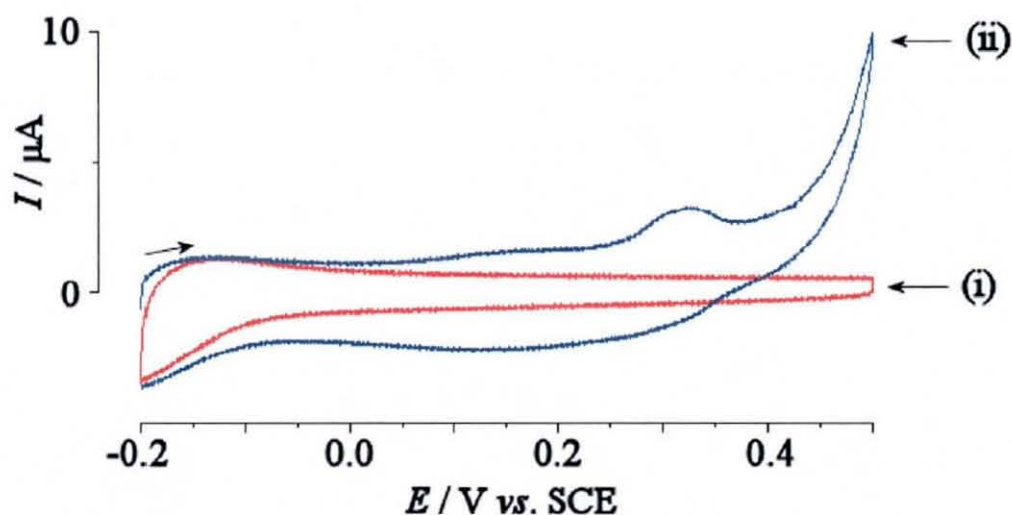

Figure 4.17. Cyclic voltammograms obtained for (i) a blank ITO, and (ii) the oxidation and re-reduction of microdroplets of 1:1 DDPD: HDOP ratio on a blank ITO (scan rates 100 mVs^{-1}) immersed in 0.1 M phosphate buffer (pH 7).

Next, 1.5 µg DDPD (3.0 nmol) in 36.8 µg HDOP (114.0 nmol) (1:38 mole ratio) was deposited onto an ITO electrode with a 300-400 nm mesoporous TiO$_2$ film both with and without a 20 nm sputter-coated gold layer. The large volume of HDOP

was necessary to ensure the TiO_2 electrode was satisfactorily coated, due to a difficulty with the HDOP acetonitrile solution to interact with the DDPD coated metal oxide surface.

Figure 4.18 shows the voltammetric response for the oxidation and re-reduction of the acid-base complex recorded using the mesoporous oxide film without a gold sputter coated layer, in 0.1 M pH 7 phosphate buffer solution. In Figure 4.18ii it is possible to see that the peak-to-peak separation is very wide, suggesting that the transfer of electrons and protons between the organic and aqueous phases is very slow and highly irreversible. It is therefore possible to state that the TiO_2 porous film modified with the DDPD: HDOP complex is not a suitable probe for pH. The influence of potential scan rate was investigated, with faster scan rates increasing both the background and reduction current response, however, the Process II oxidation current response is missing at faster scan rates (Figure 4.18i). Increasing the potential window to include more positive potentials for faster scan rates does not result in the observation of the Process II oxidation response, just an increase in the oxidative current seen at 0.45 V *vs.* SCE.
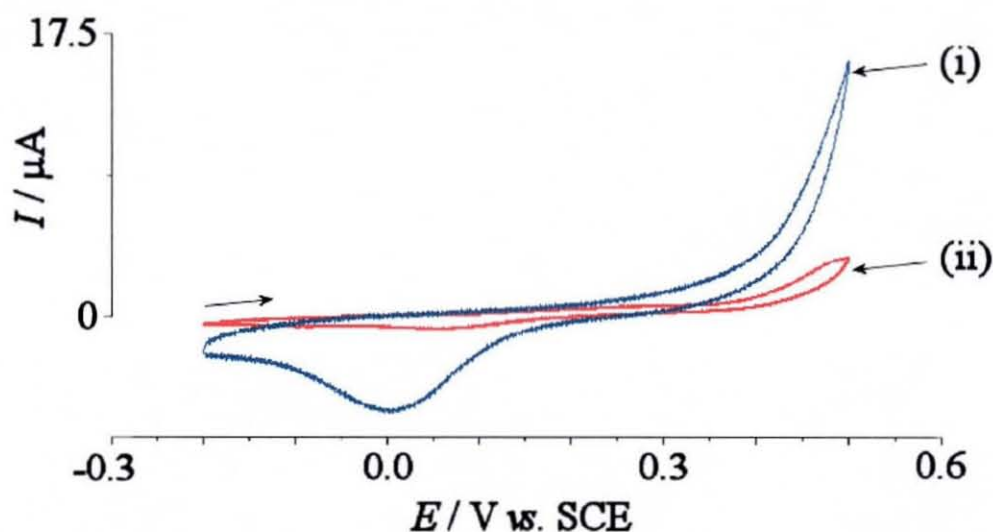

Figure 4.18. Cyclic voltammetry obtained for the oxidation and re-reduction of microdroplets of 1.5 µg DDPD (3.0 nmol) with 36.8 µg HDOP (114.0 nmol) deposited onto a 15 layer TiO_2 film on ITO immersed in aqueous 0.1 M phosphate buffer (pH 7). Scan rate (i) 100 mVs^{-1} and (ii) 10 mVs^{-1}.

After gold coating the mesoporous TiO_2 films, the voltammetric behaviour changes. Figure 4.19 shows the typical voltammetric responses obtained at pH 7 similar to those obtained at bppg electrodes. The voltammetry is stable and the charge under the peak is consistent with *ca.* 20% conversion.
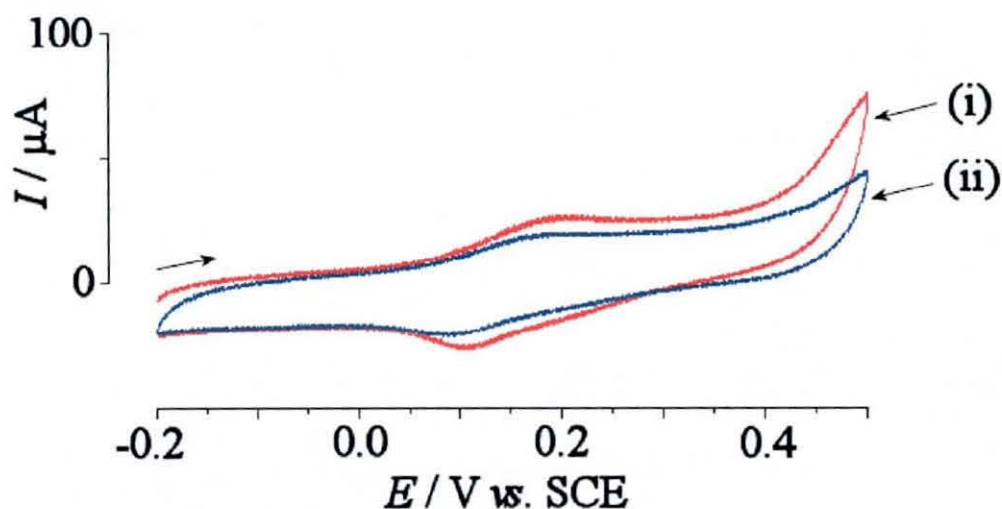

Figure 4.19. Cyclic voltammograms (scan rate 100 mVs⁻¹) for the oxidation and re-reduction of microdroplets of 1.5 μg DDPD (3.0 nmol) together with 36.8 μg HDOP (114.0 nmol) deposited onto an electrode with 15 layers of TiO_2 on ITO and gold sputter coated (*ca.* 20 nm) immersed in aqueous 0.1 M phosphate buffer (pH 7). (i) scan 1 and (ii) scan 3.

The capacitive background current observed here is increased due to the higher surface area of the porous gold and a Faradaic background response is observed starting at 0.5 V *vs.* SCE due to the oxidation of gold. However, the pH dependent signal for the oxidation of DDPD accompanied by proton exchange (Process II) is clearly observed. A shift in this signal of approximately 53 ± 6 mV per pH unit is observed (see Figure 4.20). This indicates that the TiO_2 supported gold electrode is more sensitive to the pH compared to the biphasic system at a bppg electrode.
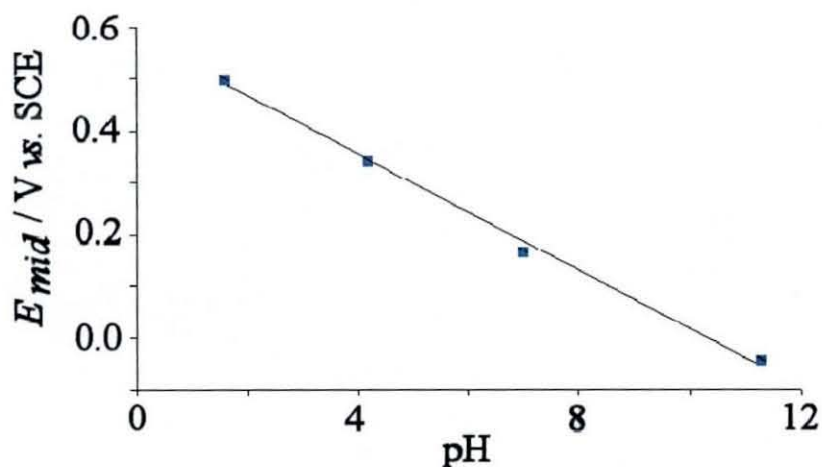
Figure 4.20. Plot of mid point potential versus pH for 1.5 μg DDPD and 57 μg HDOP deposited onto an electrode with 15 layers TiO_2 on ITO and gold sputter coated (*ca.* 20 nm) immersed in aqueous 0.1 M phosphate buffer (pH 1.6, 4.2, 7, 11.3).

4.7. Conclusions

Electrochemical processes in biphasic electrodes have been shown first using a basal plane pyrolytic graphite electrode and second employing a novel mesoporous oxide host structure with and without an outer gold layer. The biphasic system consists of a highly insoluble hydrophobic organic substance, DDPD, deposited onto the electrode and immersed in aqueous electrolyte solution. By applying a voltage to this system, it was possible to observe the transfer of phosphate and ClO_4^- anions between the aqueous and organic phase. The transfer of only protons (for monitoring proton activity) over a wide range of pH values was also observed by adding a hydrophobic organic acid (dioctylphosphate). The biphasic system deposited onto the basal plane pyrolytic graphite electrodes gave the most efficient electrochemical responses however the use of mesoporous oxide membrane electrodes with an outer gold layer has also been shown to be effective for the observation of simultaneous electron and ion transfer. The ability of mesoporous TiO_2 to conduct electrons in the presence of aqueous media could make an important contribution to the overall reaction mechanism. More experimental work will be required to explain the processes in the mesoporous TiO_2 film in more detail and to develop better electrodes for biphasic redox systems. In future, the use of

micro-structured oxide films coated with individual sensing liquids for various types of anionic and cationic analytes may be envisaged. Some general conclusions about the formation of triple phase boundary zones have been drawn

4.8. References

[1] H.H.J. Girault, D. Schiffrin, *J. Electroanal. Chem.* 15 (1989) 1

[2] P. Tasakorn, J.Y. Chen, K. Aoki, *J. Electroanal. Chem.* 533 (2002) 119

[3] M. Donten, Z. Stojek, F. Scholz, *Electrochem. Commun.* 4 (2002) 324

[4] J.D. Wadhawan, A.J. Wain, A.N. Kirkham, D.J. Walton, B. Wood, R.R. France, S.D. Bull, R.G. Compton, *J. Am. Chem. Soc.* 125 (2003) 11418

[5] A.J. Wain, J.D. Wadhawan, R.R. France, R.G. Compton, *Phys. Chem. Chem. Phys.* 6 (2004) 836

[6] S.M. MacDonald, P.D.I. Fletcher, Z-G. Cui, M. Opallo, J. Chen, F. Marken, *Electrochim. Acta* (2007) Article in press

[7] F. Marken, R.D. Webster, S.D. Bull, S.G. Davies, *J. Electroanal. Chem.* 437 (1997) 209

[8] C.E. Banks, T.J. Davies, R.G. Evans, G. Hignett, A.J. Wain, N.S. Lawrence, J.D. Wadhawan, F. Marken, R.G. Compton, *Phys. Chem. Chem. Phys.* 5 (2003) 4053

[9] F. Marken, A. Blythe, R.G. Compton, S.D. Bull, S.G. Davies, *Chem. Commun.* (1999) 1823

[10] J.D. Wadhawan, R.G. Evans, C.E. Banks, S.J. Wilkins, R.R. France, N.J. Oldham, A.J. Fairbanks, B. Wood, D.J. Walton, U. Schröder, R.G. Compton, *J. Phys. Chem. B*, 106 (2002) 9619

[11] J.D. Wadhawan, R.G. Compton, F. Marken, S.D. Bull, S.G. Davies, *J. Solid State Electrochem.* 5 (2001) 301

[12] F. Scholz, R. Gulaboski, K. Caban, *Electrochem. Commun.* 5 (2003) 929

[13] G. Bouchard, A. Galland, P.A. Carrupt, R. Gulaboski, V. Mirceski, F. Scholz, H.H.J. Girault, *Phys. Chem. Chem. Phys.* 5 (2003) 3748

[14] R. Gulaboski, F. Scholz, *J. Phys. Chem. B* 107 (2003) 5650

[15] M. Opallo, M. Saczek-Maj, *Electrochem. Commun.* 3 (2001) 306

[16] M. Saczek-Maj, M. Opallo, *Electroanalysis* 14 (2002) 605

[17] M. Opallo, M. Saczek-Maj, *Chem. Commun.* (2002) 448

[18] M. Opallo, J. Kukulka-Walkiewicz, M. Saczek-Maj, *J. Sol-Gel Sci. Technol.* 26 (2003) 1045

[19] M. Saczek-Maj, M. Opallo, *Electroanalysis* 15 (2003) 566

[20] J. Niedziolka, M. Opallo, *Electrochem. Commun.* 6 (2004) 475

[21] F. Marken, C.M. Hayman, P.C.B. Page, *Electroanalysis* 14 (2002) 172

[22] U. Schröder, R.G. Compton, F. Marken, S.D. Bull, S. Gilmour, *J. Phys. Chem. B* 105 (2001) 1344

[23] F. Marken, C.M. Hayman, P.C.B. Page, *Electrochem. Commun.* 4 (2002) 462

[24] G. Shul, K.J. McKenzie, J. Niedziolka, E. Rozniecka, B. Palys, F. Marken, C.M. Hayman, B.R. Buckley, P.C. Bulman Page, M. Opallo, *J. Electroanal. Chem* 582 (2005) 202 & refs. therein

[25] S. Kambe, S. Nakade, T. Kitamura, Y. Wada, S. Yanagida, *J. Phys. Chem. B* 106 (2002) 2967

[26] K.J. McKenzie, F. Marken, M. Opallo, *Bioelectrochemistry* 66 (2005) 41

Chapter 5

Electrochemical Properties of Core-Shell TiC - TiO$_2$ Nanoparticle Films Immobilised at ITO Electrode Surfaces

5.1. Introduction

Titanium (IV) carbide, TiC, is a typical early transition metal carbide with many desirable material properties such as extreme hardness, high electrical conductivity, and a high melting point, ideal for use as wear resistant coatings.[1] Further advantageous properties include catalytic activity[2] and electrocatalytic activity,[3] which is highly beneficial for applications as a potential electrode or sensor material. Very little is known about the electrochemical properties of TiC materials however a lot is known about the electrochemical and surface[4] properties of mesoporous and nanoparticulate TiO$_2$.[5,6,7,8] Models have been developed[9] to describe the capacitive and reactive properties of nanoporous semi-conducting TiO$_2$. TiO$_2$ is an important material in electrochemistry,[10] photochemistry[11] and in sensor systems.[12] In combination with other more electrically conducting transition metal oxides, TiO$_2$ is employed in dimensionally stable anodes[13] and in a hydrogen-reduced conducting form in Ebonex[TM] electrodes.[14] Composites of TiO$_2$ and carbon have been employed to combine the surface reactivity of TiO$_2$ and the electrical conductivity of graphite.[15]

In this study the core-shell nanostructure approach is applied to TiO$_2$ systems. Incorporation of a second component with TiO$_2$ to form core-shell structures has attracted recent interest with a variety of applications in catalysis. These include BaFe$_{12}$O$_{19}$ - TiO$_2$ core-shell nanoparticles for improving photo-catalysis[16] and the use of TiO$_2$ - Ag core-shell structures for catalysis and improved electronic transportation.[17] Other studies describe the use of TiO$_2$ - silica core-shell colloidal particles for optical trapping applications[18] and the use of TiO$_2$ coated polystyrene core-shell spheres for electronic ink.[19]

TiO_2 behaves like an insulator over a wide range of potentials.[20] It is shown here that by introducing TiC cores, it is possible to increase conductivity whilst maintaining an active TiO_2 surface. Micron-scale core-shell composites of TiO_2 and TiC have been formed recently through controlled thermal-plasma oxidation.[21] TEM observations of oxide scale formed on TiC single crystals with different faces have been reported using thermal oxidation.[22] Reducing the size of the TiC particles to nanoparticles can provide an exceptionally high surface area for adsorption and electrocatalysis. TiO_2 is a known biocompatible substrate material for the adsorption of proteins and small redox active molecules.[23]

The voltammetric detection of small biologically important molecules such as ascorbic acid or quinols for example hydroquinone and dopamine, is of considerable interest and these systems are employed here as model systems. A variety of methods have been utilised, for instance electrochemical detection in capillary electrophoresis,[24] or the use of modified electrodes using polyaniline[25] or graphite reinforced by carbon.[26] In voltammetric measurements of extra cellular fluid, ascorbic acid is reported as being the main interfering molecule with dopamine.[27] Depending on the conditions of the experiment, the surface charge of the TiO_2 may help separating the responses for the negatively charged ascorbic acid and the positively charged dopamine.

The ability to detect levels of nitric oxide (NO) has attracted significant interest due to its important role in many physiological processes.[28] NO is also a toxic air pollutant generated by vehicle engines and power plants. Chemiluminescence, colorimetry, fluorometry, and electrochemical techniques have all been utilised in the study of NO,[29] where the first electrochemical sensor for NO in biological samples was published in 1989 by Shibuki. In 1992, an electrode composed of a metalloporphyrin deposited on a carbon fiber electrode was reported. Further work showed that detection of NO was also possible using carbon fibers alone or carbon fibers modified with porphyrins with no coordinated metal.[30] The use of nano-materials in electrochemical sensors for the detection of NO include the application of nano-gold colloids, carbon nanotubes and a nano-TiO_2/Nafion® composite film.[31] The metal-like conductivity of TiC may allow the over-potential often associated

with NO oxidation to be reduced. The reversible reduction of $[Ru(NH_3)_6]Cl_3$ and the electrocatalytic behavior for the oxidation of hydroquinone, dopamine, ascorbic acid and NO using core-shell $TiC-TiO_2$ nanoparticle films on ITO electrode surfaces is investigated here.

5.2. Experimental

5.2.1. Chemicals

Demineralised and filtered water was taken from an Elga water purification system (Elga, High Wycombe, Bucks, UK) with a resistivity of not less than 18 MΩ cm. TiC nanoparticles (20-30 nm diameter) were obtained from Goodfellow, UK. Methanol, L-ascorbic acid, hydroquinone, dopamine, NO, $[Ru(NH_3)_6]Cl_3$, $NaNO_2$, NaOH, H_3PO_4, KOH, K_2HPO_4, and KH_2PO_4 were obtained commercially in analytical or the highest purity grade available. Nitric oxide saturated solution (1.8 mmol dm^{-3}) [31] was obtained by bubbling NO pure gas through 10 ml deoxygenated distilled water for 30 minutes and kept under an Ar atmosphere until use.

5.2.2. Instrumentation

Voltammetric measurements were performed with a computer controlled Eco Chemie PGSTAT20 Autolab potentiostat system. Experiments were conducted in staircase voltammetry mode with a platinum gauze counter electrode and saturated calomel reference electrode (SCE (saturated KCl), REF401, Radiometer). The working electrode was a tin-doped indium oxide (ITO) coated glass (10 mm × 60 mm, resistivity 20 Ω per square) with approximately 8% tin, obtained from Image Optics Components Ltd. (Basildon, Essex). The ITO electrode surface was modified with a porous titanium carbide film giving a geometric working electrode area of 1 cm^2. An Elite tube furnace system was employed for cleaning ITO electrode surfaces (at 500°C in air) and for calcining titanium carbide films (at 500°C in air). Prior to conducting electrochemical experiments, all solutions were purged with

argon (BOC, UK). All electrochemical experiments were carried out at a temperature of $22 \pm 2^{\circ}C$.

Scanning electron microscopy images were obtained with a Leo 1530 Field Emission Gun Scanning Electron Microscope (FEGSEM) system. Transmission electron microscopy images were obtained with a JEOL JEM-2000FX electron microscope.

A quartz crystal oscillator circuit (Oxford Electrodes) connected to a frequency counter (Fluke, PM6680B) allowed the resonance frequency of the quartz crystal sensor to be monitored simultaneously to conducting voltammetric experiments. A Faraday cage was used to contain the quartz crystal to minimize noise interference. The analogue output of the counter was fed into the ADC input of an Autolab potentiostat system (Eco Chemie, Netherlands) and data processing was possible with GPES software (Eco Chemie, Netherlands). The repeated deposition processes was monitored with the crystal suspended in air. Droplets of solution were applied to one side of the crystal and after drying the frequency measured and monitored step-by-step.

XRD measurements were obtained on a Bruker D8 Advance powder diffractometer fitted with primary monochromator using Cu Kα1 radiation and an Anton Parr HTK 1200 heated sample stage.

5.3. Deposition and Characterisation of TiC Nanoparticle Films on ITO

Mesoporous films of TiC were deposited following a repeated deposition coating method. A clean ITO surface (washed with ethanol and deionised water, dried, and 60 minute heat treatment at $500^{\circ}C$ in air) was dipped into a suspension of TiC nanoparticles in methanol (0.03 g TiC in 10 cm^3 methanol, dispersed by short ultrasonication). After 30 seconds the ITO electrode was removed and the methanol allowed to evaporate in air at room temperature. This leaves a permanently adhered

film of TiC particles on the ITO electrode surface. By repeatedly dipping the resulting nanoparticle deposit into the TiC suspension, thicker deposits of TiC were produced on the ITO surface. Typical electron microscopy images of a five 'layer' deposit are shown in Figure 5.1. It can be seen that the typical particle size is 20-30 nm and that agglomerates of spherical nanoparticles dominate. The repeated deposition growth is slow and gives rise to a patchy, porous film on the electrode surface. A key factor in the slow growth rate is the low concentration of TiC nanoparticles (0.3 %wt.). This allows control of the average film thickness.
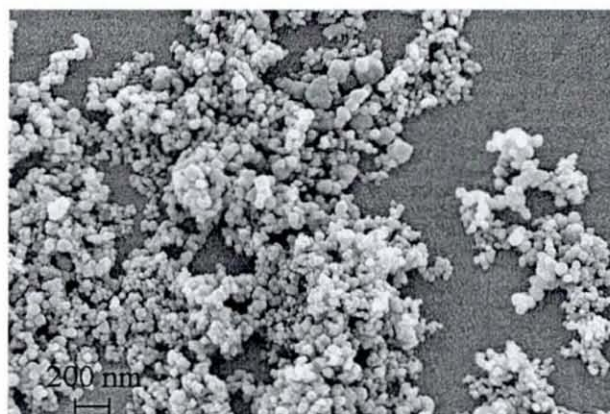
Figure 5.1. A FEGSEM image of the titanium carbide nanoparticle film manufactured after 5 depositions, on an ITO substrate.

The electron microscopy data is supported by experiments with a quartz crystal microbalance system. Figure 5.2 shows the reduction of the resonance frequency of an ITO coated quartz crystal resonator during the repeated deposition process. Each deposition reduces the resonance frequency by approximately 1230 Hz, which corresponds to 1.29 μg (according to the Sauerbrey equation,[32] see experimental). Furthermore, the weight of TiC (molecular weight 59.91 g mol^{-1}) can be estimated as 2.2 x 10^{-8} mol per layer (on a 0.2 cm^2 area of the quartz resonator).
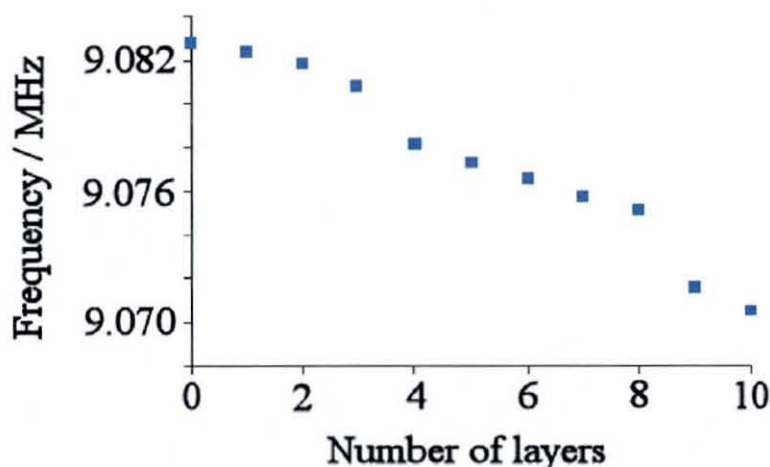
Figure 5.2. Plot of the resonance frequency change for an ITO coated quartz crystal during repeated deposition of TiC. The frequency change corresponds to a mass increase with $\dfrac{\Delta m}{\Delta f} = 1.05$ ng Hz^{-1} (see experimental).

Next, the TiC nanoparticle films were characterised electrochemically after immersion in 0.1 M phosphate buffer solution pH 7. Voltammetric experiments were conducted over a wide potential window with 3 new processes observed compared to a clean ITO electrode (Figure 5.3). Firstly, a large irreversible anodic electrochemical response at a potential of 1 V *vs.* SCE is generated. The current for this oxidation is directly proportional to the average TiC film thickness or the amount of TiC deposited. This anodic response is dominating during the first potential cycle and can be attributed to a possible surface reaction, which is resulting in carbon oxidation and formation of hydrolysed titanium oxide film (equation 5.1).

$$TiC + 5\,H_2O \rightleftharpoons TiO_2 + CO_3^{2-} + 8\,e^- + 10\,H^+ \qquad (5.1)$$

The charge under the anodic response, *ca.* 6 mC for a 'one layer' deposit, is consistent with approximately 10^{-8} mol or 10% of the TiC deposit. It can be proposed that a surface oxidation occurs and a thin film of TiO_2 is formed around the TiC particles.

The second notable feature is a capacitive background current that is again proportional with the average thickness of TiC film. Thirdly, it is possible to see a redox response at a potential of –0.8 V *vs*. SCE. The shape of this voltammetric response is characteristic for TiO_2 thin films and has been explained in terms of sequential filling electronic states within the oxide.[9]
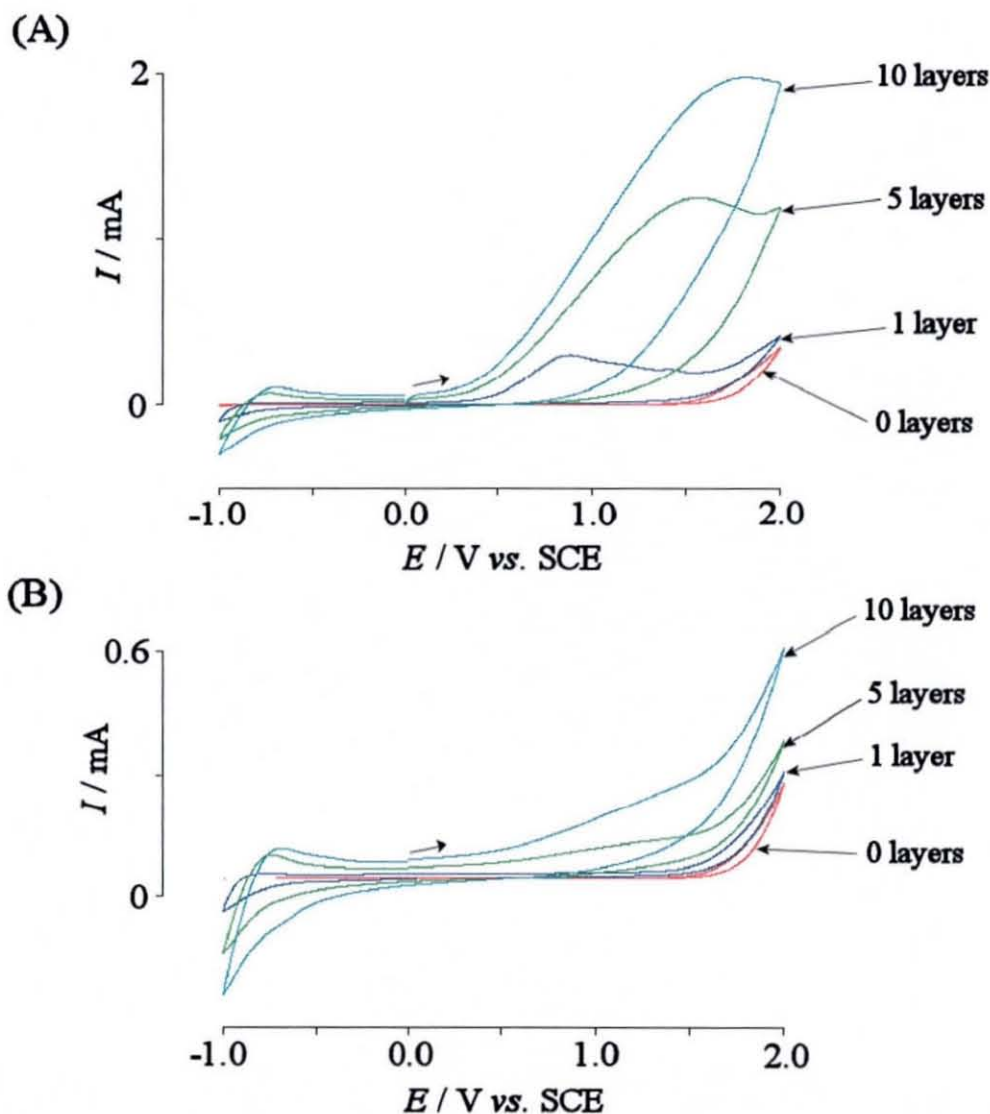

Figure 5.3. Cyclic voltammograms (scan rate 50 mVs[-1]) obtained for (a) scan 1 and (b) scan 2 of the irreversible surface oxidation of TiC films with increasing thicknesses in aqueous 0.1 M phosphate buffer pH 7.

By initially scanning to negative potentials prior to the electrochemical oxidation of the TiC, the change in redox response associated with the formation of the titanium

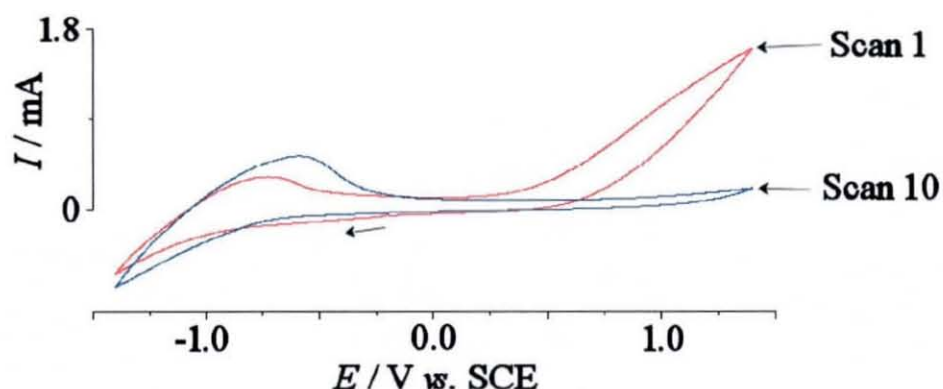(IV) oxide film becomes more apparent (refer to Figure 5.4.), confirming the process shown in equation 1.

Figure 5.4. Cyclic voltammograms (scan rate 20 mVs^{-1}) obtained for (a) scan 1 and (b) scan 10 of the irreversible surface oxidation of a '10 layer' TiC film in aqueous 0.1 M phosphate buffer pH 7.

In order to determine whether a "visible" shell of titanium oxide was formed on the TiC nanoparticle surface after electrochemical oxidation, transmission electron microscopy (TEM) images were obtained. Figure 5.5 confirms that an amorphous shell, approximately 2 nm in thickness, is indeed formed on the surface of the TiC nanoparticles upon electrochemical oxidation.
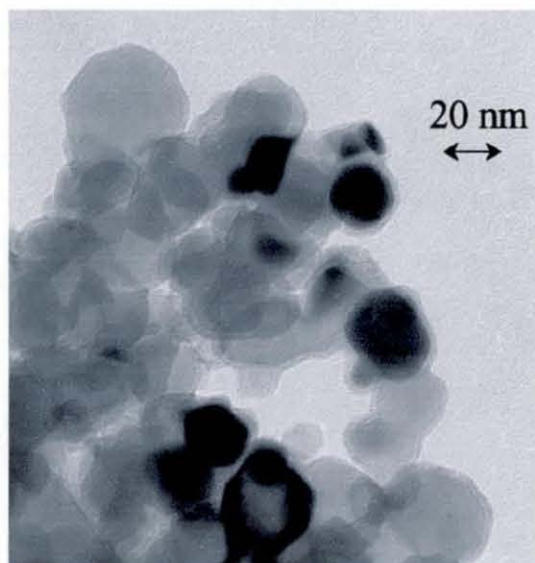

Figure 5.5. TEM of core-shell titanium carbide – titanium oxide nanoparticles formed after the irreversible surface oxidation of TiC nanoparticles in aqueous 0.1 M phosphate buffer pH 7.

From Figure 5.5 it appears as if most particles are affected by the surface oxidation but it is difficult to judge the uniformity of the conversion. The resulting particles are suggested to have "core-shell" nature based on the symmetric coating of particles with oxide.

5.4. Thermal Oxidation of Titanium Carbide Nanoparticles to TiC-TiO₂ Core-Shell Nanoparticles

As a second approach for the formation of TiO_2 surface layers thermal oxidation in air was investigated. When heated in air at 500°C, the black TiC nanoparticles were converted into a white nanoparticulate material. A '5 layer' TiC film was thermally oxidised at 500°C for 30 minutes and a typical FEGSEM image is shown in Figure 5.6. In comparison with Figure 5.1, the appearance of the nanoparticles does not change significantly during thermal treatment.
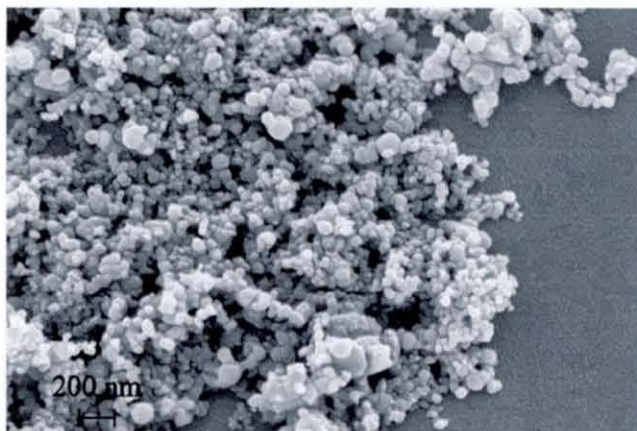

Figure 5.6. FEGSEM image of titanium carbide nanoparticle film manufactured after 5 depositions, on an ITO substrate after thermal oxidation at 500°C for 30 minutes.

Using equations 5.2, 5.3 and 5.4, it is possible to calculate that an increase in particle volume and radius (r) is expected. Based on the volume per formula unit (room temperature densities (ρ) are for anatase = 3.89 g/cm³ and for TiC = 4.93 g/cm³),

which is 20.3 Å^3 for TiC and 34.1 Å^3 for TiO$_2$, an increase in volume by 69% is expected (increase in radius 19%).

$$mass \ per \ formula \ unit = \frac{RMM}{N_A} \tag{5.2}$$

$$volume = \frac{mass}{\rho} \tag{5.3}$$

$$r = \sqrt[3]{\frac{0.75 \times volume}{\pi}} \tag{5.4}$$

To further quantify this process and to confirm the identity of the white nanoparticles, TiC nanoparticles were gradually thermally oxidised in air under XRD conditions (Figure 5.7). The sample was heated at 2°C/minute and held at temperature for 30 minutes before data were collected between 20-80° 2-θ using a 0.0147° 2-θ step over a period of 30 minutes.
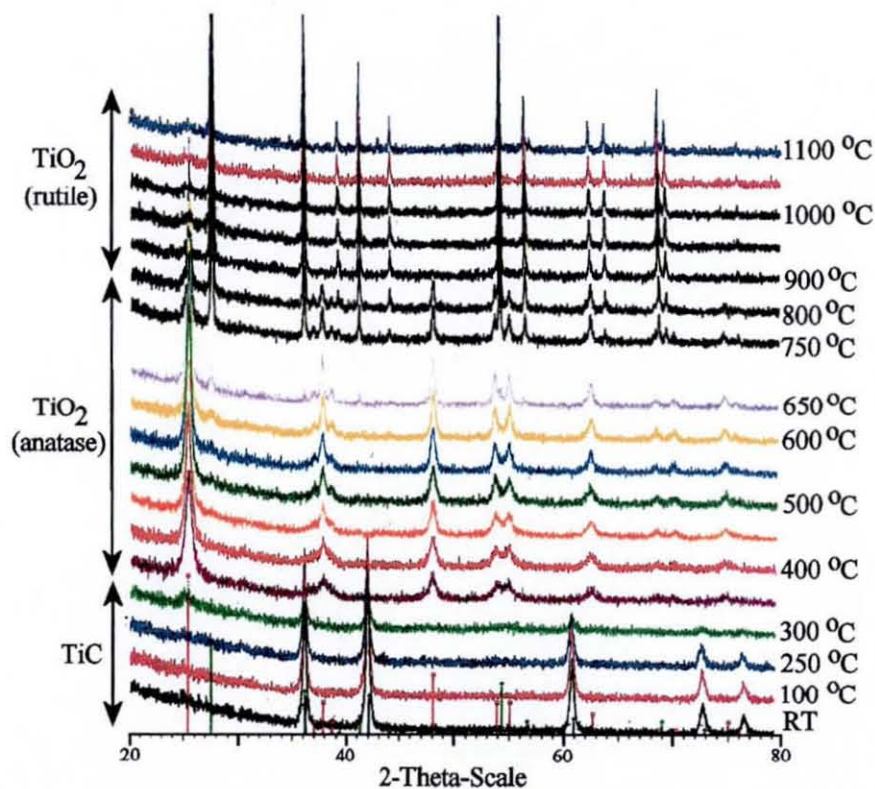

Figure 5.7. Plot of XRD data for the gradual thermal oxidation of TiC to TiO$_2$ (anatase) at 350°C and TiO$_2$ (rutile) at temperatures greater than 700°C. The vertical straight lines refer to the expected peak positions for anatase (red line), rutile (dark green) and TiC (black).[33]

The standard powder diffraction patterns expected for TiC, TiO_2 (anatase), and for TiO_2 (rutile) can be clearly identified.[33] At 300°C the TiC phase is seen to be reacting and at 350°C oxidation to the anatase form of TiO_2 has occurred. A grey intermediate product is obtained at 300°C. This intermediate product shows clear core-shell structure when investigated by TEM (see Figure 5.8). At temperatures greater than 700°C, the crystal structure of the rutile form of TiO_2 starts to appear.
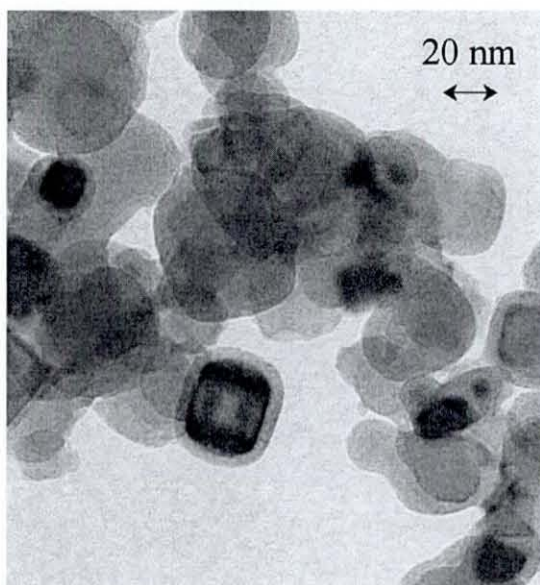

Figure 5.8. TEM image of core-shell titanium carbide - titanium oxide nanoparticles obtained after the thermal surface oxidation of TiC nanoparticles at 300°C for 30 minutes in air.

Figure 5.9 shows a plot of the percentage composition for the TiC nanoparticles with gradual thermal oxidation in air. The transition from TiC to anatase occurs rapidly over a 50°C range compared to the more gradual transition from anatase to rutile at higher temperature.
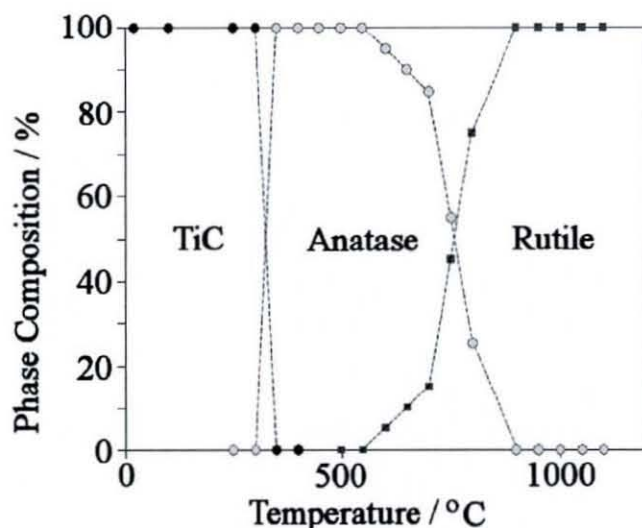
Figure 5.9. Plot of percent composition for TiC nanoparticles over gradual thermal oxidation in air under XRD conditions.

A possible reaction for the surface oxidation of TiC is shown in equation 5.5.

$$TiC + 2O_2 \rightarrow TiO_2 + CO_2 \qquad\qquad (5.5)$$

The Scherrer equation, $t = \dfrac{0.9\lambda}{\sqrt{B_m^2 - B_s^2}\cos\theta}$ (t = average crystallite size (Å), B_m and B_s = width in radians of the diffraction peaks (at half maximum height) of the test sample and a highly crystalline standard (0.1°) sample respectively, and λ is wavelength of the X-ray beam = 1.5406 Å) relates the average size of a crystal grain to the width of its diffraction peaks. As a result it is possible to show the average particle or grain size of the TiC are very similar before (approximately 30 nm) and after thermal oxidation at 500°C (approximately 28 nm). This result is consistent with the electron microscopy observations (see Figure 5.1.).

Next, the voltammetry of thermally oxidised TiC nanoparticle films was investigated. The effect of thermal oxidation on the background electrochemical properties of TiC films was investigated in 0.1 M phosphate buffer solution pH 7 as before. Figure 5.10 shows the cyclic voltammograms for the first and second scans for a '10 layer' TiC film with no prior thermal oxidation and a '10 layer' partially oxidized TiC-

anatase core-shell film produced after 30 minutes thermal oxidation of a TiC film at 300°C. Data for a '10 layer' anatase film produced after 30 minutes thermal oxidation of a TiC film at 500°C are also shown.
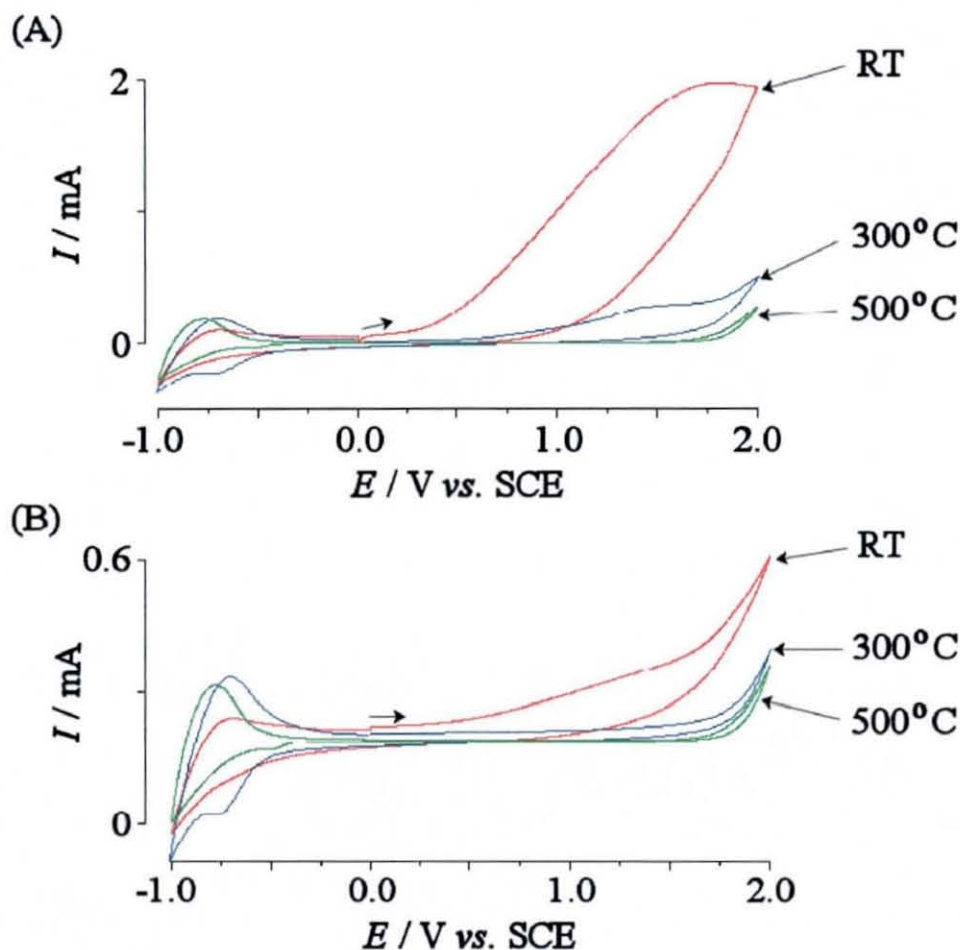

Figure 5.10. Cyclic voltammograms (scan rate 50 mVs^{-1}) obtained for (a) scan 1 and (b) scan 2 of the irreversible surface oxidation of TiC films after thermal oxidation in aqueous 0.1 M phosphate buffer pH 7.

The partially oxidised TiC-TiO$_2$ core-shell nanoparticle film demonstrates a large decrease in the electrochemical surface oxidation and slight decrease in background capacitive current compared to the TiC film. An increase in the Ti(IV/III) redox response at negative potentials is also seen. This is as expected due to the decrease in size of the highly conductive TiC core and increase in the amount of surface TiO$_2$ prior to the electrochemical experiments. The anatase film shows background capacitive currents similar to a clean ITO electrode and no surface TiC oxidation.

The Ti(IV/III) redox response is similar to that for the partially oxidised TiC-TiO_2 core-shell nanoparticles. These results clearly show that electrochemical and thermal oxidation result in similarly behaved core-shell structures. Next, the electrochemical properties for some model redox systems at TiC-TiO_2 core-shell nanoparticle modified electrodes are investigated.

5.5. The Reversible Reduction of $Ru(NH_3)_6^{3+}$ Bound onto Nanoparticulate Titanium Carbide

To ascertain the ability of the nanoparticulate TiC films to act as electrochemically active sites, the standard redox couple of $Ru(NH_3)_6^{3+}$ (equation 5.6) was studied using cyclic voltammetry.

$$Ru(NH_3)_6^{3+} + e^- \rightarrow Ru(NH_3)_6^{2+} \tag{5.6}$$

Figure 5.11 shows the multi-cycle voltammetric response for a '10 layer' TiC film in pH 7 phosphate buffer solution before and after being dipped into 0.02 M $Ru(NH_3)_6^{3+}$.
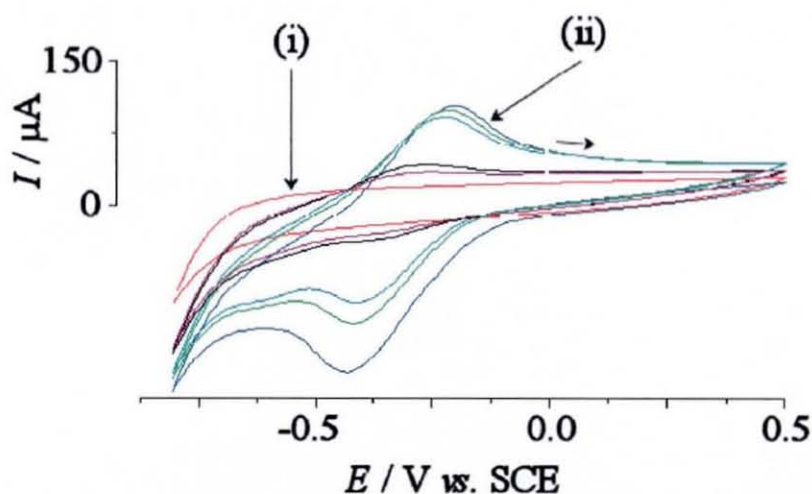

Figure 5.11. Cyclic voltammogram (scan rate 50 mVs^{-1}) of 10 layers TiC on ITO (i) before (red line) and (ii) after (blue line scan 1, green line scan 2, cyan line scan 3, black line scan 14 and magenta line scan 20) dipping in 0.02 M $Ru(NH_3)_6^{3+}$, in 0.1 M phosphate buffer pH 7.

The reversible reduction of $Ru(NH_3)_6^{3+}$ is observed which is an indication of binding of $Ru(NH_3)_6^{3+}$ to the phosphate decorated TiC nanoparticle surface. The signal is observed over 20 scans but the analyte is slowly lost from the electrode surface. A large peak separation of 202 mV is recorded, almost double that reported using a polycrystalline TiC film on a Ti substrate.[3] This can be expected due to some cell resistance and the considerable peak current. Interestingly the ratio of the peak currents, $I_{p,a}/I_{p,c}$ equals 0.9 in both cases supporting highly reversible behaviour and good electrical conductivity.

5.6. The Electrocatalytic Oxidation of Hydroquinone on Nanoparticulate Titanium Carbide

It has been demonstrated recently that bulk TiC is an attractive electrode material for electroanalytical processes and that in particular quinone systems show fast electron transfer.[3] Here, the effect of TiC nanoparticles on electrochemical processes is surveyed for comparison. The electrocatalytic oxidation of 2 mM hydroquinone in 0.1 M phosphate buffer pH 7 with new TiC films is shown in Figure 5.12 (equation 5.7).

$$-2\bar{e} - 2H^+ \longrightarrow$$
$$\longleftarrow +2\bar{e} +2H^+$$

(5.7)
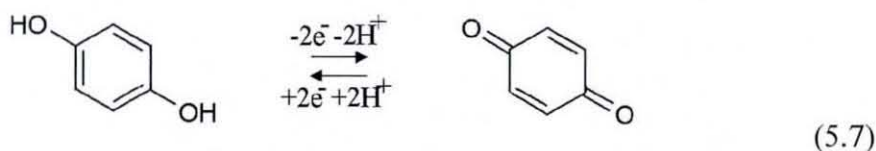
For the oxidation of hydroquinone using only a clean ITO electrode, a peak separation of 2.26 V is observed, as a large overpotential is necessary before oxidation and reduction are possible. In contrast, in the first scan using a porous '5 layer' TiC film, a much more reversible process (peak separation of 0.89 V) is produced. Increasing the amount of TiC further decreases the peak-to-peak separation to 0.61 V (see Figure 5.12A).

The electrochemical surface oxidation of TiC is seen in the first oxidation cycle as before. Interestingly, the hydroquinone oxidation and re-reduction responses are not affected by the formation of the TiC-TiO$_2$ core-shell structure (see Figure 5.12B). The interaction of the surface with the hydroquinone as well as the electrical conductivity appear to be very effective. The reactivity towards hydroquinone remains even after cycling to +2 V. The shape of the voltammogram for the oxidation and reduction of hydroquinone is consistent with that seen in the literature.[3]
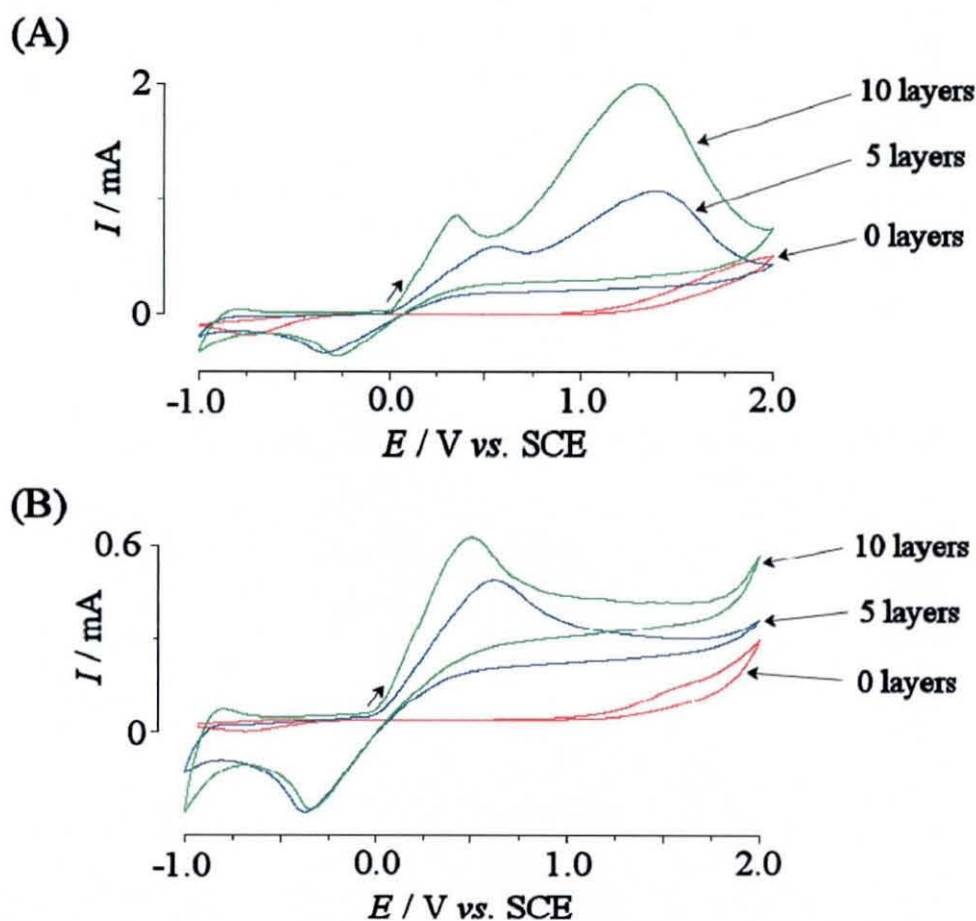

Figure 5.12. Cyclic voltammograms (scan rate 50 mVs^{-1}) obtained for (a) scan 1 and (b) scan 2 of the irreversible surface oxidation of TiC films with increasing thicknesses in aqueous 0.1 M phosphate buffer pH 7 in the presence of 2 mM hydroquinone.

For TiC films with only '1 layer', a much lower loading of TiC is achieved. Figure 5.13 shows the oxidation and reduction of 2 mM hydroquinone using a very thin TiC

electrode at slower scan rates. The same type of almost sigmoid voltammetric response is seen at 50 mVs^{-1} (data not shown). The dependence of the sigmoidal voltammogram on scan rate indicates that a micro array of TiC nanoparticles is present and overlapping diffusion zones are responsible for the shape.
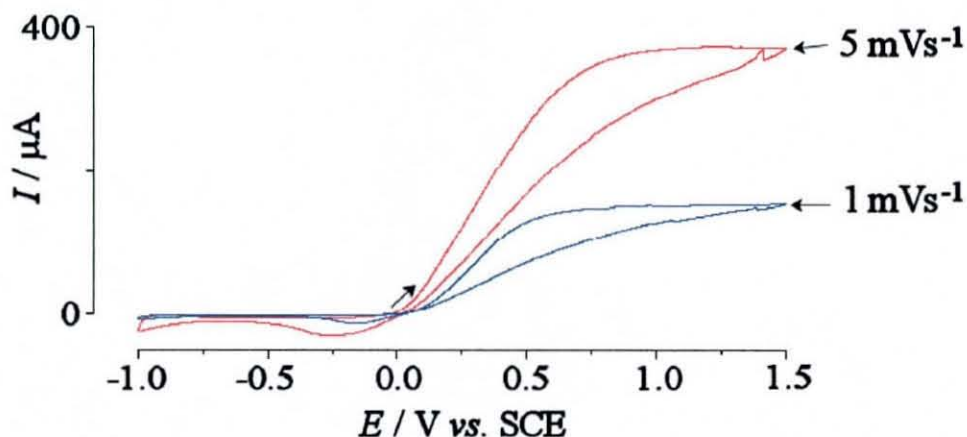

Figure 5.13. Cyclic voltammograms (scan rates 5 mVs^{-1} and 1 mVs^{-1}) for scan 2 of the oxidation of 2 mM hydroquinone using a '1 layer' TiC film in aqueous 0.1 M phosphate buffer pH 7.

Using similar '10 layer' TiC film electrodes, both oxidation and reduction can be recorded for hydroquinone concentrations as low as 10 nM (Figure 5.14A), compared to a blank ITO electrode where the lowest concentration to produce a visible reduction peak is 80 nM (Figure 5.14B).
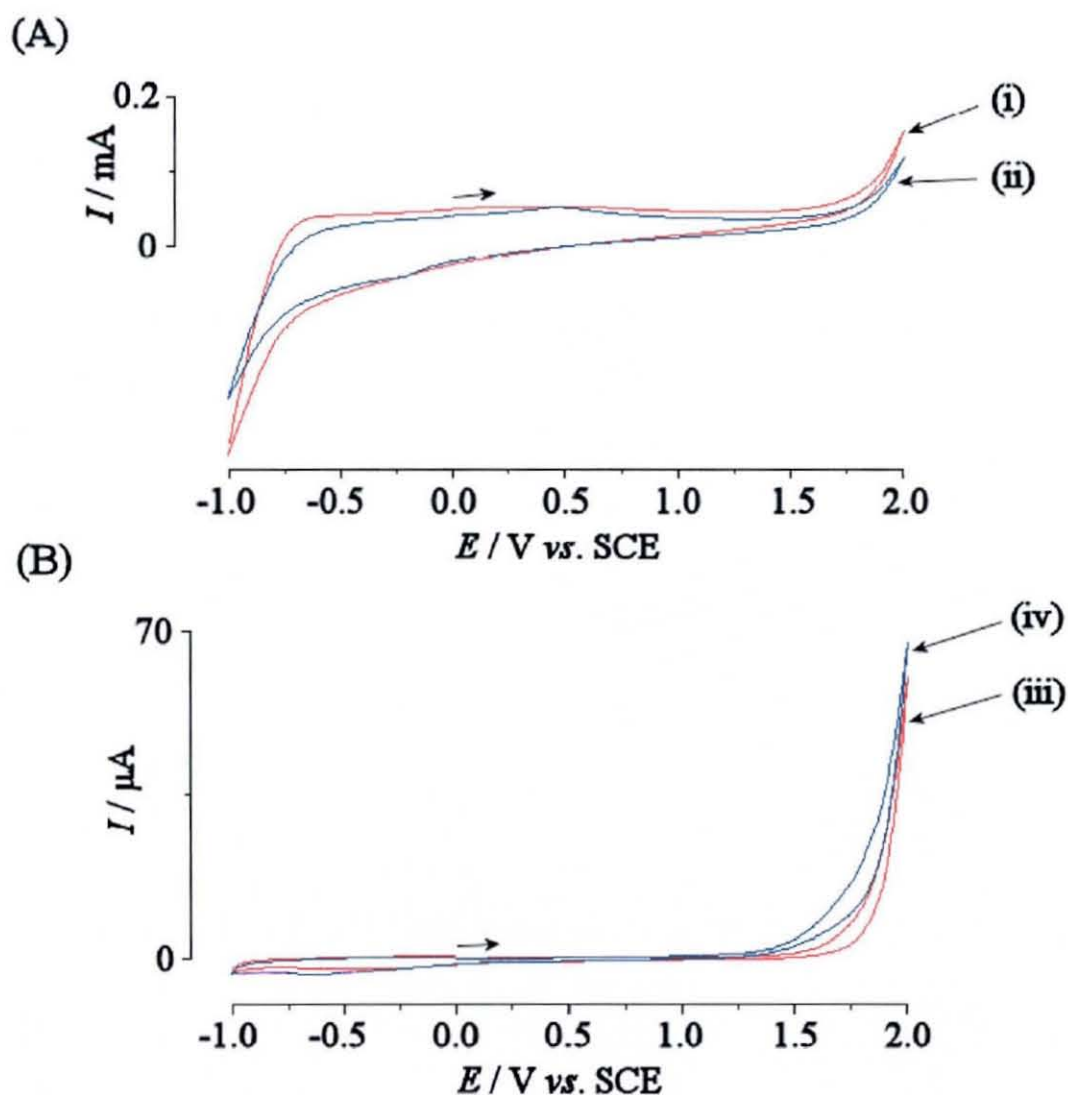
(A)

(B)

Figure 5.14. Cyclic voltammograms (scan rate 100 mVs⁻¹) for (A) scan 3 of a '10 layer' TiC film in (i) aqueous 0.1 M phosphate buffer pH 7 and (ii) in aqueous 0.1 M phosphate buffer pH 7 plus 10 nM hydroquinone and (B) scan 1 of a clean ITO electrode in (iii) aqueous 0.1 M phosphate buffer pH 7 and (iv) in aqueous 0.1 M phosphate buffer pH 7 plus 80 nM hydroquinone.

Next, the effect of TiC thermal oxidation on the electrocatalytic oxidation of hydroquinone was also investigated. Using a '10 layer' TiC film heat treated at increasing temperatures, it is shown that as the TiC film is gradually oxidised, the electrocatalytic nature of the film decreases (Figure 5.15).
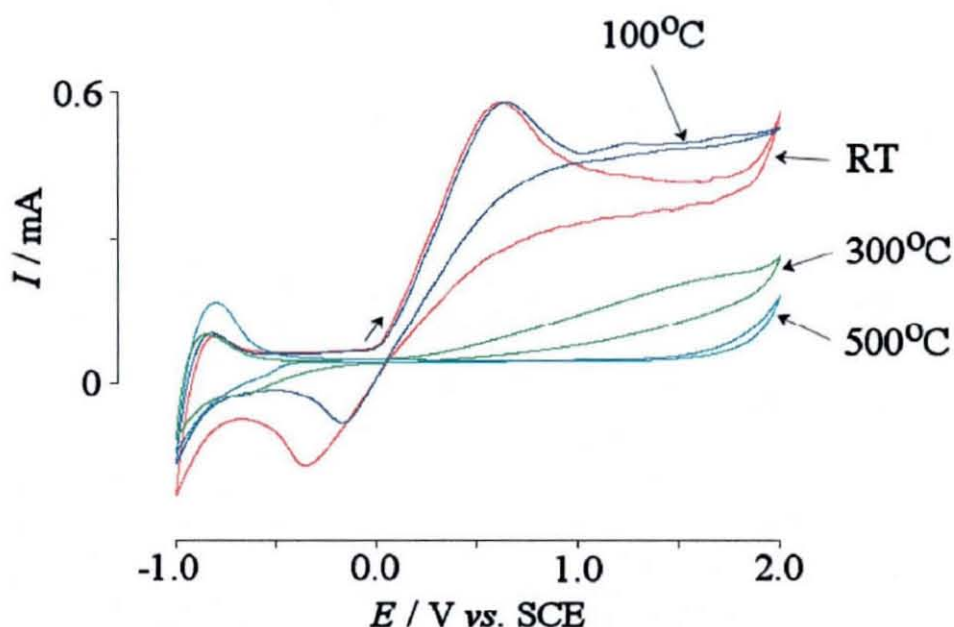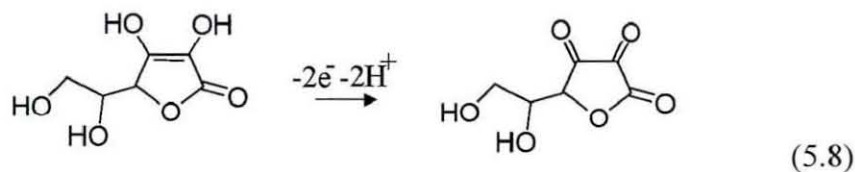
Figure 5.15. Cyclic voltammograms (scan rate 50 mVs^{-1}) obtained for (a) scan 1 and (b) scan 2 of the irreversible surface oxidation of '10 layer' TiC films after thermal oxidation in aqueous 0.1 M phosphate buffer pH 7 in the presence of 2 mM hydroquinone.

The treatment at 300°C clearly reduces the electrocatalytic effect (peak-to-peak separation) and the magnitude of the current but a well-defined current is still observed. Only after complete conversion to TiO$_2$ (anatase) the signal for the hydroquinone oxidation is lost. This indicates (i) a need for the highly conductive TiC core and (ii) that even with a substantial TiO$_2$ shell a high level of electrocatalytic reactivity can be maintained.

5.7. The Electrocatalytic Oxidation of Ascorbic Acid on Nanoparticulate Titanium Carbide

The electrocatalytic oxidation of 2 mM ascorbic acid was investigated in 0.1 M phosphate buffer solution pH 7 using a '10-layer' TiC film electrode and compared to data obtained with a clean ITO (Figure 5.16). The process is assumed to be 2-electron in nature (equation 5.8).

$$-2\bar{e} -2H^{+}$$

(5.8)

For both electrodes, a single irreversible oxidation peak is produced, consistent with experiments carried out with other modified electrodes.[27] As for the oxidation of hydroquinone, the greater conductivity and reactivity of TiC results in the oxidation for ascorbic acid at lower potentials. After surface oxidation of the TiC in scan 1, electrocatalysis of ascorbic acid is still maintained in scan 2.
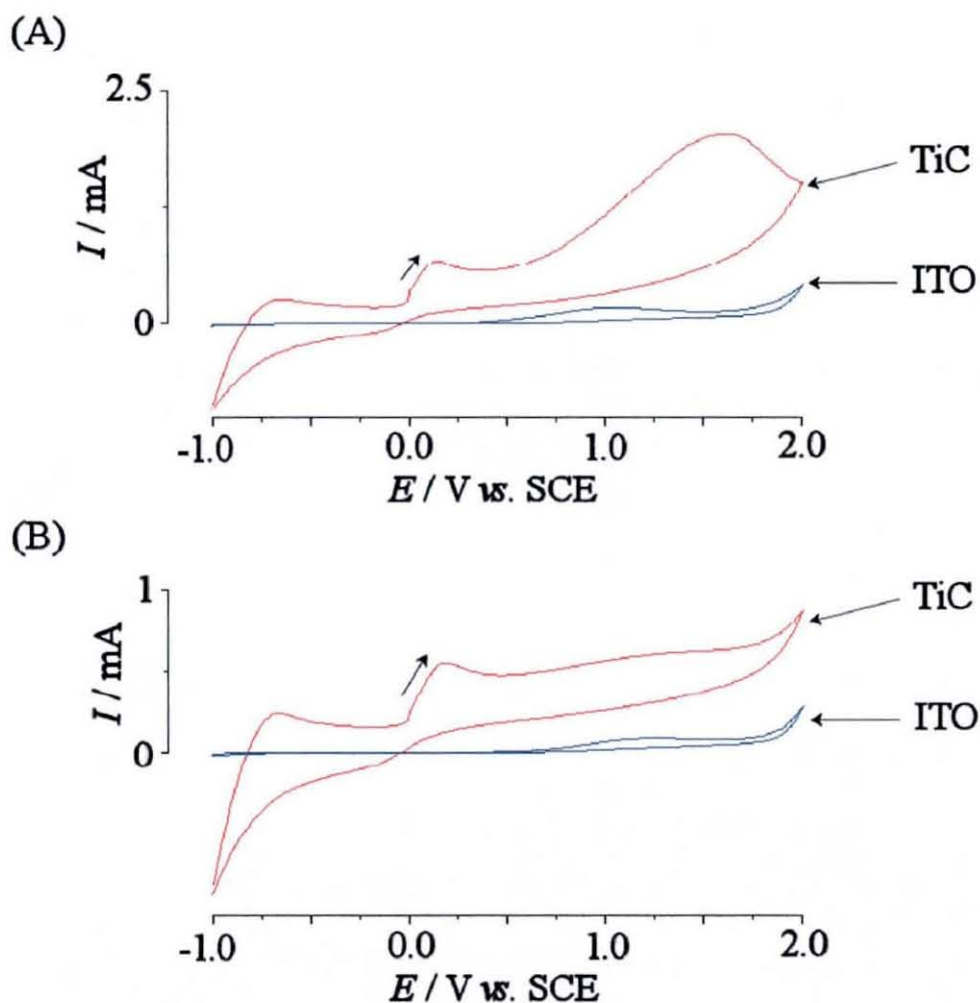
(A)

(B)

Figure 5.16. Cyclic voltammograms (scan rate 50 mVs^{-1}) obtained for (a) scan 1 and (b) scan 2 of the irreversible surface oxidation of a '10 layer' TiC film and clean ITO in aqueous 0.1 M phosphate buffer pH 7 in the presence of 2 mM ascorbic acid.

Substantial oxidation of ascorbic acid occurs at potentials of *ca.* 0 V *vs* SCE and the magnitude of the current is proportional to ascorbic acid concentration. As for the hydroquinone experiments, the effect of analyte concentration on the voltammetry was investigated using a '10 layer' TiC film electrode. Oxidation of ascorbic acid was recorded for both a TiC electrode (Figure 5.17A) and a blank ITO electrode (Figure 5.17B) for concentrations as low as 50 nM ascorbic acid.
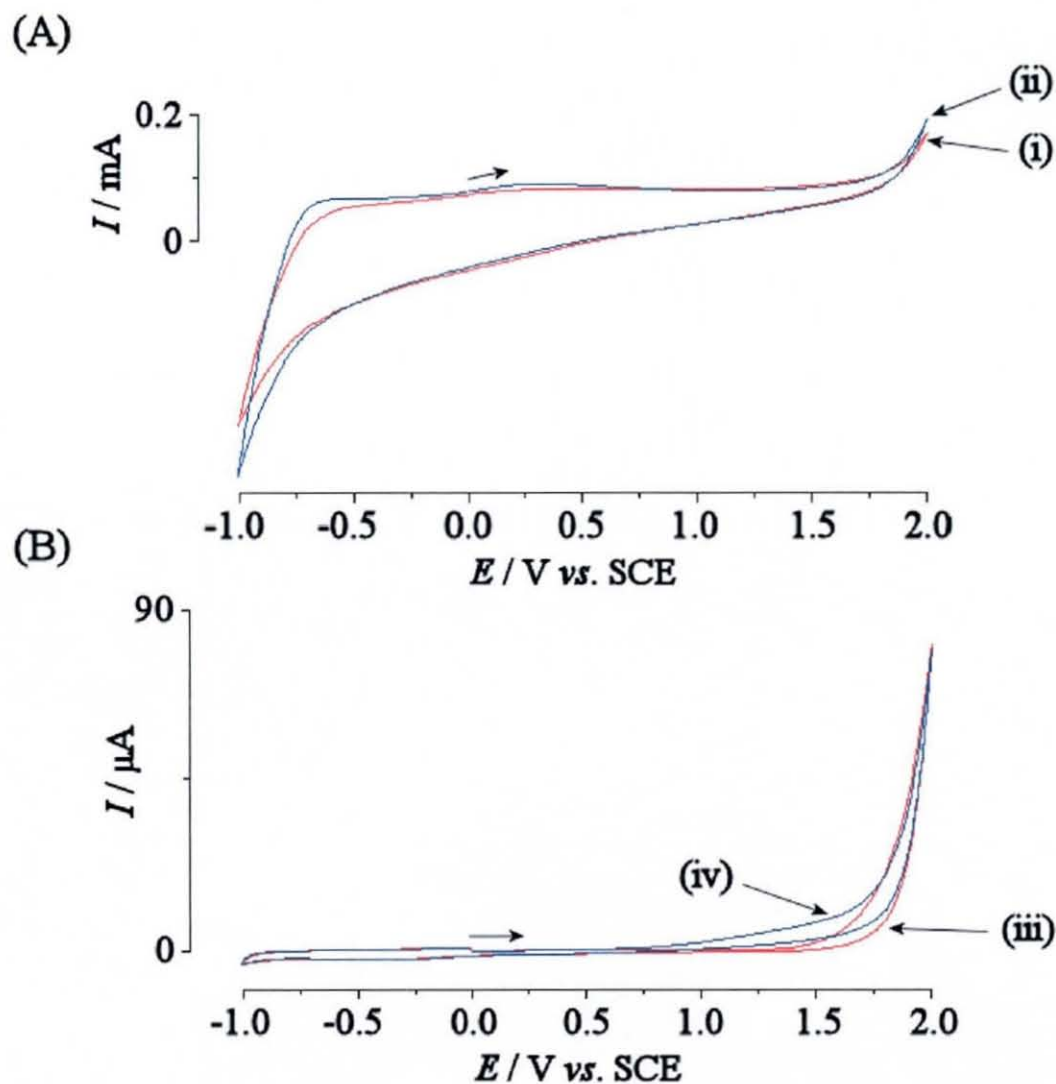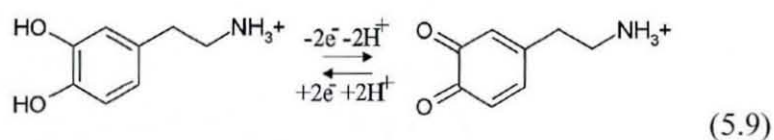

Figure 5.17. Cyclic voltammograms (scan rate 100 mVs^{-1}) for (A) scan 3 of a '10 layer' TiC film in (i) aqueous 0.1 M phosphate buffer pH 7 and (ii) in aqueous 0.1 M phosphate buffer pH 7 plus 50 nM ascorbic acid and (B) scan 1 of a clean ITO electrode in (iii) aqueous 0.1 M phosphate buffer pH 7 and (iv) in aqueous 0.1 M phosphate buffer pH 7 plus 50 nM ascorbic acid

5.8. The Electrocatalytic Oxidation of Dopamine on Nanoparticulate Titanium Carbide

A similar experiment was carried out in the presence of 2 mM dopamine and 2 broad oxidation and reduction peaks are observed (see Figure 5.18) in the absence of TiC. The oxidation and re-reduction of dopamine (equation 5.9) at clean ITO was highly irreversible and in the presence of TiC nanoparticles almost reversible responses (consistent with previous studies[27]) are observed.

$$(5.9)$$

The oxidation of dopamine occurs with a peak current proportional to dopamine concentration and at a potential approximately 0.1 V more positive compared to the oxidation of ascorbic acid under the same conditions.
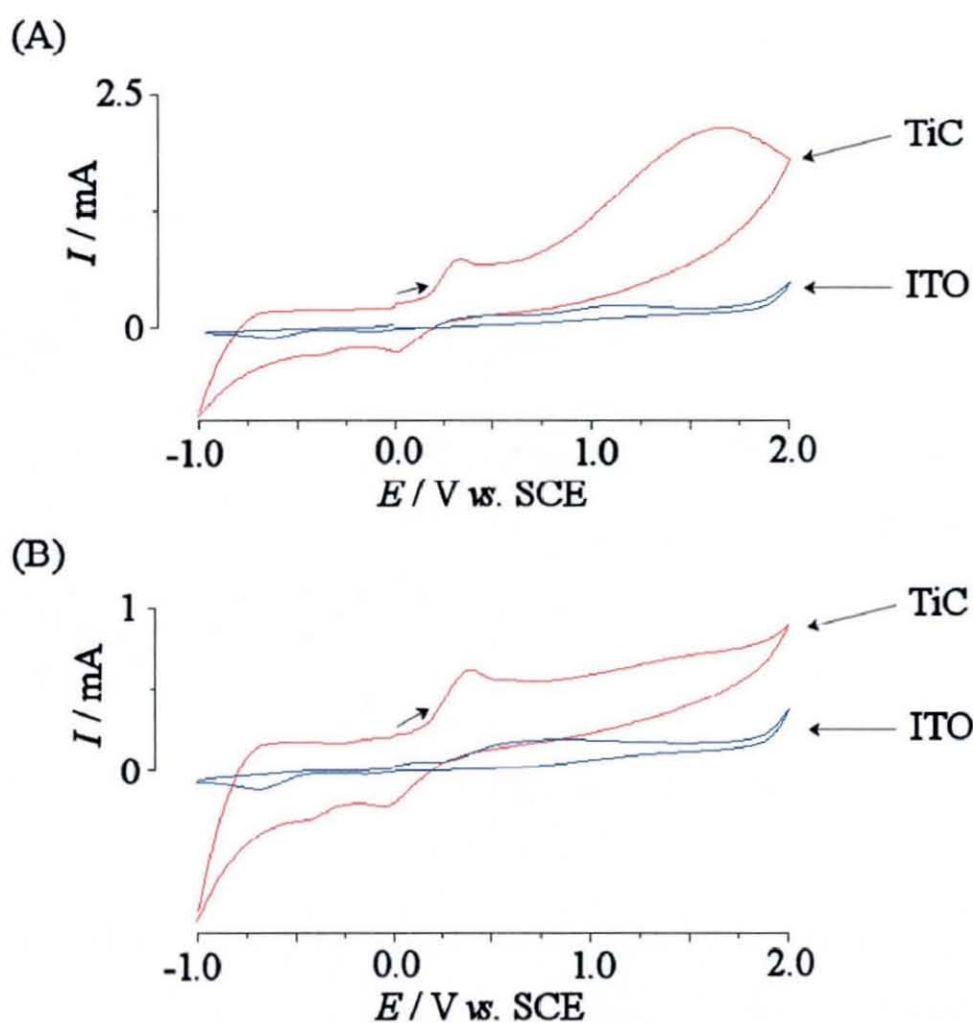
Figure 5.18. Cyclic voltammograms (scan rate 50 mVs^{-1}) obtained for (a) scan 1 and (b) scan 2 of the irreversible surface oxidation of a '10 layer' TiC film and clean ITO in aqueous 0.1 M phosphate buffer pH 7 in the presence of 2 mM dopamine.

Using a '10 layer' TiC film electrode (Figure 5.19A) and a blank ITO electrode (Figure 5.19B), redox responses can be recorded for dopamine concentrations as low as 10 nM, five times lower than the lowest concentration of ascorbic acid to produce a visible voltammetric response.
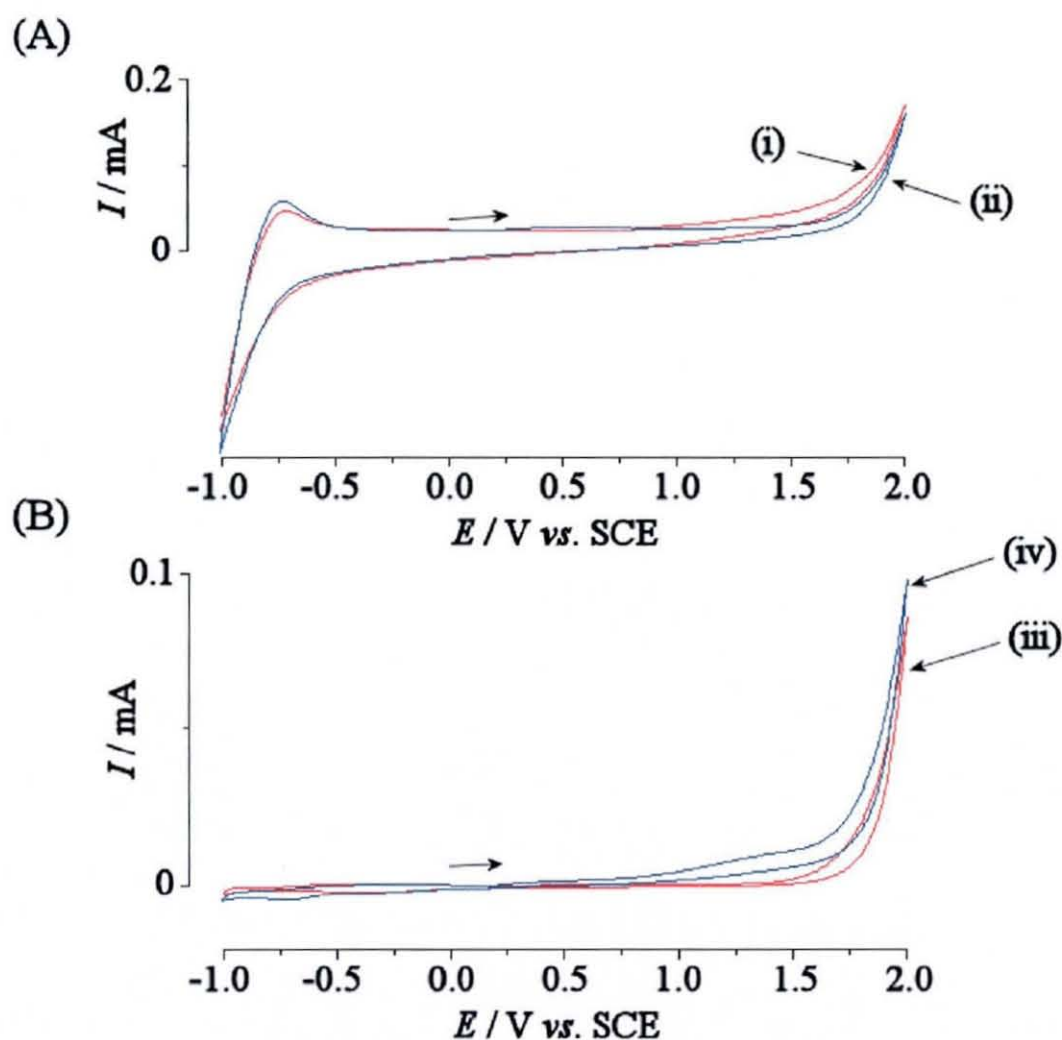
Figure 5.19. Cyclic voltammograms (scan rate 100 mVs^{-1}) for (A) scan 3 of a '10 layer' TiC film in (i) aqueous 0.1 M phosphate buffer pH 7 and (ii) in aqueous 0.1 M phosphate buffer pH 7 plus 10 nM dopamine and (B) scan 1 of a clean ITO electrode in (iii) aqueous 0.1 M phosphate buffer pH 7 and (iv) in aqueous 0.1 M phosphate buffer pH 7 plus 10 nM dopamine.

The reactivity of TiC-TiO$_2$ core-shell nanoparticles has been surveyed only in aqueous phosphate buffer media here. However, the reactivity of the surface can be expected to change depending on the availability of surface sites and the ability of the analyte to reversibly bind to the surface.

5.9. The Electrocatalytic Oxidation of Nitric Oxide on Nanoparticulate Titanium Carbide

The quantitative detection of nitric oxide (NO) in biological models is difficult due to the low concentration and relatively short half life caused by its high chemical reactivity with O_2 or haemoglobin to form nitrite (NO_2^-) or nitrate (NO_3^-).[31] Here the ability of TiC nanoparticulate films to catalyse the oxidation of NO in aqueous solution is investigated.

Using a '10-layer' TiC film electrode, the voltammetric response was recorded in 0.1 M pH 7 phosphate buffer solution before and after the addition of 60 μM NO as shown in Figure 5.20. Two oxidation peaks are seen, the first much smaller peak (peak 1) at approximately 0.64 V *vs.* SCE and a bigger broad peak (peak 2) at approximately 0.92 V *vs.* SCE.

Figure 5.20. Cyclic voltammograms (scan rate 100 mVs^{-1}) obtained for a '10 layer' TiC film in aqueous 0.1 M phosphate buffer pH 7 (i) before and (ii) after the addition of 60 μM NO.

After scanning to a more positive potential and generating the core – shell TiC-TiO$_2$ nanoparticle film, both the oxidation signals are lost (Figure 5.21). In comparison, the electrocatalytic oxidation of hydroquinone, dopamine, and ascorbic acid, is

retained after the complete surface oxidation of the TiC nanoparticles. This indicates that the TiO_2 surface is not ideal for the oxidation of NO.

Figure 5.21. Cyclic voltammograms (scan rate 100 mVs^{-1}) obtained for a '10 layer' TiC film in aqueous 0.1 M phosphate buffer pH 7 in the presence of 60 μM NO (i) before and (ii) after the irreversible surface oxidation.

The presence of two oxidation peaks and the high reactivity of NO, it is necessary to consider that after the initial one electron oxidation (equation 5.10a), the NO^+ species generated reacts with the aqueous environment forming NO_2^- (equation 5.10b) which subsequently undergoes a further 2 electron transfer process (equation 5.10c).[31]

$$NO \rightarrow NO^+ + e^- \qquad\qquad (5.10a)$$

$$NO^+ + H_2O \rightarrow NO_2^- + 2H^+ \qquad\qquad (5.10b)$$

$$NO_2^- + H_2O \rightarrow NO_3^- + 2H^+ + 2e^- \qquad\qquad (5.10c)$$

To verify this, the oxidation of NO_2^- was investigated. Using a fresh '10-layer' TiC film electrode, the voltammetric response was recorded in 0.1 M pH 7 phosphate buffer solution before and after the addition of 60 μM NO_2^-, however no oxidation peak was observed. On increasing the level of NO_2^- to 600 μM a broad oxidation peak is observed as shown in Figure 5.22 at a similar potential to peak 2 in the NO

experiment. This indicates that peak 1 corresponds to equation 5.10a, the oxidation of NO and peak 2 corresponds to equation 5.10c.
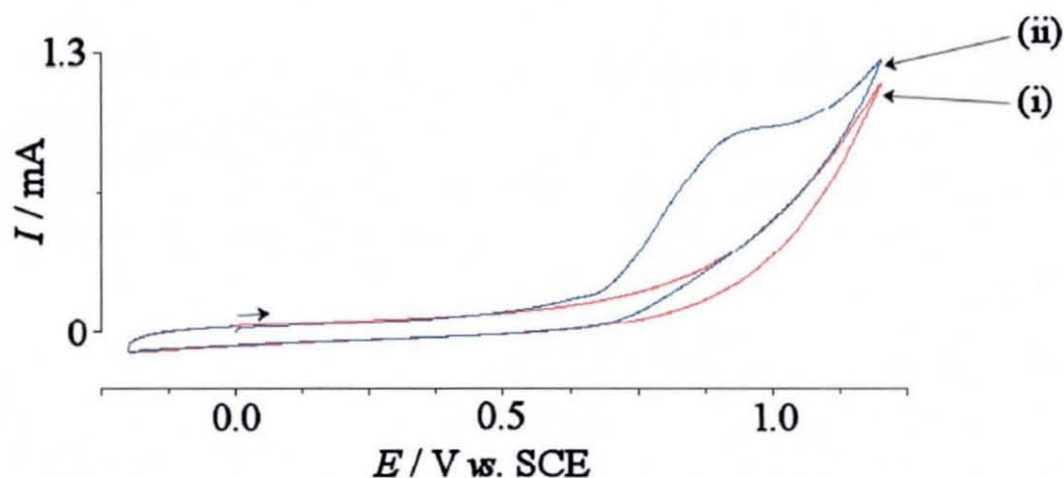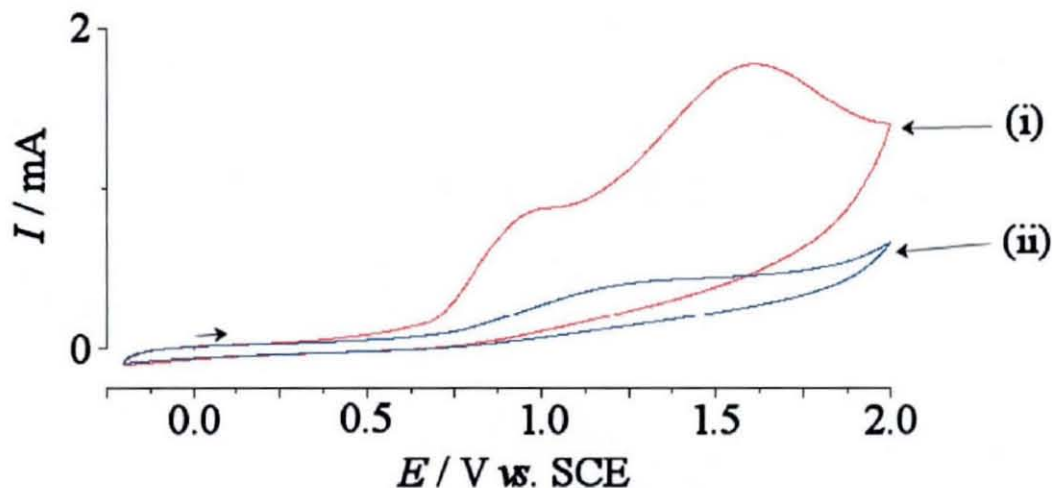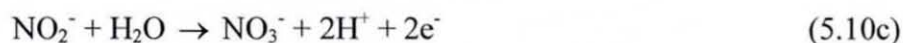

Figure 5.22. Cyclic voltammograms (scan rate 100 mVs^{-1}) obtained for a '10 layer' TiC film in aqueous 0.1 M phosphate buffer pH 7 (i) before and (ii) after the addition of 600 µM NO$_2^-$.

By scanning to more negative potentials and observing the electrochemical surface oxidation, the catalytic oxidation peak for NO$_2^-$ is lost as shown in Figure 5.23.
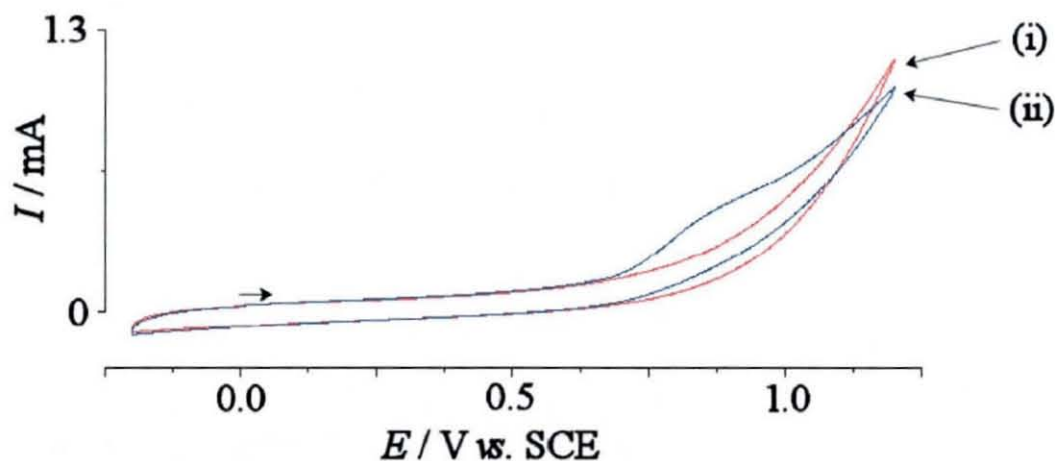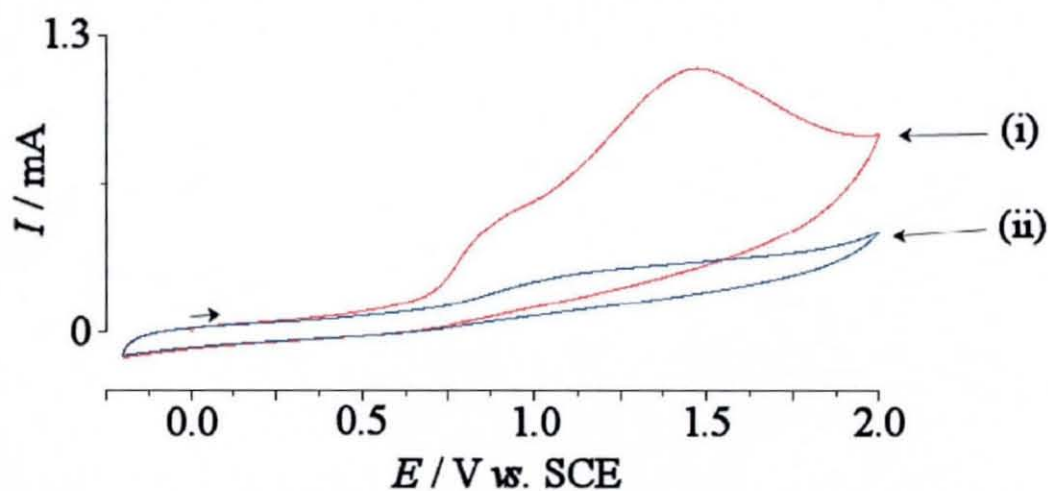

Figure 5.23. Cyclic voltammograms (scan rate 100 mVs^{-1}) obtained for a '10 layer' TiC film in aqueous 0.1 M phosphate buffer pH 7 in the presence of 600 µM NO$_2^-$ (i) before and (ii) after the irreversible surface oxidation of TiC nanoparticles.

NO gives a bigger response with respect to NO_2^-, indicating a preferred sensing system. Both signals are lost in the background in the initial scans and low concentrations.

5.10. Conclusions

It has been shown that TiC nanoparticles can be electrochemically and thermally oxidised to give core-shell $TiC-TiO_2$ nanoparticles. The shape and appearance of the particles is not affected by the solid state transformation from TiC to TiO_2 and the oxide film appears to grow symmetrically around the particles. However, the electrical properties change from those of a good conductor to a semi-conductor. Core-shell $TiC-TiO_2$ nanoparticles represent a novel electro-catalytically active material for porous thin film or other types of composite electrodes e.g. pastes. Catalytic effects have been demonstrated for oxidation of hydroquinone, dopamine, ascorbic acid and nitric oxide. TiO_2 shells provide adsorption sites and well defined surface properties whereas TiC cores provide conductivity over a wide potential window. Analytes of interest for future work include other quinones (e.g. catechol), carbon monoxide, ammonia, thiols, and hydrocarbons.[34]

5.11. References

[1] G. Radhakrishnan, R.E. Robertson, P.M. Adams, R.C. Cole, *Thin Solid Films* 420-421 (2002) 553

[2] W. Lu, D. Zhang, R. Wu, T. Sakata, H. Mori, *J. Alloy Compounds* 327 (2001) 248

[3] A. Lupu, D. Compagnone, S. Orlanducci, M.L. Terranova, V. Magearu, G. Palleshi, *Electroanalysis* 16 (2004) 1704

[4] U. Diebold, *Surf. Sci. Reports* 48 (2003) 53

[5] L. Kavan, M. Grätzel, J. Rathousky, A. Zukal, *J. Electrochem. Soc.* 143 (1996) 394

[6] G. Boschloo, D. Fitzmaurice, *J. Electrochem. Soc.* 147 (2000) 1117

[7] J. Bisquert, *J. Phys. Chem. B* 108 (2004) 2323

[8] I. Mora-Sero, J. Bisquert, *Nano Lett.* 3 (2003) 945

[9] F. Fabregat-Santiago, I. Mora-Sero, G. Garcia-Belmonte, J. Bisquert, *J. Phys. Chem. B* 107 (2003) 758

[10] K.J. McKenzie, P.M. King, F. Marken, C.E. Gardner, J.V. Macpherson, *J. Electroanal. Chem.* 579 (2005) 267

[11] N.S. Allen, M. Edge, G. Sandoval, J. Verran, J. Stratton, J. Maltby, *Photochem. Photobiol.* 81 (2005) 279

[12] P.K. Dutta, M. Frank, G.W. Hunter, M. George, *Sens. Actuators B* 106 (2005) 810

[13] S. Trasatti, *Electrochim. Acta* 45 (2000) 2377

[14] P.C.S. Hayfield, *Development of a New Electrode Material Monolithic Ti₄O₇ Ebonex Ceramic*, Finishing Publication Ltd., Stevenage, UK, 2002

[15] Y. Wang, C. Li, S. Hu, *J. Solid Sate Electrochem.* 10 (2006) 383

[16] W. Fu, H. Yang, M. Li, L. Chang, Q. Yu, J. Xu, G. Zou, *Mater. Lett.* in press (2006)

[17] I. Pastoriza-Santos, D.S. Koktysh, A.A. Mamedov, M. Giersig, N.A. Kotov, L.M. Liz-Marzan, *Langmuir* 16 (2000) 301

[18] P. Viravathana D.W.M. Marr, *J. Colloid Interface Sci.* 221 (2000) 301

[19] I.B. Jang, J.H. Sung, H.J. Choi, I. Chin, *Synth. Met.* 152 (2005) 9

[20] E. V. Milsom, H.R. Perrott, L.M. Peter, F. Marken, *Langmuir* 21 (2005) 9482

[21] Y-L. Li, T. Ishigaki, *Chem. Phys. Lett.* 367 (2003) 561

[22] H. Kiyono, S. Shimada, K. Sugawara, A. Christensen, *Solid State Ionics* 160 (2003) 373

[23] K.J. McKenzie, F. Marken, M. Opallo, *Bioelectrochemistry* 66 (2005) 41

[24] W.R. Vandaveer IV, S.A. Pasas-Farmer, D.J. Fischer, C.N. Frankenfeld, S.M. Lunte, *Electrophoresis* 25 (2004) 3528

[25] V. Zucolotto, M. Ferreira, M.R. Cordeiroo, C.J.L. Constantino, W.C. Moreira, O.N. Oliveira Jr., *Sens. Actuators B* 113 (2006) 809

[26] K. Miyazaki, G. Matsumoto, M. Yamada, S. Yasui, H. Kaneko, *Electrochim. Acta* 44 (1999) 3809

[27] S-M.Chen, W-Y. Chzo, *J. Electroanal. Chem.* 587 (2006) 226

[28] J.-K. Pak, P.H. Tran, J.K.T. Chao, R. Ghodadra, R. Rangarajan, N.V. Thakor, *Biosens. Bioelectron.* 13 (1998) 1187

[29] Z.H. Taha, *Talanta* 61 (2003) 3

[30] B.W. Allen, C.A. Piantadosi, L.A. Coury, Jr., *Nitric Oxide* 4 (2000) 75

[31] Y. Wang, C. Li, S. Hu, *J. Solid State Electrochem.* 10 (2006) 383

[32] M.D. Ward, in I. Rubinstein (ed.), *Physical Electrochemistry*, Marcel Dekker, New York, 1995, p. 293

[33] Joint Committee on Powder Diffraction Standards

[34] H.H. Hwu, J.G. Chen, *Chem. Rev.* 105 (2005) 185 & refs. therein

Chapter 6

Electrochemical Characterisation of Mesoporous CeO$_2$ Nanoparticle Films

6.1. Introduction

CeO$_2$ is used widely in a number of fields including as a polishing material,[1] and membrane material for filters.[2] Cerium (IV) oxide has been used as a substrate for heterogeneous catalysts and is a component in automobile exhausts,[3] providing a high oxygen storage capacity.[4] Further applications of CeO$_2$ include as thin films for anti-corrosion coatings,[5] and in solid oxide fuel cells.[6] In electrochromism, CeO$_2$ thin films have been employed in smart windows as ion storage materials or counter electrodes[7] because of its high optical transparency in the visible region and its ability to exchange cations and electrons.[8] CeO$_2$ may be regarded (and often is) as an inert oxide with little electrochemical activity.[9,10] However, it is shown here, that CeO$_2$ is electrochemically active and exhibits a rich surface electrochemistry in aqueous phosphate buffer solvents.

CeO$_2$ can be obtained in the form of a sol and nanoparticles can be adsorbed onto electrode surfaces. Furthermore, by applying suitable binder molecules, multi-layer films can be formed and the thickness of the resulting mesoporous CeO$_2$ surface layer can be controlled.

Work in this chapter demonstrates (i) the surface electrochemistry of CeO$_2$, (ii) effect of the binder molecule on multi-layer formation and electrochemistry, (iii) the formation of new phosphate phases during electrochemical reduction of CeO$_2$ in aqueous phosphate buffer solution and (iv) the electrochemistry of multi-layer CeO$_2$ nanoparticle films in organic solvent.

6.2. Experimental

6.2.1. Chemicals

Demineralised and filtered water was taken from an Elga water purification system (Elga, High Wycombe, Bucks, UK) with a resistivity of not less than 18 MOhm cm. Cerium (IV) oxide sol (ceranite, *ca.* 10-20 nm diameter, 20% in aqueous HNO_3, pH 2-3) was obtained from Nyacol Nano Technologies, Inc., MA, USA and diluted 50-fold with deionised water. Phytic acid dodecasodium salt hydrate, 1,2,3,4,5,6-cyclohexanehexacarboxylic acid monohydrate, acetonitrile, tetrabutylammonium hexafluorophosphate, cerium (III) carbonate, NaOH, HNO_3, H_3PO_4, KCl, KOH, K_2HPO_4, and KH_2PO_4 were obtained commercially in analytical or the highest purity grade available.

6.2.2. Instrumentation

Voltammetric measurements were performed with a computer controlled Eco Chemie PGSTAT20 Autolab potentiostat system. Experiments were conducted in staircase voltammetry mode with a platinum gauze counter electrode and saturated calomel reference electrode (SCE (saturated KCl), REF401, Radiometer). The working electrode was a tin-doped indium oxide (ITO) coated glass (10 mm × 60 mm, resistivity 20 Ω per square) with approximately 8% tin, obtained from Image Optics Components Ltd. (Basildon, Essex). The ITO electrode surface was modified with a porous metal oxide film giving a geometric working electrode area of 1 cm^2, defined using Magic tape (Scotch 3D).

A quartz crystal oscillator circuit (Oxford Electrodes) connected to a frequency counter (Fluke, PM6680B) allowed the resonance frequency of the quartz crystal sensor to be monitored simultaneously to conducting voltammetric experiments. A Faraday cage was used to contain the quartz crystal to minimise noise interference. The analogue output of the counter was fed into the ADC input of an Autolab potentiostat system (Eco Chemie, Netherlands) and data processing was possible

with GPES software (Eco Chemie, Netherlands). Layer-by-layer deposition processes were monitored with the crystal suspended in air. Droplets of solution were applied to one side of the crystal and after rinsing and drying the frequency measured and monitored step-by-step.

Prior to conducting electrochemical experiments, all solutions were purged with argon (BOC, UK). All experiments were carried out at a temperature of $22 \pm 2^{\circ}C$. An Elite tube furnace system was employed for cleaning ITO electrode surfaces (at $500^{\circ}C$ in air) and for calcining metal oxide binder films (at $500^{\circ}C$ in air).

Scanning electron microscopy images were obtained with a Leo 1530 Field Emission Gun Scanning Electron Microscope (FEGSEM) system. Prior to FEGSEM imaging, the sample surface was scratched with a scalpel blade. XRD measurements were obtained on a Bruker D8 Advance powder diffractometer fitted with a PSD detector and using Cu $K_{\alpha 1}$ radiation.

6.2.3. Deposition and Electrode Preparation Procedures

Deposition of multi-layer mesoporous films of metal oxide and organic binder on ITO glass electrodes followed a layer-by-layer dip coating method described in section 3.2.3 where pot 1 contained 0.4 %wt cerium (IV) oxide sol. The dipping process was undertaken using a robotic Nima dip coating carousel (DSG – Carousel, Nima Technology, Coventry, UK) and repeated to give multi-layer deposits. The different binders used were phytic acid (40 mM in pH 3 aqueous solution), and 1,2,3,4,5,6- cyclohexanehexacarboxylic acid monohydrate (CHHCA) (10 mM in aqueous solution).

6.3. Layer-by-Layer Deposition of CeO$_2$ with Molecular Binders

In this investigation the deposition of CeO$_2$ nanoparticles onto a clean ITO electrode surface occurs spontaneously upon dipping the electrode into a solution of cerium (IV) oxide sol for 60 seconds. It is possible to immerse these mono-layers of metal oxides into a solution of appropriate binder and build up multiple layers on the ITO coated glass surface as with the TiO$_2$ films, shown in Figure 3.1 in Chapter 3.

Figure 6.1 shows a typical FEGSEM image with a scratch line indicating a clean electrode surface. Deposited CeO$_2$ nanoparticles are typically 10-20 nm in diameter and some agglomerates are visible.
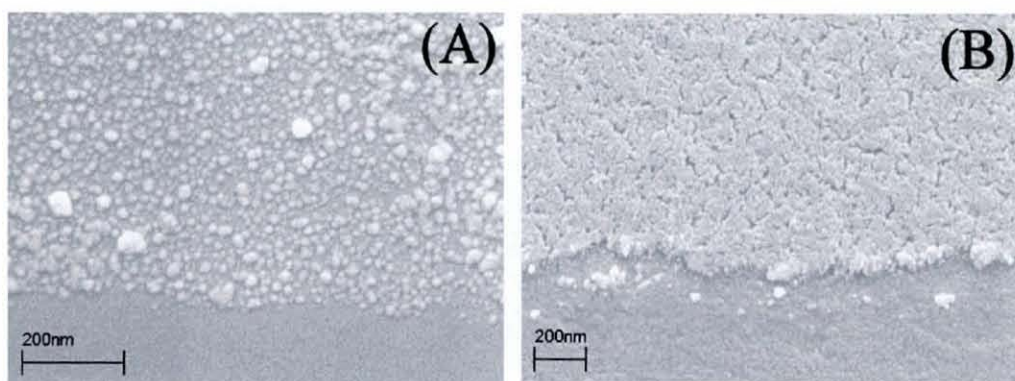

Figure 6.1. FEGSEM images of cerium oxide nanoparticles (*ca.* 10-20 nm diameter) deposited layer-by-layer with phytic acid binder onto the surface of an ITO doped glass slide. In (A) a single layer CeO$_2$ deposit and in (B) a 20 layer deposit after furnace treatment are shown.

The electron microscopy data in Figure 6.1 can be supported by experiments with quartz crystal oscillator measurements conducted in air. Figure 6.2 shows the subsequent reduction of the resonance frequency of an ITO coated quartz crystal resonator during the layer-by-layer deposition process of CeO$_2$ with the binder molecules, phytic acid and CHHCA.
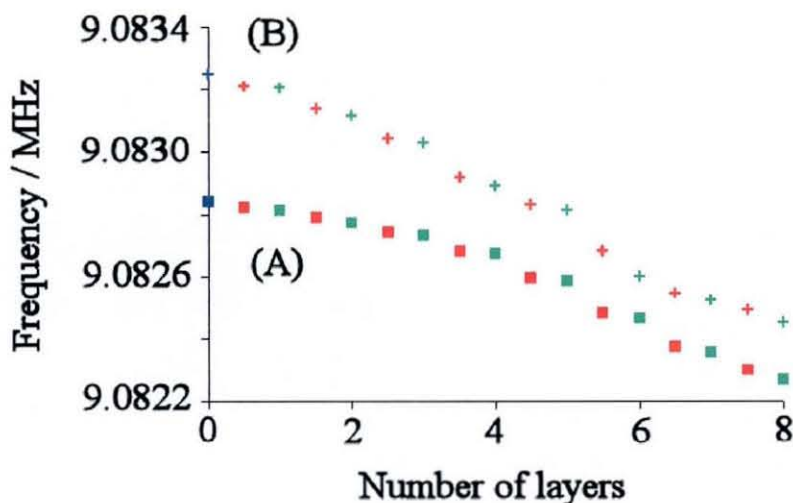
Figure 6.2. A plot of the resonance frequency change for an ITO coated quartz crystal (■,✚) during layer-by-layer deposition of (A) CeO_2 (■) with phytic acid (■) and (B) CeO_2 (✚) with CHHCA (✚).

For the deposition of CeO_2 with phytic acid, each CeO_2 phytate layer is consistent with a 72 Hz change corresponding to 76 ng (according to the Sauerbrey equation[11]), this gives a weight of approximately 60 ng CeO_2 and 16 ng phytic acid (molecular weight 924 g mol^{-1}) or 3.2×10^{-11} mol per layer (ignoring the presence of water). For the deposition of CeO_2 with CHHCA, each CeO_2 CHHCA layer is consistent with a 100 Hz change corresponding to 105 ng, this gives a weight of approximately 70 ng CeO_2 and 35 ng CHHCA (molecular weight 366 g mol^{-1}) or 9.5×10^{-11} mol per layer.

6.4. Reactivity of CeO_2 Nanoparticle Mono- and Multi-layers

The mono-layer of CeO_2 nanoparticles formed on ITO electrode surfaces is electrochemically active. Voltammograms shown in Figure 6.3 have been obtained in aqueous 0.1 M phosphate buffer solution (see Figure 6.3i and ii) and in 0.1 M KCl (see Figure 6.3iii). In the presence of KCl a strong reduction response starting at a potential of 0.25 V *vs.* SCE is clearly detected. This reduction response is reversible and upon scanning the potential positive corresponding oxidation responses are observed. The voltammetric signal remains stable over several

potential cycles and is attributed to a Ce(IV/III) process at the nanoparticle surface.
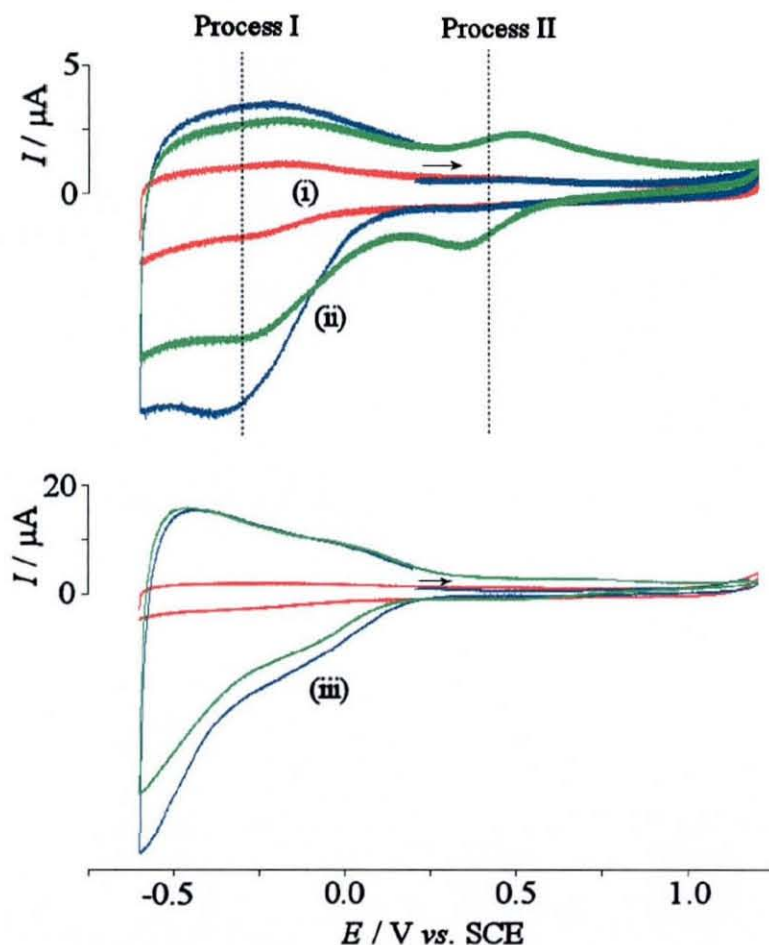

Figure 6.3. (i) Cyclic voltammogram (scan rate 100 mVs⁻¹) of a clean ITO glass electrode in aqueous 0.1 M phosphate buffer solution at pH 7 (ii) Cyclic voltammogram (scan rate 100 mVs⁻¹) obtained for a 1 layer CeO₂ nanoparticle film on ITO in aqueous 0.1 M phosphate buffer solution at pH 7. The blue line corresponds to scan 1 and the green line scan 2. (iii) Cyclic voltammogram (scan rate 100 mVs⁻¹) obtained for a 1 layer CeO₂ nanoparticle film on ITO in aqueous 0.1 M KC.

It is interesting to compare the charge under the reduction response with the estimated amount of CeO₂ on the electrode surface. Integration of the charge under the voltammetric response shown in Figure 6.3iii gives *ca.* 80 μC. In comparison, for a mono-layer of 10 nm diameter CeO₂ particles an expected charge for a one-electron process of 2 mC can be calculated. Therefore roughly about 5% of the deposit is electrochemically reduced and re-oxidised with a scan rate of 0.1 Vs⁻¹ and immersed in aqueous 0.1 M KCl. It can be assumed that only the surface of the

CeO_2 nanoparticles is affected.

Cyclic voltammograms obtained in the presence of phosphate anions reveal distinct differences (see Figure 6.3). The initial reduction process at E_{mid} = -0.28 V *vs.* SCE is now considerably smaller in current (Process I) and a new voltammetric response is detected at a potential of E_{mid} = 0.42 V *vs.* SCE (Process II). The signal associated with Process II only occurs after reduction in Process I and a gradual change with currents for Process I decreasing and currents for Process II increasing is observed upon continuous potential cycling (see Figure 6.3ii). Therefore a slow chemical reaction step, presumably the formation of a solid phosphate, must be responsible for this conversion. In order to prove this hypothesis cerium (III) phosphate was prepared by direct precipitation from Ce(III) solution with phosphate. A clean ITO electrode brought into contact with the $CePO_4$ precipitate, dried in air, and re-immersed in aqueous 0.1 M phosphate buffer shows voltammetric responses only for Process II (not shown). Therefore Process II is identified as Ce(IV/III) phosphate redox system present most likely on the surface of the CeO_2 nanoparticles.

In comparison to the similar experiments for TiO_2 films in chapter 2, the more inert nature of the TiO_2 with respect to CeO_2 allows charging and discharging processes to occur reversibly. The difference in behaviour can be explained based on the crystal structure of TiO_2 (anatase) and CeO_2 (ceranite). The former anatase structure has Ti(IV) coordinated in a distorted octahedron with bond distances of 1.96 to 2.05 Å. In contrast, in ceranite Ce(IV) is coordinated to eight oxygen atoms in a fluorite structure (see Figure 6.4) with 2.34 Å bond length. The Ce^{4+} - O^{2-} bond is weaker, and after reduction to Ce(III), rapid ligand exchange occurs.
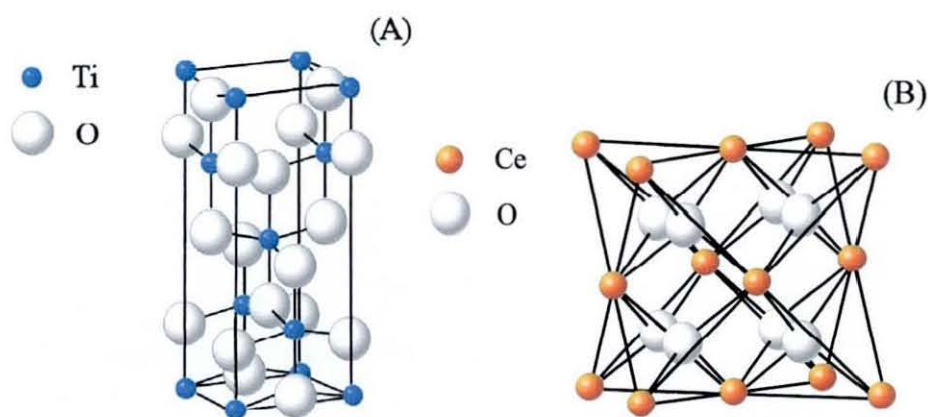
Figure 6.4. Figure to illustrate the difference in the crystal forms for (A) anatase TiO_2 [12] and (B) fluorite structure of CeO_2.[13]

In order to obtain more information about this redox system, experiments were conducted in different concentrations of phosphate (in aqueous KCl solution to maintain an overall electrolyte solution ionic strength of approximately 0.1M) and at various proton activities. Figure 6.5 shows the effect of phosphate concentration. The reduction response for Process I can clearly be seen to depend on the phosphate concentration. The higher the phosphate concentration the smaller is this voltammetric signal. Continuous potential cycling ((i) scan 2 to (ii) scan 15 are shown) leads to an increase in peak currents for Process II but the effect of the phosphate concentration dominates. Figure 6.5D shows a comparison of the fifteenth scan of cyclic voltammograms for phosphate concentrations of 0.1 M, 0.01 M, 1 mM, and 0.1 mM. A clear trend is observed with higher phosphate concentrations suppressing the voltammetric responses. Apparently, phosphate is inhibiting the formation of cerium (III) phosphate probably due to the reduced solubility of the reaction product in the presence of higher phosphate concentrations.
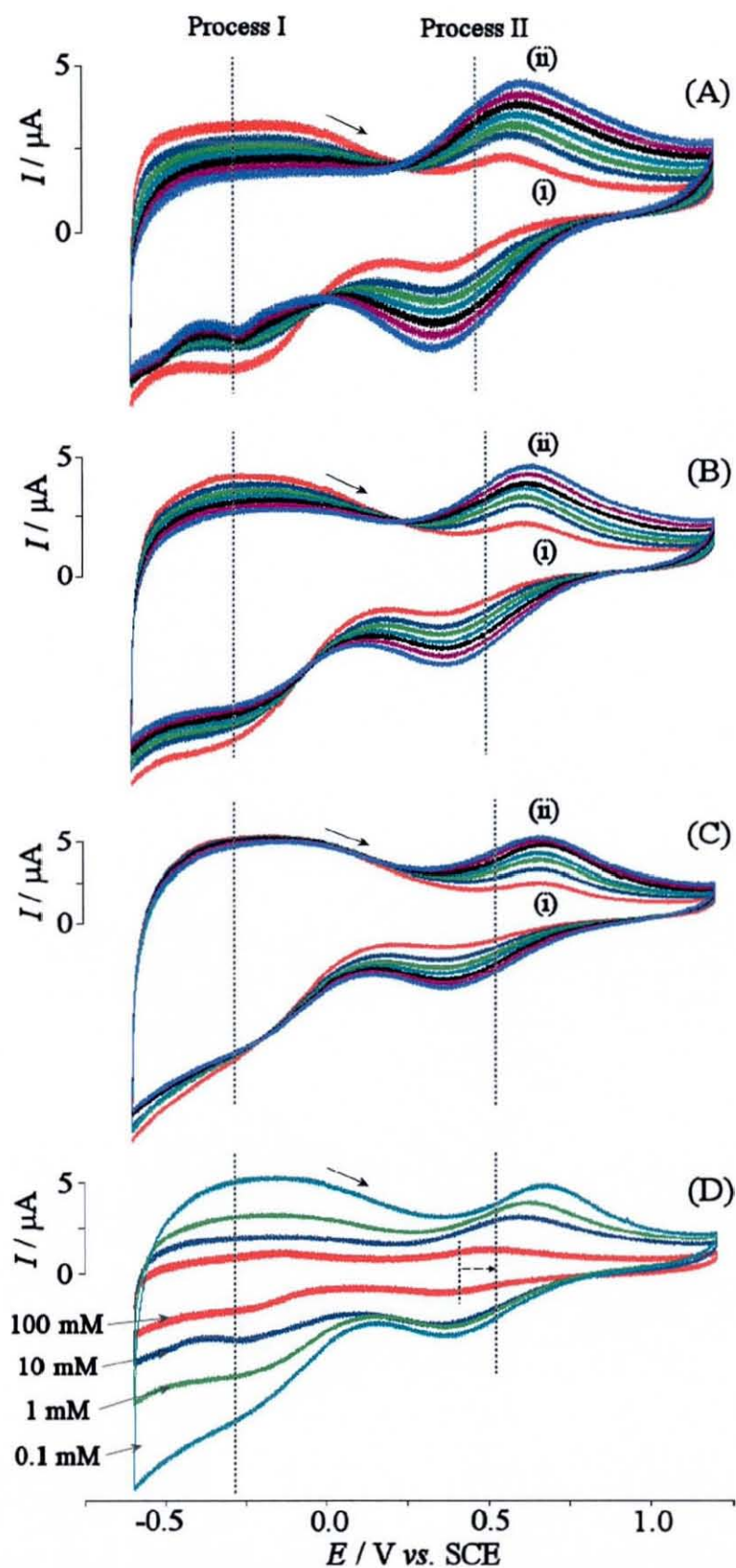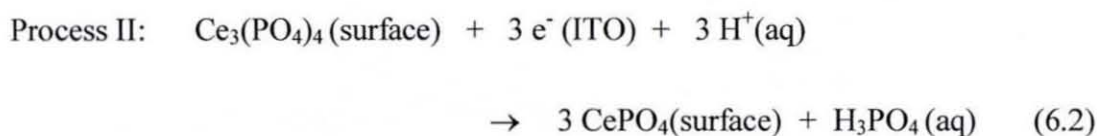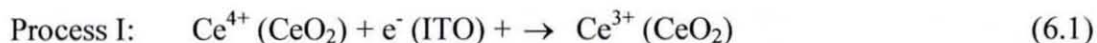
Figure 6.5. Multicycle voltammograms (scan rate 100 mVs⁻¹) for ITO electrodes with 1 layer CeO₂ on ITO in the presence of (A) 10 mM (B) 1 mM and (C) 0.1 mM phosphate in KCl. Scans 2, 5, 7, 9, 11, 13 and 15 are shown. (D) Shows a comparison of scan 15 with varying phosphate concentration.

The midpoint potential for Process II is sensitive to both phosphate concentration and proton activity (see Figure 6.6) and the slopes observed are 24 mV per decadic change in phosphate concentration and 62 mV per pH unit. This allows Process I and Process II to be tentatively assigned (see equation 6.1 and 6.2).

Process I: $Ce^{4+}(CeO_2) + e^-(ITO) + \rightarrow Ce^{3+}(CeO_2)$ (6.1)

Process II: $Ce_3(PO_4)_4(surface) + 3\,e^-(ITO) + 3\,H^+(aq)$

$$\rightarrow \quad 3\,CePO_4(surface) + H_3PO_4(aq) \quad (6.2)$$

The product of the reduction reaction in Process I, $Ce(III)O_2$, is assumed to react with phosphate in the aqueous solution phase to give $Ce(III)PO_4$ at the surface of the nanoparticle deposit. It is very likely that solid structures are formed in a hydrated state rather than according to sum formulas. This can be further supported with the increase of the voltammetric response as a function of film thickness (see below). Independent experiments were performed by precipitating $Ce(III)PO_4$ from aqueous solution and testing the voltammetric response of the precipitate. The result strongly confirms the interpretation of Process II.
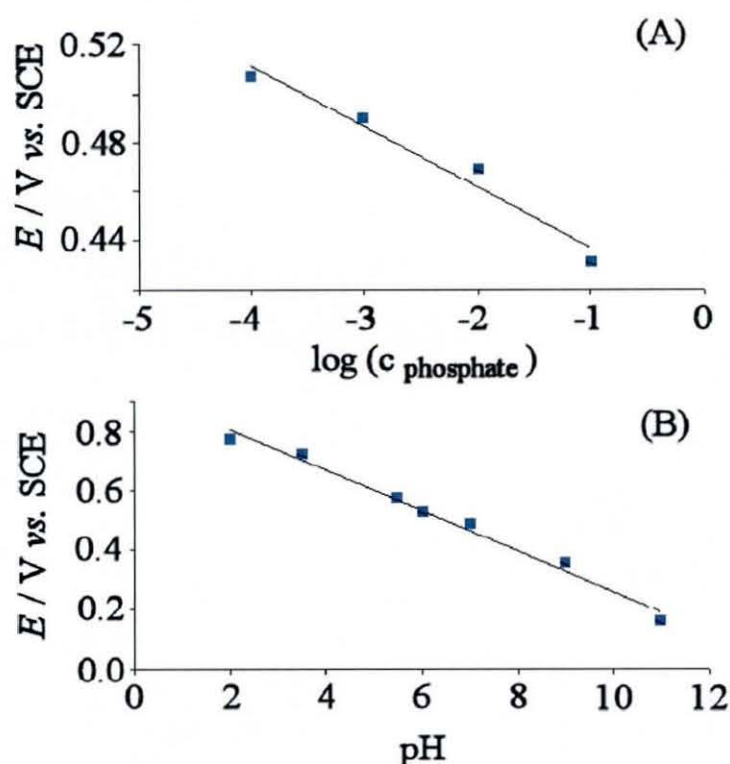
Figure 6.6. Plots of the midpoint potential (scan rate of 100 mVs^{-1}) for process II *vs.* SCE for a single layer CeO_2 nanoparticle film on ITO against (A) the log of phosphate concentration in solution and (B) the pH of a 1mM phosphate buffer solution in aqueous 0.1M KCl.

The deposition of CeO_2 nanoparticles can be continued in the presence of a suitable binder molecule. Multi-layer deposits of CeO_2 lead to increased voltammetric signals both Faradaic and capacitive in nature (see below), probably due to an electronic conduction process involving Ce(IV/III) surface states.

Figures 6.7 and 6.8 show the multicycle voltammograms obtained for ITO electrodes with multi-layer CeO_2 phytate film deposits after calcining (see experimental) in the presence of 1 mM phosphate buffer at pH 7. As seen in the mono-layer experiments without calcination, a gradual change in the peak current is observed upon scanning to negative potentials for process I and for process II. Process II is observed in the first cycle probably due to the presence of phosphate during calcinations. XRD powder diffraction experiments show that the cerunite crystal structure is not changed during the calcining process at 500°C.
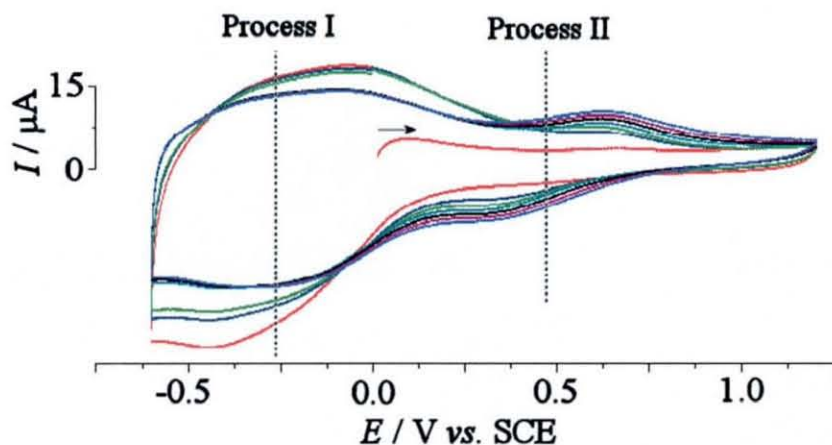
Figure 6.7. Cyclic voltammograms (scan rate 100 mVs^{-1}) for the reduction of a 2 layer CeO$_2$ phytate film on ITO after calcinations. The electrode is immersed in 1 mM phosphate buffer at pH 7 in aqueous 0.1 M KCl. Scans 1, 2, 3, 4, 6, 8 and 10 are shown.

By doubling the amount of CeO$_2$ phytate film deposited onto the ITO electrode surface, the peak current recorded is approximately doubled (see Figure 6.8). Calcining the metal oxide films is also shown to increase the current response, this again can be explained by the increase in conductivity as electron transport through the oxide structure becomes easier due to the lower inter-particle distance.
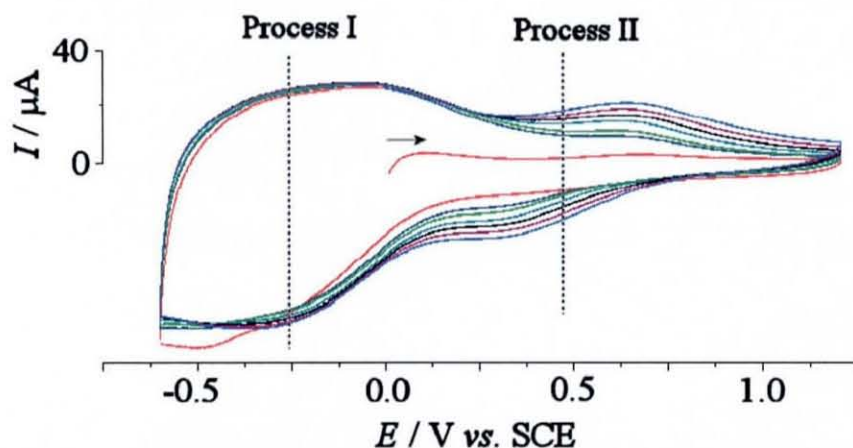

Figure 6.8. Cyclic voltammograms (scan rate 100 mVs^{-1}) for the reduction of a 4 layer CeO$_2$ phytate film on ITO after calcinations. The electrode is immersed in 1 mM phosphate buffer at pH 7 in aqueous 0.1 M KCl. Scans 1, 2, 3, 4, 6, 8 and 10 are shown.

Next, a similar set of experiments were conducted using 1,2,3,4,5,6-cyclohexanehexacarboxylic acid monohydrate (CHHCA) as a binder in the place of the phytic acid. In Figure 6.9 the multicycle voltammograms obtained for ITO electrodes with multi-layer CeO_2 CHHCA deposits in the presence of 1 mM phosphate are shown. As with the phytic acid binder, the expected changes in peak current corresponding to process I and II are clearly being generated. This indicates that not only does CHHCA function as a good binder for metal oxide particles such as CeO_2 but also enables the study of process II without the possible interference of the phosphates on the phytic acid binder molecules. The current responses using the CHHCA binder are greater than those recorded for the calcined phytic acid binder. However, there is less of an effect observed on doubling the film thickness.
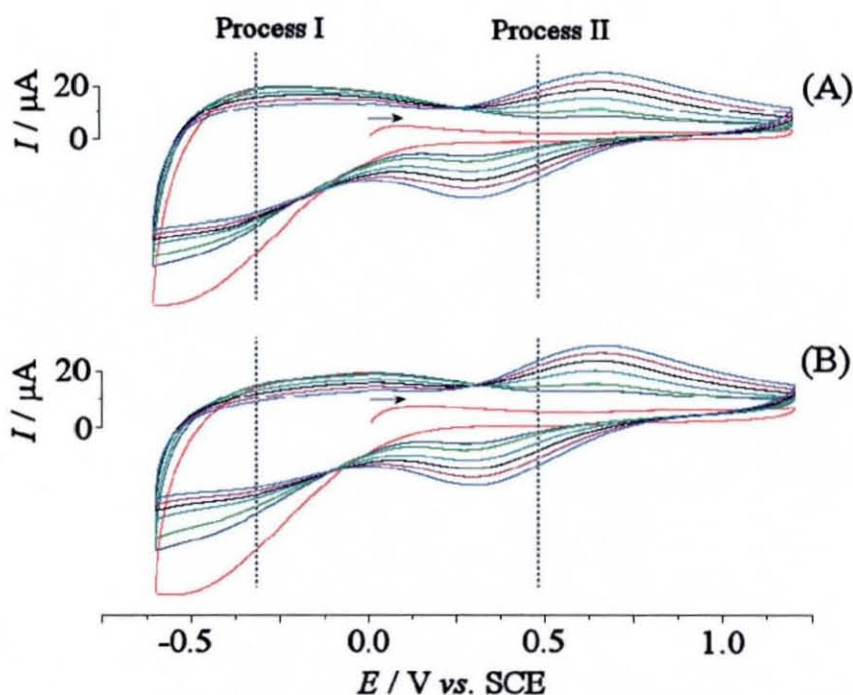

Figure 6.9. Multi-layer cyclic voltammograms (scan rate 100 mVs^{-1}) for (A) 2 layers and (B) 4 layers of CeO_2 – CHHCA deposit on ITO in the presence of aqueous phosphate solution (1 mM, pH 7) in 0.1 M KCl. Scans 1, 2, 3, 4, 6, 8 and 10 are shown in each case.

Next, similar voltammograms were recorded for calcined CeO_2 CHHCA films. Again it is possible to see the effects heat-treating the CeO_2 binder deposits has on

the electrochemical response in the presence of 1 mM phosphate (see Figure 6.10). The difference in rate of change in the peak current for process I and II for the calcined electrodes is demonstrated (slower changes at calcined electrodes) and consistent with data for the calcined CeO_2 phytate deposits.
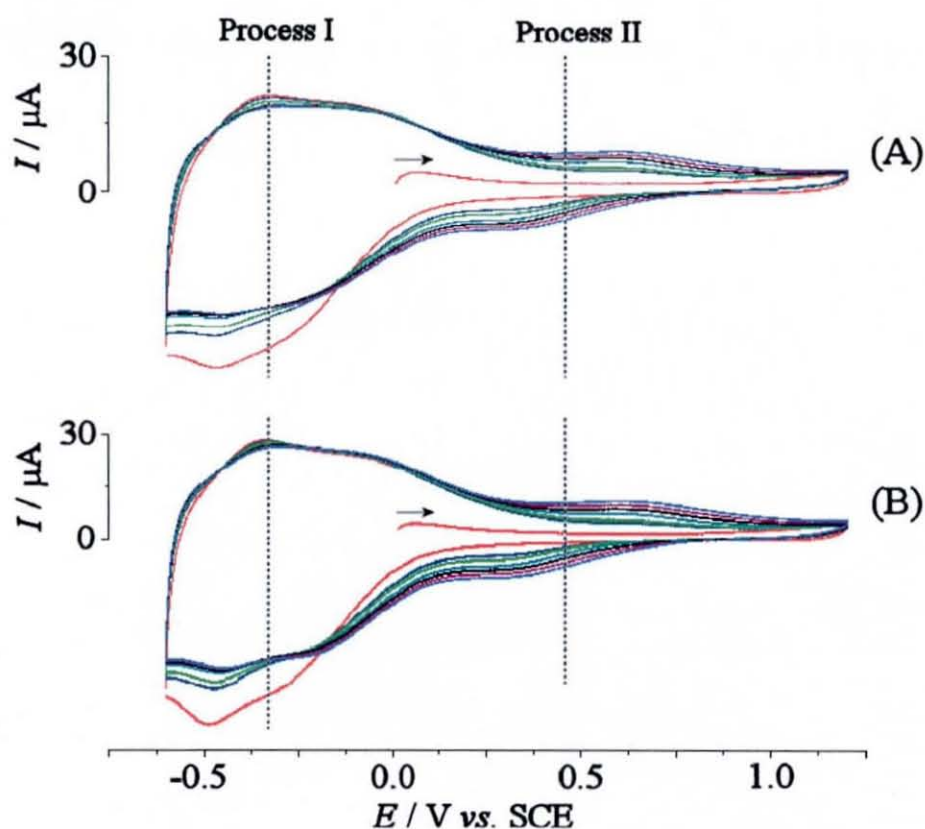

Figure 6.10. Multi-layer cyclic voltammograms (scan rate 100 mVs^{-1}) for (A) 2 layers and (B) 4 layers of CeO_2 – CHHCA deposit on ITO, heat treated at 500°C, and immersed in aqueous phosphate solution (1 mM, pH 7) in 0.1M KCl. Scans 1, 2, 3, 4, 6, 8 and 10 are shown in each case.

Next the electrochemistry of CeO_2 nanoparticle films was investigated in organic solvents.

6.5. Reactivity of CeO₂ Nanoparticle Films in Organic Solvents

The voltammetry of CeO_2 in aqueous media is very similar to that for TiO_2 but the CeO_2 is less stable. In organic solvents CeO_2 should be much more stable towards dissolution and stable voltammetric signals should be obtained. Figure 6.11 shows the voltammetry for a 10 layer CeO_2 phytate deposit in 0.1 M hexaflurophosphate in acetonitrile. The voltammetric response for Process I and Ce(IV/III) electrochemistry is seen to decrease slightly, as in aqueous KCl solution. However, the CeO_2 nanoparticle film appears more stable in the organic solvent compared to in aqueous solution with no redox peak associated with process II and the formation of $CePO_4$ being observed.
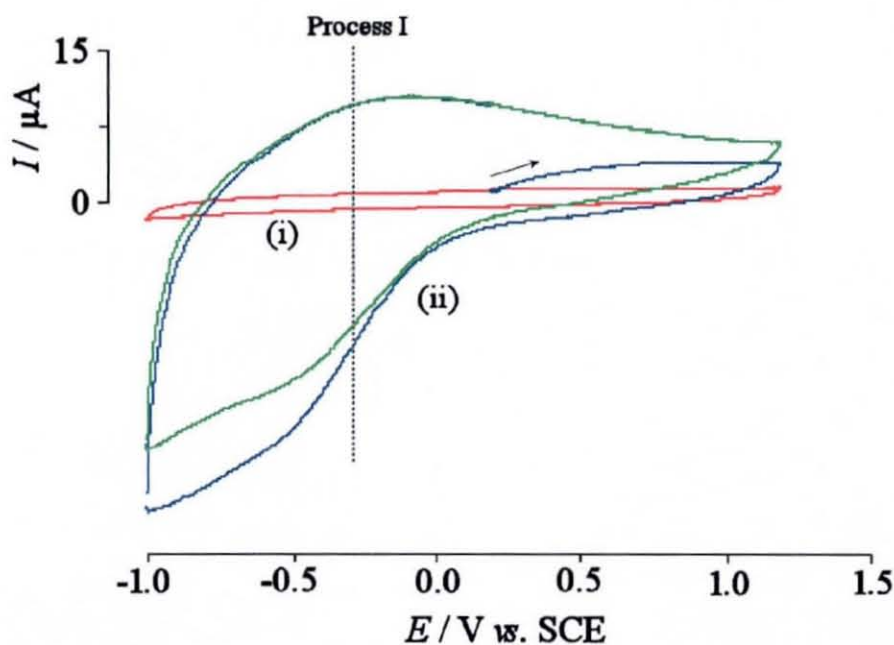

Figure 6.11. Cyclic voltammogram (scan rate 100 mVs⁻¹) for (i) a clean ITO glass electrode and (ii) a 10 layer CeO_2 phytate film deposited onto ITO and immersed in 0.1 M hexaflurophosphate in acetonitrile. The blue line corresponds to scan 1 and the green line scan 2.

Next, the effect of scan rate on the electrochemistry of the CeO_2 phytate nanoparticle films was investigated, with both the Faradaic and capacitive currents increasing.
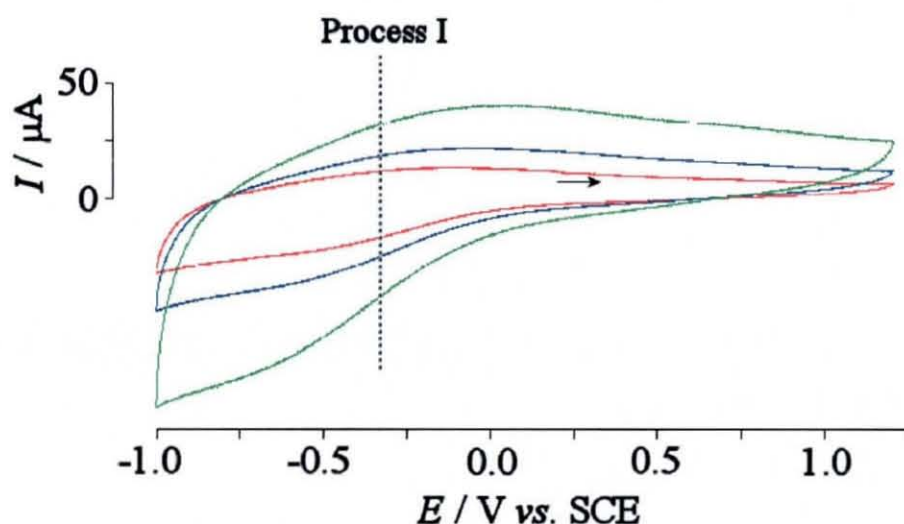
Figure 6.12. Cyclic voltammogram at various scan rates of a 10 layer CeO_2 phytate film deposited onto ITO and immersed in 0.1 M hexaflurophosphate in acetonitrile. The red line corresponds to a scan rate of $100 \, mVs^{-1}$, blue line to $200 \, mVs^{-1}$ and the green line to $500 \, mVs^{-1}$.

6.6. Conclusions

It has been shown that CeO_2 is electrochemically active and not inert. A reduction assigned to a Ce(IV/III) process has been observed and follow-up chemistry in the presence of phosphate discovered. The interfacial formation of $CePO_4$ has been proven and effects of the type of deposit, the phosphate concentration and pH on the process analysed.

In future, it is possible to use and exploit the ability of CeO_2 nanoparticles to form surface cerium phosphates and to give distinct electrochemical responses. The study could be expanded to other analytes such as arsenates and chromates to allow a novel way of determining small concentrations in solution. The importance of Ce^{4+} as an oxidation reagent in organic chemistry could lead to novel surface electrochemical processes with a heterogeneous Ce(IV) system.

6.7 References

[1] J.L. Yuan, B.H. Lu, X. Lin, L.B. Zhang, S.M. Ji, *J. Mater. Processing Technol.* 129 (2002) 171

[2] R.V. Siriwardane, J.A. Poston Jr, E.P. Fisher, T.H. Lee, S.E. Dorris, U. Balachandran, *Appl. Surf. Sci.* 217 (2003) 43

[3] S. Matsumoto, *Catal. Today* 90 (2004) 183

[4] D. Uy, A.E. O'Neill, L. Xu, W.H. Weber, R.W. McCabe, *Appl. Catal. B* 41 (2003) 269

[5] N. Mora, E. Cano, J.L. Polo, J.M. Puente, J.M. Bastidas, *Corros. Sci.* 46 (2004) 563

[6] J. Ma, T.S. Zhang, L.B. Kong, P. Hing, S.H. Chan, *J. Power Sources* 132 (2004) 71

[7] C.G. Granqvist, A. Azens, A. Hjelm, L. Kullman, G.A. Niklasson, D. Ronnow, M. Stromme Mattsson, M. Veszelei, G. Vaivars, *Sol. Energy* 63 (1998) 199

[8] M. Veszelei, M. Stromme Mattsson, L. Kullman, A. Azens, C.G. Granqvist, *Sol. Energy Mater. Sol. Cells* 56 (1999) 223

[9] For a review see M. Mogensen, N.M. Sammes, G.A. Tompsett, *Solid State Ionics*, 129 (2000) 63

[10] A.J. Bard (Ed.), *Encyclopedia of Electrochemistry of the Elements Vol. VI*, Marcel Dekker, INC Chapter VI-2 1976

[11] M.D. Ward, in I. Rubinstein (Ed.), *Physical Electrochemistry*, Marcel Dekker, New York, 1995, p. 293

[12] G. Silversmit, H. Poelman, L. Fiermans, R. De Gryse, *Solid State Commun.*, 119 (2001) 101

[13] A.Q. Wang, T.D. Golden, *J. Electrochem. Soc.*, 150 (2003) C616

Conclusions / Summary

The work carried out for this thesis is subdivided into five main experimental chapters describing (i) the characterisation of TiO_2 (anatase) mono-layer nanoparticle films, (ii) electrochemical processes in TiO_2 multi-layer films, (iii) work on novel biphasic electrode systems based on mesoporous nanoparticle assemblies, (iv) work with thin films of TiC nanoparticles, and (v) work with CeO_2 nanoparticle assemblies.

Mono and multi-layer films of TiO_2 (anatase) nanoparticles have been formed at boron-doped diamond and tin-doped indium oxide (ITO) coated glass electrode surfaces respectively. The layer-by-layer deposited films were characterised using field emission gun scanning electron microscopy (FEGSEM), the quartz crystal microbalance technique, cyclic voltammetry, and impedance spectroscopy giving insights into oxide surface processes. The incorporation of different binder molecules (carboxymethyl-γ-cyclodextrin, 1,4,7,10-tetraazacyclododecane-1,4,7,10-tetrayl- tetrakis(methyl-phosphonic acid, phytic acid, pyrroloquinoline quinone and Nafion®) into the multi-layer TiO_2 (anatase) nanoparticle films allowed further insights into the electron transport and transfer at the TiO_2 | liquid interface to be obtained. Possible analytical applications for the novel TiO_2 films have been explored.

The transport of anions and protons in biphasic electrode processes has been demonstrated on basal plane pyrolytic graphite discs and in mesoporous TiO_2 (anatase) nanoparticle membranes on ITO substrates.

It has been shown that TiC nanoparticles can be deposited onto ITO substrates and electrochemically oxidised to give core-shell TiC-TiO_2 nanoparticles, characterised using FEGSEM, transmission electron microscopy, and cyclic voltammetry. The use of thermal oxidation to generate core-shell TiC-TiO_2 nanoparticles has also been demonstrated under X-ray diffraction conditions during heating in air. Core-shell TiC-TiO_2 nanoparticles represent a novel electro-catalytically active material for mesoporous thin film or other types of composite electrodes.

The surface electrochemistry of CeO_2 nanoparticle films and the effect of the binder molecule on multi-layer formation and electrochemistry have been shown. A new phosphate phase is formed during electrochemical reduction of CeO_2 in aqueous phosphate buffer solution that is sensitive to phosphate concentration and pH. The electrochemistry of multi-layer CeO_2 nanoparticulate films in organic solvent is shown to be more stable.

Publications

- "Liquid | Liquid Ion Transfer Processes at the Dioctylphosphoric acid (N,N-didodecyl-N',N'-diethyl-phenylenediamine) | Water (electrolyte) Interface at Graphite and Mesoporous TiO₂ Substrates" S.J. Stott, K.J. McKenzie, R.J. Mortimer, C.M. Hayman, B.R. Buckley, P.C.B. Page, F. Marken, G. Shul, M. Opallo, *Anal. Chem.* 76 (2004) 5364

- "Mesoporous TiO₂ – Carboxymethyl – γ – Cyclodextrate Multi-layer Host Films: Adsorption and Electrochemistry of 1,1'-Ferrocenedimethanol" S.J. Stott, R.J. Mortimer, K.J. McKenzie, F. Marken, *Analyst* 130 (2005) 358

- "Electrochemical Reactivity of TiO₂ Nanoparticles Adsorbed onto Boron Doped Diamond Surfaces" F. Marken, A.S. Bhambra, D-H, Kim, R.J. Mortimer, S.J. Stott, *Electrochem. Commun.* 6 (2004) 1153

- "Electrochemical Properties of Core-Shell TiC-TiO₂ Nanoparticle Films Immobilized at ITO Electrode Surfaces" S.J. Stott, R.J. Mortimer, S.E. Dann, M. Oyama, and F. Marken, *Phys. Chem. Chem. Phys.* 46 (2006) 5437

- "Layer-by-Layer Deposition of Open-Pore Mesoporous TiO₂- Nafion Film Electrodes" Elizabeth V. Milsom, Jan Novak, Stephen J. Green, Xiaohang Zhang, Susan J. Stott, Roger J. Mortimer, Karen Edler, and Frank Marken *accepted by J. Solid State Electrochem.*